UNIVERSITY OF CALABRIA

Shape Memory Alloy (SMA) connectors for ultra-high vacuum applications: modeling and testing

Valentina Giovinco

Supervisors:

Prof. Carmine Maletta [1]

Dr. Cedric Garion [2]

Coordinator:

Prof. Domenico Mundo

A thesis presented for the degree of

Doctor of Philosophy

Department of Mechanical, Energy and Management Engineering (DIMEG)

Geneva, January 2024

[1] University of Calabria (UniCal)
[2] European Organization for Nuclear Research (CERN)

Alla mia cara nonna,

Con la promessa di divertirmi.

Contents

Abstract

Shape Memory Alloy (SMA) connectors have been developed at CERN in recent years for Ultra-High-Vacuum (UHV) applications in the Large Hadron Collider (LHC) as an alternative to the traditional coupling provided by metallic flanges tightly connected by several screws or heavy collars. SMA couplers offer many advantages, including low cost, compact size, ease of assembly and maintenance, ability to make bi-material connections, and ability to be remotely controlled by temperature variation, limiting the need for human presence in highly radioactive areas of the accelerator. The working principle of a SMA connector is based on thermoelastic martensitic transformations between two crystallographic structures, austenite and martensite. The object of this project is the testing and modelling of SMAs in order to investigate and describe the macroscopic behaviour of the material. Methods and measurements of an extensive experimental campaign on Nickel-Titanium (NiTi) alloy specimens are herein presented and discussed. Different stress and temperature conditions are investigated, as well as the thermo-mechanical training of different shaped connectors (rings, ovals, C-shaped) and the constrained recovery capability of ring couplers. Two analytical models based on the elastic-plastic theory of axial-symmetric bodies have been developed to describe the pre-expansion and constrained recovery of SMA rings. Systematic comparisons between the analytical predictions with Finite Element Analysis (FEA) and experimental measurements show very good agreement. Finally, SMA constitutive modelling and FE simulations by a user-defined material model have been performed. Models and results are herein presented. This thesis provides robust tools to be used for the design of SMA couplers with shape recovery capabilities.

Keywords: Shape memory alloys, NiTi alloys, vacuum connections, constrained recovery.

Abstract (IT)

Connettori in lega a memoria di forma (SMA) sono stati sviluppati recentemente al CERN per applicazioni di ultra-alto-vuoto (UHV) nel Large Hadron Collider (LHC) come alternativa alle tecniche di connessione tradizionali, effettuate mediante saldature/brasature o flange metalliche collegate da viti o collari pesanti. I connettori SMA offrono molti vantaggi, tra cui il basso costo, le dimensioni compatte, la facilità di montaggio e manutenzione, la possibilità di effettuare connessioni bimateriali e di essere controllati a distanza mediante variazione di temperatura, limitando la necessità di presenza umana nelle aree altamente radioattive dell'acceleratore. Il principio di funzionamento di un connettore SMA si basa su un comportamento unico del materiale dovuto a trasformazioni martensitiche termoelastiche tra due strutture cristallografiche, austenite e martensite. L'obiettivo di questo progetto è la sperimentazione e la modellazione delle leghe a memoria di forma con lo scopo di investigare e descrivere il comportamento macroscopico del materiale. Vengono presentati e discussi i metodi e i dati raccolti da una vasta campagna sperimentale su campioni di lega Nickel-Titanio (NiTi). Lo studio riguarda diverse condizioni di sollecitazione e temperatura, nonché il processo di formazione di diverse forme di connettori e il recupero vincolato di un anello in NiTi. La tesi presenta inoltre due modelli analitici, sviluppati sulla base della teoria elastoplastica dei corpi assialsimmetrici, utili a simulare le due fasi del processo di accoppiamento dei connettori ad anello, la formazione e l'attivazione termica (montaggio e smontaggio). I dati ottenuti dalle previsioni analitiche mostrano un ottimo accordo con i risultati delle simulazioni agli elementi finiti e le misure sperimentali. Infine, un modello fenomenologico tridimensionale è implementato in ANSYS mediante l'utilizzo di una subroutine esterna per simulare il processo di accoppiamento di diverse forme di accoppiatori in NiTi, come anelli, ovali e connettori a C. La teoria del modello e i risultati delle simulazioni agli elementi finiti sono presentati e discussi. In conclusione, la tesi fornisce strumenti di progettazione robusti per gli accoppiatori SMA con capacità di recupero di forma.

Declaration of originality

I hereby declare that this thesis entitled *Shape Memory Alloy (SMA) connectors for ultra-high vacuum applications: modeling and testing* is an outcome of my own independent and original work. The project is free from any plagiarism. Moreover, I certify that I have correctly acknowledged all the sources consulted for the completion of the dissertation.

Acknowledgments

I had the opportunity to work in one of the greatest and most important research centers in the world, such as CERN, being part of the marvelous mechanical engineering team of the University of Calabria: it was an enormous honor for me. I am aware of the privilege I had which makes me proud and infinitely grateful. I would like to sincerely acknowledge all the people who contributed to the success of this work and who accompanied me through this great experience.

To Paolo Chiggiato, TE/VSC group leader at CERN and precious guide during these years, for the kind support, valuable suggestions and always motivating me in my work.

To my supervisors, Carmine Maletta, Professor at the University of Calabria, and Cédric Garion, TE/VSC-DLM section leader at CERN, for choosing and guiding me during the three years of my Ph.D., for all their commitment to my professional education.

To Fabrizio Niccoli, a point of reference during my studies, for all the important teachings and crucial support.

To Giulia Scalet and Prof. Ferdinando Auricchio of the University of Pavia, for kindly providing me with the FORTRAN code of the subroutine used for the finite element analysis.

To my colleagues and friends, from CERN to the University, for the shared life, laughter, thoughts, knowledge and coffee, for making these years so special.

To my wonderful family, my safe harbor, for the unconditional presence and love. I will never miss an occasion to express my endless gratitude for you. Grazie di tutto.

To Alessandro, my partner in life, for always believing in me and never making me feel lonely, for letting me talk and sometimes even listening, for his encouragement and patience from the beginning of my Ph.D., for standing by me and not letting go of my hand, which spurred me on to do my best.

Introduction

CERN's accelerator complex

CERN, the European Organization for Nuclear Research (Conseil Européen pour la Recherche Nucléaire, in French), is an intergovernmental organization founded in 1954 and based in Geneva. Its primary mission is to study the fundamental particles that make up the universe and the forces that govern their interactions. CERN's infrastructure consists of a series of particle accelerators and associated facilities that make it one of the most advanced particle physics laboratories in the world. In the accelerators, charged particles, such as protons and ions, are accelerated to nearly the speed of light and made to collide with other particles traveling in the opposite direction or with a target. A schematic view of CERN's accelerator complex is shown in Figure 1. The accelerator chain starts with the linear accelerators (LINAC), where low energy particles are accelerated, proceeds with the proton ring accelerators (BOOSTER, PS and SPS) and terminates with the Large Hadron Collider (LHC). The LHC consists of a pair of superconducting storage rings where two high-energy proton or heavy ion beams are accelerated in opposite directions to finally collide at an energy of 7 TeV per beam at various detectors located around the ring.

The Large Hadron Collider

The LHC is the largest and most powerful particle accelerator in the world. It extends over a circumference of about 27 km at about 100 m underground along the French-Swiss border and works mostly at a temperature of 1.9 K, the operating temperature of the superconducting magnets [1]. Four detectors are inserted along the ring, dedicated to different experiments: ATLAS and CMS, for high luminosity proton-proton collisions, LHCb, for medium luminosity proton-proton collisions, and ALICE, for low luminosity ion collisions [2]. The general layout of the LHC is given in Figure 2.

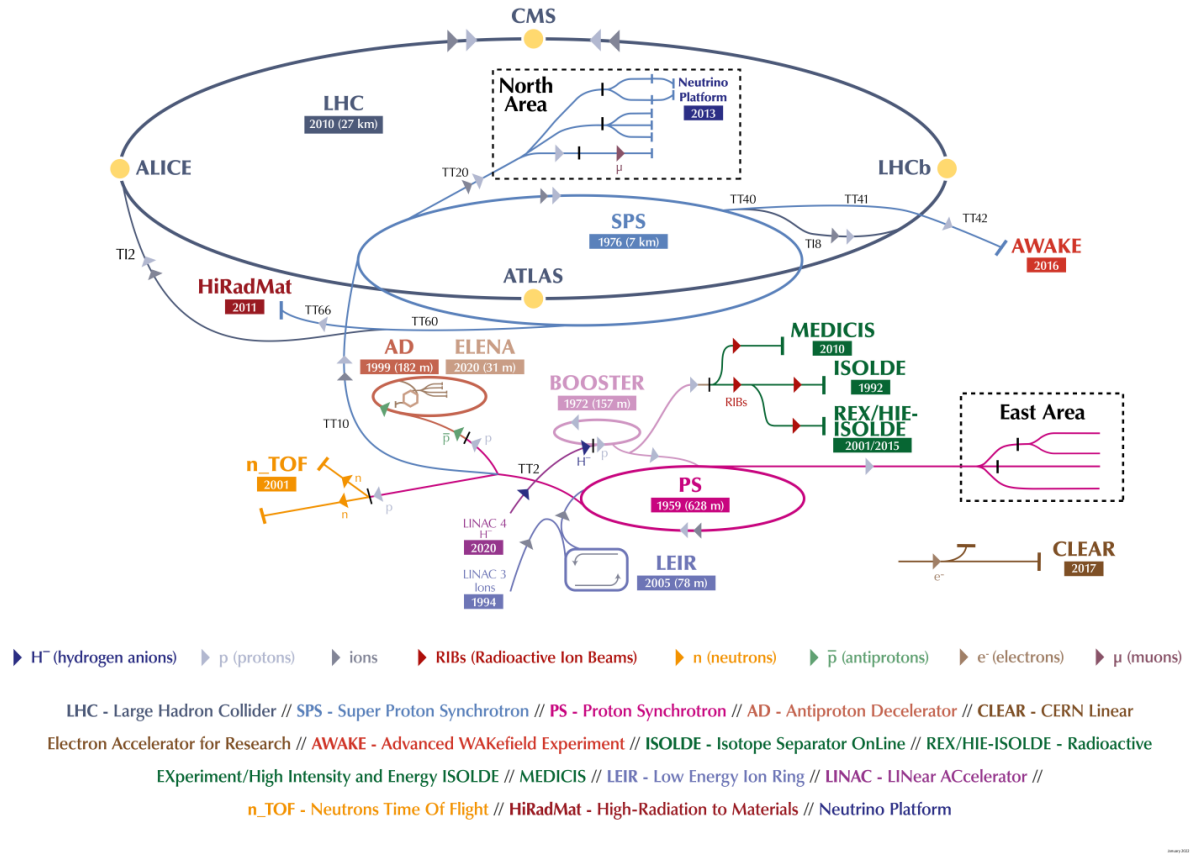

Figure 1: Schematic representation of the accelerator complex. Image credit: CERN.

The LHC is also among the largest operational vacuum machines in the world, consisting of two main systems: the cryogenic insulation, a system of 50 km of pipes operating at a pressure of $10^{-6} mbar$, and the beam vacuum, consisting of 54 km of pipes at a pressure of less than $10^{-10} mbar$. The construction of the two vacuum systems required an enormous number of components, including pumps, valves, gauges, 250 000 welds, and 18 000 vacuum seals. In particular, the coupling systems are critical to the quality of the vacuum, as they are the primary source of leakage in the accelerator. Ensuring proper vacuum in the accelerator means allowing the beam to circulate through the machine without interacting with gas molecules. In fact, such interaction would drastically reduce the probability of collision and particle detection.

Vacuum connection techniques: tradition vs innovation

Traditional vacuum joining techniques at CERN consist mainly of welding and brazing (permanent joints) and vacuum flanges (removable joints). Although these techniques have been extensively studied and are now validated and reliable technologies, they have some limita-

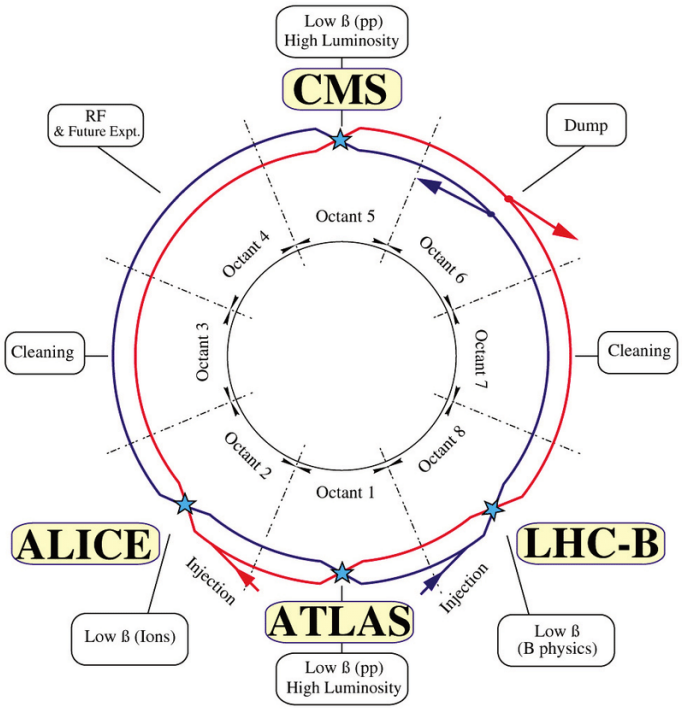

Figure 2: General layout of the LHC, from [3].

tions. Within the LHC ring, beams of protons or ions circulate and collide. The effect is the emission and transmission of energy in the form of waves and particles through space and materials, which is dangerous to human health. Therefore, the presence of operators in the radioactive areas must be strictly limited. In addition, the need for compact equipment is clearly indicated by the limited space available in the tunnel. These reasons, together with the need for low-cost, easy-to-assemble and maintain systems and bimaterial connections, led CERN to invest in research into new coupling technologies to overcome the present restrictions.

Innovative materials with unique characteristics have been identified to be used for the development of demountable coupling systems for vacuum and ultra-high vacuum applications: the Shape Memory Alloys (SMAs). SMAs are metal alloys able to recover large deformations under the action of thermal or mechanical loads. To realize the connections, the SMAs exploit the unique shape-memory effect, i.e. the ability to recover large deformations upon temperature change. This effect is related to the solid-state phase transformations occurring between two crystallographic phases, the martensite (monoclinic B19') and the austenite (body-centered cubic, B2) [4, 5]. In particular, the martensite-to-austenite transition is induced by heating and causes the SMA to contract. The austenite-to-martensite transition is not inherent in the alloy but can be induced by a so-called training process; it is triggered by cooling and causes SMA

relaxation. If the SMA is prevented from deforming by the presence of a constraint, large forces will be developed upon contact with the other element. Such a process is called constrained-recovery and is at the bases of the functioning of the SMA couplers. An image of a SMA connection system is shown in Figure 3.

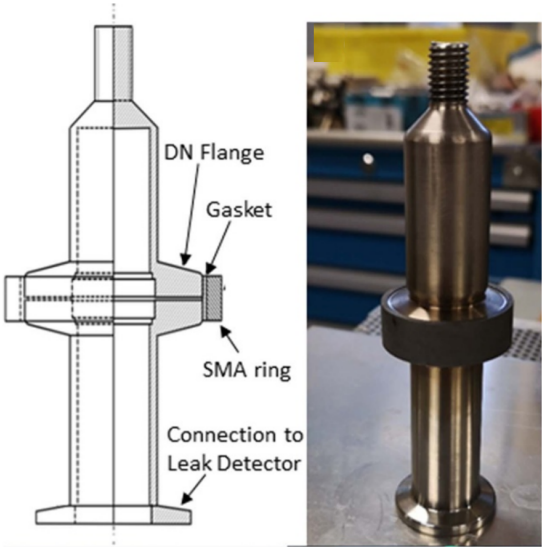

Figure 3: Prototype UHV chamber for leak tightness tests: **a)** Schematic of the coupling geometry, and **b)** DN16 chamber (outer diameter30 mm).

SMA-based systems must ensure leak-tight connections at operating temperature as well as offer the possibility of easy assembly and disassembly. Previous studies [6, 7, 8] found the Nickel-Titanium (NiTi) alloy to have the best properties for this particular application. In particular, NiTi alloys are suitable for room temperature operation, providing a fast and compact solution at a reasonable cost. Their use is particularly relevant for restricted access areas of particle accelerators, as they can be remotely mounted and dismounted due to temperature variations, preventing human operators from working *in-loco*. The connectors are designed to be compatible with commercially available flanges (DN16, DN25, DN100) used in vacuum systems worldwide, so they are easy to implement.

Motivation and contribution of the work

This thesis is carried out in the context of the project already underway and presented in the previous section, with the aim of streamlining the design phase of SMA connectors by means of dedicated analytical and numerical tools, validated by extensive experimental analysis. These

tools can be used in the initial design phase to study and analyze the performance of a specific connector, as well as the influence of various geometric and process parameters on the coupling. The same study, if carried out in a laboratory, would be very costly and time-consuming, thus slowing down the related research. Due to the complexity of the SMA behavior and the inability to include all the influencing factors in a mathematical model, a lack of accurate models for analytically simulating the constrained recovery process has been found in the literature. Also, SMA dedicated models in the commercial FE software (ANSYS, COMSOL, ABAQUS) revealed to be not accurate for the simulation of the constrained recovery process.

The research activities proposed in the dissertation have been carried out mainly towards three different sides: the *experimental analysis* to investigate the NiTi response under different stress and temperature states, covering all microstructural phases during an austenite-to-martensite transition and reproducing different operating conditions; the development of *analytical tools* to be used for predicting the response of axialsymmetric geometries, such as the ring couplers, both in the training phase and in the actual operating phase; the study of the *numerical modeling* supported by commercial FE code and the implementation in ANSYS of a user-defined material subroutine of a three-dimensional phenomenological model previously developed [9], as a flexible methodology to simulate the coupling process of different shaped connectors (rings, ovals, C-shaped).

Thesis structure outline

The thesis is organized in the following five chapters.

The first chapter is entitled *Vacuum technology in particle accelerators* and gives a general overview of the phenomena and laws related to vacuum in particle accelerators. Special attention is given to the LHC vacuum systems, which consist of a number of components coupled by permanent or removable joints. The latter are listed and discussed in order to provide the reader with an overall picture of the traditional joining techniques currently used in the LHC and in particle accelerators in general.

The second chapter is entitled *Shape memory alloys: history, properties and applications* and is dedicated to an introduction and discussion of this innovative class of materials, which includes many metal compounds with different properties. In particular, most of the references in the chapter relate to the near-equiatomic NiTi alloy, which is the most interesting and flexible

compound in terms of industrial applications. Mechanical and functional properties of the shape memory alloys are presented and analyzed, at the lattice and microstructural scale as the cause of the unique response observed at the macroscopic scale. General applications of the shape memory alloys are discussed before introducing the special case of SMA couplers developed at CERN for vacuum and ultrahigh vacuum interconnects. The advantages of these innovative systems over traditional techniques are presented.

The third chapter is entitled *Experiments: material and methods* and presents the methodology and results of an extensive experimental campaign carried out on NiTi samples. Isothermal and isobaric tests are performed to study the material response under different conditions. The training phase of NiTi couplers of different shapes is validated and related methods and results are presented.

The fourth chapter is entitled *Analytical modeling of the coupling process performed by SMA rings* and is devoted to the presentation of two analytical models developed for the simulation of the two phases of a coupling process, which are the pre-deformation and the actual operation of the ring. They include the mechanical loading/unloading of the ring in martensitic conditions and the thermal activation cycle that allows the assembly and disassembly of the joint, respectively. The models are validated by experimental data.

Finally, the fifth chapter is entitled *SMA numerical modeling and FE simulations* and deals with the numerical modeling of the coupling process performed by a shape memory alloy element. In this case, different shapes of connectors and systems are explored. The material model used for the simulations is a user-defined model implemented by a FORTRAN code subroutine. The model is validated by experimental data.

Chapter 1

Vacuum technology in particle accelerators

1.1 Abstract

This chapter provides a general overview of vacuum in particle accelerators. The first section covers basic vacuum knowledge, including ideal gases and their laws, flow regimes, gas sources, and outgassing of materials. Next, pumping is introduced as one of the fundamental factors that determine the quality of a vacuum system. In particular, the classification of vacuum pumps and distributed pumping in particle accelerators is discussed. To emphasize the importance of adequate pressure conditions in the accelerator machine, the effects of the interaction between residual gases and the particle beam are presented, such as the dramatic reduction in the probability of collisions and particle detection. The focus of the chapter remains in the accelerator domain with a presentation of the vacuum systems in the Large Hadron Collider (LHC) at CERN, namely the thermal insulation and the beam vacuum systems, which operate at different pressure levels. At the end of the chapter, a study of the traditional sealing techniques used in particle accelerators is presented, which are the main sources of leakage in the LHC machine.

1.2 Basic knowledge

Vacuum is an operating condition required by many modern high-tech systems, and the related physics is at the center of various scientific research. In engineering and physics, vacuum is defined as a volume in which the pressure is less than the atmospheric pressure. In other words, the content of gas particles, atoms and molecules in the vacuum region is significantly lower than in the atmosphere, i.e. the density of the molecules is less than 2.5×10^{19} molecules/cm^3. A perfect vacuum is a space completely empty of matter [10, 11].

Particle accelerators operate under vacuum conditions, allowing the beam to travel through the pipes avoiding unwanted collisions with gas molecules and loss of beam energy. The presence of residual gases, in fact, reduces the efficiency of the accelerator due to the gas-beam interaction. This phenomenon is more critical in circular than in linear accelerators, as in the first ones the beam circulates more than once and particle losses and instabilities accumulate. The Large Hadron Collider (LHC) at CERN is the most extensive operational vacuum system in the world, consisting of a variety of vacuum technologies and operating under different pressure conditions [12, 13].

1.2.1 Ideal gas law

The pressure-volume-temperature conditions and the number of molecules of a gas are related by the ideal gas laws. An *ideal (or perfect) gas* is a state of matter in which the molecules are independent of each other. This concept is based on the following ideal assumptions [10]:

- the molecules are tiny spheres;
- the volume of the molecules is much smaller than the volume occupied by the gas;
- the molecules do not exert forces on each other;
- the trajectory of the molecules is completely random;
- the collisions between the particles are perfectly elastic.

A *real gas* is characterized by intermolecular forces. However, the behavior of most gases under certain pressure conditions can be approximated to that of ideal gases. In particular, hydrogen, nitrogen, argon, helium, krypton, neon and xenon are considered ideal gases at atmospheric pressure. At lower pressures, such as under vacuum conditions, many other gases approximate ideal gas behavior. The *equation of state* governing the thermodynamic equilibrium of an ideal gas is given below [11]:

$$p \cdot V = N_{\text{molecules}} \cdot k_{\text{B}} \cdot T \tag{1.1}$$

where p, V and T are the pressure, the volume and the absolute temperature, respectively, $\text{N}_{\text{molecules}}$ is the number of molecules of the gas and $k_{\text{B}} = 1.38 \cdot 10^{-23} \frac{mbar \cdot l}{K}$ is the Boltzmann constant.

1.2.2 Flow regimes

The gas dynamics is characterized by an important parameter, i.e. the *Knudsen number* K_{n}, which defines the gas rarefaction, as reported below:

$$K_{\mathrm{n}} = \frac{l}{d} \tag{1.2}$$

where l is the equivalent molecular mean free path, i.e. the average distance traveled by a gas molecule before substantially changing its direction or energy, typically as a result of one or more successive collisions with other particles. and d is the diameter of the flow channel. Depending on the value of the Knudsen number, the following three regimes of gas flow are distinguished [14]:

- Viscous (or continuous): $K_{\mathrm{n}} < 0.01$
- Transitional (or Knudsen): $0.01 < K_{\mathrm{n}} < 0.5$
- Molecular: $K_{\mathrm{n}} > 0.5$

The three conditions are schematically shown in Figure 1.1. When $K_{\mathrm{n}} < 0.01$, the gas can be considered as a continuous medium because the molecules collide with each other, but less frequently with the walls of the vessel, and the pressure conditions are low vacuum (viscous regime). When $K_{\mathrm{n}} > 0.5$, the intermolecular collisions can be neglected, the molecule-surface collisions dominate, and high/ ultra-high vacuum conditions occur (free-molecular regime). An intermediate value of K_{n} represents an intermediate state between the two regimes, and medium vacuum conditions occur (transitional regime) [14]. The graph in Figure 1.2 shows the evolution of the gas flow in tubes as a function of the pressure. Particle accelerators operate in the free molecular flow regime.

Pressure in a vacuum vessel

In general, pumping and gas load are the primary factors that determine the quality of a vacuum system. The *pressure in a vacuum vessel* is given by:

$$P = \frac{Q}{S_{\mathrm{eff}}} + P_0 \tag{1.3}$$

where Q is the rate of the gas release, which in particle accelerators can range between 10^{-5} and $10^{-15} mbar\ l\ s^{-1}\ cm^{-2}$, S_{eff} is the effective pumping speed, between 1 and 1000 $l\ s^{-1}$, and

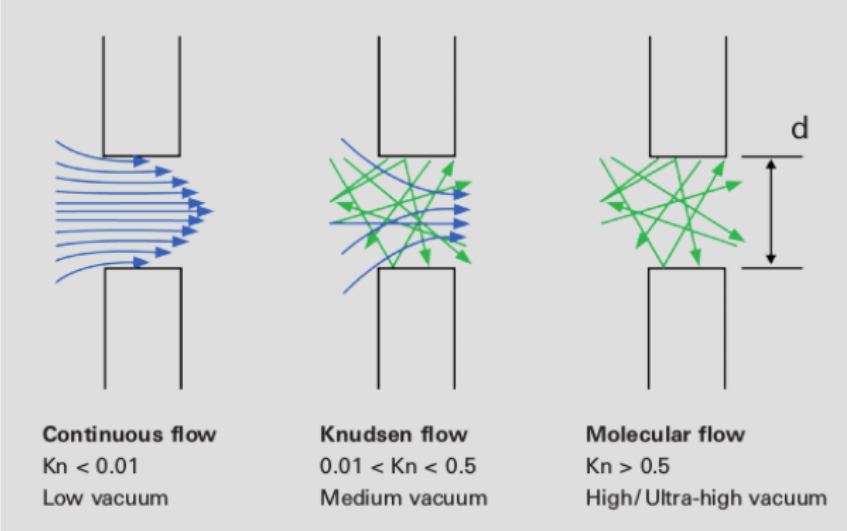

Figure 1.1: Flow regimes classification, from [15].

P_0 is the ultimate pressure, i.e. the ideal pressure in absence of gas load. In the free molecular regime, the *gas flow* Q between two generic points 1 and 2, is proportional to the pressure drop, as written below:

$$Q = C \cdot (P_1 - P_2) \tag{1.4}$$

where C is the gas conductance that is a function of circuit configuration and pressure. The conductance is relatively high at the beginning of the pump-down and then gradually decreases. The *effective pumping speed* S_{eff} is the one acting directly in the vacuum vessel and can be defined as:

$$\frac{1}{S_{\text{eff}}} = \frac{1}{S} + \frac{1}{C} \tag{1.5}$$

where S is the nominal pumping speed, i.e. the pumping speed value provided by suppliers, and C is the conductance of the interposed connection between the pump and the vessel (Equation 1.4), as shown in Figure 1.3. Therefore, if $C << S$ then $S_{\text{eff}} \simeq C$, which means that the pumping speed does not depend on the pump used if the conductance is very low. The pumping speed S can be defined as a function of the pump throughput Q_{p} and pump inlet pressure P, as follows [17]:

$$S = \frac{Q_{\text{p}}}{P} \tag{1.6}$$

More in general, the formula can be rewritten using the partial derivative, as reported below [14]:

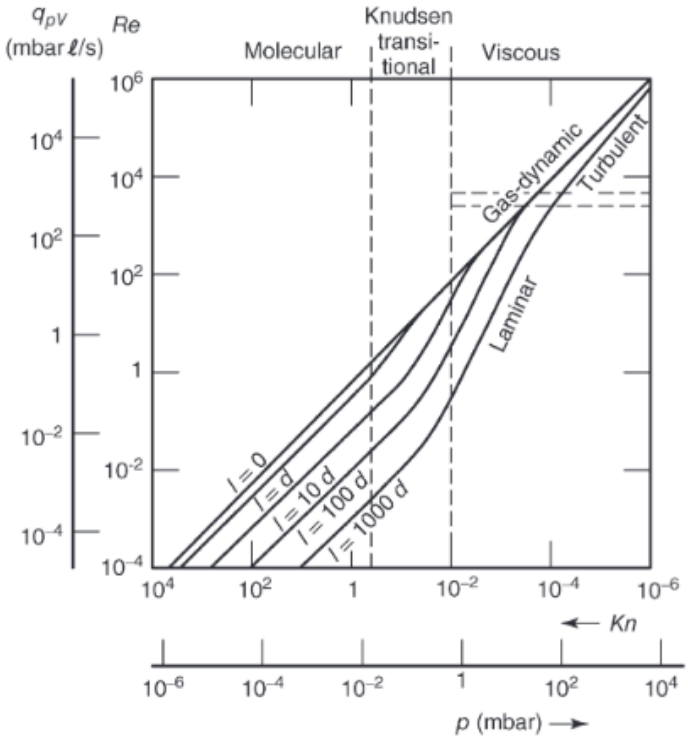

Figure 1.2: Flow types in tubes with circular cross section, diameter $d = 1cm$, and length l as indicated taken as an example. The gas is air at 20°C. Inlet pressure is taken as abscissa and the outlet pressure is assumed negligible, from [16].

$$S = \frac{\partial Q_{\mathrm{p}}}{\partial P} \tag{1.7}$$

The pumping speed can also be defined independently from the gas pressure and as a function of the pump features, as given below:

$$S = A_{\mathrm{p}} \cdot C' \cdot \alpha \tag{1.8}$$

where A_{p} is the area of the pump aperture, C' is the conductance of the unit surface area for given gas and α is the capture probability.

Vacuum ranges

In general, there are several levels and classifications of vacuum. Table 1.1 reports the vacuum ranges according to the American vacuum society (AVS) 1980. Accelerator sections operate under high to extreme-high vacuum.

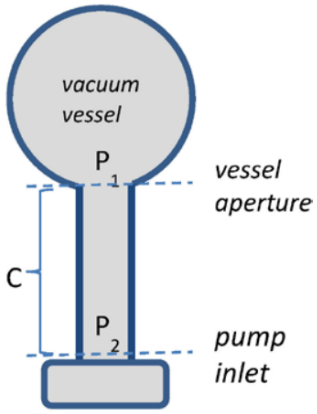

Figure 1.3: Schematic representation of a gas flow restriction of conductance C interposed between a pump and a vacuum vessel, from [18].

Table 1.1: Vacuum levels and their corresponding pressure ranges according to the American vacuum society (AVS) 1980, from [19].

Vacuum Level	**Pressure Range (mbar)**	**Typical applications**
Low Vacuum	10^{3} – 33	Vacuum cleaner, mechanical handling, vacuum forming.
Medium Vacuum	33 – 10^{-3}	Vacuum drying, vacuum freeze (food industries).
High Vacuum (HV)	10^{-3} – 10^{-6}	Production of microwave, light bulbs, vapor deposition.
Very high Vacuum (VHV)	10^{-6} – 10^{-9}	Electron microscopes, X-ray and gas discharge tubes, electron beam welding.
Ultra-High Vacuum (UHV)	10^{-9} – 10^{-12}	Particle accelerators, space simulators, material research, semiconductors.
Extreme-High Vacuum (XHV)	Below 10^{-12}	Particle accelerators, space simulators, advanced semiconductors devices.

1.2.3 Gas sources in beam vacuum

In the absence of leaks, the main sources of gas in the accelerator are [14]:

- *Outgassing*, the release of gas or vapor from materials in vacuum.
- *Degassing*, the deliberate removal of the gas from materials in vacuum.

- *Desorption*, the release of adsorbed chemical species from the surface of the material in vacuum.

The main reason for the gas release is the *surface contamination*, namely the presence of impurities on the material surfaces and in the bulk. When in bulk, dissolved atoms or molecules can diffuse through the surface. In general, there are several layers of contamination in the surface, which are shown in Figure 1.4. The first two layers are removed chemically by using solvents and detergents. The oxide and hydroxide layer is responsible for molecules gas release, in particular during their chemical transformations. Indeed, liquids and gas can be trapped in the material, due to the defects in the layers, and be released in vacuum. The outgassing phenomena are in general characterized by the *specific outgassing rate*, which gives the quantity of gas, in number of molecules, leaving a material per unit of time and surface area. Its value is strictly related to the material characteristics and ranges several orders of magnitudes [20].

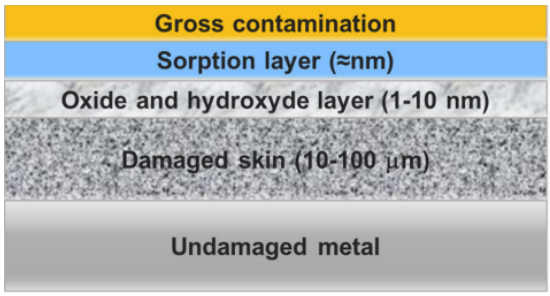

Figure 1.4: Schematic representation of the contamination layers in the materials, from [20].

1.2.4 Static outgassing

Static (thermal) outgassing is the intrinsic gas release of the material under vacuum. Molecules diffuse through the bulk material and are finally desorbed by the surface. Static outgassing depends on many factors, such as the material type, cleaning, treatments, and operation temperature. [19].

1.2.5 Dynamic outgassing

Non-thermal (dynamic) outgassing is a non-constant source of gas that depends on the characteristics of the circulating beam, as it is induced by the impact of energetic particles on the vacuum surfaces. This beam-stimulated desorption is due to the bombardment of energetic particles on the walls of the vacuum chamber, so that different phenomena take place [14]:

- *Photon stimulated desorption*, due to photons that impact or leave the surface. The photons are generated by a relativistic bent beam.
- *Ion Stimulated Desorption*, due to the ions generated by the ionization of residual gases by the circulating beam. The phenomenon gains energy from desorption because the more gas present in the chamber, the more the ionization of the particles. This results in a continuous increase in pressure.
- *Electron Stimulated Desorption*, due to the electrons impacting on the chamber walls. The specific mechanisms depends on the energy of the incident electron and the surface material.

Beam stimulated desorption is characterized by the *desorption yield*, defined as the number of gas molecules (N_m) desorbed per incident particles (N_i) [14]:

$$\mu = \frac{N_m}{N_i} \tag{1.9}$$

The desorption yield depends on many parameters, such as the type and energy of the incident particles, the roughness and cleanliness of the vacuum surfaces, the history of the material and the temperature conditions. The cross-section σ involved in the desorption process is calculated as a function of the desorption yield (μ) and the number of molecules available for desorption per unit surface area (N_d), as shown below [14]:

$$\sigma = \frac{\mu}{N_d} \tag{1.10}$$

Thus, the measurement of the desorption yield is done by measuring the incident particle flux and corresponding desorbed molecules. For charged particles, the measurement of the impinging flux is done by measuring the current. The main difficulty of this process consists in the suppression (or correction) of parasitic emission or reflection that can lead to the desorption of molecules from surfaces outside of the area under consideration and, consequently, introduce an error in the measurements. The measurement of the desorbed particle flux can be done following different methods. In the accelerator community, the mass spectrometer is used. This method consists in: 1) ionization of the desorbed particles to detect the mass spectrometer, 2) separation of the ions according to their mass-to-charge ratio by means of a magnetic or electric field, 3) detection of the separated ions, and 4) data analysis for the determination of the particle

flux.

1.2.6 Water outgassing

After the surface cleaning, the *water outgassing* is the dominant outgassing process in vacuum. The H_2O outgassing rate for unbaked metals is time dependent and can be calculated by the following empirical expression, typically applied at CERN for the design of the vacuum systems [20]:

$$q_{\mathrm{H_2O}} \simeq \frac{3 \cdot 10^{-9}}{t[h]} [\frac{mbar \cdot l}{s \cdot cm^2}] \tag{1.11}$$

There are three different ways that allow to reduce the H_2O outgassing rate [20]:

- Increase of the pumping time.
- Bakeout, i.e. the heating of the vacuum equipment *in situ* during part of the pumpdown time. For metals, the process takes 12h at 120°C.
- Cooling of the vacuum system at cryogenic temperature, to decrease the outgassing rate without decreasing the number of adsorbed water molecules. These latter remain on the surface, but are not be desorbed due to the very low temperature.

1.2.7 Hydrogen outgassing

After the reduction of the water vapor outgassing, the *hydrogen outgassing* becomes the dominant process. This is primarily the result of spontaneous diffusion and recombination at the material surface of the atomic hydrogen dissolved in the bulk. The outgassing rate in this case does not depend on the pumping time and can be permanently decreased by heating the chamber in vacuum or in air [20].

1.3 Vacuum pumping

In vacuum technology, the *vacuum pumps* are devices that can reduce and maintain the gas pressure in a vessel below the atmospheric pressure. They are distinguished according to the vacuum level to be achieved, as shown in Figure 1.5. In high and ultra-high vacuum, the gas molecules are characterized by molecular flow.

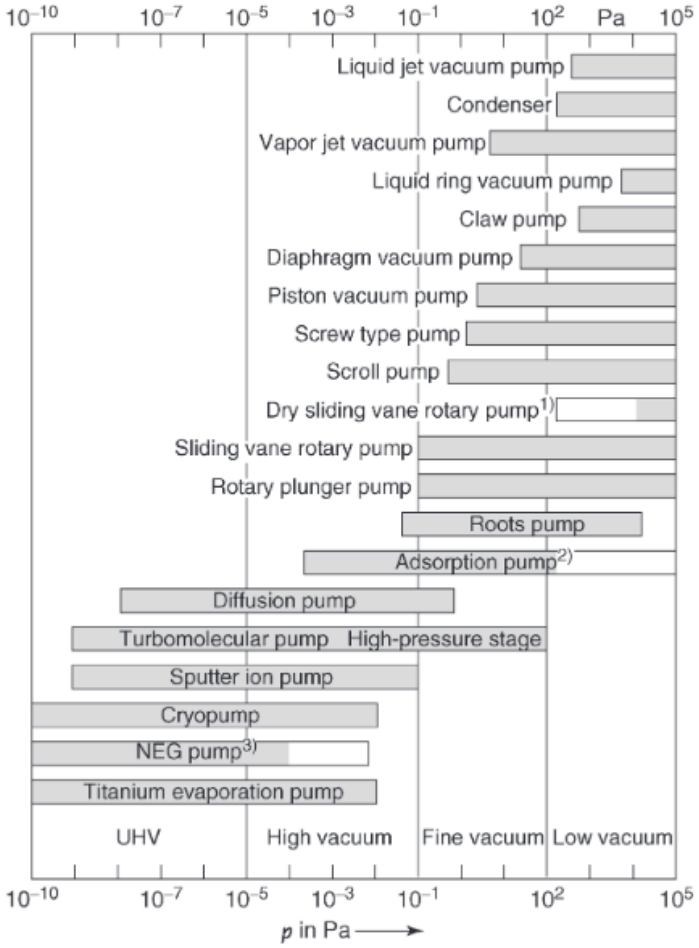

Figure 1.5: Overview of typical pump types and pressure ranges, from [19].

1.3.1 Pumps classification

Vacuum pumps operate either by transferring the gas molecules out into the atmosphere or by capturing and holding them on surfaces within the pump and can be classified as reported in Figure 1.6. In general, the main classification includes gas transfer pumps and binding pumps, which have different operating principles. In the *UHV gas transfer pumps*, the gas molecules collide with fast-moving surfaces that direct them to the pump outlet, where a primary pump, operating in viscous flow, is responsible for their final evacuation. In this type of device, the molecules do not exchange energy with each other. An example of a gas transfer pump is the *turbomolecular pump* (kinetic pump). The turbomolecular pumps operate in a pressure range of 10^{-1} to 10^{-10} $mbar$, generally below 10^{-5} $mbar$, while the operating range of a primary pump is 1 bar to 10^{-3} $mbar$. The turbomolecular pumping speed does not depend significantly on the mass of the molecule and is in the range of 10–25'000 $l \cdot s^{-1}$. This type of pump is generally a

non-permanent part of the vacuum system, i.e. it is attached when needed, and is typically used for testing (leak tests), conditioning (bakeouts), and evacuating a system from atmospheric to UHV [11].

In the *gas binding pumps*, gas molecules are attached to a surface in the vacuum, and all parts of the device are stationary. Getter, Ion pump, and Cryo pumps are examples of capture pumps. In particular, *getters* are special materials able to combine with gas molecules chemically or by absorption. Evaporable getters (or sublimation pumps) create surfaces onto which vapor and gas molecules will stick by condensation, adsorption or other mechanisms. Non-evaporable getters (NEG) operate at room temperature and remove the gas molecules from the chamber by a chemical process called activation, which consists of dissolving the surface contaminant into the bulk of the getter material. The NEG absorb most of the residual gas molecules at room temperature after thermal activation at about 200°C for 24 h. The efficiency of the getter pump is represented by the sticking probability α, which is defined as the ratio between the number of molecules captured and the number of molecules impinging on the getter surface. In general, $0.01 \leq \alpha \leq 0.1$ for H_2, and $0.5 \leq \alpha \leq 1$ for CO. However, getter materials do not pump noble gases and methane (CH_4) at room temperature, so the use of auxiliary pumps is necessary to maintain a stable pressure [17].

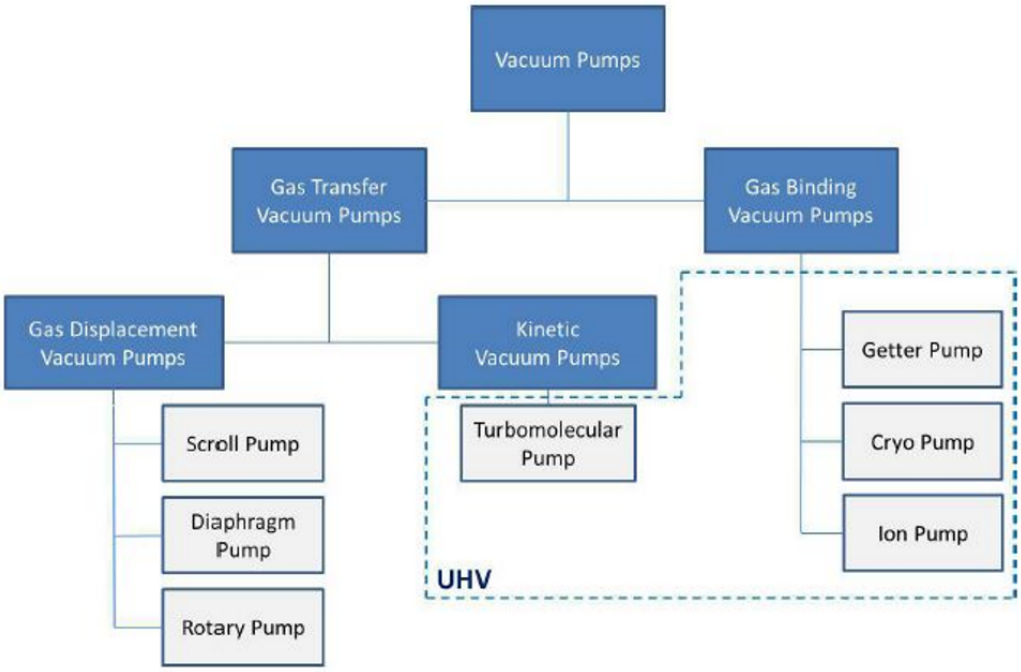

Figure 1.6: Classification of the vacuum pumps, from [21].

1.3.2 Distribuited pumping

Gas release is a distributed phenomenon throughout the accelerator. In contrast, the vacuum pumps are installed at precise points in the machine and act locally. As a result, the pressure profile along the ring is parabolic, with a maximum between two successive pumps. The pressure peak can also be amplified if the conductance of the beam pipe is low. To eliminate this problem and to create nearly constant pressure conditions along the vacuum machine, a distributed pumping system is required [22]. An innovative solution was developed at CERN in the late nineties [23] and is based on Non-Evaporable Getter (NEG) film coatings. This system works with beams from 2008 and concerns about 1400 vacuum chambers and 6 km of pipes of the LHC. In detail, the vacuum chambers are coated with Ti-Zr-V thin film and heated above 180°C for 24 h. The activation aims to dissolve the native oxide layer into the bulk of the film, so that at room temperature the surface is clean and able to pump most of the residual gas species [22]. It is worth noting that NEG coating can only be implemented in the sections of the accelerator that operate at room temperature.

1.4 The gas-beam interaction

The presence of air or other gases in the machine significantly affects the performance of the accelerator and collision experiments due to the possible interaction with the beam. First, the gas-beam interaction can cause the charged particles to lose energy and be deflected from their original path, leading to particle scattering and beam instability. The resulting increase of the beam size reduces the probability of collisions in the detectors. In addition, the presence of residual gases can degrade experimental measurements by introducing unwanted background noise and interfering with the detection of the particles produced by the collision of the beams. Finally, beam losses due to poor vacuum increase the risk of damage to accelerator components due to induced radioactivity and heat loads on cryogenic equipment [24, 1, 22].

An important indicator of the efficiency and performance of the machine is the *beam lifetime*, defined as the time duration of the particle beam in the accelerator or storage rings. The total beam lifetime, denoted as τ, is defined below [24]:

$$\tau = \frac{1}{v \cdot \sigma \cdot n} \tag{1.12}$$

where v is the speed of the beam, σ is the collision cross-section and n is the gas molecule density. The collision phenomena include the beam-beam collision (experiments) and gas-beam interaction (background). The latter consists of two different mechanisms: elastic and inelastic scattering. *Elastic scattering* occurs when the interaction does not result in a loss of kinetic energy. The beam particles can collide with residual gases, causing them to change direction and increase their betatron oscillation. When the amplitude of this oscillation becomes greater than the physical acceptance aperture of the beam, particles are lost. In the *inelastic scattering* the kinetic energy is not conserved and the interaction results in a decrease of the particles speed with consequent photon emission. If the energy loss exceeds the momentum acceptance of the accelerator, particles are lost [11]. Therefore, the beam lifetime imposed by the gas-beam interaction or other losses must be longer than the lifetime imposed by the beam collisions. In this regard, the role of the vacuum system in the accelerator is crucial, as it aims to keep gas-beam scattering negligible to prevent all the negative effects described above. In summary, vacuum systems must be designed to:

- Satisfy the required beam lifetime: τ= 100h in the LHC, equivalent to a density of hydrogen molecules of $10^{15} m^{-3}$ [13].
- Prevent transverse beam size increase at the interaction points: typical beam size in the LHC= 200–300 μm [2];
- Reduce radiation hazard.
- Provide low background in the detectors.

1.5 Vacuum system in the LHC

The LHC has three separate vacuum systems: the *insulation vacuum for cryomagnets*, the *insulation vacuum for the helium distribution line (QRL)* and the *beam vacuum*, which must meet different requirements. In the LHC, along 127 km of vacuum vessels, the pressure ranges from high to extreme-high vacuum, depending on the system. In particular, the insulation vacuum for the cryomagnets and the helium distribution line is not required to be lower than 10^{-1} mbar before cooling, but it must be established at 10^{-6} $mbar$ at cryogenic temperatures. In the case

of the beam vacuum, ultra-high and extreme-high vacuum are mandatory, since more stringent constraints must be satisfied with respect to the required beam lifetime and the background in the detectors. Specifically, the pressure must be lower than $10^{-10}\ mbar$. In addition, considering that the reference operating temperature in the beam pipes is 1.9 K (-254.15 °C), the vacuum also serves to shield the cryogenic components from heat sources [12]. Figure 1.7 shows a schematic representation of the cross-section of the LHC dipole magnet that allows to identify the three different vacuum systems. In general, LHC magnets consist of a north pole and a south pole, which create a magnetic field that bends the trajectory of the charged particles, forcing them to travel around the ring. The LHC dipole has a compact design, consisting of two beam pipes in which the charged particles travel and are held in beam vacuum conditions, inserted into a single iron yoke, operating at a temperature of 1.9 K. The insulation vacuum is the vacuum that surrounds the cryogenic system in the superconducting magnets in order to minimize heat transfer and maintain the low temperature required for superconductivity [24].

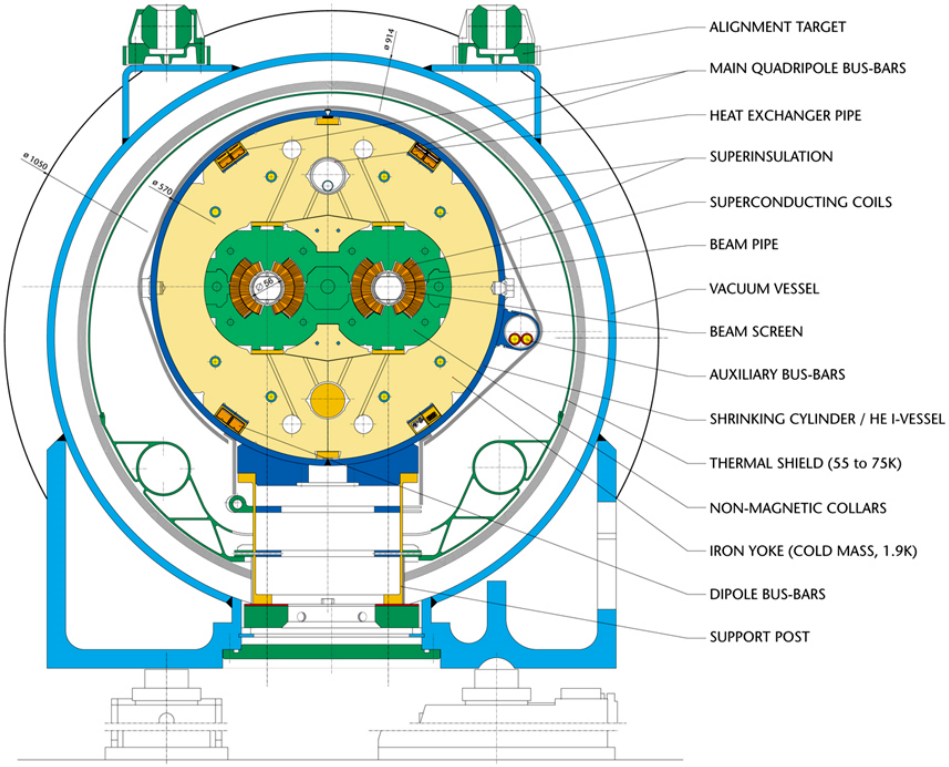

Figure 1.7: Cross section of LHC dipole, from [25].

1.5.1 Cryogenic insulation

The insulation vacuum implemented for the cryogenic systems, including the cryomagnets and the helium distribution line, aims to eliminate the heat losses due to the gas convection. It consists of a continuous cryostat that spans almost 3km in length and is divided into 14 sections, with each section measuring 214 m. Vacuum separation is achieved by means of vacuum barriers, namely thin metallic membranes that separate the wall of the cryostat, at room temperature, from the shell of the cryomagnets, as well as the cryogenic distribution line from the machine cryostat, as shown in Figure 1.8. These barriers allow to keep the individual parts of the systems separate, so that they can be pumped and tested independently [24].

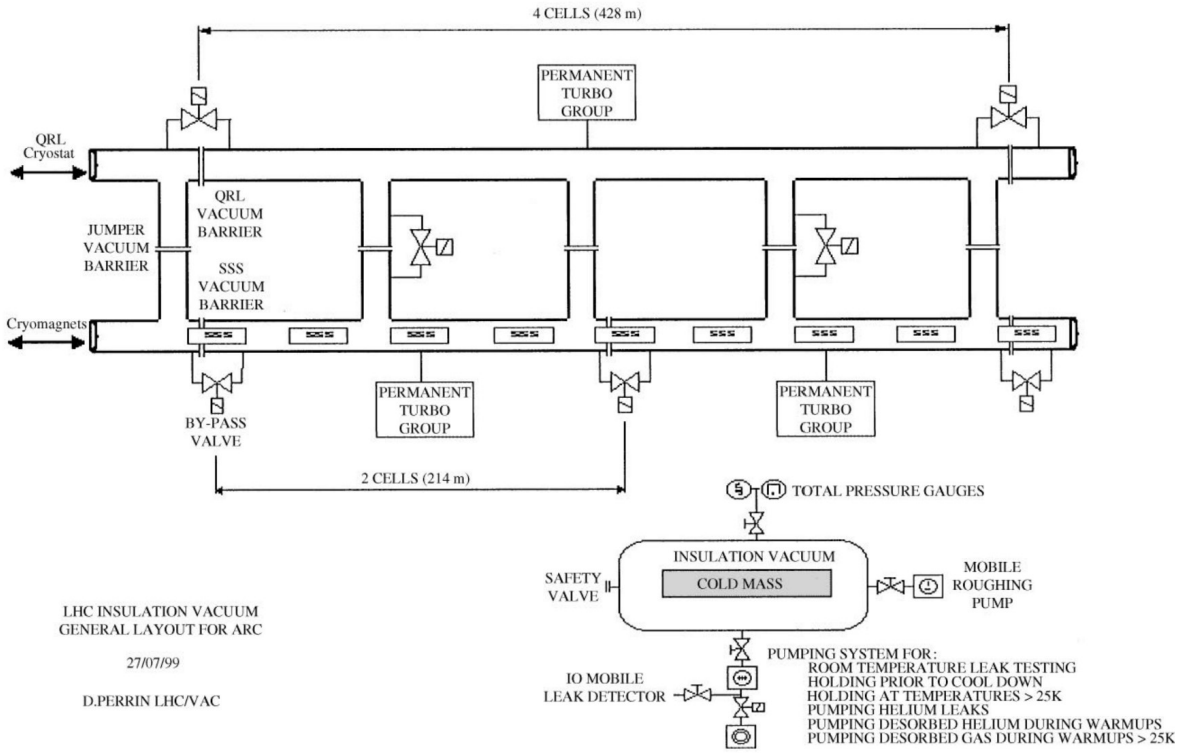

Figure 1.8: Layout of cryogenic insulation vacuum, from [24].

1.5.2 Beam vacuum

The beam vacuum is a system designed for the proper operation and efficiency of the accelerator, which aims to provide the required beam lifetime in the pipes and a low background in the experiments, as well as to shield the beam pipes from heat sources. Due to the more stringent requirements, the pressure must be at least three orders of magnitude lower than in the

vacuum insulation systems. The beam vacuum system is divided into sectors of about 2'900 m in length, namely the distance between two stand-alone cryomagnets, and several dynamic phenomena have to be taken into account in the design and installation processes. It is located in the center of the superconducting magnet coil, see Figure 1.7, and is in contact with the helium bath, at a temperature of 1.9 K. At this temperature, the walls of the vacuum chamber act as a cryopump with an infinite capacity for all condensable gases except for helium, making external pumping systems unnecessary and even inefficient. However, a very small amount of heat generated by the beam must be removed to maintain the low temperature in the system. To make it clearer, 1 kW of electrical power is required to remove 1 W of heat [1]. Therefore, it is very important to minimize any sources of heat in the cold beamline, as they can significantly increase the power required to maintain the temperature of 1.9 K in the pipes and allow the machine to operate properly. In particular, four heat sources are identified, as shown in Figure 1.9, which are described below [12, 1]:

- *Synchrotron radiation*, emitted by the circulating proton beams (distributed linear power of 0.2 $W\ m^{-1}$ per beam, with a critical energy of about 44eV).
- *Beam loss by nuclear scattering*, produced by the residual gas-beam interaction and resulting in a flux of high-energy protons from which a shower of secondary particles is created and absorbed in the 1.9 K magnet system (30 $mW\ m^{-1}$ per beam).
- *Image currents from the beam*, which cause power dissipation (0.05 $W\ m^{-1}$ per beam); it can be limited by coating the inner surface of the stainless steel beam pipe with a thin layer of copper, which has a lower resistivity than stainless steel at room temperature.
- *Photo-electrons and multipacting*, which transfer their energy to the cold wall as they are accelerated by the electric field, causing energy dissipation (0.2 $W\ m^{-1}$ per beam).

The presence of the heat loads made necessary the introduction of an additional pipe in the vacuum chamber, the *beam screen*, with the role of absorbing radiation and energy emissions to ensure an operating temperature of 1.9 K in the cryogenic system and avoid damage to the magnet coils. The beam screen operates at a temperature between 10 and 20 K and ensures the vacuum stability [22]. Figure 1.10 shows on the left a picture of a prototype of the beam screen and on the right a schematic representation of the beam screen operation.

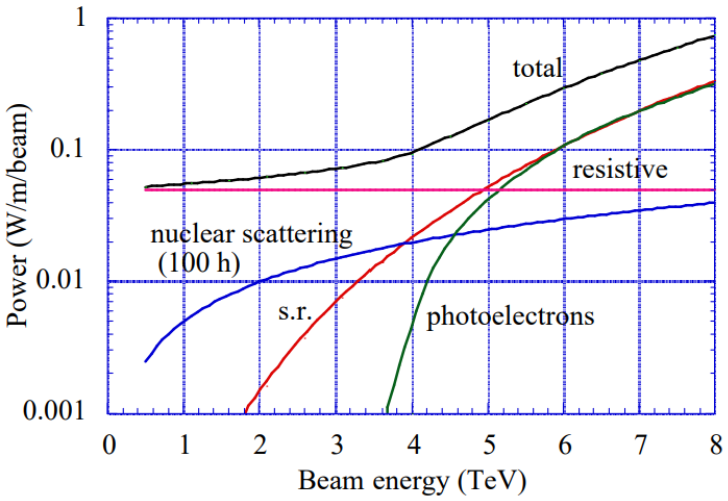

Figure 1.9: Beam-induced losses in the LHC, from [1].

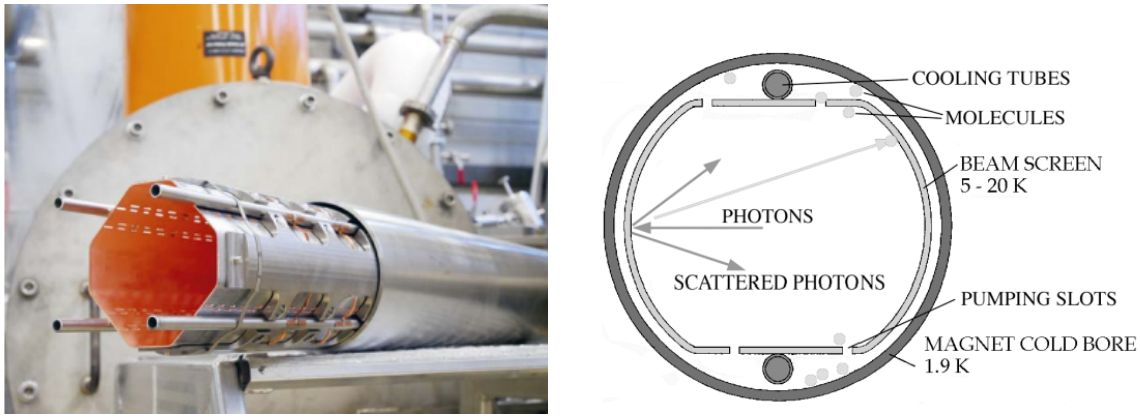

(a) **(b)**

Figure 1.10: Beam screen: **(a)** Picture of the beam screen prototype for the Q2 quadrupole magnets for High-Luminosisty (HL) -LHC, from [22], **(b)** Schematic representation of actively cooled beam screen in the magnet cold bore, from [24].

1.6 Leakages in the vacuum systems

The penetration of gases in vacuum systems can occur due to three different phenomena: permeation, atmospheric leakage and virtual leakage. The *permeation* is the diffusion of small gas molecules, such as helium, through the chamber walls and can be limited by the appropriate design of materials and geometry (adequate thickness). The permeation gas flow is proportional to the pressure gradient p_a across the wall thickness d, the surface of the vessel A and the material-dependent permeation constant k_{perm}:

$$Q_{\text{perm}} = k_{\text{perm}} \cdot A \cdot \frac{p_{\text{a}}}{d} \tag{1.13}$$

Most of the *atmospheric leakages* generate in the proximity of the joints during the assembly process. Minor leaks originate in the liquid cooling lines. Finally, *virtual leaks* are trapped volumes of gas within the vacuum chamber that the pumping process cannot remove due to geometrical restrictions. The trapped gas flows toward the chamber slowly and continuously. Therefore, over a long period, if the virtual leakage is not eliminated, it becomes a source of gas with the properties of an atmospheric leakage. A typical source of virtual leaks is fasteners in the connection systems because voids are created between the parts to be connected and not all of them are then filled by the fastener. An example is the mounting screws in a threaded blind hole under atmospheric pressure. The leak rate Q_{L}, i.e. the gas flow that enters the vacuum system through leaks, is defined as the pressure variation over time in a given volume, as reported below:

$$Q_{\text{L}} = \frac{\Delta p \cdot V}{\Delta t} \tag{1.14}$$

Figure 1.11 shows a schematic representation of the sources of penetration of gas in vacuum [16]. A sensitive test for leaks is provided by a helium leak detector used to test vacuum vessels and joints. The minimum helium influx detectable by a commercial leak detector is on the order of $10^{-11} mbarl/s$. In UHV applications, joints are considered leak-tight if their leak rate is less than $10^{-10} mbarl/s$.

1.7 Traditional joining techniques for vacuum

The LHC vacuum system consists of an enormous number of components, including several pumps, valves, gauges and controllers, as well as 250 000 welds and 18 000 vacuum seals. These elements require constant and reliable monitoring to ensure the highest standards of performance [22]. In particular, the design of the sealing systems in the LHC is of crucial importance for the quality of the generated vacuum as they represent the main source of leakage in the machine. Joining techniques in vacuum involve vessels, pipelines and other components. In this context, a number of constraints have to be taken into account for the design of a joint, such as the leak tightness and outgassing rate that must be granted in the system, the space available and the

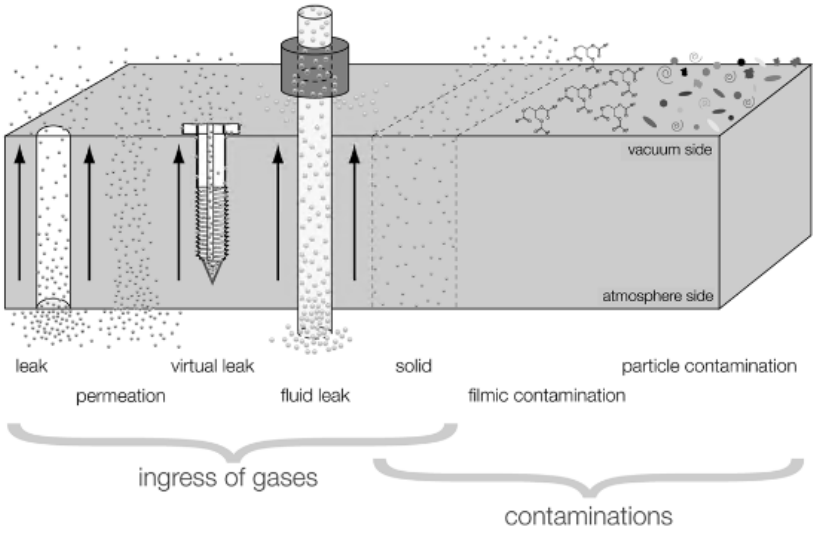

Figure 1.11: Sources of disturbance in vacuum, from [16].

radioactive environment to which the materials are exposed, as well as mechanical stability and reliability. In addition, accelerator sections operating under UHV conditions have even more stringent requirements for beamline sealing.

In general, coupling technologies are divided into permanent and dismountable connections. Depending on the type of sealing, there are different requirements in terms of space and cost of the technology. An overview of the traditional joining systems used at CERN for UHV applications is reported below [16, 14].

1.7.1 Permanent connections

The choice of the joining technique for permanent connections under vacuum conditions depends on the materials of the components to be sealed. Welding, brazing, and bonding are the most common techniques used in the accelerator. Some examples of material coupling and related joining methods and applications are shown in Table 1.2.

Welding

Welding is the joining of two or more parts by heating and/or applying force. This technique results in a continuity of materials in correspondence with the joint and may involve the use of filler materials. In vacuum, the most common welding technologies are [16]:

- *Tungsten inert gas welding (TIG)*: is a fusion welding technique in which the heat source

Table 1.2: Permanent joining technologies for different material pairings, from [16].
(+) Frequently applied joining process;
(0) possible/uncommon joining process;
(-) unsuitable/impossible/possible joining method with high technological effort.

Material pairing	**Brazing**	**Welding**	**Bonding**	**Applications**
Fe metals/Fe metals	0	+	0	Components made of corrosion-resistant stainless steel
NF metals/NF metals	+	0	0	Aluminium components, copper tubes in stainless steel flanges
NF metals/Fe metals	+	0	+	Aluminium components with flanges made of corrosion-resistant stainless steel
Metal/glass	+	-	+	Viewports
Metal/ceramic	+	-	+	Insulators, electrical feedthroughs
Glass/ceramic	-	-	+	Optical fiber feedthroughs
Plastic/metal	-	-	+	Insulating constructions, attached elastomer seals

is an electric arc between the material and the non-consumable tungsten electrode. The process is carried out in an atmosphere protected by an inert gas (argon or helium). TIG is a very flexible method and guarantees high-quality joints.

- *Microplasma welding*: uses a high-density electric arc as a heat source and a plasma gas nozzle that constricts the arc. This method is used for welding thin foils (0.01-1mm) where the low current required does not allow the use of TIG.

- *Electron beam welding*: is a fusion welding process in which the heat source is a high-velocity electron beam that converts its kinetic energy into heat upon impact with the surface of the material. This process is typically performed under vacuum to prevent beam energy dissipation. In addition, parallel welding of multiple connections is made possible by using deflection coils.

- *Laser beam welding*: uses monochromatic, coherent and strongly focused laser as a heat source, which allows very narrow and deep connection without any contact.

- *Friction welding*: consists in the relative movement of the surfaces to be joined under the application of force, which results in the generation of frictional heat and distortion heat by means of which the connection of the surfaces is done without then use of any additive.
- *Explosion welding*: uses an explosion-induced shock wave collision to weld the surfaces.
- *Diffusion bonding*: is based on the principle of solid diffusion and grain boundary migration, which allows the joining of materials without a fusion process. The surfaces to be connected go under heat and application of pressure by means of which the physical joining is performed.

In general, the success of a welding process is strictly related to the quality of the mechanical preparation of the parts to be welded. Furthermore, welds are a source of contamination and defects. Therefore, they must be handled carefully. First, accurate stress calculations must be made in the design of the joining technique to avoid localized high-stress areas. In addition, welds must be made under vacuum to avoid outgassing sources and contamination. The use of filler material is not recommended. Trapped volumes are prohibited [16].

Brazing

Brazing is an expensive thermal process that uses a furnace filled with protective gas to create high-quality joints under temperatures from about 800°C to 1150°C in a vacuum atmosphere. The components are connected with the aid of an additional liquid component, the solder. The solid temperature T_s, i.e. the melting temperature of the base materials, is not reached. The liquid solder diffuses into the material forming the permanent joints. This method allows to connect dissimilar materials and is often the only possible solution, as in this case the fusion of the base materials is not necessary and the joining of materials with different melting ranges can be done. Typical vacuum brazing include metal-ceramic, steel-cooper, and non-ferrous connections, e.g. titanium-aluminum. The interfaces of the materials to be joined must be properly prepared prior to the process, taking into account the expansion of the materials to allow the braze to flow into the gap. Post-process cleaning is fundamental to avoid corrosion problems [16, 14].

Bonding

Bonding is a non-thermal joining technique that requires the use of an additional component, the adhesive, which is applied to the surfaces of the parts to be joined, allowing multiple combinations of material connections. Unlike welding and brazing, adhesive bonding does not modify the base materials. Adhesive bonding is used when welding or brazing is not possible, such as when the materials to be joined have a low-temperature resistance (e.g. plastic, aluminum), and when distortion, stress and/or temperature loads must be kept low. However, adhesives are not very resistant and degrade easily at high temperatures and become brittle and crack at low temperatures. In addition, degassing of the bonded joint is a problem, even with high-performance adhesives. For these reasons, adhesive bonding finds limited applications in the accelerator and typically at room temperature [16, 14].

1.7.2 Dismountable connections

The choice of dismountable connections, i.e. flanges, is intended to provide maximum flexibility, e.g. the need to remove system components for transport or upgrade, and ease of maintenance of the connection systems. In general, all demountable joints for UHV applications require the use of a sealing medium, the seal, to ensure the proper permeation (leakage) rate and consequently the tightness of the connection. The seal should retain its overall stiffness, i.e. its elastic behavior; the surfaces in contact with the flanges should instead plasticize to enforce tightness. The main parameters for flange design are the strength of the material, which must withstand bolting or clamping, and the quality and hardness of the surface on which the seal is positioned.

Elastomer-sealed connections

Elastomer-sealed connections rely on force-activated materials that deform when pressed between two sealing surfaces to form a flat seal that prevents or minimizes gas leakage. Elastomer seals can be used up to $10^{-8} Pa$ of ultimate pressure. The sealing surfaces and the seal can be shaped in a variety of forms, such as toroidal ring (O-ring), X-form, and H-form. The sealing principle of elastomer-based connections allow them to be employed from over-pressure to vacuum conditions. Figure 1.12 shows a schematic representation of the sealing principles

for elastomer-sealed connections. The sealing effect of elastomers is limited within a material-dependent temperature range. At $T<T_G$ (glass transition temperature), the material is in a glassy state and consequently it loses the elastic properties at the base of the elastomer-sealing working principle. This process is reversible. At $T>T_Z$ (decomposition temperature), polymer chains are destroyed and the sealing effect is lost. This process is irreversible. The reference period for operating temperatures is 1000 h. Elastomers mainly employed for vacuum applications are NBR (acrylonitrile butadiene rubber), FKM (fluoro rubber), FFKM ((perfluoro rubber), VMQ (methyl vinyl silicone rubber) and EPDM (ethylene propylene diene monomer rubber). A chart showing the elastomers operating temperatures/ durations in vacuum is reported in Figure 1.13 [16]. The sealing force per mm required from an elastomer seal depends on the type of vacuum flange used and the nominal diameter. Figure 1.14 shows the Klein quick-release flange type that uses clamps to realize the connection and the standard ISO-F flange with screw holes.

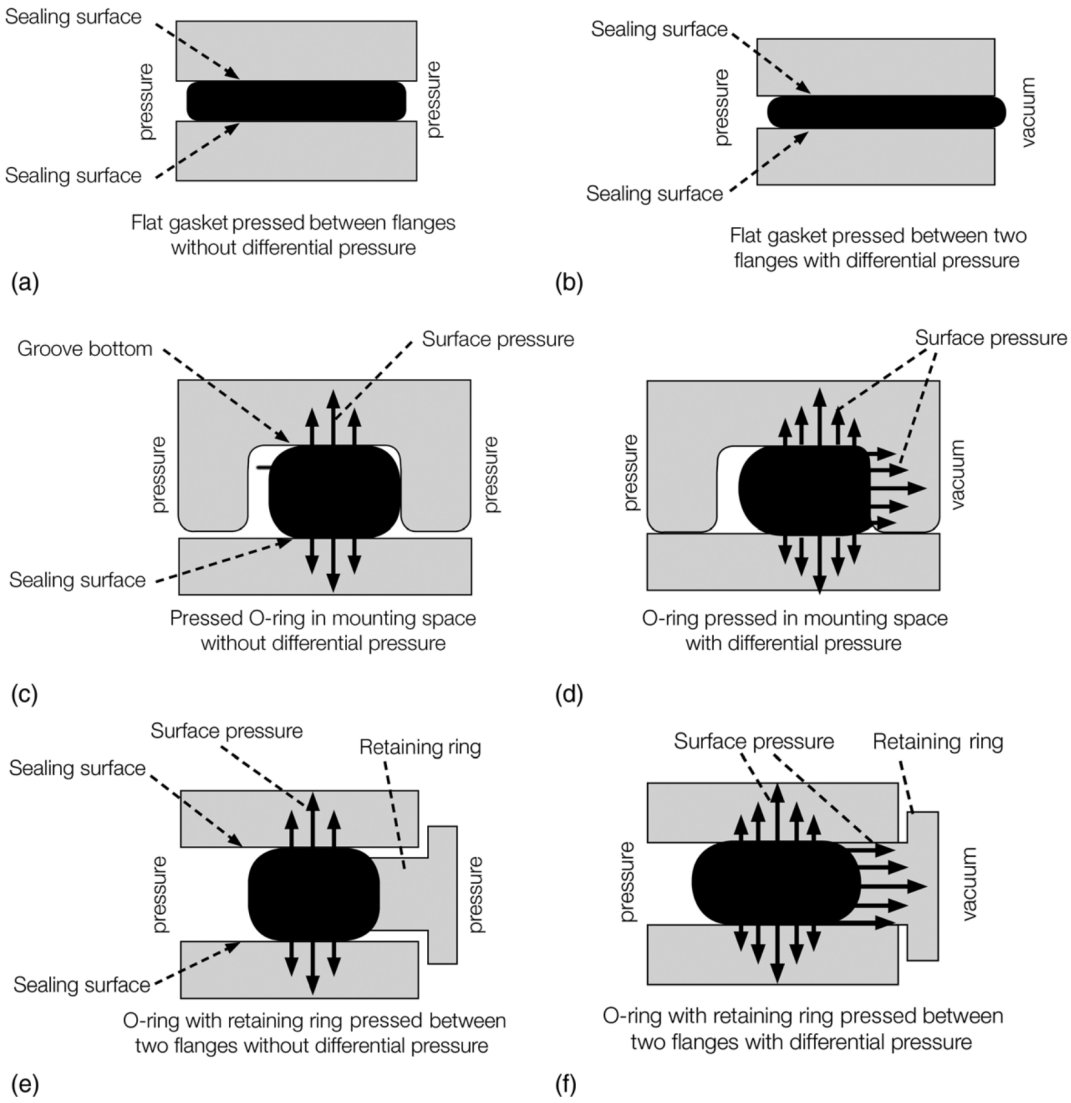

Figure 1.12: Schematic representation of the working principle for elastomer-sealed connections, from [16].

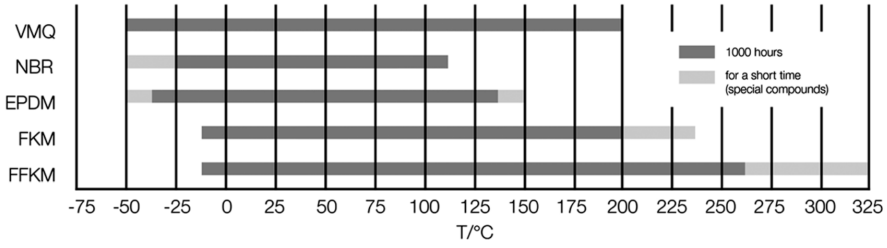

Figure 1.13: Operating temperatures/duration of elastomer materials for vacuum applications, from [16].

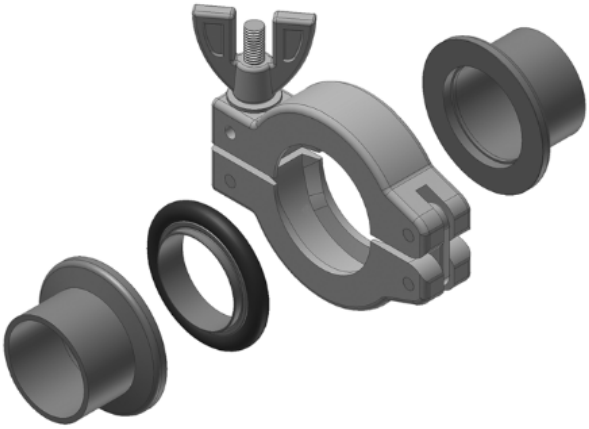

(a)

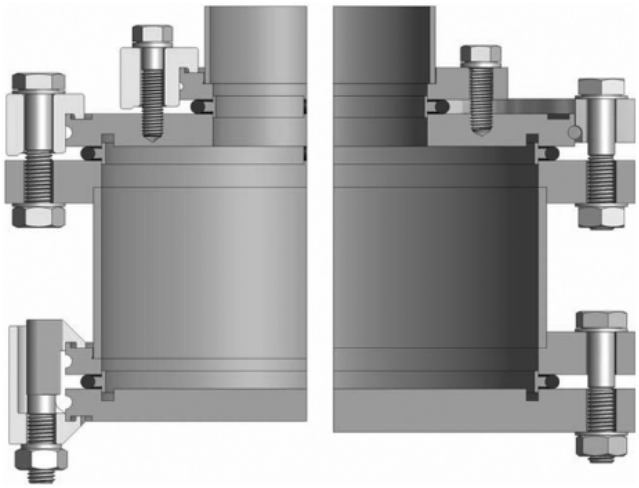

(b)

Figure 1.14: Schematic drawing of Klein flange quick release coupling (KF) and clamp flange joints (ISO-F): **(a)** Klein flange (KF) quick release system, **(b)** Clamp flange (ISO-F) system, from [16].

Metal-sealed connections

Metal sealers are required for UHV and XHV applications. In this case, the metal gasket must be plastically deformed to provide sealing at the required pressure. Plastic deformation allows for the compensation of manufacturing irregularities and waviness of sealing surfaces, as well as the filling of valleys caused by surface roughness. Oxygen-free, high-purity copper is the primary seal material; aluminum is rarely used. Other materials can be employed for special applications, such as the silver-plated copper that is used to protect the seal against oxidation when the system is baked out at more than 200°C. Baked systems can also use HELICOFLEX ® seals, with exceptional compression and elastic recovery properties. They are

composed of an elastic core that is a close-wound helical spring with a specific compression resistance surrounded by one or more metal jackets with greater ductility than the flange materials. During the compression process, the specific pressure applied causes the jacket to deform, which is able to fill any imperfections present on the flange surface. This is possible due to the helical spring, as each coil can operate independently, enabling the seal to adapt to the flange surfaces. The combination between both elasticity and plasticity makes HELICOFLEX ® one of the most high-performing sealing solutions available for UHV systems. Aluminum diamond seals are used for unbaked systems. They have two opposite knives which provide sealing by plastic deformation during tightening. Due to the relative lack of elasticity, this type of seal is not recommended for bake-out temperatures. Standard ConFlat® flanges (CF) and Quick Connect Flanges (QCF) are generally used as demountable joints in particle accelerators. The QCF connection represents a further advancement of the CF flange. Unlike CF flanges, QCF flange systems do not use screws because the sealing force is applied to conical flanges by a clamp chain. As a result, QCF-based systems provide the same tightness and operational safety as the CF flange, with a simpler, faster, and more space-saving connection system that can be applied to any type of flange geometry. A schematic drawing of the CF flange system and the QCF flange system is shown in Figure 1.15. Most metal-sealed vacuum connections involve a combination of a flat seal and a knife edge sealing surface, as shown in the cross-section drawing in Figure 1.16. In this case, the forces required for sealing and the developed contact pressure depend on the hardness of the flange and the materials to be sealed, as well as the geometry of the knife edge.

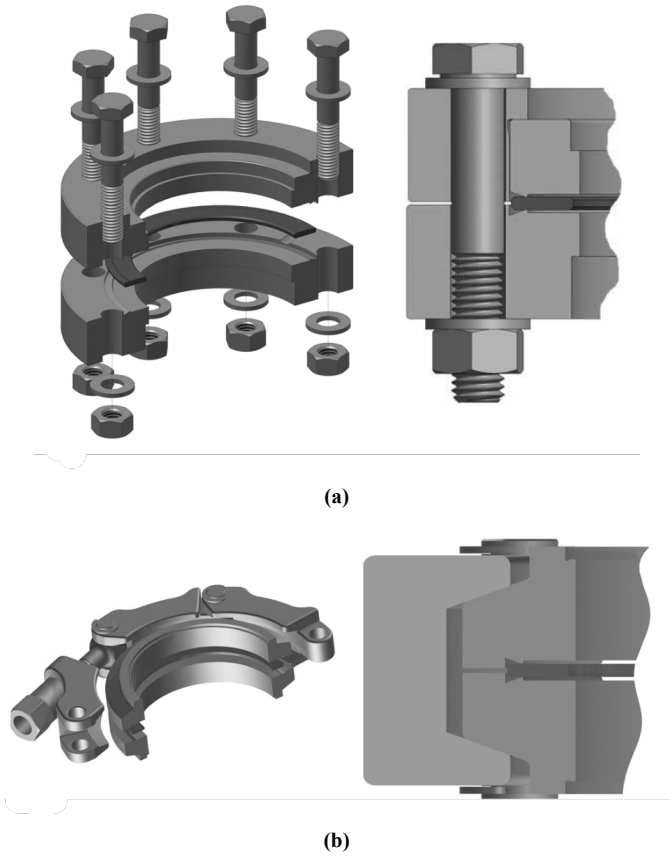

Figure 1.15: Schematic drawing of Standard ConFlat Flange (CF) and Quick Connect Flange (QCF) metal-sealed connections: **(a)** ConFlat Flange (CF) system, **(b)** Quick Connect Flange (QCF) system, from [16].

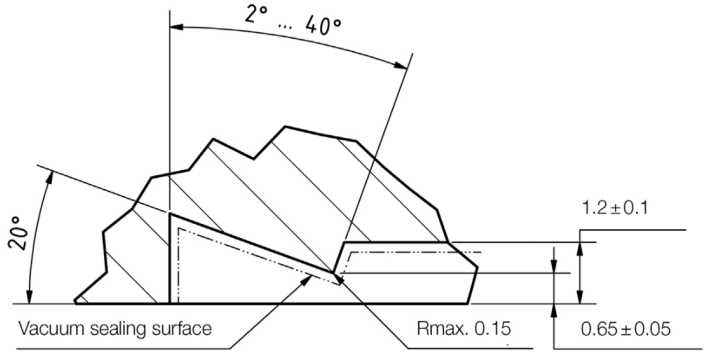

Figure 1.16: Cross-section drawing of the knife edge in a CF flange system: **(a)** CF flange system, **(b)** QCF flange system, from [16].

1.8 Chapter summary

The present chapter gives a general overview of vacuum technology as an introduction to the accelerator field, in particular to the Large Hadron Collider (LHC) at CERN, and the joining techniques used for vacuum applications.

In general, gas sources and vacuum pumps determine the quality of the vacuum in a system. In particular, different pressure levels may be required depending on the purpose of the vacuum system. In particle accelerators, ultra-high vacuum (UHV) is generally needed in the beamline, as the presence of residual gases leading to gas-beam interactions can affect beam lifetime and particle detection. Specifically, the LHC consists of two vacuum systems, the cryogenic isolation ($10^{-5} - 10^{-6} mbar$), which serves to thermally isolate the cryomagnets and the helium distribution line, and the beam vacuum ($< 10^{-10} mbar$), where the particle beam circulates. In general, the higher the vacuum requirements to be fulfilled, the higher the number of constraints to be considered in the design of the machine.

The design of connection systems in the LHC is particularly critical because they are the primary source of leakage in the machine. Traditionally, vacuum joints can be permanent, such as welding, brazing (especially for bimaterial connections), and bonding (rarely used), or demountable, such as standard bolted or quick-release flanges, using elastomer or metal sealers to realize the leak-tightness of the joint. They are well-known and validated sealing techniques widely used in the accelerator machine.

Chapter 2

Shape memory alloys: history, properties and applications

2.1 Abstract

This chapter provides a general overview of shape memory alloy (SMA) materials, including definition, history, mechanical and functional properties, and engineering applications. Initially, the historical background is given, from the discovery of the shape memory property to the definition of different shape memory materials (SMMs), such as SMAs, ceramics, polymers, and gels. The properties of the different SMMs are described, with a special focus on SMAs, which are widely used today in various industrial fields. Next, the functional properties of SMAs, such as the shape-memory and the pseudo-elasticity are introduced as macroscale effects of microstructural elastic transformations between two solid phases: martensite and austenite. Special attention is given to the equiatomic NiTi alloy, as it is the most interesting alloy in terms of shape recovery properties, which makes it widely used in many different engineering fields. General applications and industrial uses of SMA, and in particular of the NiTi compound, are then discussed to pave the way for the final section on SMA-based connection systems for UHV applications, developed at CERN and implemented in the LHC accelerator.

2.2 General definition and historical background

Shape Memory Alloys (SMAs) are defined as a class of smart materials characterized by two or more crystallographic structures between which a reversible transition is possible by diffusionless transformation mechanisms [26, 27, 28]. At the macroscopic level, this phase

transition results in unusual material behavior, namely the ability to recover the original shape, after large apparent plastic deformations, upon temperature or stress variation, and under certain external conditions. The unique properties of SMAs are nowadays known as the Shape Memory Effect (SME) and the Pseudoelastic Effect (PE).

2.2.1 The discovery of the shape recovery

The history of the SMAs began decades ago when the recovery properties of PE and SME were first observed in metal alloys. In particular, the discovery of the *superelasticity* was due to Arne Ölander, a Swedish metallurgist who, during his experiments on a gold-cadmium (AuCd) alloy in 1932, noticed an unusual behavior of the material, which he defined as ”so elastic that it almost reminded of rubber” [29]. Slightly later, other scientists investigated the phase transformation mechanisms of gold and copper-based alloys, observing the already defined *rubber-like* behavior [30, 31], and finding that different alloy compositions are characterized by different microstructural phases [32]. Nevertheless, memory properties were identified and recognized only in 1951 by Chang and Read, following some experimental studies on the Au-47.5Cd alloy [33]. The authors spoke for the first time about *shape recovery* of the material, as a phenomenon due to the solid transformations between two crystallographic phases, which in the specific case are body-centered cubic (austenite) and orthorhombic (martensite). The reversible phase transition was studied by measuring the changes in the electrical resistivity of the Au-47.5Cd single crystal during cooling and heating cycles, with and without applied stress. It was found that the electrical resistivity of the material depends on the crystallographic structure and, in particular, decreases with the formation of the orthorhombic phase. A critical temperature range for the transformation phenomena was defined, and shape recovery was shown to be related to the material phase change. Although the phenomenon remained to be precisely defined, these studies are the very first scientific evidence of what we now know as *shape memory effect*. A decisive step in the knowledge of SMA was taken in 1961 thanks to Bueheler and Wiley of the Naval Ordinance Laboratory (NOL). The two scientists were working on a project to develop the cone nose of a missile that could withstand the high caloric heat of re-entry from the atmosphere. To this end, they were conducting fatigue experiments on various materials and, during a laboratory meeting, they observed the shape memory properties of a NiTi alloy. In 1965, the two scien-

tists received a patent for various NiTi alloy compositions exhibiting these unusual properties [34]. In particular, the alloy consisting of 50 to 70 weight percent nickel and the corresponding percentage of titanium was named NITINOL (Nickel Titanium NOL). This discovery aroused great interest in the scientific community and endorsed the possibility of industrial use of the shape memory alloys. Many researchers started to put their efforts in the investigation of SMA behavior and possible applications.

2.2.2 Shape memory materials

A series of studies came up early concerning *Nichel-Titanium-based* alloys and their recovery properties, showing right away the commercial potential of these materials [26, 35, 5]. However, the understanding of the microstructural phenomena from which the unconventional material behavior originates did not come rapidly, because of the complexity of the Ni-Ti system, characterized by the presence of precipitates and an intermediate phase (R-phase) [4, 5]. Thus, before the 1970s, most works focused only on the macroscopic aspects of shape memory and pseudoelastic effects. In addition, the excellent mechanical properties, such as high strength, ductility and fatigue resistance, and biocompatibility made this type of alloys suitable for many possible applications in various engineering fields.

The idea of SME as a peculiarity of the Nitinol was abandoned early on when experiments showed that other compounds exhibited shape memory capabilities. In particular, the work of Otsuka and Shimizu on copper-aluminium-nickel (Cu-Al-Ni) alloys in the 1970s demonstrated that SME is a property of materials that exhibit thermoelastic martensitic transformations [36, 37]. Following, many studies focused on the potential of *copper-based* alloys due to their good shape memory ability coupled with interesting material properties, such as workability, excellent heat and electrical conductivity, and low cost, when compared to the Ni-Ti systems. These characteristics made the alloys very attractive for commercial purposes, and many researchers put their efforts into the study of various types of compounds that can be basically divided into three groups: Cu-Zn, Cu-Al and Cu-Sn [38]. However, the basic binary systems cannot be considered useful for a real application due to some limitations difficult to be overcome, such as the poor workability of Cu-Zn, the high transformation temperatures (out of a common operating range) of Cu-Al, and the too large temperature hysteresis (high

martensitic stability) of Cu-Sn compounds. The addition of a ternary or quaternary element was demonstrated to improve and/or stabilize the material properties, allowing Cu-based alloys to find application in many engineering fields [4, 39, 40, 41]. In particular, copper-zinc-aluminum (Cu-Zn-Al) alloy represents the cheapest commercial SMA available, with good PE (up to 5%) and martensite stability at room temperature, and copper-aluminum-nickel (Cu-Al-Ni) alloy offers the possibility of high-temperature applications (transformation range: 80-200°C) with a small hysteresis loop. In general, the most conventional use of the Cu-based alloys is as actuators and sensors. On the other hand, some disadvantages exist and can be found in the thermal instability, brittleness, poor mechanical strength, and low flexibility in changing the composition of the alloy without modifying the recovery properties [38]. All these challenges still limit their availability and commercial use.

Simultaneously in the 1970s, research studies at the Fulmer Research Institute (UK) focused instead on the *gold-based* alloys, leading to the discovery of many compounds with shape recovery capabilities [42, 43]. Such materials (in polycrystalline form) were found to be suitable for a variety of applications, thanks to their ductility, mechanical strength, and workability, where shape memory properties can play a role (wire connectors, jewelry, body implants, etc.). In particular, gold-copper-zinc (Au-Cu-Zn) alloys were examined and shape memory properties were observed in a wide range of compositions [43, 44], such that the optimization of the mechanical properties of this material also seemed possible. Such types of alloy are nowadays used especially in jewelry, but industrial use could not be realized for many applications due to the high cost of the material.

As seen, traditional alloys have essentially two problems: poor machinability and high cost, which made their use on a large scale particularly hostile. Specifically, the potential application of SMA in the construction industry pushed the research towards a new promising group, the *iron-based* alloys, and in particular, the iron-manganese-silicium (Fe-Mn-Si) compound [45, 46, 47, 48, 49, 50]. Their expected advantages can be basically summarized in excellent corrosion resistance, ductility, fatigue resistance, and good shape recovery capabilities. However, their application is still pioneering.

Although metal alloys are the most common and widely used shape-memory materials, a number of ceramics and polymers showed martensitic transformations and associated recovery

properties. Thus, they are candidates as shape memory materials. In particular, *shape memory ceramics* (SMCs) were studied due to their lightweight, very high strength and temperature resistance [51, 52], which allow applications where conventional metal SMA cannot be employed (for example, solid-state actuators). Many researches focused on the properties of SMCs, and the expected strain recovery range was found to be comparable to that of the traditional SMA [53, 54, 55, 56]. For example, zirconia ($Zr0_2$) is characterized by phase transition that can be induced by either stress or temperature [57, 58]. The single/oligo crystal structure helps to absorb the mismatch stresses due to the martensitic transformation so that cracking can be limited or avoided. This is due to the high surface area-to-volume ratio (free surface contributes to stress relaxation) and the absence/reduction of grain boundaries (where individual grain transformation strain accumulate) [59, 60, 61]. However, in the polycrystalline form, shape memory ability can be exploited for only a few cycles at low strain values (around 2%) [60]. This limitation is due to the tendency of ceramics to crack and represents the main problem to be overcome for the use of these materials. Shape memory properties were also observed in a variety of polymers with different chemical compositions. Their intriguing functionality attracted the interest of many researchers which contributed to demonstrate the potential of *Shape memory polymers* (SMPs) for various applications [62, 63, 64]. Compared to traditional shape memory alloys, SMPs exhibit a wider range of strain recovery (up to more than 200%), with a lower weight and cost for most materials. Recently, researches have developed biocompatible and biodegradable SMPs [65] to design new organs and coronary stents. However, the critical point with polymers is the low mechanical strength and the creep risk under stress and high-temperature conditions. Finally, *shape memory gels* (SMGs), a special class of SMPs, were studied for their ability to respond to external stimuli by undergoing substantial volume changes, either swelling or shrinking. In this case, many methods of stimulation are possible in addition to temperature change. Examples are electrical, magnetic, light, and chemical variations [62]. Here, poor mechanical stability is the main limitation of SMGs. The efforts of the scientific community are now aimed at overcoming the constraints imposed by the intrinsic properties of the basic materials (ceramics and polymers) for their practical use.

Table 2.1 summarizes the main physical, mechanical and functional characteristics of the different shape memory alloy systems, such as Ni-Ti, copper, gold and iron-based alloys. In conclusion, although there is still a lot of work to be done in the optimization of different classes

of shape memory materials, especially for improving fatigue life and stability, their unusual and promising properties are a strong motivation to pursue this research work.

Table 2.1: Comparison between the mechanical and functional properties of different types of SMAs, from [66, 63].

Parameter	**Ni-Ti-based**	**Cu-based**	**Au-based**	**Fe-based**
Density (kg/m^3)	6-8	7-8	13.5	6.5-7.5
Unconstrained recovery strain (up to) %	8	4-6	1.5	4
Young's modulus (up to) (GPa)	Austenite: 85 Martensite:30	Austenite: 85 Martensite:80	Austenite: 100 Martensite:96	Austenite: 210 Martensite:140
Yield stress (up to) (MPa)	Austenite: 500 Martensite:100	Austenite: 400 Martensite: 130	Austenite: 400 Martensite: 130	Austenite: 400 Martensite: 130
Transformation temperature range (°C)	[-50, 110]	[-180, 200]°C	[30, 100]°C	Around -130°C
Thermal hysteresis (up to) (°C)	30	35	15	100

2.3 Material properties and microstructure

The outstanding properties of SMAs, such as the shape memory effect and the pseudoelasticity, are the consequence of thermoelastic martensitic transformations. Therefore, the shape recovery represents the macroscopic effect associated with a structural change at the lattice level. Specifically, phase transitions can be induced by temperature variation or mechanical loading and, depending on the external conditions, one or a combination of the two effects (SME and PE) may occur. In general, recovery takes place in two ways:

- *Shape memory effect*: Shape recovery is obtained by temperature variation after prior deformation at low temperatures.
- *Pseudoelasticity*: Shape recovery is obtained by removing the applied load after prior deformation at high temperatures.

2.3.1 Martensite and austenite

SMAs can exist in two distinct stable phases, with different crystallographic structures. *Austenite* is the high-temperature and low-stress stable phase. It is also known as the parent or memory phase and presents a body-centered-cubic crystal structure, as schematically reported in Figure 2.1a. *Martensite* is the low-temperature and high-stress stable phase, with a lower symmetry crystal structure, such as a tetragonal, orthorhombic, or monoclinic structure. The martensite can occur in two different configurations: *twinned* and *detwinned*, depending on the orientation of the variants with respect to the material axes. The twinned martensite is characterized by many variants (up to 24 for the NiTi) as they are self-accommodated in the crystal lattice. In the detwinned martensite, a specific variant prevails, and maximum elongation occurs in the direction of the applied force. A schematical representation of the martensitic structure with reference to the NiTi alloy is shown in Figure 2.1b. Figure 2.2 reports in situ optical micrograph of a polycrystalline Cu66.9Zn23.7Al9.4 (at.%) alloy during uniaxial tensile loading, showing the formation of different martensitic variants in single grain [67].

In general, the functional properties are linked to the martensite-austenite transformations, which can be induced either by temperature (TIM, temperature-induced transformation) or stress (SIM, stress-induced transformation). These properties can vary widely depending on the type of alloy and the direction of the transformation: austenite and martensite formation does not occur over the same temperature or stress range in all SMAs. A thermal and a stress hysteresis cycle characterizes both types of reversible transitions.

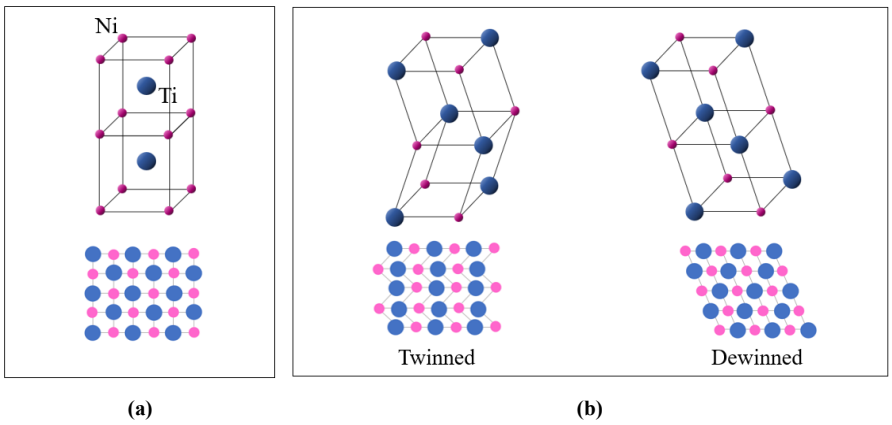

Figure 2.1: Schematic three and two-dimensional representations of the NiTi alloy crystallographic phases: **(a)** Austenite, **(b)** Martensite.

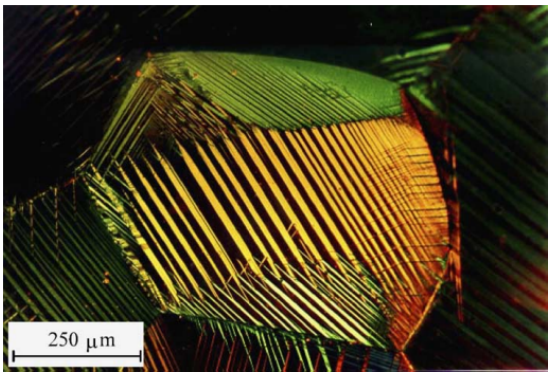

Figure 2.2: Different martensitic variants in a single grain of a polycrystalline Cu66.9Zn23.7Al9.4 (at.%) alloy during uniaxial tensile loading, from [67]

Thermally induced phase transformations are governed by specific material properties, such as the Transformation Ttemperatures (TTs). These are the critical values of temperature at which the phase transitions occur. Table 2.2 gives a definition and description of these parameters. The SME is thermally induced and can manifest as a one-way or two-way shape memory effect (OW-SME and TW-SME, respectively).

Stress-induced direct (A→M) or reverse (M→A) phase transformations are governed by the mechanical parameters reported in Table 2.3. The PE is stress-induced by applying and subsequently removing a mechanical load.

Table 2.2: Definition of the Transformation Temperatures (TTs) governing the SME process under no-load conditions.

Temperature	**Definition**	**Description**
A_s	Austenite start temperature	Temperature at which the M→A phase transformation starts to take place
A_f	Austenite finish temperature	Temperature at which the M→A phase transformation is completed
M_s	Mastensite start temperature	Temperature at which the A→M phase transformation starts to take place
M_f	Martensite finish temperature	Temperature at which the M→A phase transformation is completed

Table 2.3: Definition of the transformation stresses (TSs) governing the PE process.

Stress	Definition	Description
σ^{s}_{AM}	Martensite start stress	Stress value at which the A→M phase transformation starts to take place
σ^{f}_{AM}	Martensite finish stress	Stress at which the A→M phase transformation is completed
σ^{s}_{MA}	Austenite start stress	Stress at which the M→A phase transformation starts to take place
σ^{f}_{MA}	Austenite finish stress	Stress at which the M→A phase transformation is completed

2.3.2 Thermoelastic martensitic transformations

A thermoelastic martensitic transformation (TMT) is a *first-order*, *diffusionless*, and *solid-state* phase transition. It consists of the nucleation and growth of single crystals of the product phase (martensite) within the parent phase (austenite) according to diffusionless (or displacive or military) mechanisms, where the phase change occurs without atomic diffusion and does not involve the rearrangement of atoms in the crystal lattice. In the case of displacive phenomena, groups of atoms move cooperatively in the microstructure, causing the distortion of the crystal into a new shape, without changing the chemical composition or atomic order of the material. The transformation proceeds by small range (the atoms move less than one interatomic spacing) and shear-like motion of the *habit plane*, i.e., the invariant interface between the parent and the product phases. It is also defined as the non-deformation plane that minimizes the elastic energy [68]. Martensite variants that form into the austenite phase are usually thin *plates* (needles and laths were also observed). The plates lie on distinct crystallographic planes and grow until a grain boundary or another martensite plate is encountered. The growth of one plate can trigger the formation of other plates. A schematic diagram of the formation and growth of the martensite plates is shown in Figure 2.3. The consequent macroscopic distortion of the crystal is a homogeneous shear. The inside of the martensite plate is sheared (single variant) or twinned (multi variants).

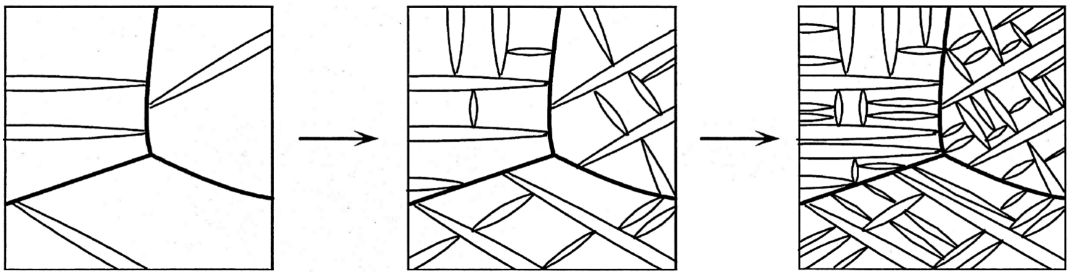

Figure 2.3: Sequence of the martensite plate formation, from [69].

This type of transformation involves small volume change and good *reversibility*. The strains associated with the phase transition, i.e., the transformation strains, are so small that the elastic limit is not exceeded and the reverse transformation is possible. In particular, the thermally induced phase transitions, such as the OW-SME and the TW-SME, occur in a range of critical temperatures (Table 2.2) whose values depend on the specific alloy composition and thermomechanical history. From a microstructural point of view, the first martensitic plate formed during cooling at $T=M_s$ is the last one remaining upon heating. Coherently, the last plate formed at $T=M_f$ is the first to retransform at $T=A_s$. Phase transformations can also be induced by stress (PE). Typically, this type of transition occurs under isothermal conditions at any temperature in the range $A_s<T<A_f$ and between critical values of stress (Table 2.3). The presence of plastic deformations can induce martensite variants at temperatures higher than A_f, up to a maximum value of M_d, i.e., the *martensite desist*, which represents the upper-temperature limit for phase transformations. At $T>M_d$ the martensite is no longer stable due to the high temperature and only plastic irreversible deformations due to the movement of the dislocations can occur in the austenite. The reason is to be found in the evolution of plastic (τ_{NP}) and transformation (τ_{sit}) shear stresses as a function of the temperature, as shown in Figure 2.4. In general, the energy required for phase transformations increases with temperature. When $T<M_d$, the stress required to plastically deform the material is higher than the stress required to realize the phase transformation, so the latter is the mechanism that takes place. Conversely, for $T>M_d$, the two effects are reversed and only plastic deformation mechanisms occur because the stress required for them is lower than the stress needed for transformations.

The martensitic phase transformation is a time-independent phenomenon. The lattice parameters change discontinuously and as a function of the temperature. In particular, at each intermediate step of the transformation, martensite and austenite coexist under stable condi-

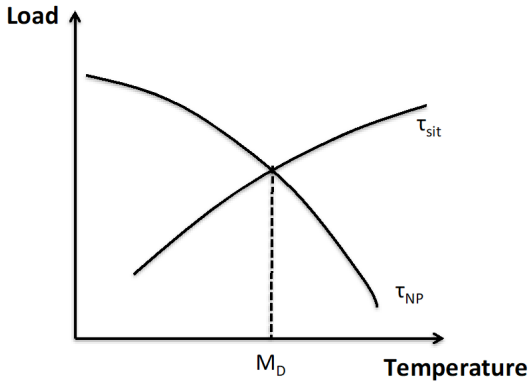

Figure 2.4: Transformation (τ_{sit}) and plastic (τ_{NP}) shear stress as a function of the temperature, from [21].

tions. The dominant mechanism at the basis of the thermoelastic martensitic transformations is the *equilibrium of the energy* of the system. The growth of individual variants causes an increase in the strain energy, which is conversely relaxed by the formation of groups of variants and their rearrangement in the microstructure. As a result, the transformation is characterized by a metastable equilibrium, at each step of the process, between the elastic strain energy stored in the material and the one dissipated, so plastic deformations due to the infinite increase in energy are prevented. The elastic strain energy due to the transformation is balanced by the chemical free energy ΔG_{ch}, which is the difference between the Gibbs free energies of martensite and austenite. The phase transformation is driven by a decrease in the total Gibbs free energy due to the accommodation of variants in the microstructure. The consequence is a change or not of the shape of the crystal. Figure 2.5 shows the Gibbs free energy-temperature diagram for the parent phase and the martensite. T_0 is the temperature value at which the two phases are in thermodynamic equilibrium. Below this value the martensite is stable and above this value the austenite is stable. At $T=M_s$ the energy difference reaches the critical value, so $\Delta G_{ch}=\Delta G_{crit}$, and the A→M transformation takes place, being completed at the lower temperature of M_f.

A general thermodynamic analysis of the one-way shape memory effect process (Figure 2.9) is given below, as an example of the relationship between macroscopic and microscopic effects [69]:

- *Detwinning:* M_{tw}→M_{dw}: Stress loading causes crystal deformation, which can be addressed by a) distorting the lattice or b) rearranging the variants and creating a new microstructure. The latter method is preferred as it follows the principle of conservation of energy. In fact, the different variants come from the same parent phase and therefore have

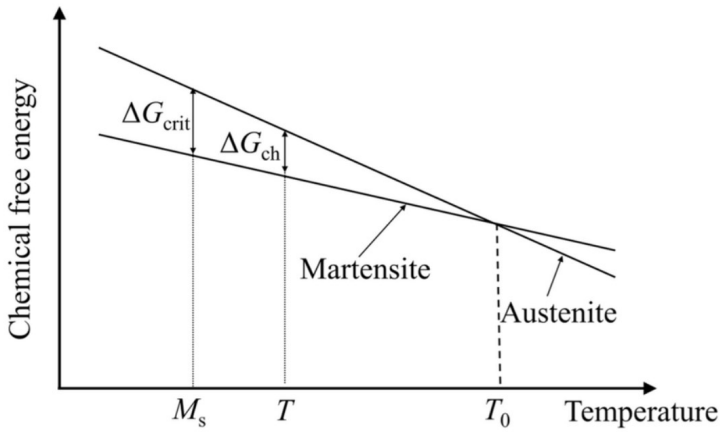

Figure 2.5: Chemical free energy trend with temperature, from [70].

the same energy. By changing the microstructure without distorting the lattice, it is possible to deform the crystal and give the material a new shape, without changing the internal energy. Thus, twinned martensite (self-accommodated variants) and detwinned martensite (single variant) are characterized by the same energy and, as a result, the crystal does not revert to the original twinned configuration after the load is removed.

- *Heating:* $M_{dw} \rightarrow A$: Each variant of detwinned martensite is converted back to austenite when heated. In this case, the material is able to return to its original shape because the austenite phase is characterized by a single variant.

- *Cooling:* $A \rightarrow M_{tw}$: Each region of the austenite transforms into different variants of martensite. As they are self-accommodated in the crystal there is no macroscopic change in the shape of the material.

2.3.3 The crystallographic theory

At the crystallographic level, some mechanisms take place during the thermoelastic martensitic transformations that explain how the phase change occurs and the atoms are rearranged in the structure. The general crystallographic theory of martensitic transformation deals with lattices; thus, it is independent of the nature of the atoms in the lattice sites. In general, a given vector in the parent phase transforms into a specific vector in the product phase due to the diffusionless nature of the process. This relationship is referred to as a *lattice correspondence* [71]. From a crystallographic point of view, the change of crystal structure occurs by a first homogeneous lattice deformation and an additional geometrical arrangement of the distorted variants

of martensite in order to keep the habit plane undistorted and unrotated after the transformation [71]. Therefore, phase transformations can be considered as the result of the combination of two different phenomena: the *Bain strain*, namely the lattice distortion that serves to create the martensite structure, and the *lattice invariant shear*, occurring by a slip or twinning, which generates the same lattice in a different orientation [69]. Thus, from a given orientation of the parent phase, it is possible to get several variants of martensite. Some geometrical requirements have to be satisfied to get the crystal deformation with minimal elastic energy dissipation. For the sake of simplicity, the two-dimension case is considered in order to understand the crystallographic theory of martensite. Following, a description of the two main processes is reported.

Bain strain

The Bain strain is a theory proposed by Bain in 1924 according to which a phase transformation is accommodated by lattice deformation. In particular, the term *Bain strain* indicates the pure strain component of a martensitic transformation. In general, it can be defined as a series of atomic movements along the same direction and over small ranges, since the atoms move less than one interatomic spacing. The parent phase exhibits a symmetrical structure (cubic in the specific case of the austenite). It is homogeneously deformed along the direction of the strain to obtain a rectangular phase. The simple Bain strain alone does not describe the whole process since experimental evidence shows that the axes of the martensite unit cell are rotated with respect to the axes of the austenite unit cell. This is a consequence of the fact that the individual distorted variants of the product phase are no longer geometrically compatible with the original phase after the homogeneous strain. Thus, they are subjected to further rearrangement, according to the lattice invariant shear theory described below, and this generates a new surface capable of reconnecting with the original structure.

Lattice invariant shear

The lattice invariant shear is an atomistic model whose general idea is based on the length matching between the transformed and the original structure across the habit plane. In this case, the phase transformation from austenite to martensite is accommodated to minimize the principal strains. The lattice invariant shear can occur as a slip or twinning (in most SMAs) of the martensite units, where different dislocation mechanisms occur.

The *slip* process is shown in Figure 2.6. The undeformed symmetric parent phase is reported in 2.6a. The lattice section under consideration is shown in 2.6b and selected according to the direction of the habit plane, which changes with the Bain strain and is identified by the slip angle Θ defined below:

$$\Theta = arccos(1/(1+\epsilon)) \tag{2.1}$$

After homogeneous deformation (Bain strain), the region is subjected to slip (2.6c) and, subsequently, to rotation to fit well with the original parent phase (2.6d).

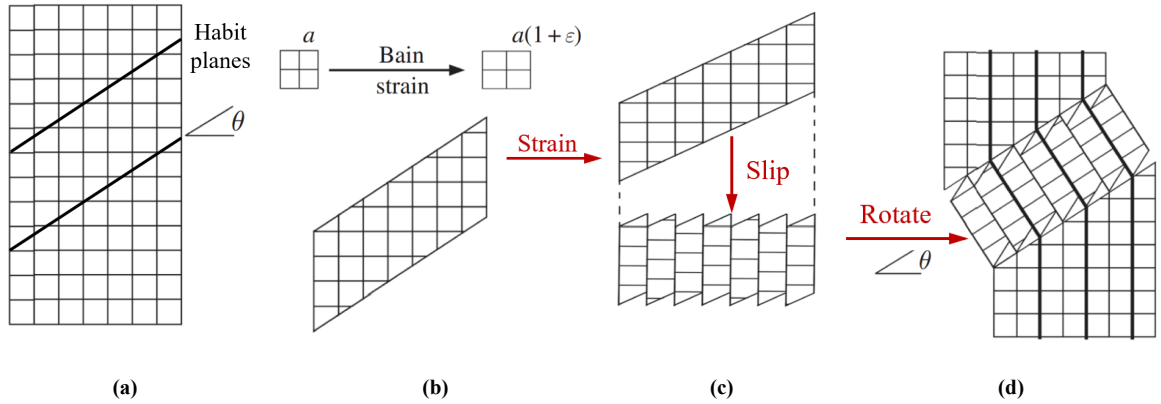

Figure 2.6: Schematic bi-dimensional representation of Bain strain and slip process steps: **(a)** Original austenite crystal, **(b)** Bain strain and pre-selected region., **(c)** Slip of the region, and **(d)** Rotation of band, adapted from [69].

The *twinning* is the process that occurs when two variants accommodate in a symmetrical way with respect to a mirror plane, called the *twin boundary plane*, sharing some lattice points [71]. Apparently, the twinning plane is generated from a symmetry plane in the parent lattice. The existence of twins means that there are two orientations of the martensite and two lattice strains in the martensite [72]. Such a process is schematically described in Figure 2.7. Two different crystallographic variants of martensite (2.7b) are formed from the symmetrical austenite phase (2.7a). The variants have different orientations and conjugate along the symmetry plane (dark line) in 2.7c by matching the two slightly rotated triangles of the two variants. The small rotation that the two triangles make to close the gap of the vacuum results in a rotation of the planes of austenite greater than 90°. The macro-scale shear components of strain are eliminated. The martensite plate that is generated is characterized by a lower symmetry with respect to the parent phase and is composed of multiple units of twins (2.7d).

A 3D schematic representation of the final configuration of martensite is reported in Figure 2.8 for both slip and twinning processes.

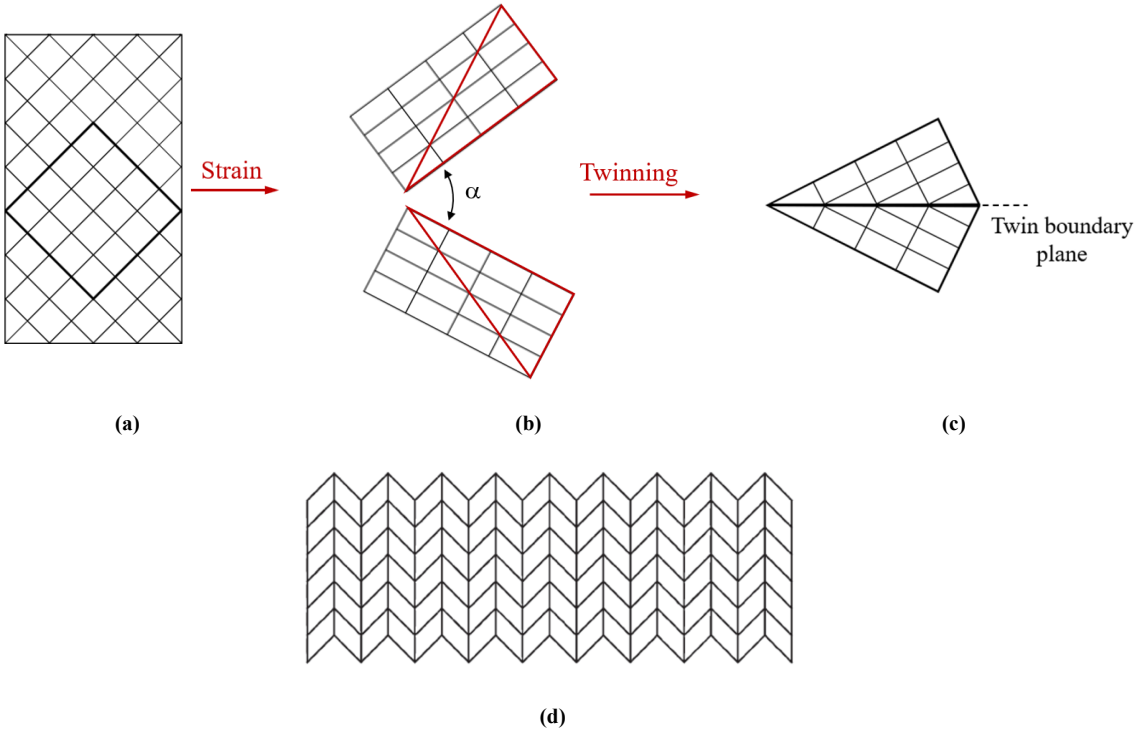

Figure 2.7: Schematic bi-dimensional representation of Bain strain and twinning process steps: **(a)** Original austenite crystal, **(b)** Two martensite variants with different orientations, **(c)** Twinning of the two variants, and **(d)** Martensite plate with multiple units of twins, adapted from [69].

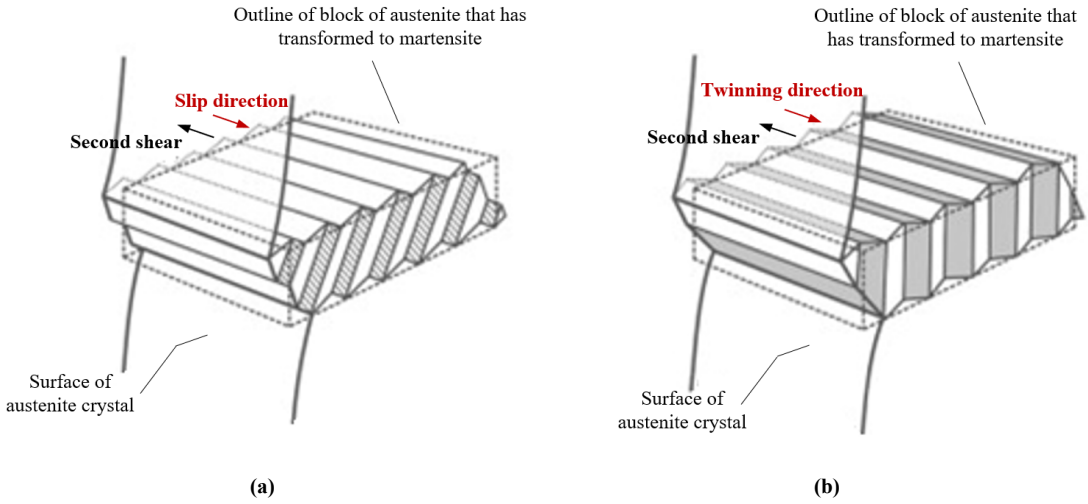

Figure 2.8: Three-dimensional final configuration of martensite: **(a)** By slip, and **(b)** By twinning, adapted from [73].

2.3.4 Shape memory and pseudoelastic effects

One-way shape memory effect

The OW-SME is a phenomenon that occurs when the material is apparently plastically deformed at low temperatures in the martensitic state; it regains the original shape upon heating, following the phase transition from martensite to austenite (M→A). This property is inherent to the SMA. Figure 2.9 provides a schematic representation of the OW-SME stress-strain-temperature diagram (2.9a) and phase transformations circle diagram (2.9b). The different stages of the process are described below:

- A→B) Stress load: twinned→detwinned martensite transformation *($T=T_{const}$, $T<M_f$)*.
- B→C) Stress unload of the detwinned martensite *($T=T_{const}$, $T<M_f$)*.
- C→D) Heating: detwinned martensite→austenite transformation *($T_{final}>A_f$)*.
- D→A) Cooling: austenite→twinned martensite transformation *($T_{final}<M_f$)*.

The phenomenon described is called one-way SME because the material has the ability to remember only the high-temperature shape. In addition, the cooling occurs under no load, so no macroscopic changes in the shape are observed between austenite (point D) and twinned martensite (point A).

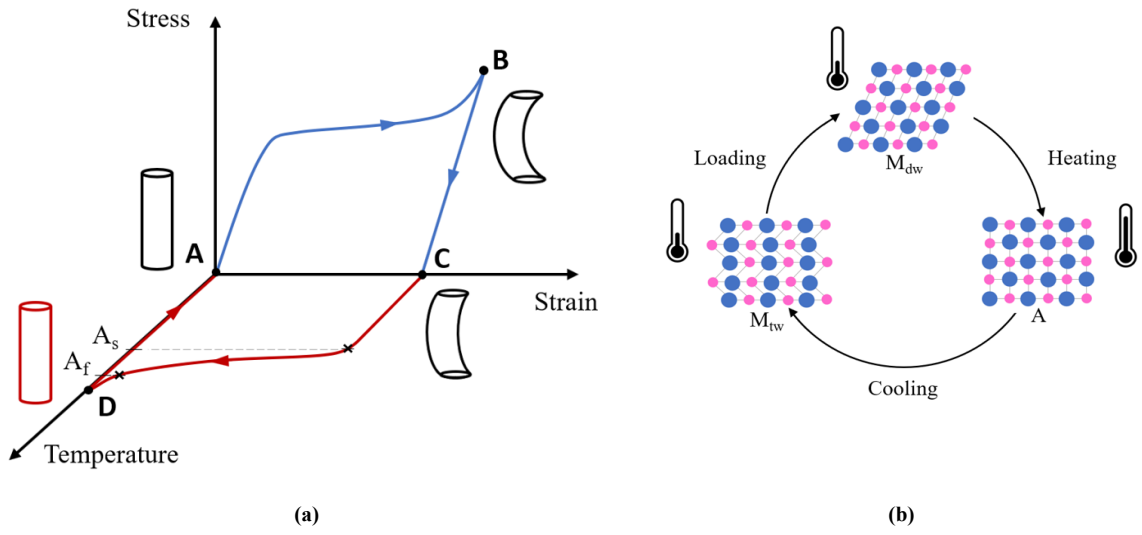

(a) **(b)**

Figure 2.9: Schematic representation of the one-way shape memory effect (OW-SME): **(a)** Stress-strain-temperature diagram, **(b)** Microstructural phases.

Two-way shape memory effect

The TW-SME is a property of metallic SMA, which is induced by a specific treatment, the so-called *thermo-mechanical training*. This process aims to induce stable detwinned martensitic variants in the material and is typically performed in two different ways [74, 75]:

- Severe (plastic) pre-deformation of martensite under a constant temperature.
- Different repeated stress-temperature cycles.

The result is that the material acquires a new property that allows direct and cyclic phase transformations between detwinned martensite and austenite. The TW-SME is shown schematically in Figure 2.10. The strain-temperature diagram (2.10a) shows the hysteresis cycle of the phase transformations and the transition between the low and high temperature shapes. Figure 2.10b provides the cyclic thermal path between the two crystallographic phases: detwinned martensite (deformed shape) and austenite (original shape). The two steps of the process are reported below:

- C→D) Heating: detwinned martensite→austenite transformation $(T_{final}>A_f)$.
- D→C) Cooling: austenite→detwinned martensite transformation $(T_{final}<M_f)$.

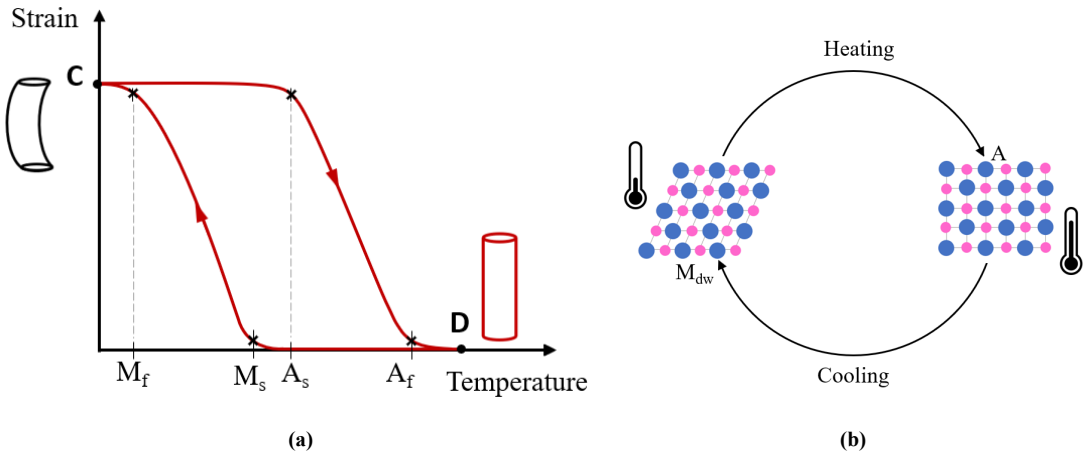

Figure 2.10: Schematic representation of the two-way shape memory effect (TW-SME): **(a)** Stress-strain-temperature diagram, **(b)** Microstructural phases.

Pseudoelasticity

The PE is the stress-induced property of SMA that occurs under isothermal conditions and involves the storage of potential energy. In particular, the material can recover large pseudo-elastic deformations after a load-unload cycle, by inducing both the direct (A→M) and reverse (M→A) phase transformations, respectively, as shown in Figure 2.11 and described below:

- A→B) Stress load: austenite→detwinned martensite transformation ($T=T_{const}$, $T>A_f$).
- B→A) Stress unload: detwinned martensite→austenite transformation ($T=T_{const}$, $T>A_f$).

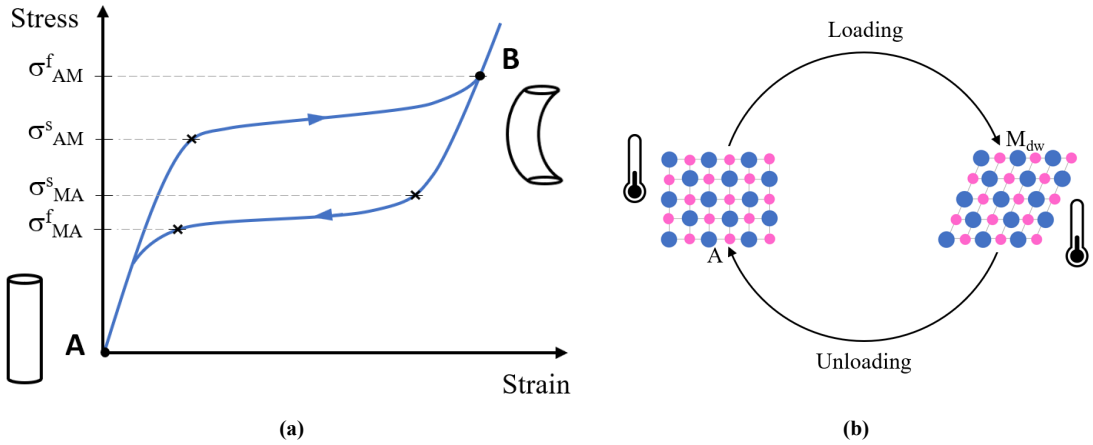

Figure 2.11: Schematic representation of the pseudoelastic effect (PE): **(a)** Stress-strain-temperature diagram, **(b)** Microstructural phases.

2.4 NiTi alloys

Although the shape recovery capabilities have been observed in various materials (section 2.2.2), NiTi alloys cover the majority of industrial applications due to their most exploitable functional properties, mechanical performance and biocompatibility (section 2.5.2). In this regard, many studies have been done with the aim of investigating different alloy compositions and relative properties, also with reference to the microstructural mechanisms.

2.4.1 The near-equiatomic NiTi system

The equilibrium phase diagram of the Ni-Ti systems is reported in Figure 2.12. The region of interest with reference to the shape memory alloys is between the Ti_2Ni and the $TiNi_3$ phases

because here the single TiNi B2 parent phase (austenite) is able to transform into the monoclinic B19' phase (detwinned martensite). Therefore, NiTi shape memory alloy is obtained by an *equiatomic composition* of nickel and titanium, where an excess of the nickel content (1%) is the most common variation in composition and serves to decrease the transformation temperatures so that at the ambient temperature the SMA can exhibit PE. The addition of other elements, such as iron and chromium, helps to further decrease the TTs; the addition of copper reduces the thermal hysteresis. The near-equiatomic NiTi compound exhibits a transformation temperatures range of [-50, 110] ºC with a thermal hysteresis of around 30°C and a maximum recoverable strain of about 8%. The alloy can be machined and obtained in various sizes and forms, e.g., wires, strips, rods, tubes, and plates.

The intermetallic TiNi compound is characterized by a melting temperature of 1310°C and different solubility of Ti and Ni in the system. In the TiNi phase, the boundary on the Ti-rich side is nearly vertical at a value close to 50%. On the Ni-rich side, the solubility limit is larger and reaches a maximum of 57% at 1118°C, but it decreases rapidly with the temperature, becoming negligible at a temperature of 500°C. However, a rapid quenching or slow cooling of the material at room temperature makes it possible to retain the B2 phase corresponding to a certain alloy composition and create a metastable material. The possibility to freeze the B2 phase is fundamental for the shape memory characteristics, as it plays an essential role in the phase transformations. In addition, depending on the temperature and aging time, Ni-rich precipitates are formed in the NiTi phase. An example is the Ti_3Ni_4 compound that may be formed at low temperatures and short aging, while the precipitation of stable Ni_3Ti only appears at very long aging treatments. The consequence of Ti_3Ni_4 precipitates is the R-phase, an intermediate phase that forms between the B2 and the B19' transformation.

2.4.2 Phase transformations in NiTi alloys

The NiTi alloy exhibits a B19' (monoclinic) martensite and a B2 austenite. Among the SMAs, the B19' structure appears only in the NiTi system. The twinned martensite has a B19 (orthorhombic) structure. Under certain conditions, an additional phase transformation takes place in the NiTi systems and the so-called *R-phase* is formed. The presence of the R-phase in the Ni-Ti alloys made the understanding of the thermoelastic martensitic transformation mech-

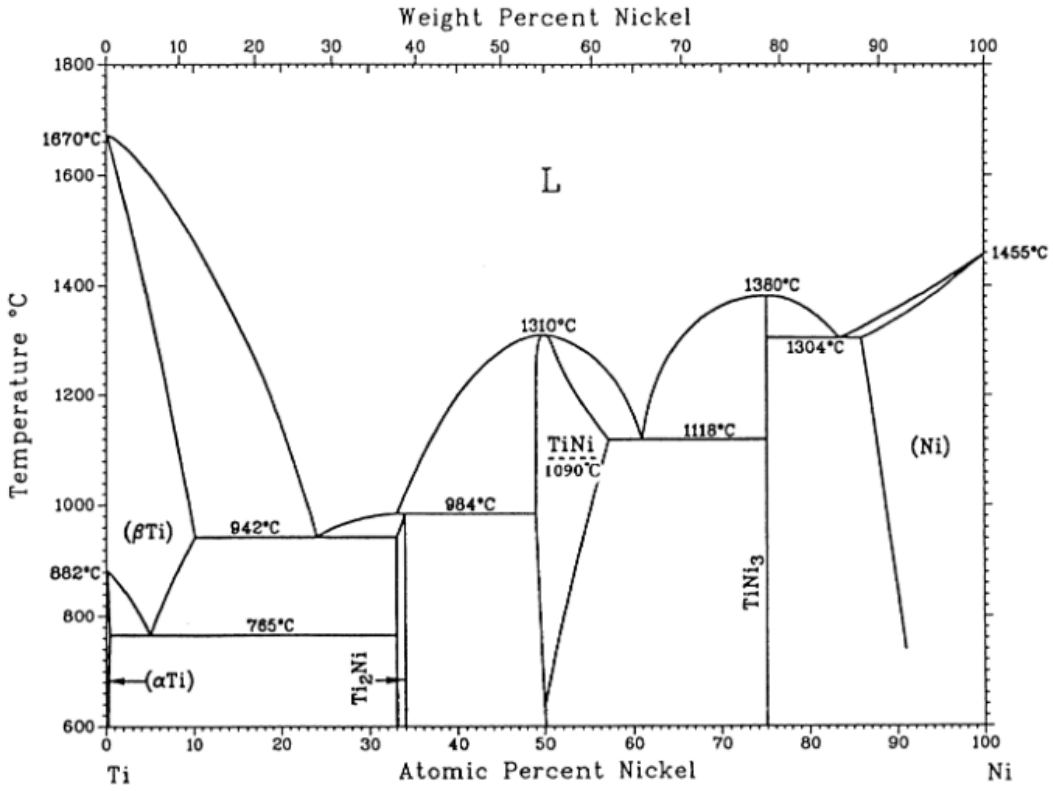

Figure 2.12: Phase diagram of Ti-Ni systems, from [76]

anisms and related shape memory effects particularly difficult for several years in comparison with other alloys, and it was only thanks to many extensive research studies in the 1970s and 1980s that the phenomenon was finally understood. The R-phase is defined as an intermediate phase that occurs prior to martensitic transformation. It has a different lattice from austenite and martensite, which is obtained by stretching the cubic austenite in order to achieve a rhombohedral configuration. In the presence of the R-phase, the transformation B2→R→B19' occurs. If the B19' appears first, the R-phase is suppressed. The R-phase is formed in the following three cases [5]:

- A few percentages of Ni in the equiatomic Ti-Ni system is replaced by Fe or Al.
- Ni-rich Ti–Ni alloys are aged at certain temperatures (around 400 °C) to cause the precipitation of Ti_3Ni_4 phase; (as described in section 2.4.1).
- Ti–Ni alloys are heat-treated after cold-working to create rearranged dislocation structures.

The presence of the R-phase is clearly shown by the cooling curve in the heat flux vs temperature diagram in Figure 2.13, obtained by the DSC (Differential Scanning Calorimetry) mea-

surements, with reference to a binary NiTi alloy. As shown by the graph, the cooling curve has two peaks corresponding to: first, the A→R phase transformation; second, the R→M phase transformation. The A→R transition is characterized by an increase in the electrical resistivity and a very low thermal hysteresis (1-2 K). In the absence of the R-phase, the DSC cooling curve shows only a single peak at the A→M transition.

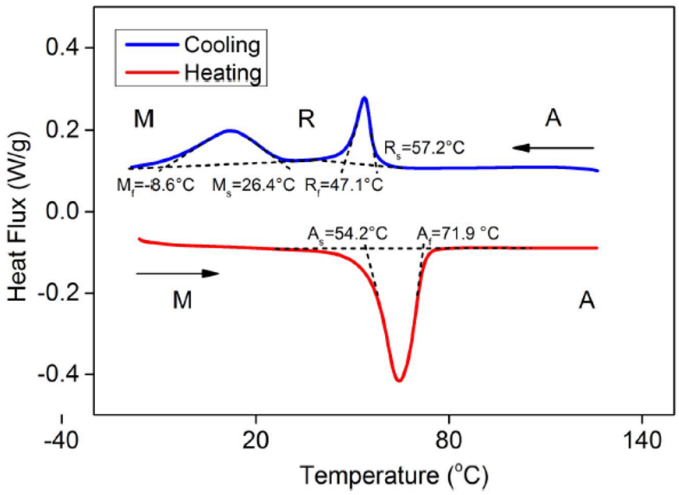

Figure 2.13: DSC thermogram of NiTi SMA, from [77].

The presence of the R-phase in the NiTi SMA is not a desired effect. In fact, it has been experimentally demonstrated that the intermediate phase transformation causes a decrease in the shape memory performance of the material, reducing the maximum recoverable strain. For example, when the NiTi alloy is heat-treated at 550°C, it exhibits a shape memory that is three times higher than the same alloy treated at a temperature between 400 and 500°C, due to the formation of the precipitates. In summary, many factors contribute to the final performance of an SMA. The thermomechanical history experienced by the material during the initial preparation phase has a significant impact on the final properties of the material that are exploited during the operational phase. Therefore, when designing a SMA-based device, it is important to know not only the material composition, but also the ensemble of thermomechanical processes that the alloy has undergone, from the manufacturing to the final use of the material.

2.5 General applications and market interest

The use of shape memory alloys in a wide variety of fields has been driven, especially in the last few decades, by the needs of engineering applications that demand increasingly better

performance and more stringent requirements. Thus, smart materials with the ability to recover the original shape and large deformations in the presence of the right stimulus became the turning point for the design of various devices.

2.5.1 SMAs applications

Since the 1980s, the SMAs and in particular NiTi applications grow in many areas. In the 1990s, this technology was introduced in the Shape memory material community [78]. The first relevant application of NiTi alloys was related to their unique biocompatibility properties. In particular, vascular stents were one of the first SMA-based devices developed on an industrial scale. However, potential users of NiTi medical devices initially rejected them because of the presence of Ni, which has been shown to have toxic, carcinogenic and immunosensitizing effects, and its potential release in corrosive environments such as the human body. Fortunately, research quickly demonstrated that NiTi has good corrosion resistance and tissue compatibility [79, 80]. Since then, the use of Nitinol in the medical industry expanded and paved the way for its use in many other fields. Nowadays, the application of SMAs spans a vast range of industries, where these materials are primarily used for the design and development of sealing/connection systems, actuators, dampers, biomedical devices, and microsystems. In general, SMAs devices exploit SME and/or PE, so they can be based on different working principles depending on the type of input stimulus and the output generated. In particular, four categories are identified: free recovery, constrained recovery, work production, and superelasticity [26, 81, 82, 83]. The respective operating principles are schematically reported in Figure 2.14.

In short, recovery applications take advantage of the material's ability to recover the original shape after a load-unload cycle by raising the temperature above the transition point to trigger the martensite to austenite transformation. *Free-recovery* applications, where the memory element generates strain (or motion) with no load applied, are rare. The most representative example of commercial devices are the Ni-Ti eyeglass frames [84], which are comfortable to wear and are able to recover their original shape after accidental deformation by immersion in hot water.

In *constrained recovery* applications, SMA is prevented from changing shape after the thermal stimulus, and the result is the development of stress (or force). Most commercial applications fall into this category, such as joints and fasteners. In general, the assembly is performed

after the memory element has been appropriately expanded in the martensitic state. Then, the temperature is raised in order to trigger the phase transformation and the connection is realized by the shape recovery of the SMA element against a rigid constraint, that is the part to be fixed. This type of system is widely used especially in aerospace for coupling applications [85, 86, 87]. In particular, hydraulic tubing coupling on F-14 in 1971 was the first commercial use of SMAs and this type of application is still one of the most successful. In this case, the hysteresis loop is wide enough to allow connection stability in operating conditions.

Work production is the general operating principle of actuators: the work necessary to deform the martensitic SMA is much smaller than the work generated after the shape recovery by heating above the austenite transition temperature. Therefore, a motion is generated against stress, allowing the shape memory element to produce mechanical work. Actuators are classified into two groups, depending on the type of stimulus: thermal actuators, which are driven by the change in ambient temperature, and electrical actuators, which are driven electrically [88]. This type of application requires a narrow thermal hysteresis of the memory element as it allows a shorter response time of the actuator in recovering its original shape. In addition, actuators can easily be integrated and miniaturized, so various successful attempts to introduce SMAs in microsystems were done with reference to this application. Specifically, Ni-Ti alloys become the prevalent choice in the field of micro-electromechanical systems (MEMS) due to their high actuation force and displacement at a relatively low frequency (up to 100 Hz), efficiency, and non-linear behavior [89].

Finally, *superelasticity* allows a large amount of recoverable strain during isothermal phase transformation, so that the accumulation of great potential energy is possible. This particular feature is exploited especially for civil structures applications, where the use of the SMAs improves the seismic response, i.e. buildings or bridges [90, 91, 92]. In general, superelasticity applications require that the temperature is controlled, such as in the biomedical field, to avoid undesired thermal-induced phase transition, which would affect both the recovery and the mechanical properties of the material. An example is the orthodontic braces invented in 1971 [93, 94], one of the first and most successful applications of NiTi alloys. Another significative example is constituted by the stents, an invention by Dotter's group in 1983 [95] and whose usage grew in the global market rapidly.

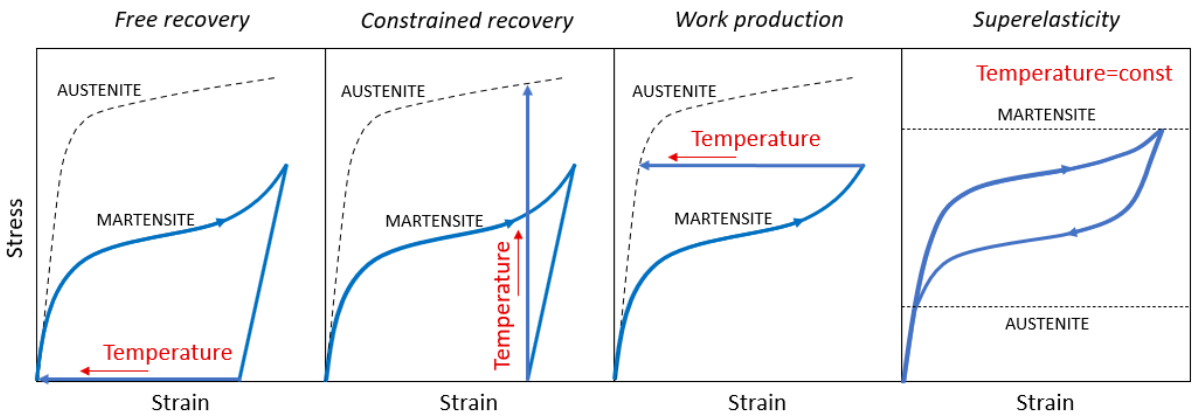

Figure 2.14: Application categories of SMAs, adapted from [83].

2.5.2 SMAs market: industries, trends and forecast

The market for shape memory alloys is growing continuously, driven by the increasing demand for SMA in automotive applications, biomedical devices, aircraft components, the automation and control sector, and electronic devices. Some of these applications apply the same concepts and operating principles, which are thus shared between different sectors.

Currently, the growth of the *automotive* industry has a significant impact on the growth of the global SMA market. Modern vehicles are increasingly demanding greater comfort and performance, more advanced safety systems, and in general, more sophisticated technology. As a result, SMA-based devices are used in many functional areas of a vehicle, primarily as linear and thermal actuators. Practical examples are the NiTi thermovariable rate (TVR) springs, a device used in Mercedes-Benz automatic transmissions to have smooth gear shifting (Figure 2.15a), and the electrically actuated antiglare rear-view (EAGLE) mirror (Figure 2.15c). Furthermore, SMA morphing capabilities enable aerodynamic and aesthetic applications, as shown in Figure 2.15b. Most of these applications use commercial binary NiTi alloys, which offer reliable mechanical properties, good fatigue resistance, and transformation temperatures from -50°C to 110°C, which are compatible with the standard automotive operating range (-40°C to +125°C). Copper-based alloys, such as Cu-Al-Ni, could work at higher temperatures in the engine compartment (transformation temperatures up to 200 °C), but they are brittle, unstable, and with a low fatigue resistance [83]. Therefore, Ni-Ti-based systems remain the most widely used for such applications.

Technological progress has also contributed to the increasing demand for high-quality medi-

cal devices and surgical tools, as well as the introduction of SMA in minimally invasive surgery (MIS). Therefore, the market growth can also be attributed to the increasing demand for SMA in the *biomedical* sector. Medical implants are the most common applications and represent a very large share of the SMA market despite their high costs. As a part of internal medical devices, in contact with tissues and body fluids, SMAs must meet some basic criteria, such as biofunctionality, biostability, biocompatibility, and remain non-toxic during the implantation. They also exhibit high corrosion resistance and unique physical properties. In particular, superelasticity mimics the stress-strain response of the human bone and tendons, as shown in Figure 2.16. This special feature is exploited for many medical equipment and devices. Examples include dental implants, such as superelastic braces, stents, medical tweezers, sutures, anchors for attaching tendons to bone, aneurysm treatments, eyeglass frames, and guidewires, used in many medical

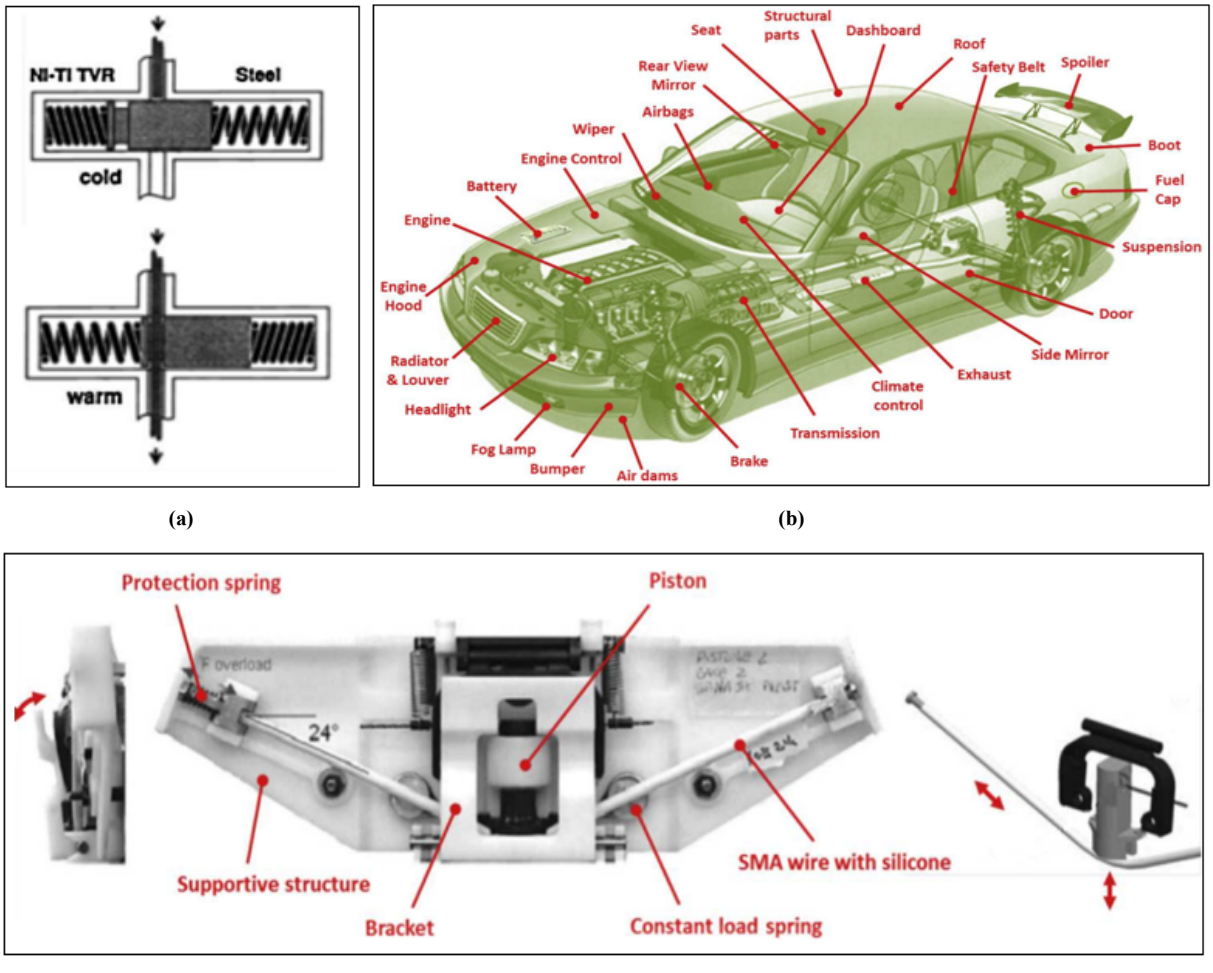

Figure 2.15: SMAs applications in the automotive field: **(a)** Mercedes-Benz TVR, **(b)** Existing and potential applications in different automobile areas, and **(c)** EAGLE mirror prototype, from [83].

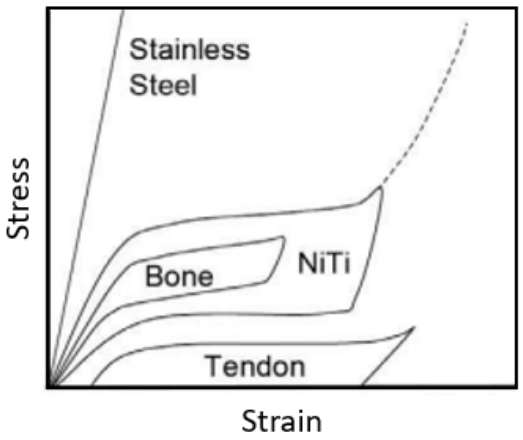

Figure 2.16: Comparison of stress-strain relationship for superelastic NiTi alloy, stainless steel, bone, and tendon tissues, from [96].

fields including orthopedics, neurology, cardiology, and interventional radiology [96]. Some examples of SMA devices are reported in Figure 2.17. Again, NiTi alloys are the preferred materials.

Moving ahead, SMAs represent an attractive solution for many complex engineering problems also in *aerospace* and *aeronautics* due to their great power/weight ratio and morphing capabilities. The last two features are significantly relevant in applications where dynamic loads and limited geometric space establish important design constraints. Therefore, SMAs find applications as actuators, connectors, vibration dampers, manipulators, adaptive structures, and many others. Smart Wing Program, for aircraft smart wings, and Aircraft and Marine Propulsion System Demonstration (SAMPSON), for jet engines, are the two most important projects on the development of SMA-based systems for fixed wings aircraft, both recognized by the Defence Advanced Research Projects Agency (DARPA) [98]. The first project regards the development of SMA actuation systems for wings shape to improve the aerodynamic and aeroelastic performance of military aircraft [99]. A schematic representation of various morphing devices employed on the wing airplanes is reported in Figure 2.18a, which shows how such devices change the aerodynamic profile by either stretching or compressing. The second one addresses the development of shape-adaptive structures for aircraft and marine propulsion systems. In particular, the smart materials are here used to actively induce inlet deformation in order to optimize the performance at all flight conditions [100] (Figure 2.18b). Furthermore, Boeing has also developed the variable geometry chevron (VGC), installed on a GE90-115B jet engine. This technology consists of a controlled chevron deflection, which is maximized

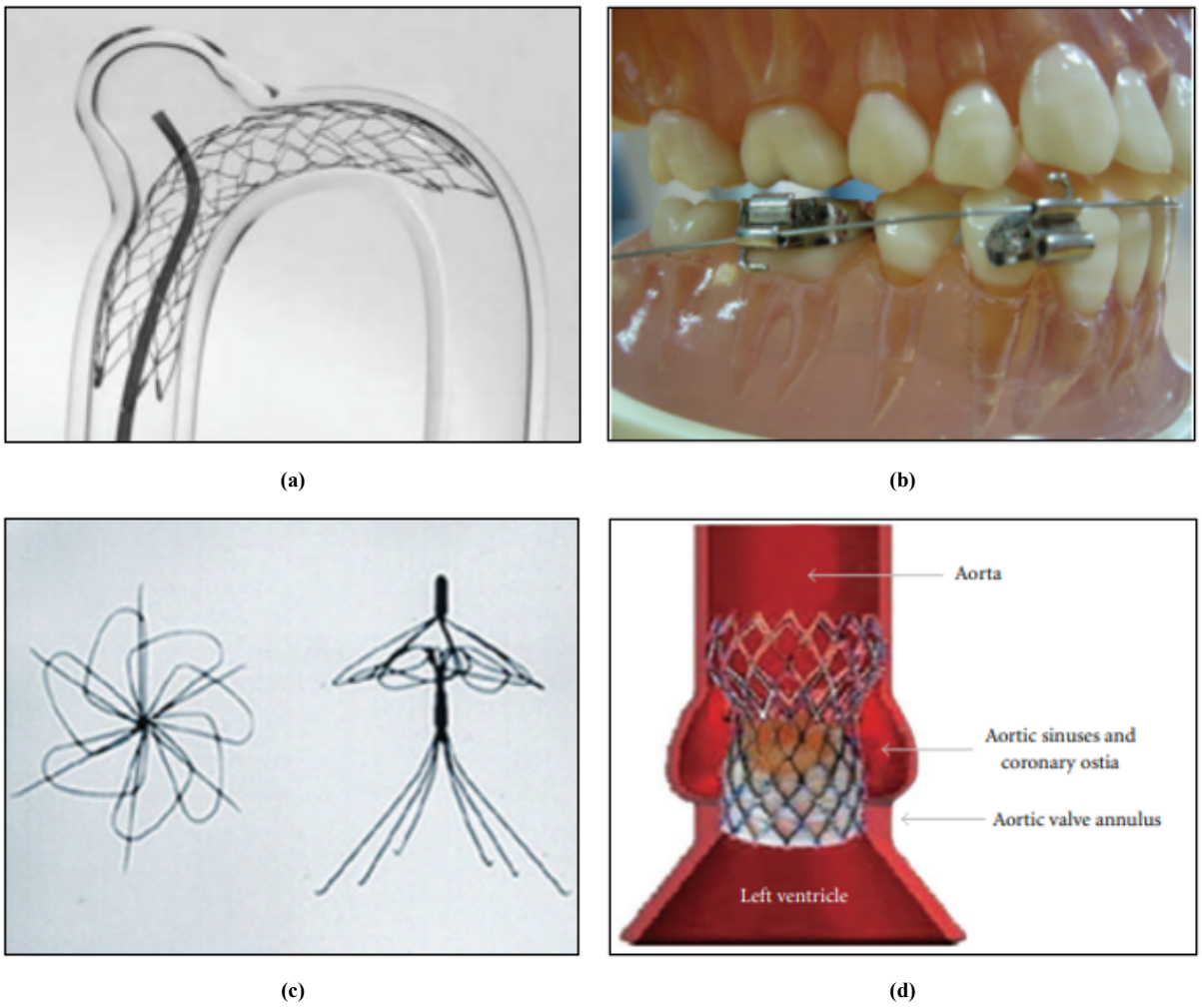

Figure 2.17: SMAs applications in the biomedical field: **(a)** NiTi self-expandable neurosurgical stent, **(b)** SMA orthodontic wires, **(c)** Venous filter, and **(d)** CoreValve aortic valve, from [97].

during the take-off in order to reduce the noise, and is minimized during the cruise to increase its efficiency [101, 102] (Figure 2.18c).

Table 2.4 summarizes the main applications of the different types of SMAs, from Ni-Ti-based alloys, which are the most widely used, to copper- and gold-based alloys, which have a more restrictive application, to finish to the iron-based alloys, which are mainly employed in the civil engineering industry.

The SMA market is segmented on the basis of the following discriminatory factors:

a) Type of alloy: Ni-Ti, Copper-based, Iron-Manganese-Silicon, and others alloys.

b) End-use Industry: Biomedical, Aerospace & Defense, Automotive, and others.

c) Geographical Region: North America, Europe, Asia Pacific, and LAMEA (Latin Amer-

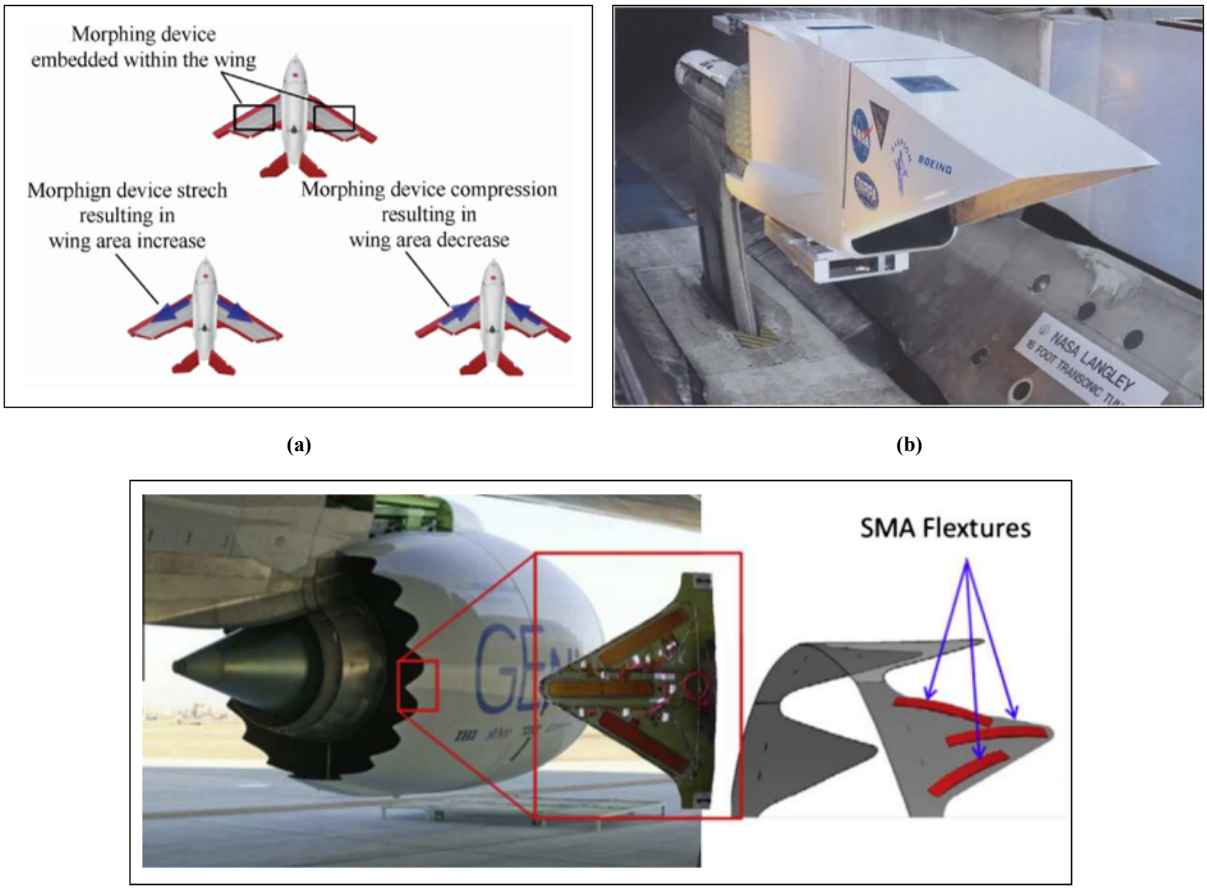

Figure 2.18: SMAs applications in the aerospace field: **(a)** Schematic representation of various morphing devices employed on the wing airplanes, from [98], **(b)** The SAMPSON F-15 inlet tested in the facility at Langley (NASA), from [98], **(c)** Boeing's variable geometry chevron (VGC), from [83].

ica, Middle East & Africa).

Temperature sensitivity, lightweight, biocompatibility, and morphing capability make SMAs ideal for many uses and in different fields of engineering, as explained above. Most of the feasible applications of SMAs are covered by the commercially available NiTi binary alloy. Regarding the global market, the scarcity of resources due to the Covid-19 worldwide crisis (2020-present) had a negative impact on manufacturing and industrial industries. Nevertheless, the value of the global SMAs market has been estimated at more than $9 billion in 2020 and is expected to reach $19.5 billion by 2023, with a compound annual rate (CAGR) of more than 8% over the forecast period from 2021 to 2030. Concerning the region segment, Asia-Pacific accounted for the largest SMAs market share in 2020 and is expected to be the most profitable market in 2030 [103].

Table 2.4: Main application of the different types of SMAs, from [66].

Type of alloy	**Main applications**
Ni-Ti-based	Pipe couplings Electrical connectors Actuators Orthodontics Stents Surgery implants
Cu-based	Seismic attenuation Isolators and dampers in civil construction Reinforcing elements Connectors and couplings Safety devices
Au-based	Dental Jewelry
Fe-based	Tube couplings Rail couplings Seismic attenuation Large-scale dampers

2.6 SMA coupler developed at CERN

Joining techniques for vacuum, either permanent connections and CF and QCF demountable flanges, represent well-assessed technologies, especially in particle accelerators (see paragraph 1.7). However, they present some limitations, such as poor compactness, inability to connect dissimilar material and the need of *in situ* assembly/disassembly and maintenance, which represent major constraints in the case of space-limited and radioactive work area. Recently, research studies undertaken at CERN investigated for the first time the use of active SMA leak-tight pipe connectors for room-temperature vacuum systems of particle accelerators [6, 7, 8, 9, 104, 105, 106]. SMA connectors are lighter and smaller than traditional devices, including standard bolted CF and quick-connect QCF systems, and can be implemented without the use of connecting flanges. In addition, they are more efficient and easier to use in the case of bimaterial connections than traditional bimaterial joining techniques, such as welding and brazing, offering also the option of dismountables seals. Such innovative connectors are compact system, radiation resistant, and can easily connect dissimilar materials, so their implementation in the domain of high-energy

physics provides important benefits to the entire machine. SMA-based connectors offer, above all, the possibility of being installed and dismounted by remote thermal control, since SMAs have special properties that allow them to respond to thermal stimuli with large deformations. Robot-friendly heating/cooling collars can be developed to completely eliminate the need for human operators in very high radiation areas.

The operating principle of a SMA connector is based on the two-way shape memory effect. The SMA connector is installed at room temperature and in the martensitic state, so the material presents a slightly larger shape that allows the mounting of the system. Then, it is heated (exploiting possible bakeout processes) to undergo a phase transformation to austenite and, consequently, to obtain the contracted shape that allows the sealing of the vacuum accelerator pipes. The dismounting of the system is performed by cooling down the SMA element to recover its martensitic shape and the unsealed system configuration.

The versatility of the innovative SMA-based joining systems offers the possibility to cover different application areas and systems connections, allowing the development of different devices in terms of material and shape. In particular, different shaped connectors have been developed at CERN, for potential applications in the LHC and in the context of the High-Luminosity (HL)-LHC and Future Circular Collider (FCC) projects, for the connection of different accelerator parts and materials. An overview of ring, oval and C-shaped couplers is given below. A commercial NiTi alloy (50.8Ni-49.2Ti at. %) was selected to realize such connectors.

2.6.1 Ring connectors

Ring-shaped SMA couplers can be used to connect pipe without the need for a connecting flange and are suitable for bimaterial connections, especially where welding is an issue. However, the primary advantage is the ability to remotely control both the assembly and disassembly processes, limiting human presence in highly radioactive areas. This latter represents the first motivation in pursuing the research toward the study of SMA couplers, within the HL-LHC project at CERN. High Luminosity-LHC project, which will be completed in 2026, aims to increase the particle collision rate by a factor of 10 [107] and consequently the radiation in the tunnel and in the vicinity of particle detectors and beam collimators will also increase. SMA rings can be designed and developed to be compatible with commercial conical flanges

(DN16,DN25,DN50,DN100) and metals (steel, aluminum, copper, etc.).

A schematic drawing of SMA ring-based coupling system is shown in Figure 2.19, where a soft gasket (usually copper or aluminum) is interposed between the SMA ring and the pipes to be connected, in order to improve the tightness of the connection. A photograph of a prototype of a vacuum pipe assembly is given in Figure 2.20. Due to the axisymmetric geometry, SMA rings can be relatively easily pre-strained in the training phase, by imposing a severe expansion deformation at the inner radius of the ring, applying a uniform radial stress state in order to obtain a SMA ring with uniform shape memory characteristics along the radial direction after unloading. This serves to provide a constant distribution of the sealing pressure across the SMA ring-gasket-pipe interfaces. In addition, both planar and axial symmetries are exploited during the first design stage, for both analitical and FE simulations, reducing significantly time and computational costs. The first studies on the design and experimental testing of ring-shaped couplers and the relative performance of NiTi- and NiTiNb-based connectors have been performed by Niccoli & al. and are available in the following literature [6, 7, 8].

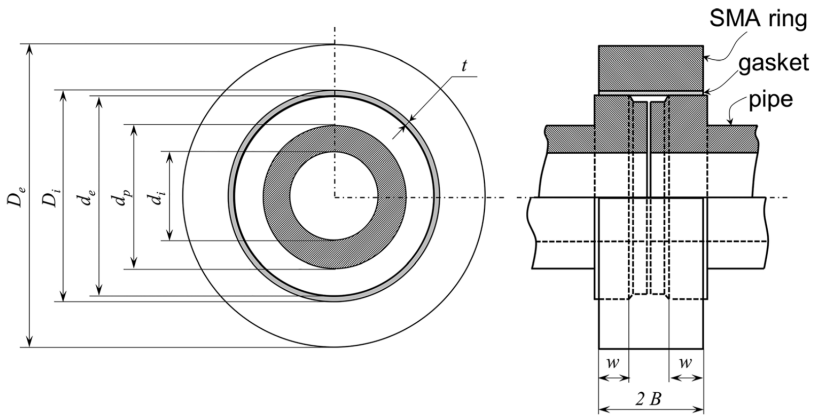

Figure 2.19: Schematic depiction of a SMA-pipe coupling system including pipes, SMA ring and soft gasket, from [7].

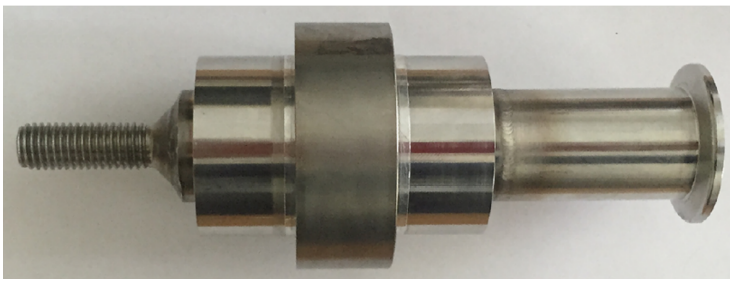

Figure 2.20: Picture of the prototype vacuum chamber, from [7].

The first ring-shaped connectors based on the binary NiTi alloy have been installed at CERN in 2022 for bimetallic pipe joints (DN25mm), the steel-titanium connections in the LHC dump entrance windows. Many prototypes have been manufactured and validated by leak detection tests after multiple thermal cycles (-10 /200°C) before implementation, showing no leaks by using a leak detector with a sensitivity of $10^{-10} mbar \cdot l \cdot s^{-1}$. A photograph of the ring coupler installed in the LHC tunnel is shown on the left side of Figure 2.21; a technical drawing and a picture of the connection system are reported on the right side.

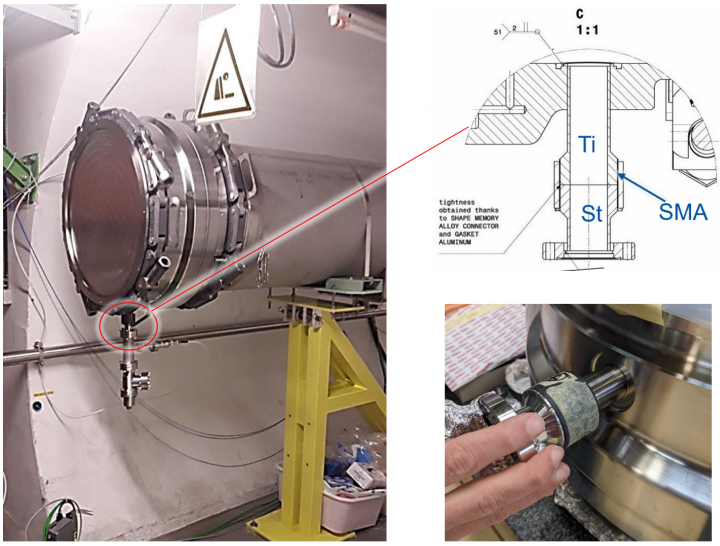

Figure 2.21: Photographs of the SMA ring coupler installed in the LHC tunned and technical drawing of the steel-titanium connection system.

2.6.2 Oval connectors

Oval-shaped SMA couplers are currently under study for the connection of oval chambers within the context of FCC-ee (electron-positron collisions) studies at CERN. In particular, the FCC project aims to create an advanced infrastructure capable of accommodating future and more powerful particle colliders. The aim is to increase the energy and intensity of particle collisions (proton-proton and heavy ions, and electron-positron) to reach energies of 100 TeV. The main obstacle in the development of such connectors is identified in the complexity of the manufacturing and thermomechanical processes for couplers functionalization, the so-called training. *Ad-hoc* procedures and equipment have been designed and developed to produce oval connectors by two different processes: a first pre-expansion of an SMA ring and a subsequent ovalization of the already trained ring. This procedure allows to simplify the preparation process

without compromising the final performance of the connector.

Figure 2.22 shows a schematic drawing of a SMA coupler for oval chamber connection (on the left) and a photograph of a first prototype of such a coupler obtained after training, with the reference of a perfect oval in correspondence of the inner face (blue line).

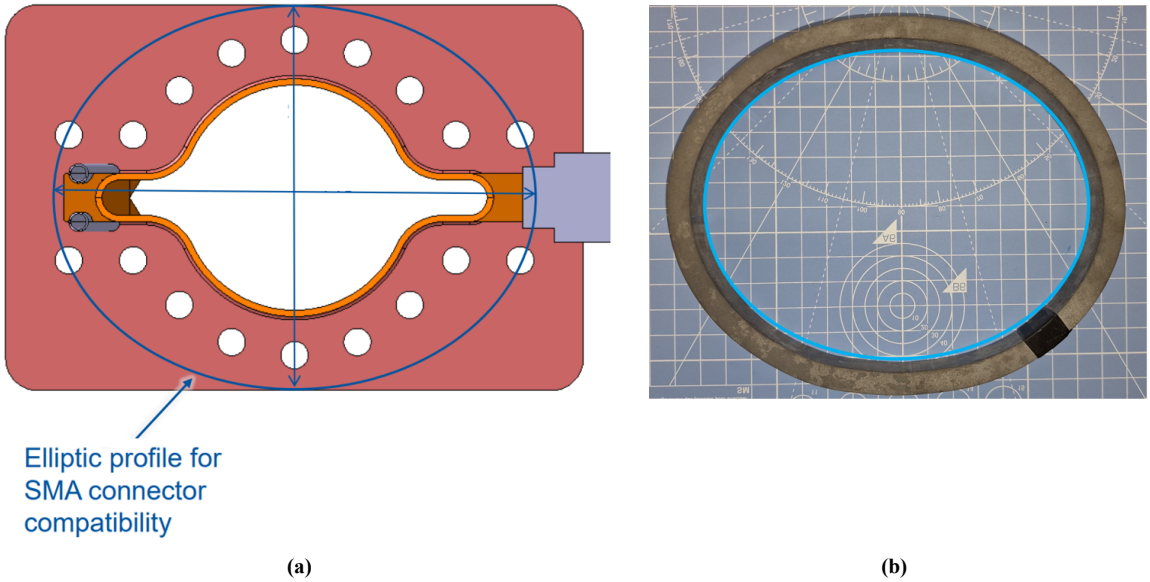

Figure 2.22: Oval connectors design: **(a)** Schematic representation of an oval-shaped SMA coupler for oval chamber connection, and **(b)** Picture of a SMA oval connector obtained after *ad-hoc* developed training and ovalization stages.

2.6.3 C-shaped connectors

C-shaped SMA connectors have recently been studied as a valid and innovative alternative to traditional vacuum pipe connection systems [108]. Traditional joining systems typically use very large stainless steel conical chain clamps to apply axial forces to the QC flanges in order to create leak-tight joints by plastically deforming the gasket placed at the tubes interface. However, the use of such chained flanges introduces some critical operational issues and design limitations with respect to space-constrained and radioactive work areas. For example, potential lubricant contamination must be considered when using traditional coupling systems. An alternative smart solution is provided by the C-shaped SMA connectors. They are smaller and lighter than traditional QC collars, can provide clean joints for UHV applications by eliminating the need for lubrication between the SMA elements and the flanges, and offer the possibility to connect dissimilar materials. This SMA chain can be installed on the flanges to realize active

bolt-free chains for system assembly and disassembly by remote temperature variation. The shape recovery properties allow the SMA elements to generate significant axial forces on the flanges to ensure the leak-tightness of the joint. In addition, the intrinsic modularity of SMA elements makes them a very flexible solution that can be applied to a variety of commercially available flanges of different sizes.

Figure 2.23 shows a simplified geometry of the C-shaped SMA connectors, which is the result of preliminary finite element (FE) analysis and analytical/empirical considerations. The geometry of the individual SMA fasteners is developed with reference to the commercially available QC flanges (DN100 or larger).

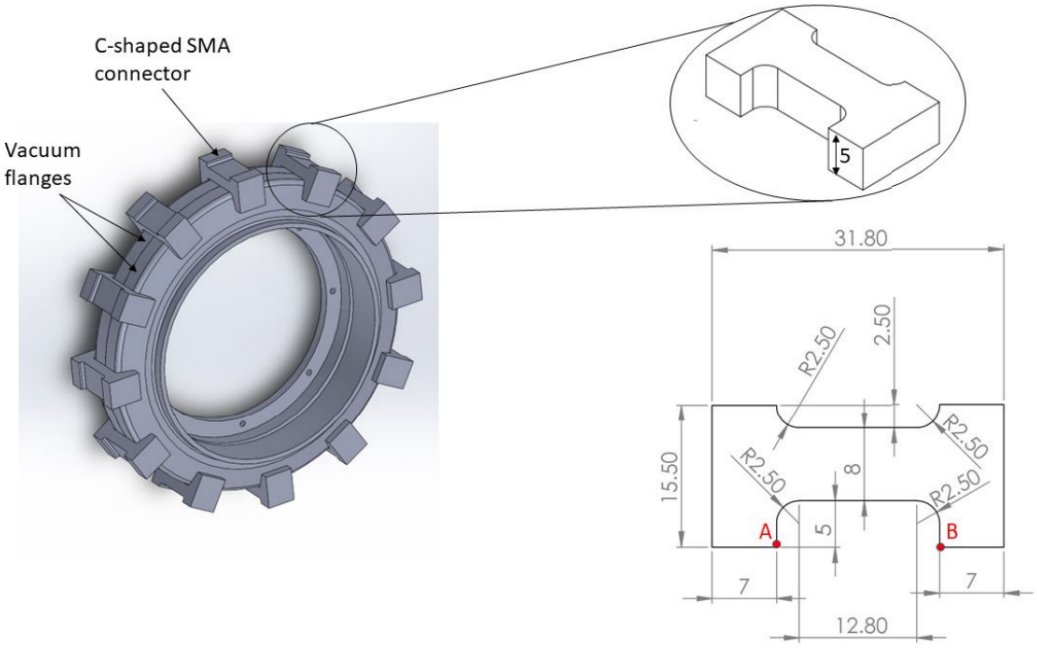

Figure 2.23: Schematic depiction of a chain of C-shaped SMA connectors for steel vacuum flanges and geometry of single C-shaped SMA-connector, from [108].

The SMA elements exhibit a dogbone-like shape with one plane of symmetry to simplify the martensitic training phase. The $5x8mm$ cross section is chosen to provide adequate recovery forces on the flanges, strictly related to the recovery stress generated by the alloy. The maximum recovery stress generated by the selected NiTi alloy is 280MPa at room temperature [9]. The recovery force of a single SMA element after activation is evaluated experimentally (Chapter 3) and is approximately 6kN at room temperature. In comparison, traditional bolts or chains in commercial Conflat® flanges exert a minimum axial force per unit arc length of 350N/mm, which ensures the leak-tightness of the system. The total axial force required for DN100 joints

divided by the force generated by a single NiTi fastener gives the minimum number of C-shaped connectors considered for the active SMA chain.

2.7 Chapter summary

This chapter presents an overview of shape memory alloys, with a special focus on the NiTi alloy, which is today widely used in many industrial domains, including the nuclear physics field of particle accelerators, where SMA-based systems can be used as connectors for UHV applications.

First, the historical background and the classification of the shape memory alloys are treated, as well as the larger domain of the shape memory materials. Thus, a focus on the shape memory alloys is made and the properties and performance of Ni-Ti, Cu, Au and Fe-based alloys are discussed and summarized in Table 2.1.

Subsequently, the functional properties of shape memory and pseudoelastic effects (SME and PE) are defined and described at macro and micro scales. First, the SMA behavior in both cases is analyzed in relation to temperature and stress conditions and as an effect of microstructural changes. Thus, the SME is the result of temperature-induced martensitic transformations (TIM) and the PE is the result of stress-induced martensitic transformations (SIM) between two crystallographic structures, which are the symmetrical parent phase (austenite, in the case of NiTi systems) and the lower symmetry martensite. The phase transformations that give rise to the properties of SMAs are thus addressed and treated from a thermodynamic point of view, in terms of elastic and chemical energy, showing that the elastic strain energy is equilibrated at each step of the process and a decrease in Gibbs free energy drives the transformation. The crystallographic theory behind the phase change is reported to understand the phenomenon at the lattice level, which completes the comprehension of what happens during a transformation from a parent to the product phase, showing the relationship between the micro and macro effects.

A special focus is given to the Ni-Ti systems due to the most exploitable mechanical and functional characteristics that make them widely used in the different engineering fields. A general overview of the binary alloy is provided starting from the equilibrium diagram with respect to the SMA. The near-equiatomic system is analyzed in terms of microstructural phases and transformations (B2 austenite and B19' martensite), Ni and Ti contents, and precipitates that can be

formed depending on the alloy composition, aging time and temperature. A consequence of the presence of the Ti_3Ni_4 precipitate in the Ni-rich NiTi compounds is the formation of an intermediate phase prior to martensite, which is the R-phase. This particular condition occurs only in the NiTi alloy and is undesirable because it causes a reduction in shape recovery compared to the same alloy that does not undergo the intermediate phase transformation.

Next, the general applications and industrial uses of these systems are presented, including the automotive, biomedical, and aerospace sectors. Table 2.4 provides a list of the main applications of the Ni-Ti, Cu, Au, and Fe-based SMAs, with the aim of summarizing the possible use of these materials and the different employment of the alloys based on the shape-memory and mechanical characteristics. A brief analysis of the current and forecast SMAs market is provided.

Finally, the special application of the NiTi alloys as couplers for vacuum systems is introduced, as a smart alternative to the traditional joining techniques. The limited space, the need for reliable dismountable and bimaterial connections, and the highly radioactive working environments have led CERN to invest in the development of innovative coupling systems for UHV applications based on shape memory alloys, which, due to their material functional properties, allow simple, tight and dismountable couplings that can be remotely controlled by temperature variation. In the context of the High-Luminosity (HL) LHC and Future Circular Collider (FCC) projects at CERN, ring, oval and C-shaped couplers have been designed and experimentally tested to verify possible future implementations in the accelerators.

Chapter 3

Experiments: material and methods

3.1 Abstract

This chapter deals with the experimental activity carried out at the laboratory of the Department of Mechanical, Energetic and Management Engineering (DIMEG) of the University of Calabria. Tests were conducted on different NiTi (50.8Ni-49.2Ti % at.) and NiTiNb (46.4Ni-45.0 Ti-8.6Nb % at.) samples, from dog bones to couplers of different shapes. The experimental campaign consisted mainly of two parts. A first part concerned the characterization of the material. In particular, isobaric and isothermal tensile tests were carried out, providing a comprehensive characterization of the material under different temperature/stress conditions. The second part deals with NiTi couplers, in particular ring, oval and C-shaped connectors. The thermomechanical training of these connectors is investigated, as well as their constrained recovery behavior. The experimental setup and data obtained from the tests are presented and discussed in this chapter.

3.2 Uniaxial tests

The material used for NiTi samples manufacturing was a Ni-rich NiTi alloy (50.8Ni-49.2Ti % at.). This alloy was selected on the basis of preliminary studies [9, 105, 106] on the thermomechanical training process of the material with the aim of tuning the mechanical and functional properties of the couplers to make them suitable for room temperature vacuum system applications. In fact, proper alloy selection and training are essential to avoid premature thermal activation and disassembly of the system. The NiTi binary alloy is characterized by *narrow thermal hysteresis* ($A_f - M_s \sim 30°C$) and a fully austenitic structure at room temperature ($A_f = 12°C$).

The DSC thermogram of this alloy is shown in Figure 3.1.

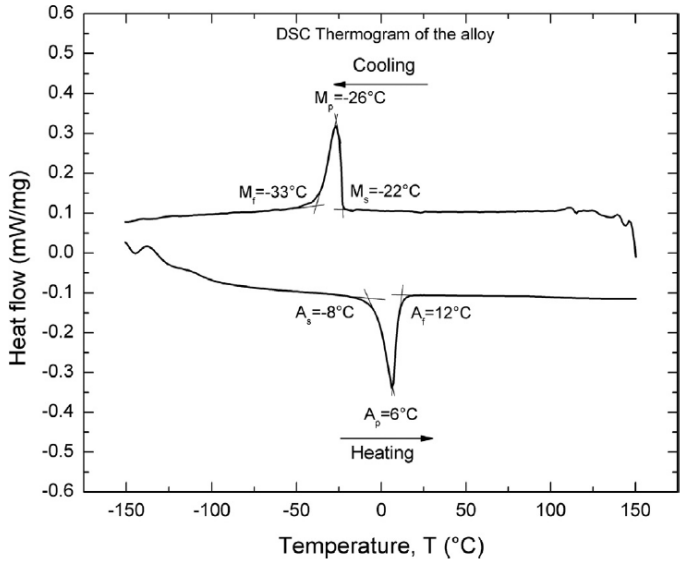

Figure 3.1: Differential Scanning Calorimetry thermogram of the investigated NiTi alloy, from [9].

The properties of shape memory alloys are strongly influenced by the thermomechanical history of the material as well as its chemical composition. Therefore, the alloy may have slightly different properties depending on the supplier and this must be taken into account in the design of a SMA-based device.

Data from uniaxial tests on NiTi dog bones were used to calibrate both the analytical and numerical models of SMA ring behavior under different loading conditions presented in Chapters 4 and 5. The tests were carried out in a *servo hydraulic universal testing machine* (Instron E10000, 10 kN) equipped with a climate chamber (-170 °C/+300 °C). Chamber cooling was performed by liquid Nitrogen. NiTi dog-bones with a gauge length of $10mm$ and a cross section of $1.55 \times 3mm^2$ and from three different batches of specimens were used for the tests. Strain and temperature were measured/controlled by an extensometer and a k-type thermocouple, respectively. A picture in Figure 3.2 shows the experimental setup for uniaxial tests.

Figure 3.2: Experimental setup used for uniaxial tests.

3.2.1 Mechanical pre-deformation

Isothermal martensitic predeformation of SMA specimens ($T = -80 < M_f$) is aimed at obtaining appropriate OW and TW-SME as well as suitable transformation temperatures and thermal stability range [9, 105, 106]. The effects of mechanical pre-strain, ϵ_{max}, on one-way deformation, ϵ_{OW}, two-way deformation, ϵ_{TW}, and on TTs were systematically analyzed in [6]. In particular, both ϵ_{OW}, and ϵ_{TW} as a function of the total strain ϵ_{max} show a non-monotonic trend. Moreover, austenitic TTs can be increased for the first heating cycle. This is particularly evident for ternary NiTiNb SMAs [7]. The cross-head speed of the testing machine during loading was set to $5 \cdot 10^{-4} s^{-1}$. Subsequent unloading was performed under load control at a rate of $5 \cdot 10^{-1} MPas^{-1}$. Maximum displacement values achieved in the training tests were chosen according to the results of previous analyses, with the aim of providing suitable mechanical pre-strain to cope with the strict functional requirements for room-temperature vacuum applications, such as a maximum two-way strain higher than 1% and a specific range of transformation temperatures ($A_s > 30°C, M_s < -20°C$) [9, 106]. Figure 3.3 shows the stress-strain curves obtained from the pre-strain tests.

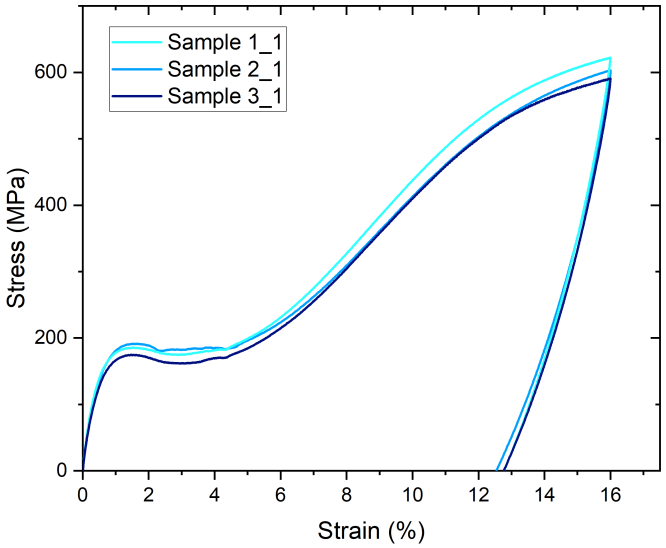

(a)

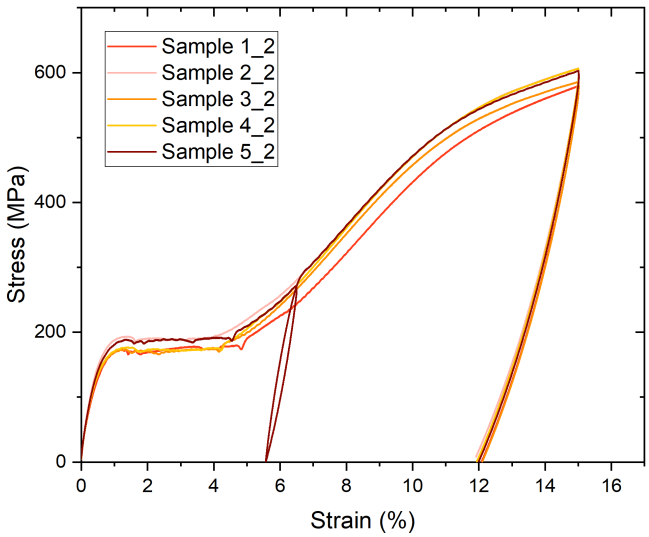

(b)

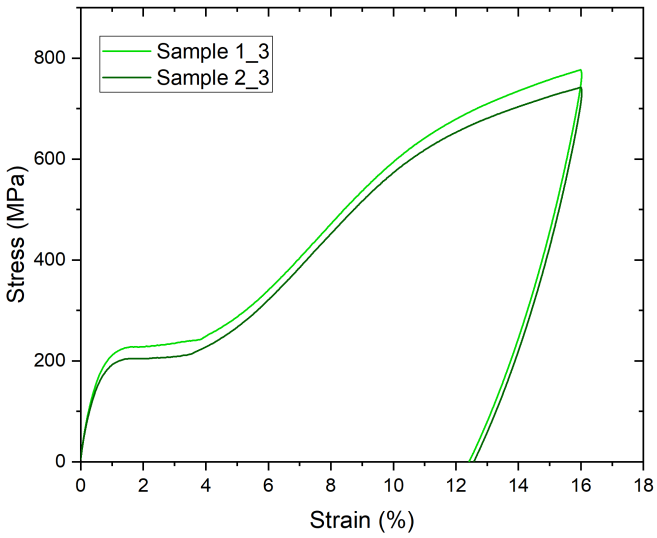

(c)

Figure 3.3: Uniaxial stress-stress curve from thermomechanical training of dog-bones: **(a)** Group 1, **(b)** Group 2, and **(c)** Group 3.

All samples were subjected to complete loading/unloading cycles (Sample 2_1 was subjected to two cycles at 6% and 15% strain), showing the optimum repeatability of the material response for each batch of specimens. Uniaxial stress-strain curves allow the identification of most of the material properties. This is essential in the initial design stage to model and simulate varius SMA ring/pipe configurations.

3.2.2 Isobaric thermal cycles and isothermal tensile tests

Isobaric thermal cycles and isothermal tensile tests were performed on specimens previusly pre-strained (see paragraph 3.2.1). Specimens were heat treated and pre-strained ($\epsilon_{max} > 7\%$) to induce the shape memory properties in the material through the alignment of the martensitic variants. Figure 3.4 shows the true strain vs temperature curve ($\epsilon - T$) obtained from the first stress-free ($\sigma = 0$) heating/cooling cycle ($= 3 \cdot 10 - 2°Cs^{-1}$) between TTs. K-type thermocouples and high-temperature extensometers were used. The figure shows the one-way, ϵ_{OW}, and two-way strain, ϵ_{TW}, obtained by heating above A_f and cooling below M_f, respectively.

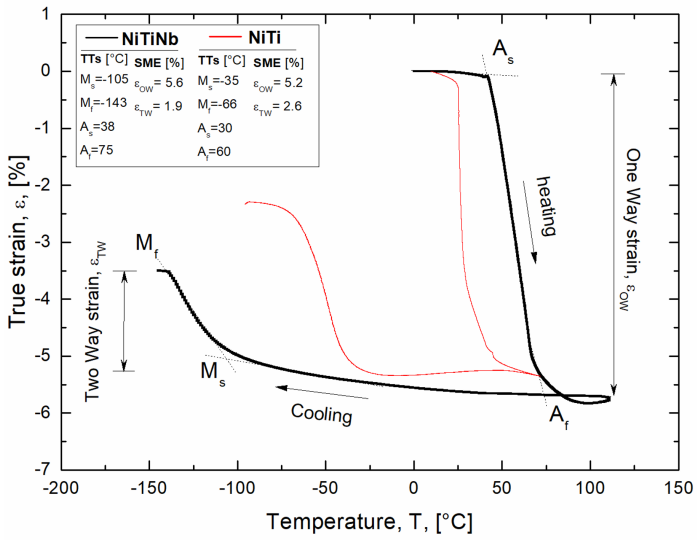

Figure 3.4: Thermo-mechanical properties of the investigated NiTi and NiTiNb alloys: true strain vs temperature ($\epsilon - T$) curve obtained from stress-free ($\sigma = 0$) thermal cycle between the TTs.

Isobaric strain-temperature tests ($\sigma = 0, 100, 200, 300MPa$) were carried out on NiTi specimens in order to identify the evolution of the austenitic and martensitic TTs as a function of the applied stress and the Clausius Clapeyron coefficients. Results in terms of TTs as a function of the applied stress are reported in 3.5. The evolution of σ^s_{cr} and σ_y with temperature are shown

in the figure. In particular, σ_{cr}^{s} increases with temperature from M_s to A_f^{σ}, but it deviates from Clausius-Clapeyron regime ($\beta_{M\to A} \neq \beta_{Ms} \approx \beta_{A\to M}$). σ_y has limited variation with temperatures. Instead, a complete characterization of NiTiNb samples is reported in [6].

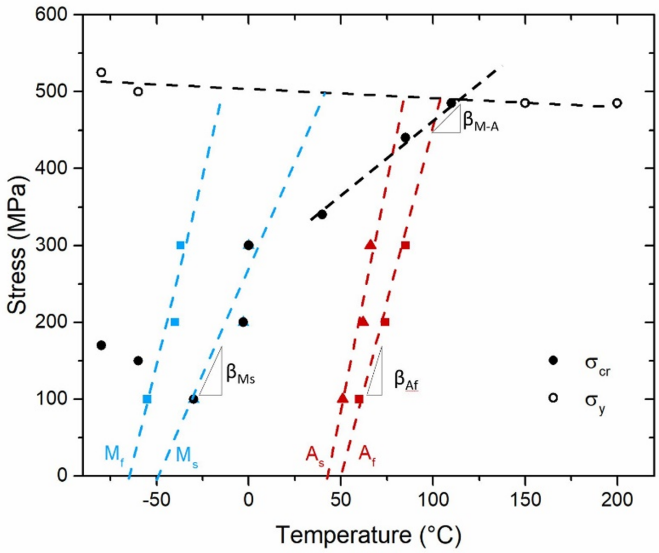

Figure 3.5: Stress versus temperature NiTi phase diagram obtained from isobaric and isothermal tests.

Figure 3.6 illustrates the isothermal true stress-true strain ($\sigma\epsilon$) response of NiTi alloy ($= 5{\cdot}10^{-1} MPa{\cdot}s^{-1}$) at different temperatures: $T = -80, 40, 85, 110, 150, 200°C$. At $T = -80°C$ the material has a completely martensitic structure; At $T = 150°C$ the material is assumed to be completely austenitic.

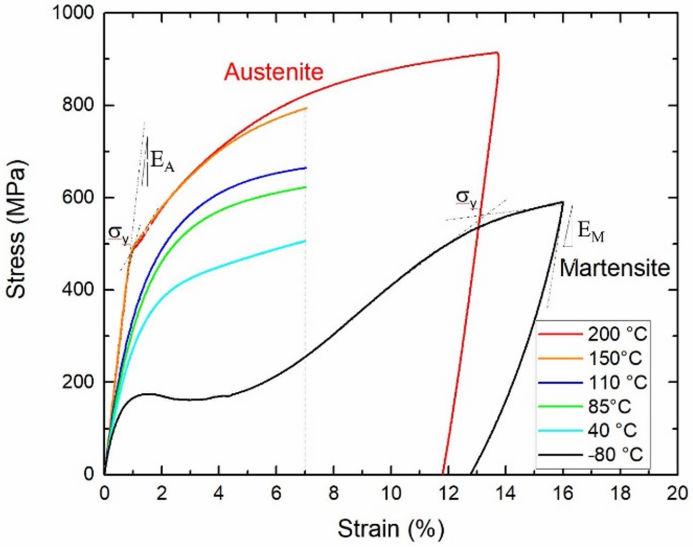

Figure 3.6: Isothermal stress-strain experimental curves of NiTi.

Further isothermal tensile tests were performed to measure the properties of the material at different temperatures. Samples were pre-heated to the highest temperature ($T = 150°C$) and then cooled to the testing temperature. The experiments were performed under load control in both the loading and unloading phases at a force rate of $= 5 \cdot 10^{-1} MPa \cdot s^{-1}$. Figure 3.7 shows the resulting stress-strain curves of NiTi in the investigated temperature range ($-60/150°C$).

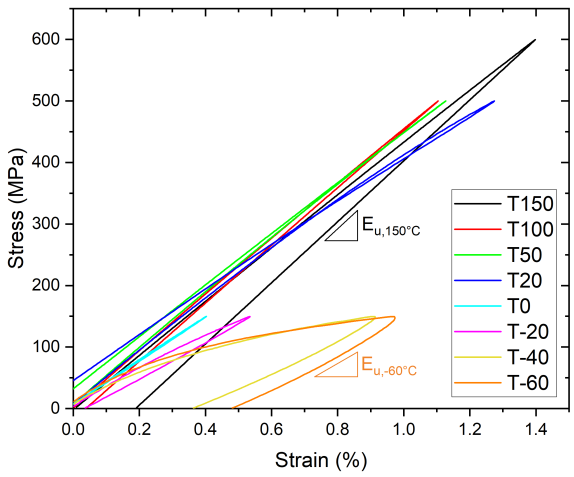

Figure 3.7: Stress-strain response under different temperature conditions and identification of the unloading modulus in the austenitic (high temperature) and martensitic (low temperature) phases.

Figure 3.8 shows the evolution of the tangent modulus at unloading E_u (indicated in Figure 3.7 at $T = 150°C$ and $T = -60°C$) as a function of temperature. The figure shows that a significant decrease of E_u occurs from 200 to 20°C (austenite). This is in agreement with experimental data reported in the literature concerning the austenite Young's modulus variation with temperature [109].

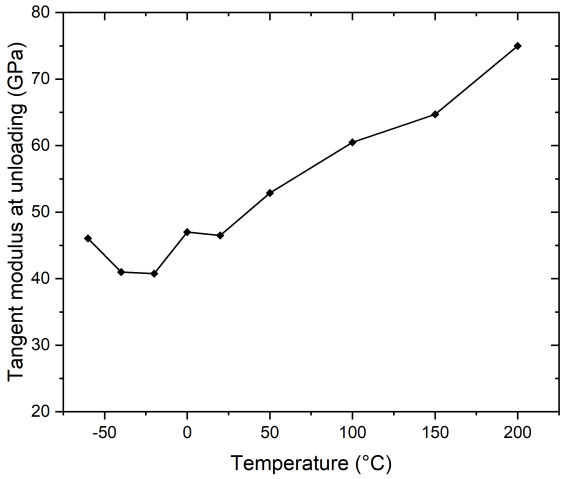

Figure 3.8: Tangent modulus at unloading over temperature.

3.3 Ring connectors

3.3.1 Thermomechanical training

The essential step to induce proper OW/TW shape memory capabilities in SMA rings consists of a severe pre-deformation of the ring under martensitic conditions. All specimens were tested at $T = -80°C$, using a machine developed *ad-hoc*. In particular, such a machine was designed and developed by 2SMArtEST, a startup and spinoff company of University of Calabria, in collaboration with an industrial partner. The machine, shown in the picture in Figure 3.9, is able to apply a uniform pressure to the inner surface of the rings. The deformation mechanism is based on a tapered punch moving within a mandrel that expands as the punch diameter progressively increases, as shown in Figure 3.10.

Figure 3.9: Photograph of the *ad hoc* designed and developed machine for SMA ring expansion.

The ring is mounted on the mandrel, whose dimension depends on the initial/final size of the ring, so it is forced to expand during punch feed. Such a system is encased within a steel structure that protects the surroundings from any sudden breakage of the ring during expansion. The final SMA ring diameter is chosen based on previous studies and simulations to provide the ring with suitable functional properties, such as OW and TW-SME, TTs and thermal stability range [106, 9]. The process is set up and controlled by means of a small touch-screen and is completely performed in less than $1min$.

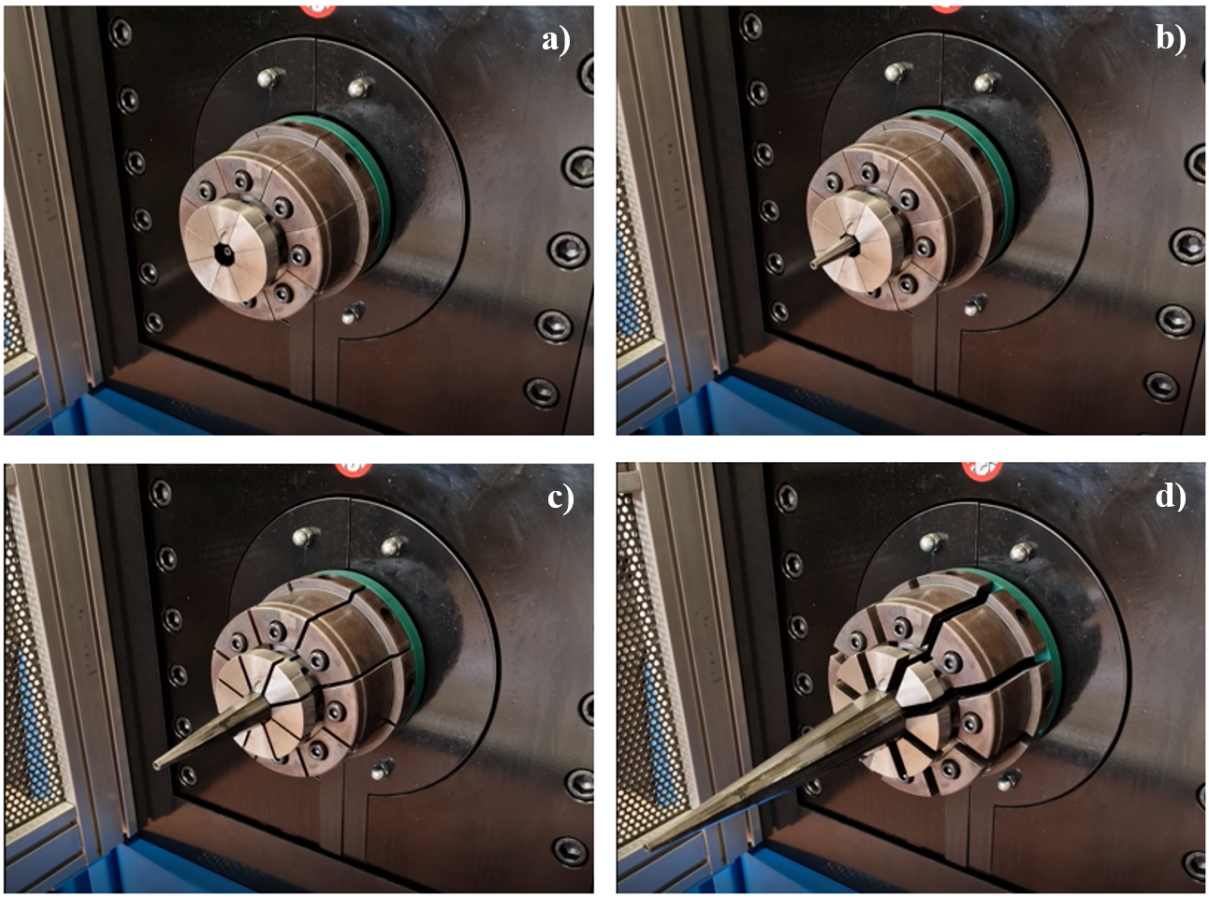

Figure 3.10: Sequence of actions of the expansion mechanism: **(a)** Closed cylindrical petal systems to allow ring mounting o the cylinder. **(b)** Beginning of the expansion: the tapered punch starts to move inside the cylinder. **(c)** Petals are opening forced by puch moving inside the cylinder. **(d)** Maximum opening of petal system.

Table 3.1 shows the value of the maximum circumferential strain achieved during ring expansion (ϵ_{max}), the mean value of inner diameter (ID), and the maximum error in the ID dimensions along the circumference ($E(ID)$) of the tested rings in the following three cases: 1) before training, 2) after training at $T = -30°C$, and 3) 24h after the training process at $T = 6°C$. Figure 3.11 shows the profile of the rings before and after expansion process.

Table 3.1: SMA ring geometries before and after training (dimensions in mm).

Ring #	ϵ_{max}	**BEFORE TRAINING T=20°C**		**AFTER TRAINING T=-30°C**		**24h AFTER TRAINING T=6°C**	
		ID_0	$E(ID_0)$	ID_1	$E(ID_1)$	ID_2	$E(ID_2)$
1	12%	127.95	0.72	140.78	1.06	139.41	0.26
2	7%	134.68	0.63	142.81	0.08	142.71	0.31
3	7%	133.07	0.58	140.89	2.35	142.78	0.24

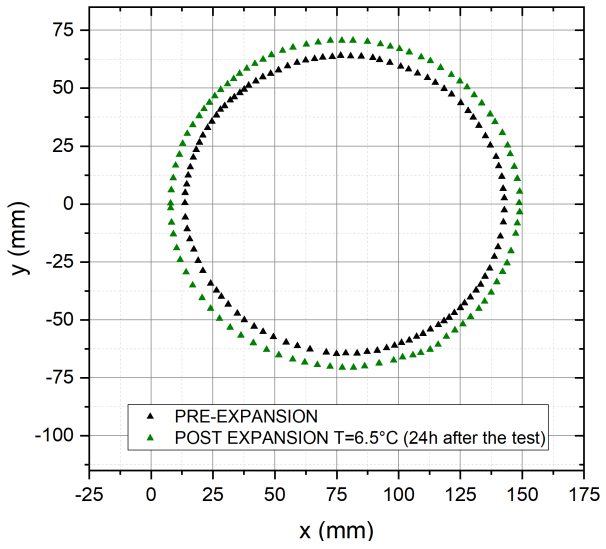

(a)

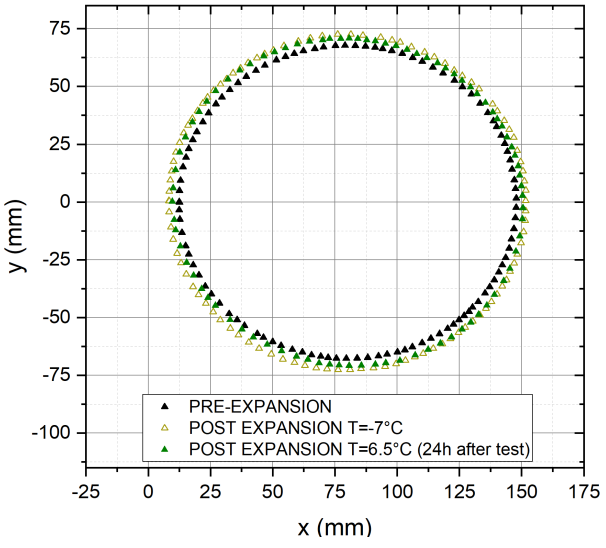

(b)

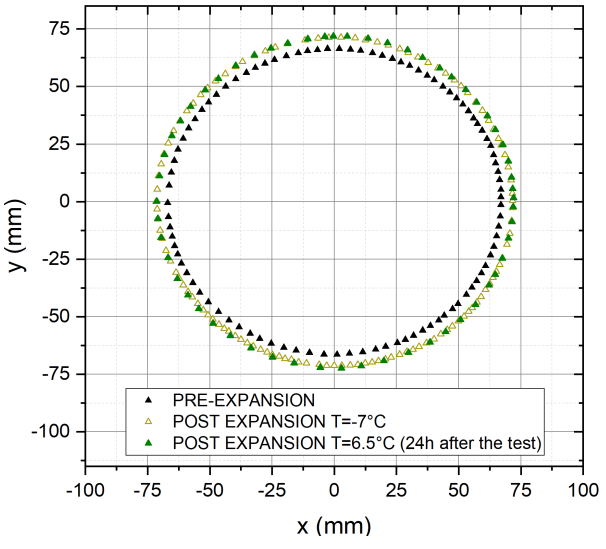

(c)

Figure 3.11: Internal profile of the rings before and after the training process: **(a)** Ring 1, **(b)** Ring 2, and **(c)** Ring 3.

3.3.2 Stress-applied tests

Stress-applied tests were performed on NiTi rings to measure the constrained recovery capabilities of the couplers on a 316LN steel ring. The tests were conducted in an Instron E10000 machine equipped with a climate chamber with a temperature range of -170°C/+300°C. Direct measurements of temperature and strains were carried out using k-type thermocouples and biaxial strain gages mounted on the inner surface of the steel rings. Axial and circumferential strain signal were recorded. An insulating glue was brushed inside the ring in the area corresponding to the terminals of the strain gauges to avoid undesired contact with the ring itself. The setup is shown in Figure 3.12. Thermal loading/unloading cycles were performed at a constant rate of 1.5°C/min in order to keep quasi-static conditions. Both temperature and strain data acquisition were done at a frequency of 2 Hz. A quarter-bridge configuration was adopted for strain measurements. As well known, this configuration gives an apparent strain during temperature change, namely thermal output. This apparent strain signal was preliminary measured by stress-free thermal tests between − 170 °C and 200 °C. The measured thermal output was subtracted from the strain signals obtained from the SMA-steel coupling. The gauge factor variation with temperature was also taken into account. The associated pressure-temperature curve was obtained from experimental circumferential and radial strains, ϵ_z and ϵ_θ, respectively, by applying the theory of elasticity for axisymmetric bodies:

$$p = -\frac{E}{2(1+\nu)} \cdot \frac{OD^2 - ID^2}{OD^2} \cdot (\epsilon_\theta - \epsilon_z) \tag{3.1}$$

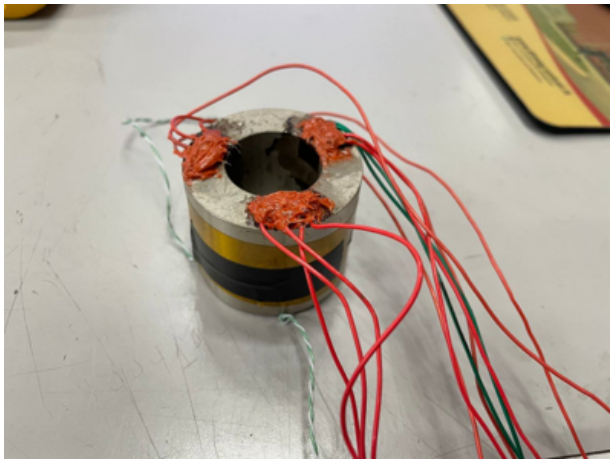

Figure 3.12: Internal steel ring instrumented with a k-thermocouple for the temperature acquisition and three pairs of strain gauges for axial and circumferential strain measurements.

The material used for the internal ring is an austenitic stainless steel 316LN (UNS S31653) with a Young's modulus of $E = 205GPa$, a Poisson's coefficient of $\nu = 0.3$ and a coefficient of thermal expansion (CTE) of $\alpha = 1.7 \times 10^{-5}$. The inner and outer diameters of the steel ring measure, respectively, $ID_{316LN} = 24mm$ and $OD_{316LN} = 43.5mm$. The SMA coupler dimensions are $ID_{NiTi} = 45mm$ and $t_{NiTi} = 5mm$. Therefore, a radial gap of $\Delta r = 0.75mm$ is estimated between the inner and outer rings at the beginning of the process.

Figure 3.13 shows the results obtained by the thermal cycles on the steel ring and on the steel/NiTi rings coupling system. In particular, Figure 3.13a shows the thermal output, i.e., the apparent strain due to the mismatch between the thermal expansion coefficient of the strain gauge grid and the steel, in both axial and circumferential direction, obtained during the first step of the experimental process. Figure 3.13b shows the total strain evolution as a function of the temperature along axial and circumferential directions obtained from thermal cycles on the entire system. The contact pressure-temperature curve is shown in Figure 3.14.

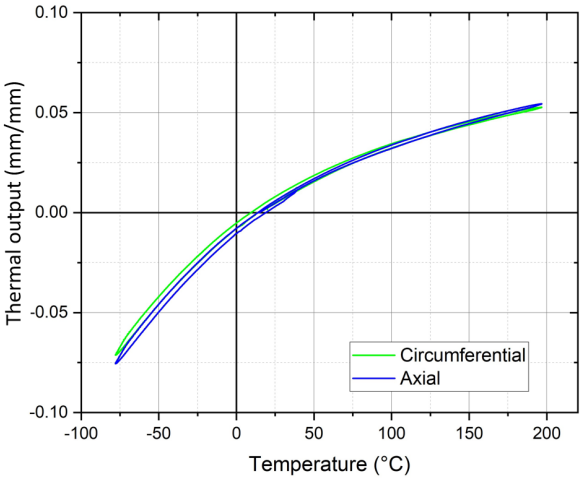

(a)

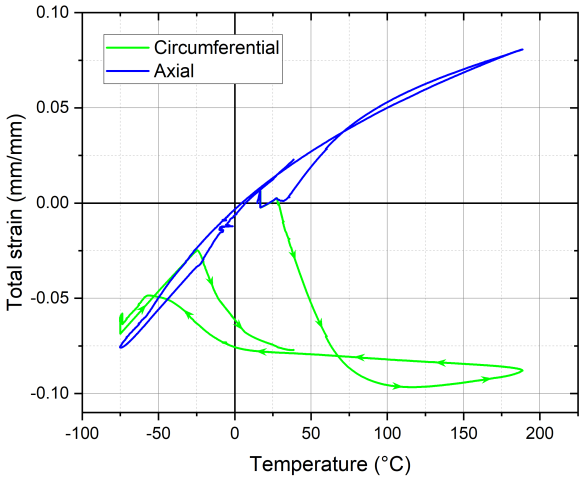

(b)

Figure 3.13: Strain vs temperature measurements at the internal diameter of the steel ring obtained in the thermal output and constrained recovery phases of the experimental process: **(a)** Pure thermal strain evolution as a function of the temperature, and **(b)** Total (recovery+thermal) strain evolution as a function of the temperature.

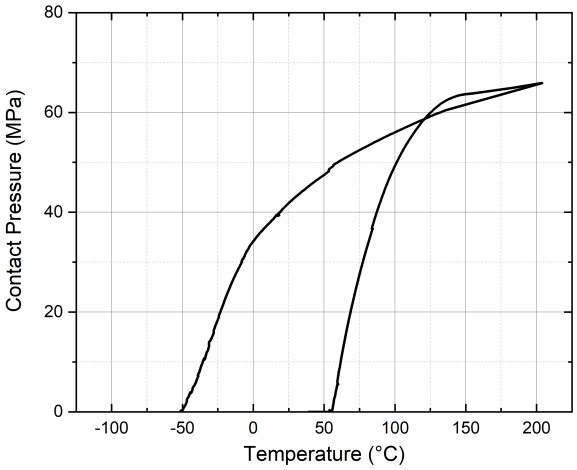

Figure 3.14: Contact pressure evolution during the thermal activation cycle.

3.4 Oval connectors

3.4.1 Ovalization process

The oval-shaped connectors were obtained by deforming already trained SMA rings (see Table 3.1) under martensitic conditions to induce the oval shape. The rings were compressed along a specific direction to induce plastic deformation and then released to allow elastic recovery. Tests were performed at T=-80°C to ensure martensitic conditions. Temperature measurements were done by a k-type thermocouple. The ovalization process was performed on the three trained rings in a servo-hydraulic machine (Instron 1276, 1MN) equipped with a climatic chamber (-170°C/+300°C) and two crossheads: the lower crosshead is fixed while the upper crosshead can move vertically. An appropriate set up was designed and built to allow the assembly and compression/ovalization of the intial ring, as well as the easy removal of the final oval connector. A picture of the machine and setup used for such a process is reported in figure 3.15.

The tests were performed under quasi-static conditions, with a displacement rate of the crosshead in the compression phase of $0.5mm/min$ and an unloading rate of $0.5kN/min$. The maximum displacement of the crosshead for the compression of each connector was defined based on previous FE simulations, in order to test different material responses and the final oval shape obtained. These displacement values, together with the initial geometry of the circular-shaped

Figure 3.15: Machine and set up used for oval-shaped connectors tests.

connector, are given below:

- *Connector 1*: initial ring dimension: $ID_2 = 139.41mm, t = 10mm$, maximum compression: $50mm$.
- *Connector 2*: initial ring dimension: $ID_2 = 142.71mm, t = 10mm$, maximum compression: $40mm$.
- *Connector 3*: initial ring dimension: $ID_2 = 142.78mm, t = 10mm$, maximum compression: $30mm$.

Figure 3.16 shows the tested connectors in the following three configurations: 1. ring shape after training, 2. oval shape after the oval test at T=-20°C, and 3. oval shape 24h after the oval test at T=6.5°C. All pictures were taken on a graph paper to have a reference for the dimension and shape of the connector. As expected, oval shapes after test are not regular shapes, but can be approximated by an ellipse. Figure 3.17 reports internal profile of the connectors in the three configurations of the ovalization process. In particular, for each connector three graphs are reported, showing the internal profile of the ring before and after expansion process, compared with internal profile of oval at T=-20°C with associated ellipse, and oval at T=6.5°C (first graph); oval shapes after the test at T=-20°C and 24h after the test at T=6.5°C (second graph); initial

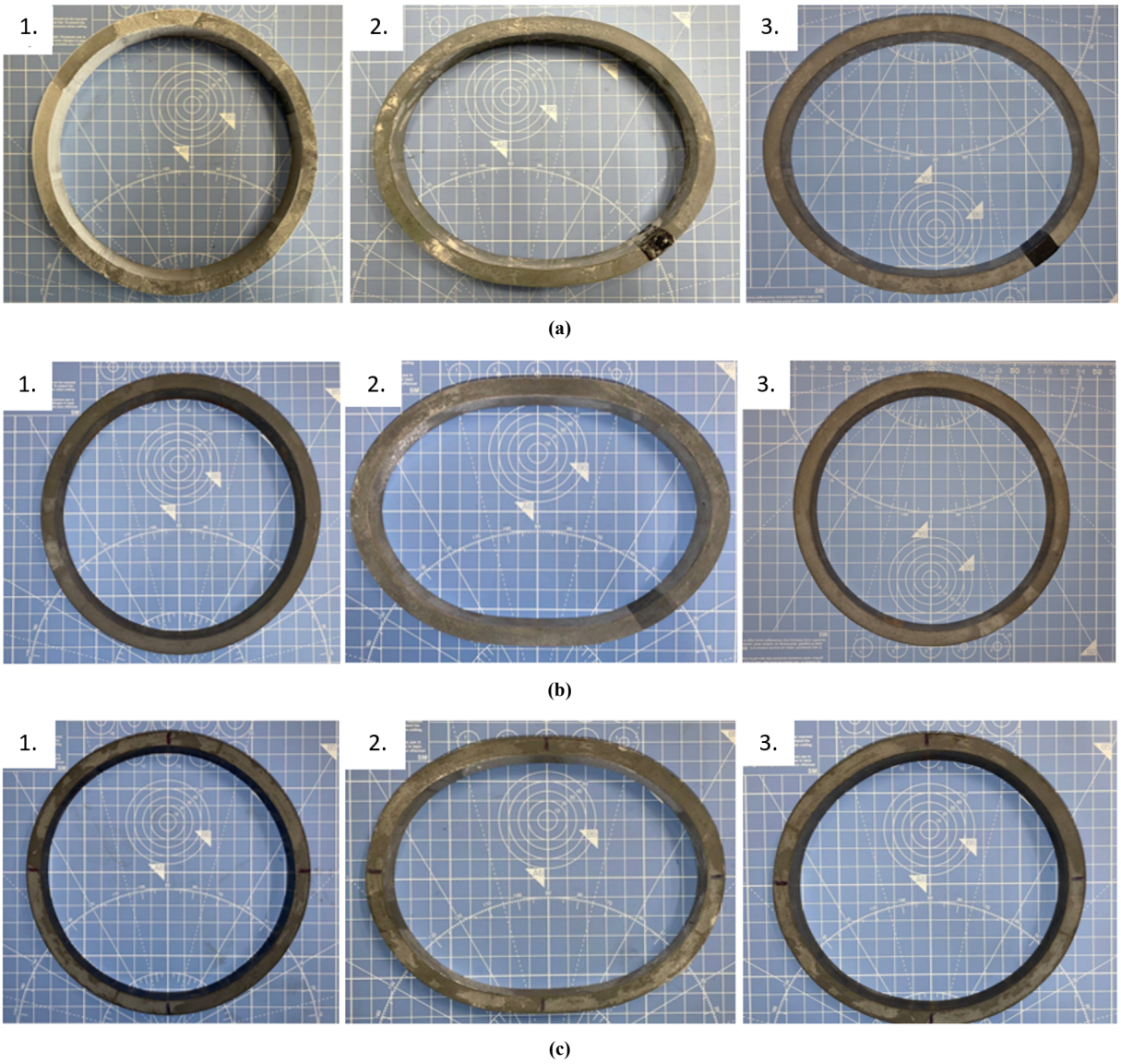

Figure 3.16: Pictures of tested connectors in different stages of the ovalization process: **1.** before the test, **2.** after oval test at T=-20°C, **3.** 24 h after the test at T=6.5°C: **(a)** Connector 1, **(b)** Connector 2, and **(c)** Connector 3.

trained ring profile and final oval profile (third graph). As shown by the figure, the internal profile of the connector 1 is kept almost unchanged between the configuration obtained just after the oval test (at T=-20°C) and the one at 24h after the test (at T=6.5°C). In the other two cases (connectors 2 and 3) instead the deformation is almost completely recovered 24h after the test (at T=6.5°C) with respect to the configuration obtained just after the ovalization (at T=-20°C). The recovery of the deformation in the last case is considered to be due to the reverse phase transformation of the material from martensite to austenite. The force-displacement curves from the ovalization tests are reported in Figure 3.18.

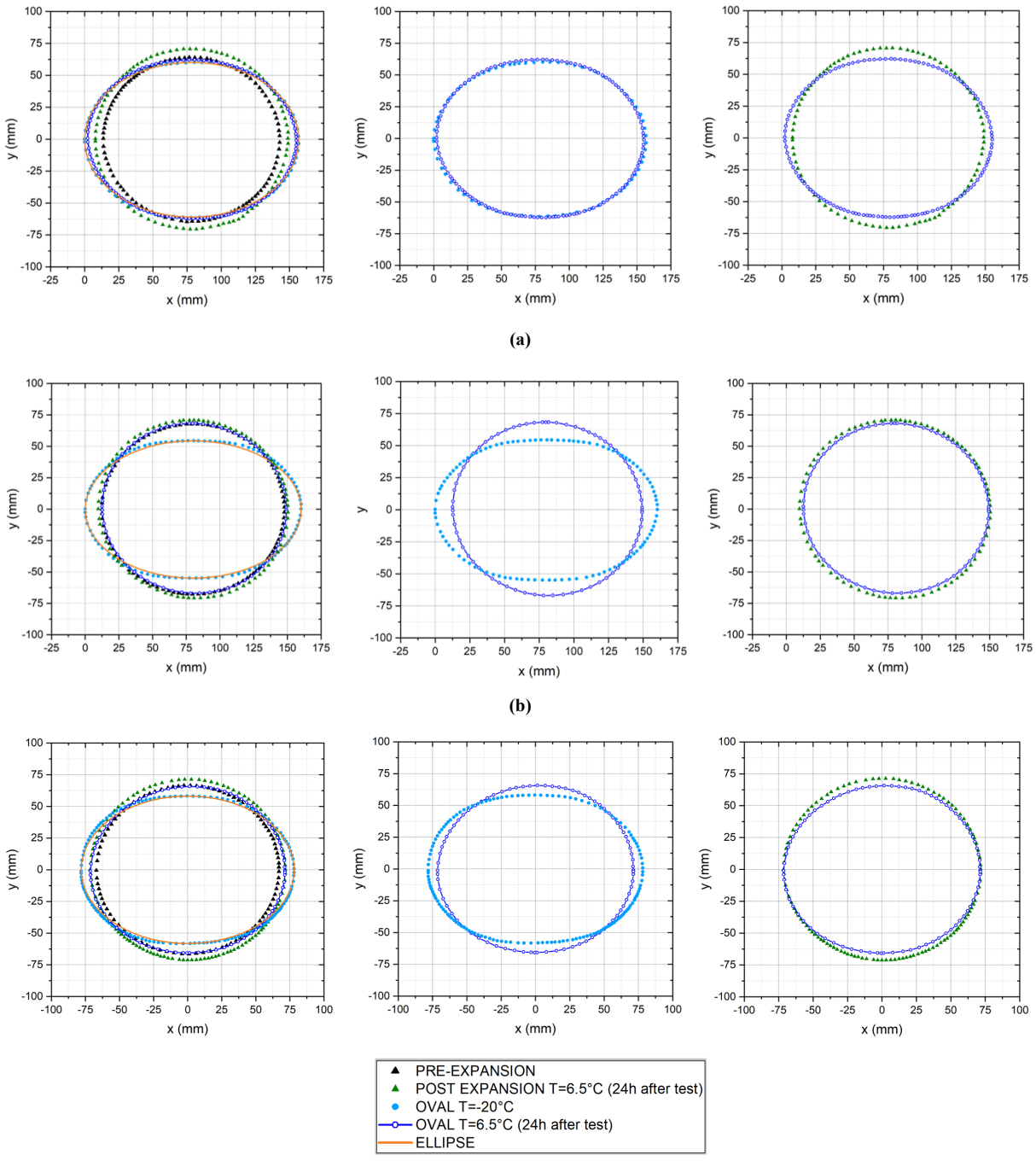

Figure 3.17: Comparison between the internal profile of connectors during the ovalization process for: **(a)** Connector 1, **(b)** Connector 2, and **(b)** Connector 3. The internal profile of each connector is reported into three different graphs: the first graphs shows the profile of the connector in the pre- and post-expansion phase, and after the oval test at T=-20°C with the associated ellipse and 24 h after the oval test at T=6.5 °C. The second graph shows a comparison between the two ovals at T=20°C and 24 h after the test at T=6.5°C. The third graph shows a comparison between initial (post-expansion of the ring) and final (oval at T=6.5°C) shapes of the oval test.

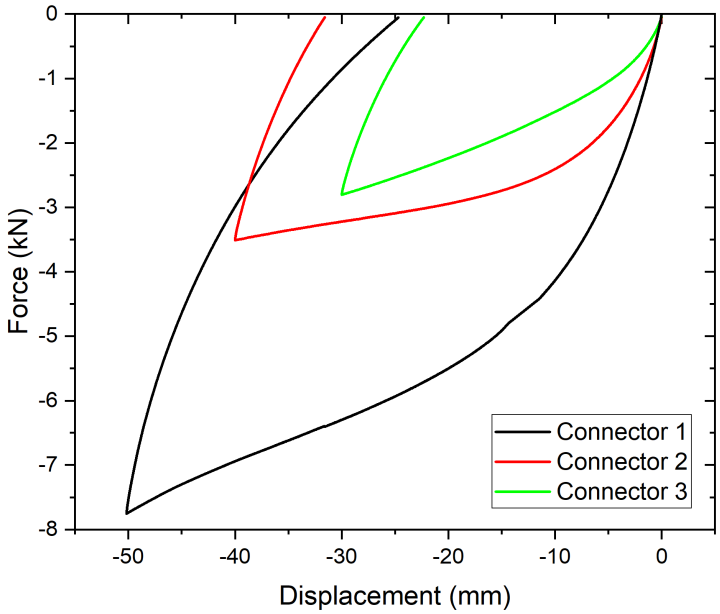

Figure 3.18: Force-displacement curves from the ovalization process of the three connectors.

3.5 C-shaped connectors

3.5.1 Thermomechanical training

The training process of the C-shaped samples consists in the uniaxial tensile test of the samples in martensitic conditions (T=-65°C) up to a pre-defined value of strain that is chosen according to the shape memory properties to be reached. An *ad-hoc* system was designed and developed for the training of the C-shaped samples. It consists of two rod forks, depicted in Figure 3.19, that are connected to the ends of the specimen by means of four high-rigidity pins. Such a system is then mounted inside a servo-hydraulic machine (Instron 1276, load capacity 1MN) equipped with a climatic chamber (-170 °C/+300 °C). Two C-shaped samples (Sample 1 and Sample 2) were trained and are shown in Figure 3.20. The specimens were loaded under displacement control and unloaded in load control. The same process parameters were used for both samples and are reported below:

- Maximum crosshead displacement in the load phase: $4mm$; crosshead speed: $0.5mm/min$.
- Minimum crosshead load in the unloading phase: $2kN$; crosshead speed: $0.5kN/min$.

The force-displacement curves obtained during the tests are reported in Figures 3.21. Figure 3.22 reports the shape profile of sample 2 before and after the training process. The specimen

results to be elongated after training, as expected, because of the longitudinal plastic deformation induced during the test. Table 3.2 reports final dimensions of the samples 24h after the training process measured at T=11.5°C.

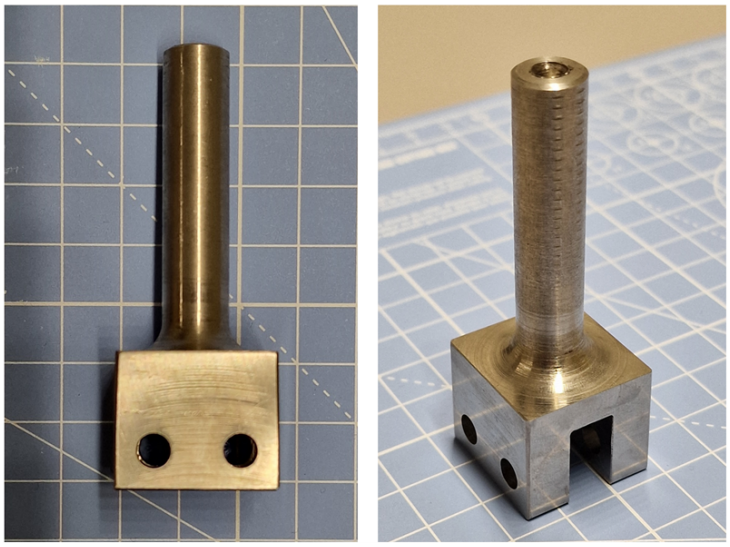

Figure 3.19: Rod forks designed and constructed for the training process of the C-shaped samples.

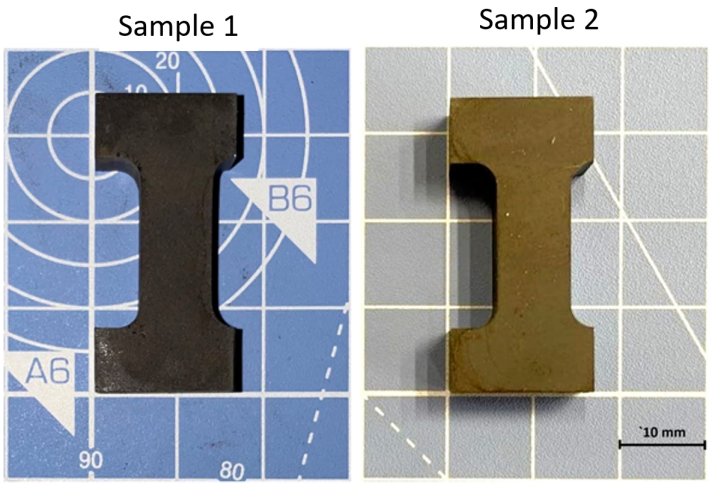

Figure 3.20: Picture of the C-shaped samples.

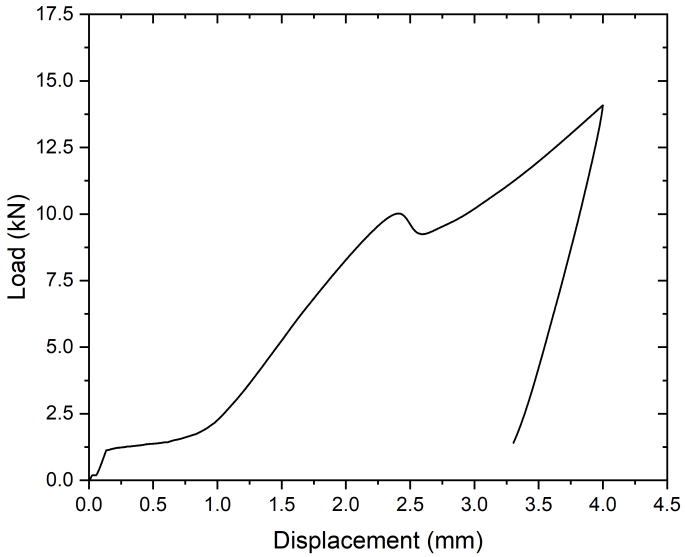

Figure 3.21: Force-displacement curves from the pre-strain test of the C-shaped sample 1.

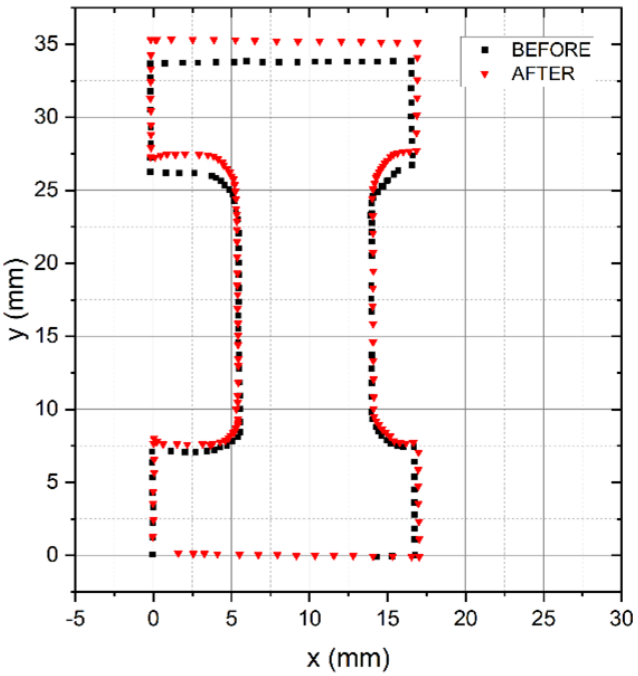

Figure 3.22: External profile of C-shaped sample 2 before and after training.

Table 3.2: Initial (before training) and final (24h after training at T=11.5°C) dimensions (in mm) of C-shaped samples #1 and #2.

	Samples 1,2 initial dimensions	**Sample 1 final dimensions**	**Sample 2 final dimensions**	
a	15.54	15.55	15.54	
b	15.54	15.55	15.54	
c	6.38	7.02	7.02	
d	6.38	7.02	7.02	
e	28.35	31.86	31.86	
f	15.59	17.8	17.8	
g	15.59	17.84	17.84	
h	7.78	7.78	7.79	

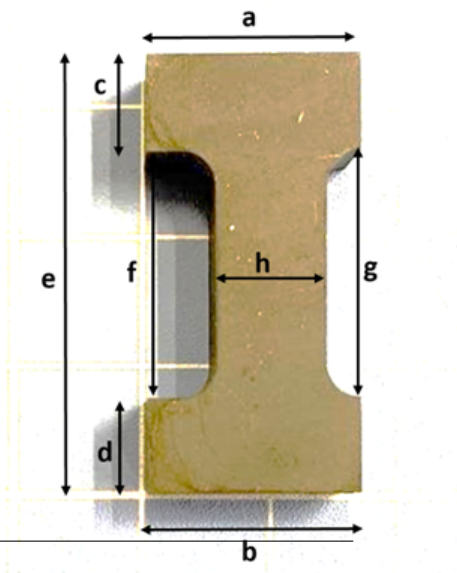

3.6 Chapter summary

This chapter presents the results obtained from an extensive experimental campaign carried out on NiTi and NiTiNb specimens. The first part of the chapter presents the results of uniaxial tests under different stress and temperature conditions. One-way and two-way recovery properties of NiTi and NiTiNb are investigated by stress-free heating/cooling cycles between TTs. Results show that NiTiNb has a larger hysteresis than NiTi. NiTi has a larger TW-SME. The phase diagram of NiTi is constructed by stress-applied heating/cooling cycles. The evolution of material mechanical parameters with temperature is studied by isothermal tensile tests. Results show a slope of the TTs around $8MPa/°C$ and an almost linear increase of the critical stress σ_{cr}^{s} with increasing temperature. The yield stress σ_y remains almost unchanged over the studied temperature range (-80/+200°C).

The second part of the chapter deals with the discussion of the results obtained from experimental tests on different shapes of NiTi connectors. In particular, the experimental setup used for thermomechanical training of the different connectors and the results obtained from tests are presented. The ring couplers are trained by a specially developed machine, which allows

for a very quick and easy training. Oval connectors are trained in the ring configuration and then compressed to obtain the oval shape. C-shaped fasteners are easily trained with tensile tests from the universal machine. Further results related to the constrained recovery of SMA rings are presented. A stainless steel (316LN) ring is used as the internal constraint for the SMA coupler, and the NiTi-316LN ring system is subjected to thermal cycling (-80/+200°C). Mounting and dismounting of the system are performed by OW-SME and TW-SME obtained by heating (M→A) and cooling (A→M), respectively. The evolution of the contact pressure with temperature is determined by strain/temperature measurements.

Chapter 4

Analytical modeling of SMA rings

4.1 Abstract

This chapter deals with the analytical modeling of the coupling process performed by a SMA ring. In particular, two models are presented. The first model describes the mechanical loading/unloading training process of SMA rings. The second model describes the SMA ring constrained recovery activated by the thermal cycle, responsible for the assembly and disassembly of the system. Both models are coded in Wolfram and implemented in Mathematica. The results are herein presented and discussed in comparison with experimental data.

4.2 SMA-based pipe coupling: training, mounting and dismounting operation

The coupling process consists of the following steps:

1. **Predeformation**: as-manufactured SMA ring are heat treated and pre-strained in martensitic state to induce proper geometrical and functional properties in terms of TTs, OW-SME (mounting) and TW-SME (dismounting) capabilities. In this phase, the ring is pre-strained at a temperature lower than the martensite finish temperature ($T < M_f$). This occurs in two subsequent steps: 1.1) Mechanical expansion of the ring up to a pre-defined value of circumferential strain ϵ_{max} in order to induce stable detwinned martensitic variants. 1.2) Elastic unloading of the ring in order to get the final dimension of the coupler, that represents the initial geometric condition in the subsequent assembly/disassembly process.

2. **Coupling assembly**: the ring-pipe system is assembled at a temperature T_i with an initial assembly clearance (ϵ_{free}). The clearance corresponds to the gap between the initial internal radius of the SMA ring and the external radius of the pipe;

3. **Thermal mounting**: The trained SMA ring is heated above its austenite finish temperature ($T > A_f$) to activate OW-SME up to a maximum temperature T_{max} and then cooled down to the operative temperature (T_o). This occurs in four subsequent steps: 3.1) Initial heating ($T_i < T < A_s$): no transformation mechanisms occur, and both the rings expand, according to their linear thermal coefficients, under stress-free conditions. 3.2) beginning of the M→A transition (OW-SME) at $T = A_s$ and stress free contraction until $T = T_c$ (ring-pipe contact), corresponding to full recovery of ϵ_{free}; 3.3) complete activation at $T > A_f$, giving the maximum contact pressure (p_{max}) at T_{max}; M→A transition continues until the rings reaches a certain temperature A_f^σ, at which the martensitic variants are not anymore thermo-mechanically stable and the ring is fully austenitic. A radial pressure is developed at the contact interface which increases with increasing temperature. It results from the prevented OW-SME as well as from SMA/steel thermal expansion coefficient mismatch. 3.4) cooling down to $T = T_o$, giving the final contact pressure of the assembly p_o. Only thermo-elastic effects occur in this phase as $T_o > M_s^\sigma$, where M_s^σ is the martensite start temperature under stress. The contact pressure decrease is only due to SMA/steel thermal expansion coefficient mismatch.

4. **Thermal dismounting**: it can be obtained by cooling down to a temperature to $T_{min} < M_f$, thanks to the TW-SME capabilities of the ring which induce its diameter expansion (see Figure 2). Initially, from T_o to M_s^σ, both SMA and steel rings are subjected only to thermoelastic contraction. At $T = M_s^\sigma$, the A→M phase transformation takes place and a further decrease in temperature causes significant stress relaxations due to the SMA expansion (TW-SME). The contact between the rings is lost at $T = T_s$ (separation temperature) and the process continues under free recovery conditions until T_{min} is reached, allowing the disassembly of the system thanks to SMA/steel clearance.

The *training* phase, including both loading and unloading of the ring, is described in the first model proposed in section 4.4. The *coupling, mounting* and *dismounting* phases are described in

the second model presented in section 4.5. Both formulations are based on on modified elastic-plastic theories for axisymmetric bodies and are calibrated by using uniaxial measurements of a commercial Ni-rich NiTi alloy.

4.3 Constitutive equations: equilibrium and compatibility

4.3.1 Linear elastic region

Thanks to axisymmetric conditions the problem can be studied in polar coordinates (r, θ), as shown in Figures 4.1. Stress and strain (σ, ϵ) components are function of the radius r, and there is only one independent displacement component, the radial displacement $u_r(r)$. The equilibrium condition in terms of radial and hoop stresses $(\sigma_{rr}, \sigma_{\theta\theta})$ without body forces can be expressed as follows:

$$\frac{d\sigma_{rr}}{dr} + \frac{\sigma_{rr} - \sigma_{\theta\theta}}{r} = 0 \tag{4.1}$$

The compatibility condition in terms of radial and hoop strains $(\epsilon_{rr}, \epsilon_{\theta\theta})$ is given by:

$$\frac{d\epsilon_{\theta\theta}}{dr} - \frac{\epsilon_{rr} - \epsilon_{\theta\theta}}{r} = 0 \tag{4.2}$$

Equations 4.1 and 4.2 represent the governing equations of the problem and they can be solved simultaneously in terms of stress or strain components by considering the constitutive relation $(\sigma_{ij} = C_{ijhk}\epsilon_{hk})$ and taking into account the boundary conditions. The compatibility condition (Equation 4.2) can be re-written in terms of stress components, considering the stress-strain curve of the material and the equivalent von Mises stress. The elastic region is governed by the generalized Hooke's law:

$$\epsilon_{ij}^{el} = \frac{1}{E_{el}}[(1+\nu)\sigma_{ij} - \nu\delta_{ij}\sigma_{kk}] \tag{4.3}$$

Where E_{el} and ν represent the Young's modulus and Poisson's ratio, respectively, and δ_{ij} is the Kronecker's delta. Under plane stress conditions, the compatibility condition in the elastic region can be re-written in terms of stress components by substituting equation 4.3 into equation 4.2:

$$\frac{d\sigma_{\theta\theta}}{dr} - \frac{\sigma_{rr} - \sigma_{\theta\theta}}{r} = 0 \tag{4.4}$$

The linear elastic solution, in terms of stress components, can be obtained by solving the

system of differential equations (Equations 4.1 and 4.4) and by considering consistent boundary conditions. For the sake of simplicity, from now on the following symbolic notation is adopted: if $i = j$, $\sigma_{ij} = \sigma_i$, and $\epsilon_{ij} = \epsilon_i$.

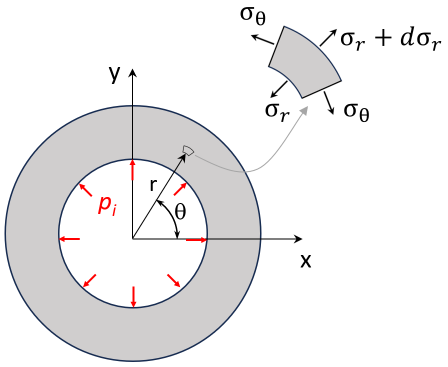

Figure 4.1: Schematic representation of the SMA ring during training and assembly/disassembly process.

4.3.2 Inelastic region

The equilibrium equations in the inelastic region in terms of radial and hoop stresses (σ_r, σ_θ) is the same as in the elastic region (Equation 4.1), whereas compatibility equations must be rewritten to consider inelastic strain occurring beyond the elastic limit. The total strain can be split into elastic and inelastic strain components (ϵ_{ij}^{el} and ϵ_{ij}^{in}) as follows:

$$\epsilon_{ij} = \epsilon_{ij}^{el} + \epsilon_{ij}^{in} \tag{4.5}$$

Inelastic components include transformation strain, plastic deformations and thermal strains in case of temperature variation. If considering Equation 4.5 and the elastic constitutive conditions (Equation 4.3), the compatibility condition of Equation 4.2 becomes:

$$\frac{d\epsilon_\theta^{in}}{dr} - \frac{\epsilon_r^{in} - \epsilon_\theta^{in}}{r} = -\frac{1}{E_{el}}\left(\frac{d\sigma_r}{dr} + \frac{d\sigma_\theta}{dr}\right) \tag{4.6}$$

Equations 4.1 and 4.6 represent the governing equations in the inelastic region but they cannot be directly solved without defining the evolution of inelastic strain as a function of the stress components. If using the von Mises criteria and assuming that the inelastic strains (ϵ_{ij}^{in}) are following the plastic flow, the latter can be computed, based on the total strain theory, as follows:

$$\epsilon_{ij}^{in} = \frac{3}{2}\frac{\epsilon_e^{in}}{\sigma_e} S_{ij} \tag{4.7}$$

where σ_e is the equivalent von Mises stress, and S_{ij} are the deviatoric stress components:

$$\sigma_e = \sqrt{\frac{3}{2} S_{ij} S_{ij}} \tag{4.8}$$

$$S_{ij} = \sigma_{ij} - \frac{1}{3}\sigma_{kk}\delta_{ij} \tag{4.9}$$

The evolution of the equivalent inelastic strain (ϵ_e^{in}) as a function of the equivalent stress (σ_e) can be obtained from the uniaxial stress-strain curve. In particular, the deformations beyond the elastic limit are considered as inelastic/plastic-like deformation and the von Mises yield criteria together with the total strain theory are applied.

4.4 *Model 1* Martensite reorientation and plasticity: the thermomechanical training

A simplified analytical model is described in this section to analyze the reorientation/ transformation mechanisms in SMA rings, either during martensite isothermal pre-strain or pseudoelastic loading. It is based on elastic-plastic theory for axisymmetric problems (see paragraph 4.3). The effectiveness of the analytical model was demonstrated by analyzing a wide range of SMA ring geometries and different martensitic pre-deformation levels. The predictions of this model in terms of mechanical stresses and deformations were compared with those obtained by axisymmetric finite element (FE) analyses based on multi-linear hardening material models. Experimental martensitic ring expansions were also performed to validate the analytical results.

4.4.1 Analytical modeling of thermomechanical pre-deformation

Stress-strain distribution in a SMA ring

Figure 4.2 shows a general simplified piecewise linear representation of the stress-strain response of a SMA together with a schematic depiction of the reorientation (or stress-induced transformation) mechanisms in a SMA ring.

The initial crystallographic structure of the material can be either martensite or austenite. Accordingly, in the region #1 (at the outer diameter of the ring), elastic deformation of martensite or austenite occurs. The second nearly flat curve (region #2) may represent either the martensite

reorientation or the stress-induced martensite transformation. Region #3 describes the elastic deformation of the oriented martensite (fully transformed/reoriented region). Region #4 describes the plastic deformation of oriented martensite that occurs at the inner diameter of the ring. However, experimental evidence shows that in polycrystalline alloys it is not possible to define precise stress-strain ranges for the four different mechanisms shown in Figure 4.2, i.e., with sharp transitions, because they can coexist on a microstructural scale depending on the thermomechanical history of the SMA. Stress-induced/detwinned martensite formation and plastic deformations are coupled and both occur in regions #2, #3, and #4. The values of the parameters in Figure 4.2 are chosen according to the initial crystallographic state of the material, as reported in Table 4.1.

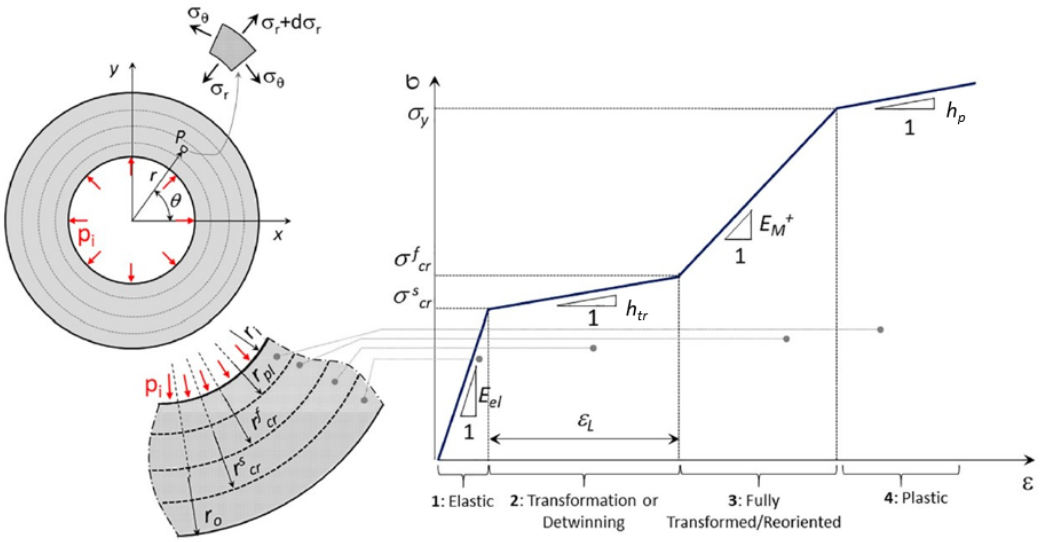

Figure 4.2: Mechanical response of SMA ring subjected to martensite reorientation (or stress induced transformation) and plasticity.

Re-orientation/transformation region

The equivalent inelastic strain in the transformation plateau can be obtained from stress strain curve (see Figure 4.2) as follows:

$$\epsilon_e^{in} = \frac{\sigma_e - \sigma_{cr}^s}{h_{tr}} - \frac{\sigma_e - \sigma_{cr}^s}{E_{el}} \tag{4.10}$$

Equation 4.10 can be rewritten as a function of the compliance parameter c_1 as reported below:

Table 4.1: Mechanical parameters of the stress-strain curve for the two crystal structures of NiTi.

Parameter	Martensite	Austenite
σ_{cr}^{s}	Detwinning start stress, σ_{det}^{s}	Martensite start stress, σ_{AM}^{s}
σ_{cr}^{f}	Detwinning finish stress, σ_{det}^{f}	Martensite finish stress, σ_{AM}^{f}
σ_y	Yield stress of detwinned martensite, σ_y	Yield stress of detwinned martensite, σ_y
E_{el}	Young's modulus of twinned martensite, E_M^-	Young's modulus of austenite, E_A
E_M^+	Young's modulus of oriented martensite	Young's modulus of oriented martensite
ϵ_L	Martensite reorientation plateau, ϵ_{det}	Stress induced martensite plateau, ϵ_{AM}
h_{tr}	Reorientation hardening coefficient, h_R	Transformation hardening coefficient, h_T
h_p	Plastic hardening coeff. of detw. martensite	Plastic hardening coefficient of detw. martensite

$$\epsilon_e^{in} = (\sigma_e - \sigma_{cr}^{s})c_1 \tag{4.11}$$

where c_1 is defined as follows:

$$c_1 = \frac{E_{el} - h_{tr}}{E_{el} \cdot h_{tr}} \tag{4.12}$$

and h_{tr}, the slope of the reorientation/transformation plateau, is a function of the respective stresses and strain, as reported below:

$$h_{tr} = (\sigma_{cr}^{f} - \sigma_{cr}^{s})/\epsilon_L \tag{4.13}$$

The inelastic strain components in the reorientation/transformation region can be obtained by substituting Equations 4.8 and 4.11 into Equation 4.7:

$$\begin{bmatrix} \epsilon_r^{in} \\ \epsilon_\theta^{in} \\ \epsilon_z^{in} \end{bmatrix} = c_1 \frac{\sigma_e - \sigma_{cr}^{s}}{2\sigma_e} \begin{bmatrix} 2\sigma_r - \sigma_\theta \\ -\sigma_r + 2\sigma_\theta \\ -\sigma_r - \sigma_\theta \end{bmatrix} \tag{4.14}$$

The compatibility condition of Equation 4.6 can be rewritten according to Equation 4.14 as follows:

$$\frac{1}{E_{el}}\left(\frac{d\sigma_\theta}{dr} + \frac{d\sigma_r}{dr}\right) + \frac{1}{2r\sigma_e}\left[3(\sigma_\theta - \sigma_r) + r\left(2\frac{d\sigma_\theta}{dr} - \frac{d\sigma_r}{dr}\right)\right](\sigma_{cr}^{s} - \sigma_e)\left(\frac{1}{E_{el}} - \frac{\epsilon_L}{\sigma_{cr}^{f} - \sigma_{cr}^{s}}\right) +$$

$$- \frac{1}{4\sigma_e^3}\left[(2\sigma_\theta - \sigma_r)\left(\sigma_\theta\left(2\frac{d\sigma_\theta}{dr} - \frac{d\sigma_r}{dr}\right) - \sigma_r\left(\frac{d\sigma_\theta}{dr} - 2\frac{d\sigma_r}{dr}\right)\right)\right]\left(\frac{\sigma_{cr}^{s}}{E_{el}} - \frac{\sigma_{cr}^{s}}{\sigma_{cr}^{f} - \sigma_{cr}^{s}}\epsilon_L\right) = 0 \tag{4.15}$$

The system of differential equations (Equations 4.1 and 4.15) defines the governing equations of the problem in the reorientation/transformation region.

Fully reoriented/transformed region

The equivalent inelastic strain in the fully oriented/transformed region can be obtained from stress strain curve as reported below:

$$\epsilon_e^{in} = \epsilon_L - \frac{\sigma_{cr}^f - \sigma_{cr}^s}{E_{el}} + (\sigma_e - \sigma_{cr}^f)c_2 \tag{4.16}$$

where the compliance parameter c_2 is given by:

$$c_2 = \frac{E_{el} - E_M^+}{E_{el} \cdot E_M^+} \tag{4.17}$$

The inelastic strain components in the fully oriented/transformed region can be computed by substituting Equations 4.8, 4.9 and 4.16 into Equation 4.7:

$$\begin{bmatrix} \epsilon_r^{in} \\ \epsilon_\theta^{in} \\ \epsilon_z^{in} \end{bmatrix} = \frac{\epsilon_L - \frac{\sigma_{cr}^f - \sigma_{cr}^s}{E_{el}} + (\sigma_e - \sigma_{cr}^f)c_2}{2\sigma_e} \begin{bmatrix} 2\sigma_r - \sigma_\theta \\ -\sigma_r + 2\sigma_\theta \\ -\sigma_r - \sigma_\theta \end{bmatrix} \tag{4.18}$$

The compatibility condition of Equation 4.6 can be rewritten according to Equation 4.18:

$$\frac{1}{E_{el}}\left(\frac{d\sigma_\theta}{dr} + \frac{d\sigma_r}{dr}\right) + \frac{1}{2r\sigma_e}\left[3(\sigma_\theta - \sigma_r) + r\left(2\frac{d\sigma_\theta}{dr} - \frac{d\sigma_r}{dr}\right)\right]\left(\frac{\sigma_{cr}^s}{E_{el}} - \frac{\sigma_{cr}^f}{E_M^+ + \epsilon_L + c_2\sigma_e}\right)$$

$$- \frac{1}{4\sigma_e^3}\left[(2\sigma_\theta - \sigma_r)\left(\sigma_\theta\left(2\frac{d\sigma_\theta}{dr} - \frac{d\sigma_r}{dr}\right) - \sigma_r\left(\frac{d\sigma_\theta}{dr} - 2\frac{d\sigma_r}{dr}\right)\right)\right]\left(\frac{\sigma_{cr}^s - \sigma_{cr}^f}{E_{el}} + \epsilon_L - c_2\sigma_{cr}^f\right)$$

$$= 0 \tag{4.19}$$

The system of differential equations (Equations 4.1 and 4.19) represents the governing equations of the problem in the fully reoriented region.

Plastic region

The equivalent inelastic strain can be determined based on the von Mises yield criteria together with the total strain theory:

$$\epsilon_e^{in} = \epsilon_L - \frac{\sigma_y - \sigma_{cr}^s}{E_{el}} + \frac{\sigma_y - \sigma_{cr}^f}{E_M^+} + (\sigma_e - \sigma_y)c_3 \tag{4.20}$$

where the compliance parameter c_2 is given by:

$$c_3 = \frac{E_{el} - h_p}{E_{el} \cdot h_p} \tag{4.21}$$

The inelastic strain components in the plastic region can be obtained by substituting Equa-

tions 4.8, 4.9 and 4.20 into Equation 4.7:

$$\begin{bmatrix} \epsilon_r^{in} \\ \epsilon_\theta^{in} \\ \epsilon_z^{in} \end{bmatrix} = \frac{\epsilon_L - \frac{\sigma_y - \sigma_{cr}^s}{E_{el}} + \frac{\sigma_y - \sigma_{cr}^f}{E_M^+} + (\sigma_e - \sigma_y)c_3}{2\sigma_e} \begin{bmatrix} 2\sigma_r - \sigma_\theta \\ -\sigma_r + 2\sigma_\theta \\ -\sigma_r - \sigma_\theta \end{bmatrix} \tag{4.22}$$

The compatibility condition of Equation 4.6 can be rewritten according to Equation 4.22:

$$\frac{1}{E_{el}}\left(\frac{d\sigma_\theta}{dr} + \frac{d\sigma_r}{dr}\right) + \frac{1}{2r\sigma_e}\left[3(\sigma_\theta - \sigma_r) + r\left(2\frac{d\sigma_\theta}{dr} - \frac{d\sigma_r}{dr}\right)\right]\left(\frac{\sigma_{cr}^s}{E_{el}} - \frac{\sigma_{cr}^f}{E_M^+} - c_4\sigma_y + \epsilon_L + c_3\sigma_e\right)$$

$$- \frac{1}{4\sigma_e^3}\left[(2\sigma_\theta - \sigma_r)\left(\sigma_\theta\left(2\frac{d\sigma_\theta}{dr} - \frac{d\sigma_r}{dr}\right) - \sigma_r\left(\frac{d\sigma_\theta}{dr} - 2\frac{d\sigma_r}{dr}\right)\right)\right]\left(\frac{\sigma_{cr}^s}{E_{el}} - \frac{\sigma_{cr}^f}{E_M^+} - c_4\sigma_y + \epsilon_L\right)$$

$$= 0 \tag{4.23}$$

where c_4 is defined as follows:

$$c_4 = \frac{E_M^+ - h_p}{E_M^+ \cdot h_p} \tag{4.24}$$

Equations 4.1 and 4.23 represent the governing equations in the plastic region.

4.4.2 Load cases and boundary conditions

The non-linear axisymmetric problem is set up in terms of stress distribution and solved by the equilibrium (E) and compatibility (C) equations reported in the previous sections. Consistent boundary conditions are also taken into account. The system of differential equations to be solved depends on the maximum and minimum equivalent stress at the inner and outer radii ($\sigma_e(r_i)$ and $\sigma_e(r_e)$), respectively. Stress regions in the ring range from completely elastic condition (region 1 in Figure 4.2) to plastic deformation of fully reoriented/transformed martensite (region 4 in Figure 4.2). Also, martensitic pre-strain can be carried out within the reorientation/transformation plateau ($\epsilon_{ei} \approx 4\%$) to exploit the OW-SME or even well beyond this limit (up to $\epsilon_{ei} \approx 28\%$) to tune the thermo-mechanical response of the alloy in terms of Two Way Shape Memory Effects (TW-SME) and transformation temperatures (TTs) as demonstrated in previous investigations [4, 110, 111, 5]. The most complex stress distribution involves four different regions, as schematically shown in Figure 4.2. It can be obtained only under special conditions that have no practical interest, as the combination of plastic and elastic deformation at the inner and outer diameter, respectively, occur only with very thick rings. Figure 4.3 shows the possible load cases in SMA rings during thermomechanical training. The hypothesis of zero

volumetric strain under inelastic/plastic deformation regime implies an inverse square law of the strain (circumferential, radial, and equivalent) with the radius ($\epsilon(r) \propto 1/r^2$). Therefore, the ratio between the equivalent strain at the outer diameter ϵ_{eo} and that at the inner diameter ϵ_{ei} is proportional to $(r_i/r_2)^2$. This proves that even under sever predeformation strains ($\epsilon_{ei} \approx 28\%$) it is possible to obtain elastic strains at the outer diameter only in case of very large rings with $r_e/r_i > 5$. Such dimensions are not interesting from an engineering point of view. Also, SMA couplers developed at CERN have ring radius ratio in the range 1.1–1.4. This range covers most of SMA couplers studied in literature [4, 110, 112, 111, 7, 8, 113, 9, 114, 115, 116], and those commercially available.

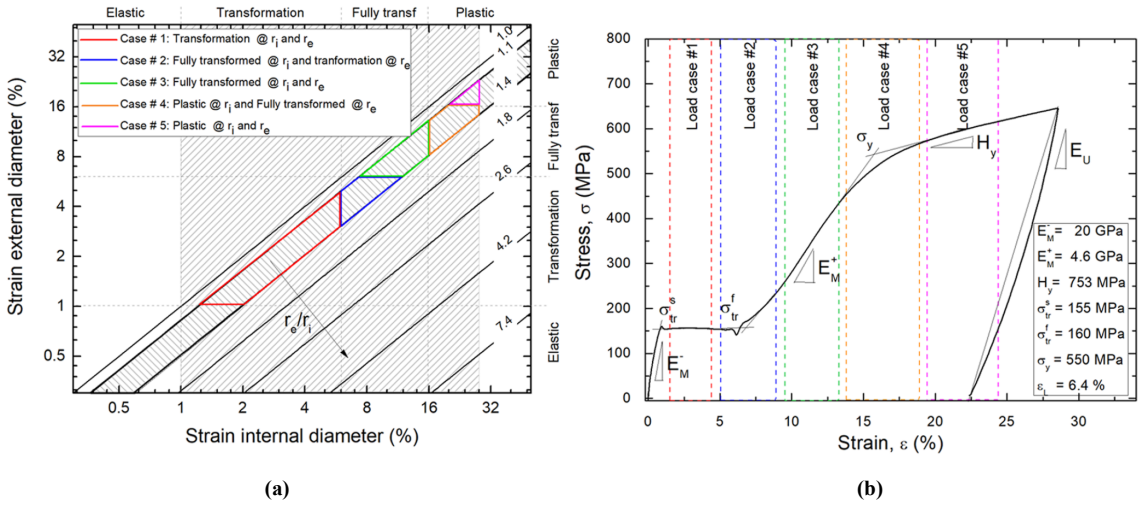

(a) **(b)**

Figure 4.3: Estimation of the possible load cases in SMA rings during pre-strain: **(a)** equivalent strain at the inner and outer diameter, and **(b)** representation on the stress-strain curve of a martensitic NiTi (Ti-50.8 at. % Ni).

The chart in Figure 4.3a is a log-log plot of $\epsilon_{eo}(\epsilon_{ei})$ referred to different values of the ring radii ratio ($r_e = r_i$). The regions of practical engineering interests are highlighted; they are bounded by the allowable range for the ring radius ratio ($1.1 < r_e/r_i < 1.4$) and by feasible values of the maximum strain at the inner diameter ($4\% < \epsilon_{ei} < 28\%$). The same load cases are schematically shown on the measured stress-strain curve of the material in Figure 4.3b. The parameters identified for the analytical simulations are also reported in the figure.

Five different load cases are expected depending on ring geometry and pre-strain values:

- **Load case #1**: Partial reorientation/transformation at r_i and partial transformation/reorientation at r_e;

- **Load case #2**: Fully reorientation/transformation at r_i and partial reorientation/transformation at r_e;
- **Load case #3**: Fully reorientation/transformation at both r_i and r_e;
- **Load case #4**: Plastic deformation at r_i and fully reorientation/transformation at r_e;
- **Load case #5**: Plastic deformation at both r_i and r_e.

The five load cases defined above are solved by equilibrium and compatibility equations described in previous sections with proper boundary conditions, as summarized in Table 4.2. External boundary conditions are defined in terms of prescribed stress and/or strain values at the inner and outer diameters (r_i and r_e). Internal boundary conditions are expressed in terms of equilibrium at the interface between different stress regions within the ring, that is at the detwinning/fully detwinned (or transformation/fully transformed) radius (r_{cr}), and fully reoriented/plastic radius (r_{pl}) (see Figure 4.2).

In all cases, no load acts on the outer diameter of the ring ($\sigma_r(r_e) = 0$). The boundary condition at the inner diameter can be enforced either by direct application of the equilibrium equations in the case of prescribed pressures ($\sigma_r(r_i) = -p_i$) or by a compatibility condition in the case of prescribed radial expansion ($u(r_i) = u_{i0}$). In the last case, the compatibility condition is given by:

$$u(r_i) = u_{i0} = \epsilon_\theta(r_i) = r_i \tag{4.25}$$

For the load case #1 the boundary condition is obtained by combining Equation 4.25 with Equations 4.3, 4.5, and 4.14, as follows:

$$u_{i0} = \frac{r_i}{E_{el}}\left[\sigma_\theta(r_i) - \nu\sigma_r(r_i)\right] + r_i\frac{c_1(\sigma_e - \sigma^s_{cr})}{2\sigma_e}\left[2\sigma_\theta(r_i) - \sigma_r(r_i)\right] \tag{4.26}$$

For load cases #2 and #3, the boundary conditions are obtained by combining Equation 4.25 with Equations 4.3, 4.5, as follows:

$$u_{i0} = \frac{r_i}{E_{el}}\left[\sigma_\theta(r_i) - \nu\sigma_r(r_i)\right] + r_i\frac{\epsilon_L - (\sigma^f_{cr} - \sigma^s_{cr})/E_{el} + (\sigma_e(r_i) - \sigma^f_{cr})c_2}{2\sigma_e(r_i)}\left[2\sigma_\theta(r_i) - \sigma_r(r_i)\right] \tag{4.27}$$

For load cases #4 and #5, the boundary conditions are obtained by combining Equation 4.25 with Equations 4.3, 4.5, and 4.22, as follows:

$$u_{i0} = \frac{r_i}{E_{el}}[\sigma_\theta(r_i) - \nu\sigma_r(r_i)] + r_i \frac{\epsilon_L - (\sigma_y - \sigma_{cr}^s)/E_{el} + (\sigma_y - \sigma_{cr}^f)/E_M^+ + (\sigma_e(r_i) - \sigma_y)c_3}{2\sigma_e(r_i)}$$

$$[2\sigma_\theta(r_i) - \sigma_r(r_i)] \tag{4.28}$$

The internal boundary conditions are set up at the radii r_{tr} and r_{pl}. However, they are not known a-priori, so the equations of Table 4.2 cannot be directly applied. In these cases, an iterative approach is needed. The first trial values of r_{tr} and r_{pl} are obtained from the elastic solution ($\sigma_e^{el}(r_{tr0}) = \sigma_{cr}^f$, $\sigma_e^{el}(r_{pl0}) = \sigma_y$) and the iteration is carried until the equivalent von Mises stress at the radii r_{tr} or r_{pl} is equal to σ_{cr}^f or σ_y, respectively.

In the case of martensitic ring predeformation, the final size of the coupler can be obtained by elastic unloading. The elastic modulus at unloading is assumed equal to E_u (see Figure 4.3b). It is worth noting that E_u is significantly affected by the pre-strain value (see section 4.4.4). The E_u values used in the calculations were selected by considering the maximum circumferential strain at the inner diameter of the ring. The system of equations governing the unloading phase involves the elastic equilibrium and compatibility (Equations 4.1 and 4.4) and it is solved by applying the following boundary conditions:

$$\begin{cases} \sigma_r^{unl}(r_i) = p_i \\ \sigma_r^{unl}(r_e) = 0 \end{cases} \tag{4.29}$$

where $-p_i$ is the final pressure achieved at the end of the loading phase. The elastic contraction at the inner radius of the ring at the end of the unloading is calculated by combining Equation 4.25 with Equation 4.3, as follows:

$$u_{iU} = \frac{1}{E_U}\left[\sigma_\theta(r_i) - \nu\sigma_r(r_i)\right](r_i + u_{i0}) \tag{4.30}$$

Residual state variables, in terms of stress, strain, and displacement, are obtained by the sum of the respective loading components to the unloading ones, as reported below:

$$\begin{cases} \sigma_r^{res}(r) = \sigma_r^{load}(r) + \sigma_r^{unl}(r) \\ \sigma_\theta^{res}(r) = \sigma_\theta^{load}(r) + \sigma_\theta^{unl}(r) \end{cases} \tag{4.31}$$

$$\begin{cases} \epsilon_r^{res}(r) = \epsilon_r^{load}(r) + \epsilon_r^{unl}(r) \\ \epsilon_\theta^{res}(r) = \epsilon_\theta^{load}(r) + \epsilon_\theta^{unl}(r) \end{cases} \tag{4.32}$$

$$u_r^{res}(r) = u_r^{load}(r) + u_r^{unl}(r) \tag{4.33}$$

Table 4.2: Systems of differential equations and boundary conditions for selected load cases.

Load case #	Condition	System of equations	Boundary conditions
1	$\begin{cases}\sigma_{cr}^{s} < \sigma_e(r_i) \leq \sigma_{cr}^{f} \\ \sigma_e(r_e) > \sigma_{cr}^{s}\end{cases}$	$\begin{cases}E_{tr}(Eq.4.1) \\ C_{tr}(Eq.4.15)\end{cases}$	$\begin{cases}\sigma_r^{tr}(r_i) = -p_i \text{ or } u(r_i) = u_{i0} \\ \sigma_r^{tr}(r_e) = 0\end{cases}$
2	$\begin{cases}\sigma_{cr}^{f} < \sigma_e(r_i) \leq \sigma_y \\ \sigma_{cr}^{s} \leq \sigma_e(r_e) < \sigma_{cr}^{f}\end{cases}$	$\begin{cases}E_{tr}(Eq.4.1) \\ C_{tr}(Eq.4.15) \\ E_{ft}(Eq.4.1) \\ C_{ft}(Eq.4.19)\end{cases}$	$\begin{cases}\sigma_r^{ft}(r_i) = -p_i \text{ or } u(r_i) = u_{i0} \\ \sigma_r^{tr}(r_e) = 0 \\ \sigma_r^{tr}(r_{cr}) = \sigma_r^{ft}(r_{cr}) \\ \sigma_\theta^{tr}(r_{cr}) = \sigma_\theta^{ft}(r_{cr})\end{cases}$
3	$\begin{cases}\sigma_{cr}^{f} < \sigma_e(r_i) \leq \sigma_y \\ \sigma_e(r_e) \geq \sigma_{cr}^{f}\end{cases}$	$\begin{cases}E_{ft}(Eq.4.1) \\ C_{ft}(Eq.4.19)\end{cases}$	$\begin{cases}\sigma_r^{ft}(r_i) = -p_i \text{ or } u(r_i) = u_{i0} \\ \sigma_r^{fr}(r_e) = 0\end{cases}$
4	$\begin{cases}\sigma_e(r_i) > \sigma_y \\ \sigma_{cr}^{f} \leq \sigma_e(r_e) < \sigma_y\end{cases}$	$\begin{cases}E_{ft}(Eq.4.1) \\ C_{ft}(Eq.4.19) \\ E_{pl}(Eq.4.1) \\ C_{pl}(Eq.4.23)\end{cases}$	$\begin{cases}\sigma_r^{pl}(r_i) = -p_i \text{ or } u(r_i) = u_{i0} \\ \sigma_r^{ft}(r_e) = 0 \\ \sigma_r^{ft}(r_{pl}) = \sigma_r^{pl}(r_{pl}) \\ \sigma_\theta^{ft}(r_{pl}) = \sigma_\theta^{pl}(r_{pl})\end{cases}$
5	$\sigma_e(r_e) \geq \sigma_y$	$\begin{cases}E_{pl}(Eq.4.1) \\ C_{pl}(Eq.4.23)\end{cases}$	$\begin{cases}\sigma_r^{pl}(r_i) = -p_i \text{ or } u(r_i) = u_{i0} \\ \sigma_r^{pl}(r_e) = 0\end{cases}$

4.4.3 Solution procedure

The analytical model herein proposed is implemented in *Wolfram Mathematica* ®. The systems of equations are solved numerically. An example of the solution procedure is summarized in Figure 4.4. The flowchart reports step-by-step the calculation process.

The first step consists in the load case selection; the geometry (inner diameter ID_0 and thickness t) and the radial displacement at the inner diameter (u_{i0}) are given as input to firstly estimate the equivalent strains at both inner and outer diameters, ϵ_{ei} and ϵ_{eo}. Equivalent stresses at the inner and outer diameters, σ_{ei} and σ_{eo} are calculated, combining Equation 4.5 with equations 4.11, 4.16, and 4.20, for the transformation/reorientation, fully transformed/ reoriented and plastic regions, respectively. The load case selection is then obtained based on the stress condition reported in Table 4.2.

For non-mixed load cases (#1, #3, and #5), the stress/strain values in the ring (both at the inner and outer radius) are within a single region (cfr. Figures 4.2 and 4.3b). The respective equilibrium and compatibility equations are combined with the boundary conditions (Table 4.2) to calculate the stress, strain, and displacement distributions during the loading phase. The mixed load cases (#2 and #4) are the most computationally demanding ones since the stress/strain

values at the inner and outer radius of the ring are in different regions (cfr. Figures 4.2 and 4.3b). The critical radius between the two regions is defined as transformation radius for load case #2, and plastic radius for load case #4. In general, the critical radii are iteratively calculated by assuming increasing values starting from the inner ring radius ($ID_0/2$).

The equilibrium and compatibility equations for both the internal and external regions are solved imposing the boundary conditions at the internal, critical, and external radius (Table 4.2). The iterations continue until the difference between the equivalent stress at the critical radius and the critical finish stress σ_{cr}^{f} (load case #2) or yield stress σ_y (load case #4) is lower than the imposed tolerance value, $\delta\sigma$. The stress and deformation fields in output of the loading phase calculation process are given as input for the unloading phase governed by equations 4.1, 4.4, and 4.29.

Many variables influence the computational cost of the proposed analytical formulation, in particular the number iterative calculations (depending on the specific load case) and the chosen numerical tolerance values. In general, thanks to the limited number of the equations to be solved, the computational cost in terms of solution time (about 30% lower) and computer memory is advantageous if compared to FE simulations.

Moreover, the analytical model has further significant advantages if compared to FEA as it is more flexible (no geometry/no mesh needed) and can be easily implemented in commercial codes such as Matlab® or Mathematica® and adopted by users without any particular expertise in FE simulations.

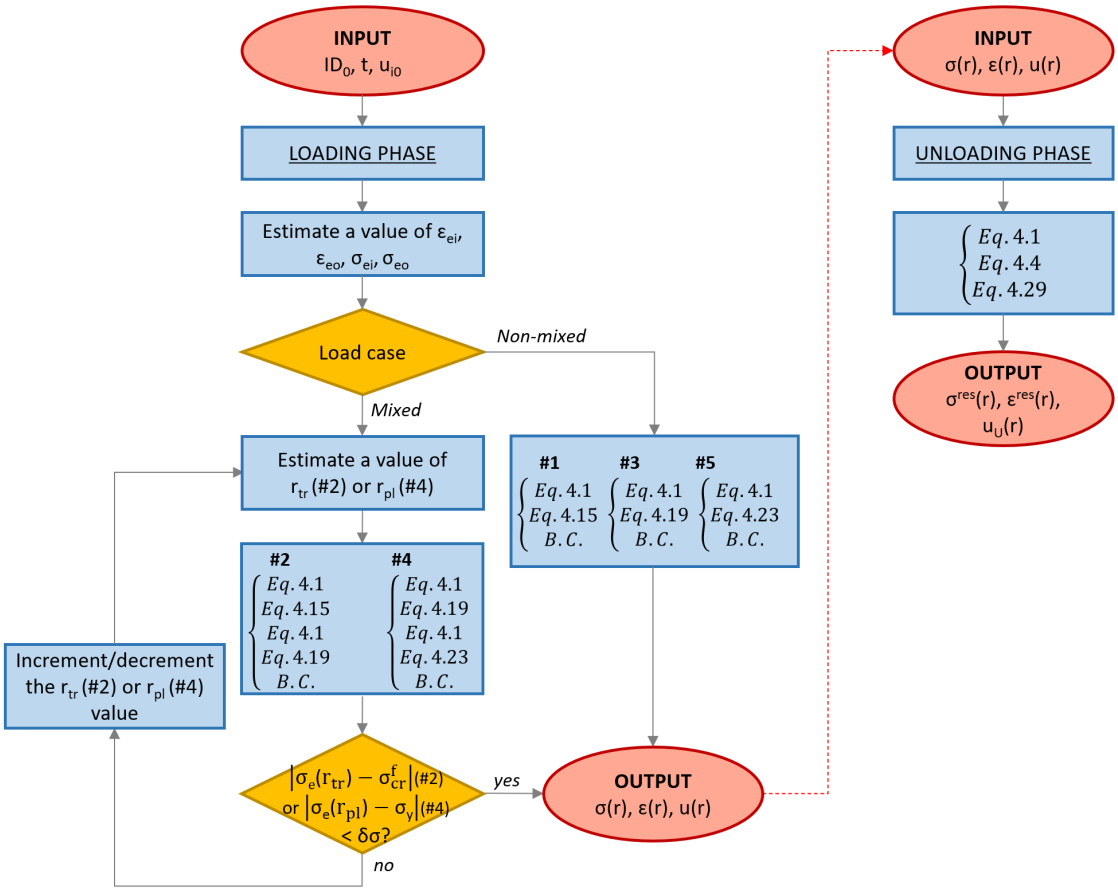

Figure 4.4: Schematic representation of the calculation procedure by flow chart.

4.4.4 Model calibration

SMA material

The material used for ring manufacturing is a binary Ni-rich NiTi alloy (Ti-50.8 at. % Ni). This alloy has been selected based on preliminary studies aimed at designing a suitable thermo-mechanical process, the so-called training, to satisfy the functional requirements for UHV applications, which include reversible shape memory recovery properties with transformation strains higher than 2% and a strict transformation temperature range (Austenite start, $A_s > 30°C$, Martensite start, $M_s < 20°C$), as described in [6, 7, 8] and [9]. Figure 4.5a illustrates the isothermal stress-strain curve of the alloy in martensitic conditions. It is obtained from tensile test specimens of an isothermal ($T = -80°C$) tensile loading up to a fixed pre-strain value (ϵ_{tot}) followed by complete unloading and measurement of the residual strain (ϵ^{res}). Thermal cycles were subsequently carried out to measure the shape recovery capabilities of the trained alloy.

Figure 4.5a also reports the main mechanical parameters of the alloy, that is those reported in Table 4.1 and Figure 4.2, together with the measured values of the TTs. The elastic modulus on unloading (E_U) shown in Figure 4.5a, is reported as a function of the applied maximum deformation in Figure 4.5b. This parameter is strongly dependent on the pre-strain level, that is, it ranges between about $10GPa$, at the maximum strain of 28.8%, and $21GPa$ at the lowest strain level of 4.8%.

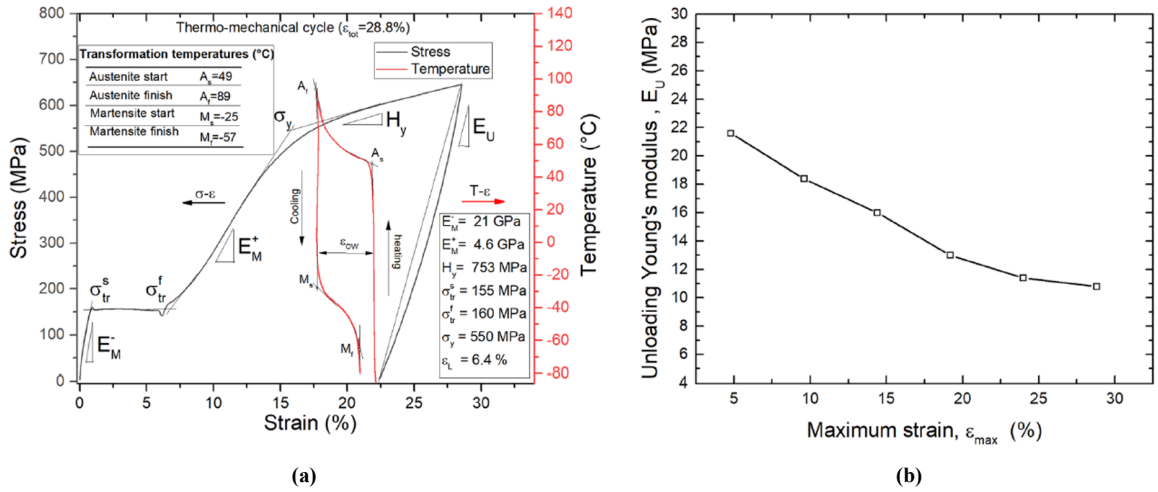

Figure 4.5: Thermo-mechanical properties of the investigated NiTi alloy: **(a)** isothermal stress-strain curve ($T = -80°C$) and subsequent strain-temperature curve obtained from a complete thermal cycle between TTs and **(b)** unloading modulus E_U, as a function of the pre-strain level, ϵ_{max}.

SMA ring geometries and case studies

A wide range of ring geometries were considered in this study. Three values of internal diameter ($ID_0 = 28, 40, 118mm$) and three values of wall thickness to inner diameter ratio ($t/ID_0 = 0.09, 0.15, 0.20$) were selected according to possible SMA ring applications at CERN. Similarly, a large martensitic pre-strain range was investigated through analytic and numerical (FE) analyses. All load cases reported in Table 4.2 (from #1 to #5) were considered. The applied circumferential strain at the inner diameter, $\epsilon_{\theta i}$, ranges from values within the detwinning plateau ($\epsilon_{\theta i} = 4\%$) to a fully plastic behavior ($\epsilon_{\theta i} = 25\%$) in order to tune properly the SMA thermo-mechanical response (TW-SME and TT) for various applications. Eight pre-strain values were considered for all ring geometries ($\epsilon_{\theta i} = 4\%, 7\%, 10\%, 13\%, 16\%, 19\%, 22\%$, and 25%). Table 4.3 reports the ring geometries and case studies considered in this work.

Table 4.3: SMA rings geometries.

Ring type #	**Initial internal diameter,** $ID_O(mm)$	**Wall thickness,** $t(mm)$
1	28	2.4
2	28	4.2
3	28	5.7
4	40	3.5
5	40	6
6	40	8.2
7	118	10.3
8	118	17.7
9	118	24.2

Mechanical expansions of SMA couplers

Isothermal mechanical expansions ($-80°C$) of three martensitic rings—ring types #1, #2 and #5, were carried out at by a tapered punch mounted in a servo hydraulic testing machine (Instron 1276, load capacity 1 MN) equipped with a climatic chamber ($-180°C/+300°C$). Special care was adopted to accurately control the process parameter, including the cross-head speed rate and the ring temperature as they significantly affect the geometric and dimensional tolerance of the ring couplers. The test was carried out in displacement control mode at a rate of about 10 mm/min. The ring temperature was measured by a k-type thermocouple glued directly on the sample. The maximum punch diameter was chosen to provide a suitable mechanical pre-strain for ring training.

4.4.5 Finite Element simulations

The SMA ring expansion process was modeled by a commercial FE software code (Ansys Workbench). It consists of a mechanical pre-strain in martensitic condition ($T = -80°C$). Axisymmetric analyses were carried out by using a 2D quadrilateral-dominant mesh of about 1500 four-nodes elements, as shown in Figure 4.6. A sensitivity test was performed to determine the optimum number of elements to be used. Only half of the SMA cross section was modeled due to symmetric geometry and loading conditions. A particular mesh refinement was adopted at the inner diameter, due to the higher stress gradients. The SMA behavior was modeled by two different constitutive relationships: a quadrilinear isotropic elastic-plastic model, whose

stress-strain relationship is identical to that used in the proposed analytical model (Figure 4.2), and a multilinear hardening elastic-plastic material based on 150 stress-strain points which fit accurately the experimental uniaxial stress-strain curve (Figure 4.3b).

The mechanical pre-strain of the SMA ring was simulated by applying a fixed radial displacement (u_{i0}) at the internal diameter (ID_0), corresponding to a hoop strain ($\epsilon_{\theta i} = 2u_{i0}/ID_0$) ranging from 4% to 25%. The residual stress and deformation after unloading were calculated similarly to the analytical approach, that is, using the actual unloading modulus values, E_U, which were experimentally evaluated (see Figures 4.3b 4.5b).

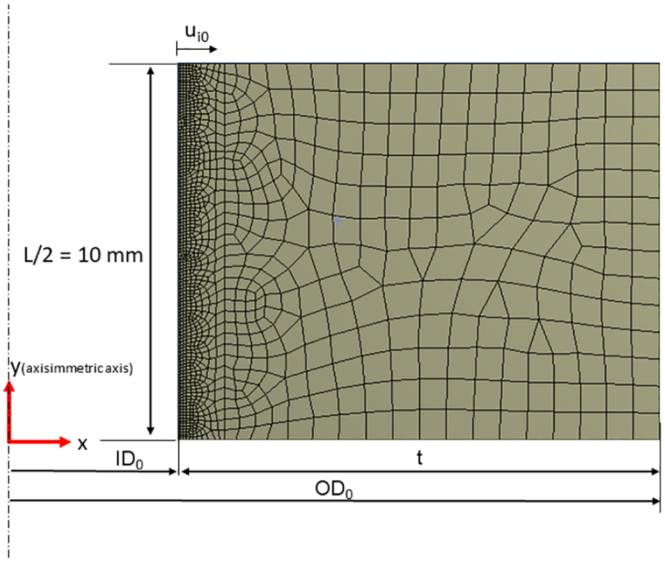

Figure 4.6: Two-dimensional axisymmetric FE model of the coupling assembly.

4.4.6 Results and discussions

Effect of pre-strain

The results of the five selected load cases for ring type #5 ($ID = 40mm, t = 6mm$), with pre-deformation $\epsilon_{\theta i} = 4\%, 10\%, 13\%, 16\%25\%$, as obtained from the analytical model herein proposed, are reported in Figure 4.7. The equivalent stress (Figure 4.7a) and radial/circumferential stress components (Figure 74.7b) at the end of martensitic pre-strain are plotted as a function the normalized radius, $(r - r_i)/(r_e - r_i) = \Delta r/t$. The selected pre-strain levels correspond to the five different load cases in Table 4.2 and significant differences were captured among the corresponding stress solutions, as highlighted in Figure 4.7. The equivalent stress either is almost

constant ($\epsilon_{\theta i} = 4\%, 25\%$) or decreases along the radius ($\epsilon_{\theta i} = 10\%, 13\%, 16\%$), depending on the actual slope of the stress-strain curve for each load case.

The negative radial stress at the inner diameter represents the radial force per unit area (p_i) required for ring expansion and plays a crucial role in the design/ choice of proper expansion tools and machines. A slight increase of the circumferential stress is observed from the inner to the outer diameter for load cases with $\epsilon_{\theta i} = 4\%, 25\%$. This is an unusual behavior if compared with standard elastic solutions, where circumferential stress increases with $1/r^2$ from the outer to the inner diameter. It is attributed to the slight slope of the equivalent stress-strain curve in both reorientation and plastic regions. In fact, the equivalent stress is almost constant and, considering that σ_r is maximum at the inner diameter (absolute value), σ_θ must increase accordingly. At $\epsilon_{\theta i} = 13\%$ the ring is in the fully reoriented region (load case #3), where the slope of the equivalent stress-strain curve (E_M^+) is significantly higher (Figure 4.5b) than other load cases. It results in a decrease of the circumferential stress along the radius, similar to the conventional elastic solution.

The other pre-strain levels ($\epsilon_{\theta i} = 10\%, 16\%$) generate a different microstructure at the inner and outer diameters, corresponding to load cases #2 and #4, respectively. This results in a more complex stress distribution, that is a C^0 function with a discontinuity point in the first derivative at the critical radii (reorientation or plastic), namely at the interface between different regions (see Figure 1). As an example, at $\epsilon_{\theta i} = 10\%$ the ring is in the fully reoriented martensite region for $0 < \Delta R/t < 0.75$ and partially reoriented one at $0.75 < \Delta R/t < 1$. The point $\Delta R/t = 0.75$ is actually the normalized critical radius (r_{cr} in Figure 4.2) and it represents a first derivative discontinuity, according to the implemented quad-linear law (Figure 4.2). This is also evident from the circumferential stress distributions, as shown in Figure 4.7b. Similar consideration applies for the 16% prestrain case #4 where the critical radius (plastic) is identified at about $\Delta R/t = 0.05$.

For the sake of completeness, the evolution of the normalized plastic radius ($Deltar_p/t$) with respect to the internal pre-strain ($\epsilon_{\theta i} = 16\%, 17.5\%, 19\%, 22\%$) for ring type 9 (Table 4.3) is reported in Figure 4.8. Clearly, plastic radius $Deltar_p/t$ increases with prestrain more than linearly and a full plasticization is induced in the ring for $\epsilon_{\theta i} = 22\%$.

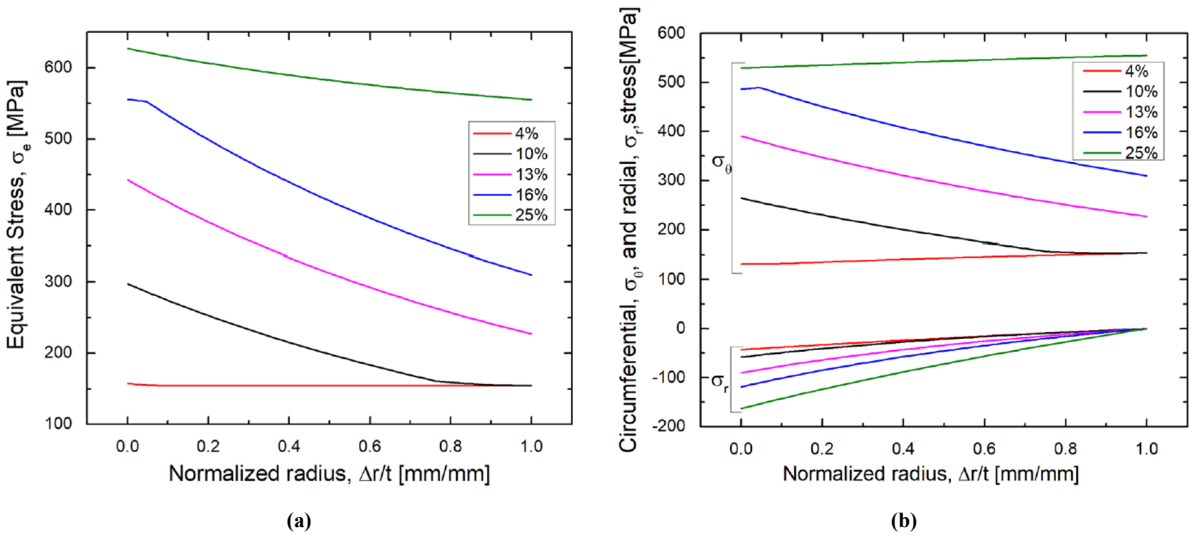

Figure 4.7: Stress distribution after pre-strain for ring #5 under five pre-deformation levels ($\epsilon_{\theta i} = 4\%, 10\%, 13\%, 16\%, 25\%$) as a function of the normalized radius: **(a)** equivalent von Mises stress and **(b)** radial and circumferential stress components.

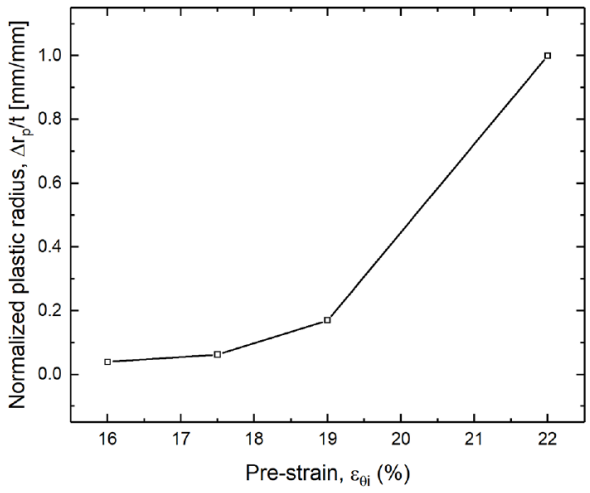

Figure 4.8: Normalized plastic radius, $\Delta r_p/t$ as a function of the prestrain, $\epsilon_{\theta i}$ for ring #9.

The proposed analytical model was validated by systematic comparison with FE results. The circumferential and radial stress distributions of ring type #7 predeformed at $\epsilon_{\theta i} = 4\%, 16\%, 25\%$ are reported in Figures 4.9 and 4.10. Figure 4.9a and 4.9b shows the radial and circumferential stress distribution along the normalized ring radius, respectively, at the end of martensitic pre-strain.

Depending on the circumferential strain input at the inner diameter, the ring is subjected to different load cases. Load case #1 (partial reorientation) and #5 (fully plastic) are obtained for

$\epsilon_{\theta i} = 4\%, 25\%$, respectively. Mixed load case #4 (plastic-fully reoriented) occurs at $\epsilon_{\theta i} = 16\%$. The latter represents the most computationally demanding load case, due to the iterations related to the estimation of the plastic radius, often needing relaxed convergence tolerance. In this case, the stress predictions obtained from the simplified analytical model show the largest differences with FE results. Maximum differences on circumferential and radial stress components of about 7.2% and 3.2%, respectively, were obtained with respect to the multilinear FE analyses. This gap is related to intrinsically different $\sigma - \epsilon$ relationships of the two models, especially in the reorientation region (strain around 15%). In fact, FE multilinear analyses consider a smooth $\sigma - \epsilon$ curve, based on more than 150 small slope variations ($\Delta\sigma/\Delta\epsilon$), with significantly lower stress values than the quadrilinear model.

Conversely, a direct comparison between the analytical and FE quadrilinear simulations (based on identical stress-strain curves) results in a minimum error, in terms of both stress components (differences lower than 2%) and plastic radius predictions (see Figure 4.9b). The agreement between the FE quadrilinear and analytical predictions is even higher for stress distributions corresponding to $\epsilon_{\theta i} = 4\%, 25\%$ and confirms the effectiveness and the robustness of the proposed model.

Figure 4.10a and 4.10b show the residual radial and circumferential stress distribution (after unloading) along the normalized radius, respectively. Radial stresses are almost negligible for all case studies (up to $2.5MPa$) while circumferential residual stresses are significantly affected by the applied pre-strain. Maximum stresses around $55MPa$ were obtained at $\epsilon_{\theta i} = 25\%$ whereas values lower than $20MPa$ were observed at $\epsilon_{\theta i} = 4\%$ and 16%. Results confirm the viability of the analytical model in predicting the stress distributions, especially for load cases with $\epsilon_{\theta i} = 4\%, 25\%$ where an absolute error lower than 5% was calculated between analytical and numerical models. Again, similarly to the loading phase, higher differences occur for load case with $\epsilon_{\theta i} = 16\%$. For this case study, stress field calculated through the FE multilinear model differs significantly from the analytical and FE quadrilinear ones, both in terms of values and trend (errors higher than 100%). Similarly, to the loading stage, this can be attributed to the different hardening law implemented for FE multilinear analyses.

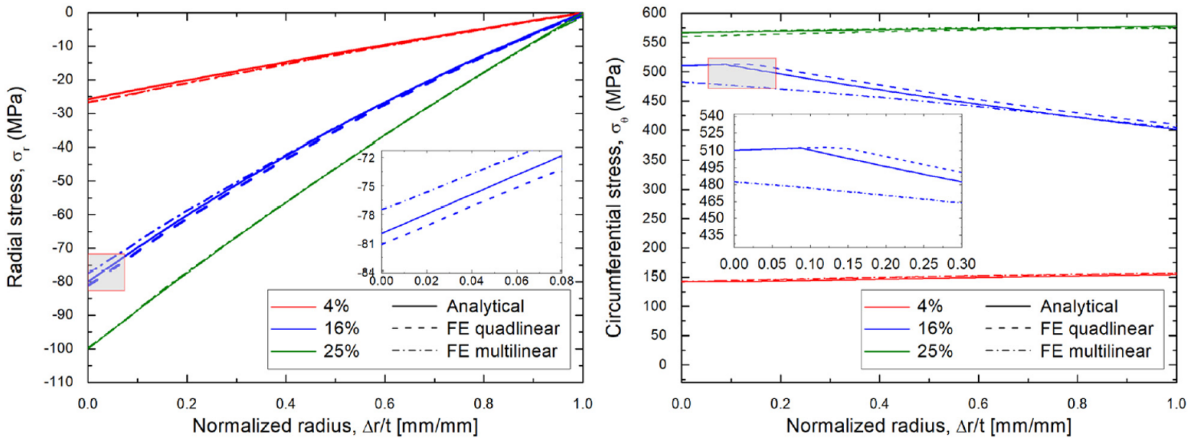

(a) **(b)**

Figure 4.9: Analytical versus FE predictions of stress distributions along the ring radius for ring type #7 and three values of prestrain: $\epsilon_{\theta i} = 4\%, 16\%, 25\%$:**(a)** radial stress, σ_r, and **(b)** circumferential stress, σ_θ.

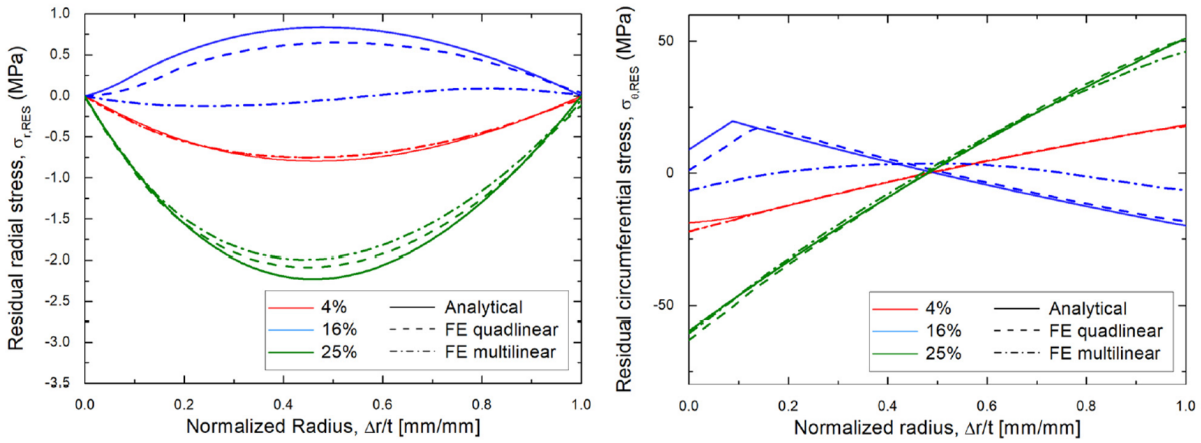

(a) **(b)**

Figure 4.10: Analytical versus FE predictions of stress distributions along the ring radius for ring type #7 and three values of prestrain: $\epsilon_{\theta i} = 4\%, 16\%, 25\%$:**(a)** residual radial stress, $\sigma_{r,RES}$, and **(b)** residual circumferential stress, $\sigma_{\theta,RES}$.

Effect of SMA ring thickness

The effect of SMA ring thickness on stress distributions was analyzed. Figure 4.11 report comparisons between the analytical and the FE (multilinear) stress distributions along the ring radius for ring type #1, #2, and #3 ($ID_0 = 28$ and $t = 2.4, 4.2, 5.7mm$) at a fixed prestrain level: $\epsilon_{\theta i} = 16\%$. The latter was selected as it gives the highest differences between the analytical model and the FE multilinear one, as discussed above.

Analytical results reveal that critical radii do not depend on ring thickness. Consequently,

the higher the ring thickness, t, the lower the normalized plastic radius corresponding to the discontinuity in the equivalent stress first derivative (Figure 4.11). Furthermore, the higher the ring thickness the higher the stress difference between the internal and external radius. A direct comparison between FE and analytical solutions show that the predictive capability of the proposed model improves for higher values of the normalized radius and ring thickness. This comes again from the intrinsic differences between the stress-strain curves the two models are based on, which is very high for strains around 16% (see Figure 4.5b) and decreases for lower strain values (occurring at higher radii).

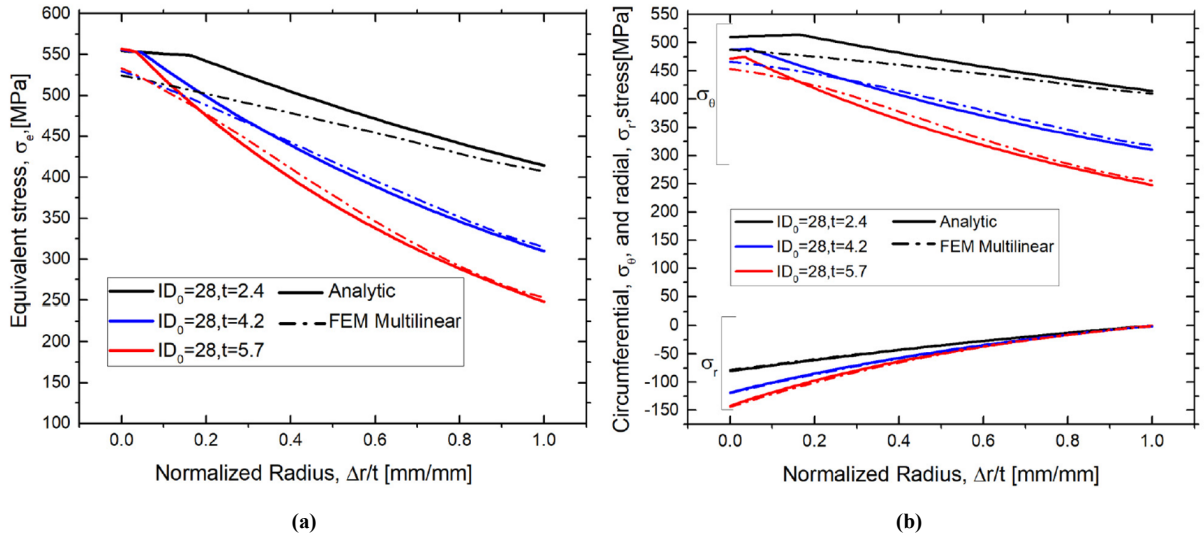

Figure 4.11: Analytical versus FE multilinear predictions of stress distributions along the rings radius for ring type #1, #2, #3 at a fixed pre-strain level: $\epsilon_{\theta i} = 16\%$:**(a)** equivalent stress, σ_e, and **(b)** radial, σ_r, and circumferential stress, σ_θ.

The internal pressure (p_i) needed for ring expansion, that is the maximum radial stress after pre-strain, was analyzed for all ring geometries in Table 4.3 at pre-strain levels ranging from 4% to 25%. Results revealed that expansion pressure, p_i, increases nearly linearly with the thickness to diameter ratio (t/ID_0), for a given pre-strain level. Moreover, for a fixed values of t/ID_0, the pressure p_i does not depend on ID_0 and increases when increasing $\epsilon_{\theta i}$. Results obtained from the analytical model are summarized in Figure 4.12. Maximum differences between analytical and FE predictions are lower than 3% for all investigated cases. The curves at $\epsilon_{\theta i} = 4\%, 7\%$ are almost superposed because they correspond to a partial reorientation condition (load case #1) which is described by a plateau in the sigma-epsilon response (see Figure 4.5b). The graph of Figure 4.12 represents a quick tool to design the expansion process of SMA rings with various

geometry/sizes, suitable for different applications.

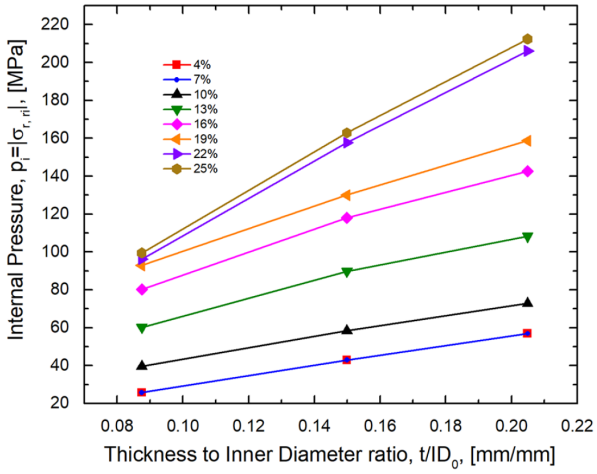

Figure 4.12: Ring internal pressure as a function of the thickness to inner diameter ratio (t/ID_0) and pre-strain level, $\epsilon_{\theta i} = 4\%, 7\%, 10\%, 13\%, 16\%, 19\%, 22\%, 25\%$.

Residual deformation

The final value of the SMA ring internal diameter after pre-strain (ID) according with Equation 4.33, can be calculated by the following expression:

$$ID = ID_0 + 2(u_0 + u_U) \tag{4.34}$$

where ID_0 is the initial internal diameter, u_0 is the radial displacement given as input for the pre-strain and u_U is the negative radial displacement recovered due to the elastic unloading. Results reveal that the normalized diameter variation after pre-strain $((ID - ID_0)/ID_0)$ as a function of thickness to inner diameter ratio (t/ID_0) is almost constant while it increases when increasing the pre-strain value $(\epsilon_{\theta i})$. Maximum differences between analytical and FE numerical multilinear results in terms of SMA internal diameter were calculated by using error E_{FE}, defined as follows:

$$E_{FE} = \left| \frac{(ID_A - ID_0) - (ID_{FE} - ID_0)}{(ID_{FE} - ID_0)} \right| = \left| \frac{ID_A - ID_{FE}}{ID_{FE} - ID_0} \right| \tag{4.35}$$

where ID_A is the internal diameter after unloading calculated analytically and ID_{FE} is the one calculated by FE analysis using the multilinear hardening model for the SMA. Similarly, it is possible to define the error function E_{EXP} calculated with respect to the experimental data,

in absolute value:

$$E_{FE} = \left| \frac{ID_A - ID_{EXP}}{ID_{EXP} - ID_0} \right| \tag{4.36}$$

Results for some selected load cases are reported in Table 4.4, which contains the geometrical characteristics and load conditions for each ring.

Analytical, FE and experimental results in terms of SMA inner diameter after training (ID) are in very good agreement as demonstrated by the error values, E, always below 7% for all the investigated cases. Moreover, based on the comparison between the FE and the analytical stress/deformation fields, it can be observed that the higher the t/ID_0 ratio the higher the accuracy of the analytical results. In particular, for $t/ID_0 > 5$ the error value is lower than 4%. These results confirm the robustness of the analytical model and its good predictive capabilities.

Table 4.4: Geometrical characteristics and loading conditions for each type of investigated ring.

Ring type #	**Initial internal diameter**, $ID_0(mm)$	**Wall thickness**, $t(mm)$	**Internal radial pressure**, $p_i(MPa)$	**Pre-strain**, $\epsilon_{\theta i}$ (%)	**Internal diameter after expansion**, $ID(mm)$			**Error**, E_{FE} (%)	**Error**, E_{EXP} (%)
					ANAL	FE_{multi}	EXP		
1	28	2.4	80.5	16	31.32	31.52	31.55	5.68	6.48
2	28	4.2	42.92	4	28.93	28.88	28.87	5.68	6.90
3	28	5.7	205.3	21	32.63	32.72	/	1.91	/
4	40	3.5	60.6	13	44.05	44.22	/	4.03	/
5	40	6	152.6	19	45.56	45.84	45.80	4.79	4.14
6	40	8.2	159	10	43.32	43.45	/	3.77	/
7	118	10.3	25.87	7	125.29	125.18	125.61	1.53	4.31
8	118	17.7	162.9	25	139.88	140.29	/	1.84	/
9	118	24.2	158	19	134.39	134.30	/	0.55	/

4.5 *Model 2* Constrained recovery mechanisms: assembly and disassembly

4.5.1 Nomenclature

Material properties

$E(\xi)$	Equivalent Young's Modulus	β	Stress-temperature slope coefficient
E_M	Young's modulus of martensite	ξ	Volume fraction of martensite
E_A	Young's Modulus of austenite	ξ_0	Volume fraction of martensite at the initial state
H	Tangent Modulus in the inelastic region	α_{PIPE}	Linear thermal expansion coefficient of the pipe
ν	Poisson's coefficient	α_{SMA}	Linear thermal expansion coefficient of the SMA ring

Geometry

$r_{i,PIPE,N}$	Internal radius of the internal ring at the end of the N^{th} phase	$r_{c,N}$	Contact radius at the end of the N phase
$r_{e,PIPE,N}$	External radius of the internal ring at the end of the N^{th} phase	$\bar{r}_N$	Critical radius (load step #2)
$r_{i,SMA,N}$	Internal radius of the SMA ring at the end of the N^{th} phase	Δr_N	Gap between the rings at the end of the N phase
$r_{e,SMA,N}$	External radius of the SMA ring at the end of the N^{th} phase		

Process Temperatures

A_s	Austenite start Temperature in free recovery conditions	T_o	Operating Temperature
A_f	Austenite finish Temperature in free recovery conditions	T_c	Contact Temperature
A_f^σ	Austenite finish temperature in constrained recovery conditions	T_{max}	Maximum process temperature
M_s	Martensite start Temperature in free recovery conditions	T_s	Separation temperature
M_s^σ	Martensite start Temperature in constrained recovery conditions	T_{min}	Minimum process temperature
M_f	Martensite Finish Temperature in free-recovery conditions		

Stresses/Strains

ϵ_r	Radial Strain	σ_r	Radial Stress
ϵ_θ	Circumferential strain	σ_θ	Circumferential Stress
ϵ_{irr}	Irrecoverable strain	σ_e	Equivalent Von Mises Stress
ϵ_c	Total strain at the end of the free-recovery	σ_{cr}^s	Critical Start Stress
ϵ_{ct}	Contact strain	σ_{cr}^f	Critical Finish Stress
ϵ_t	Total strain	σ_y	Yield Stress
ϵ_{OW}	Maximum one-way recoverable strain	p_i	Contact pressure
ϵ_{TW}	Maximum two-way recoverable strain	p_{tr}	Component of the contact pressure due to phase transformation phenomena
ϵ_{free}	Free-recovered strain	p_{th}	Component of the contact pressure due to thermoelastic strains
ϵ_{el}	Elastic Strain		
ϵ_{tr}	Transformation Strain		
ϵ_{pl}	Plastic Strain		
ϵ_{th}	Thermal Strain		

4.5.2 SMA recovery stress modeling

Figure 4.13 shows the thermo-mechanical behavior of a SMA ring exhibiting both a one-way and a two-way shape memory effect (OW-SME and TW-SME). The contact pressure as a function of the temperature developed during constrained thermal recovery (pipe coupling) is

schematically depicted in the upper side while the evolution of the SMA ring (red curve) and pipe (blue curve) deformation in terms of circumferential strain is shown in the lower side. Such curves are obtained from a complete thermal cycle between TTs and refer to a sufficiently rigid elastic pipe. The stress-free thermal recovery curve (without mechanical obstacle) of the SMA ring is also reported (dotted red curve) as well as the related one-way (ϵ_{OW}) and two-way (ϵ_{OW}) shape recovery deformations.

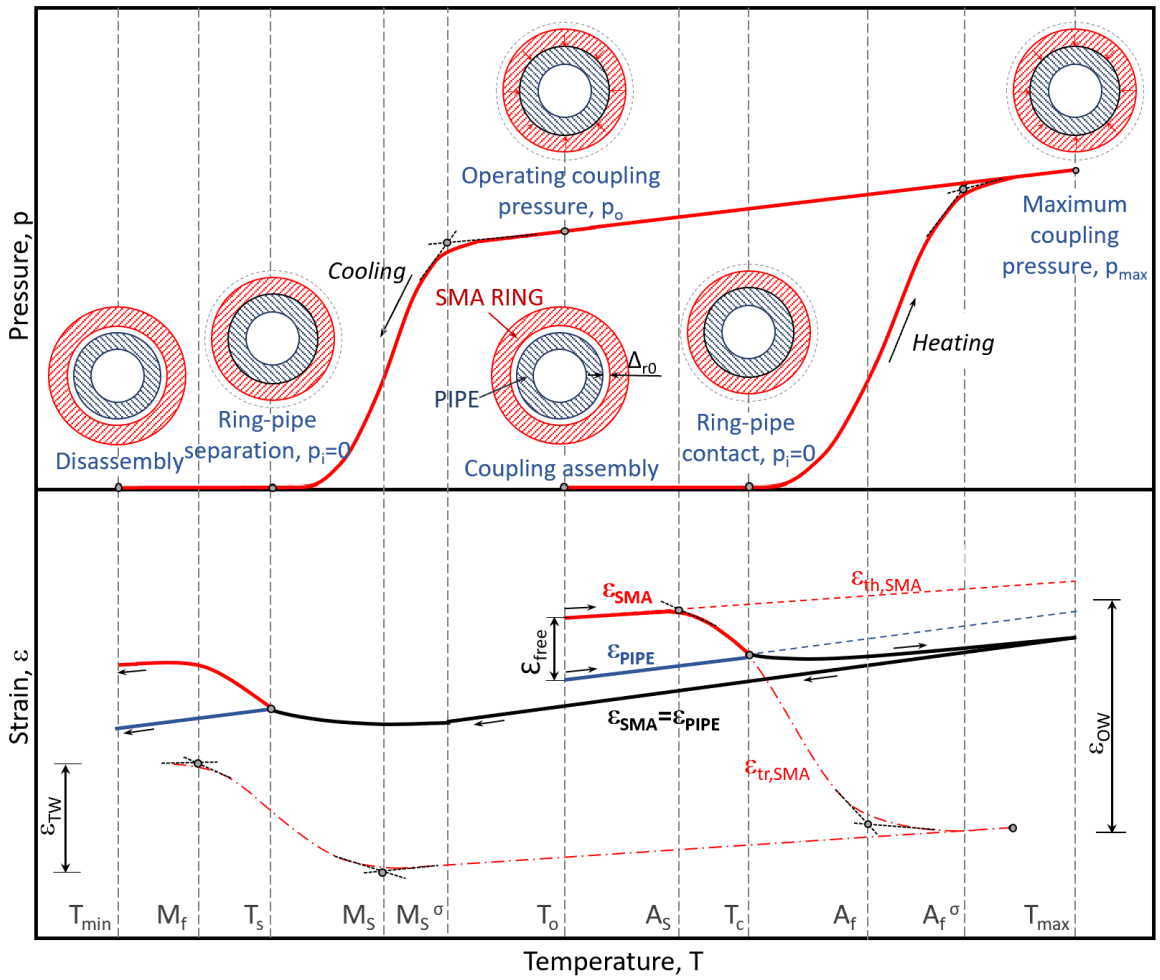

Figure 4.13: Schematic depiction of the SMA ring-steel pipe coupling mechanism.

If the recovery of the austenitic shape of a material showing SME is prevented during heating above A_s, recovery stresses are generated. A uniaxial case is analyzed in Figure 4.14. The generation of recovery stresses is due to the previous macroscopic deformation, up to a maximum value ϵ_{max}, at a temperature T_{def} aimed to induce stable detwinned martensitic variants (Figure 4.14a). ϵ_{unl} represents the residual inelastic deformation after unloading. During subsequent heating, free recovery occurs due to SME. In the absence of mechanical obstacles (red

curves), the entire one-way deformation ϵ_{OW} can be recovered during the thermally-induced martensite to austenite transformation. ϵ_{irr} represents the irrecoverable part of deformation. If the material shows TW-SME capabilities, an elongation corresponding to ϵ_{TW} can be induced by cooling below its martensitic TTs. Instead, in the presence of a mechanical obstacle, the free recovery stage occurs only up to a temperature T_c (Figure 4.14b), namely the contact temperature. The material partially transforms back to austenite recovering a deformation equal to $\epsilon_{free} = \epsilon_{unl} - \epsilon_c$. The recovery of the remaining deformation, the contact strain $\epsilon_{ct} = \epsilon_c - \epsilon_{irr}$, is impeded. Therefore, increasing the temperature above T_c, recovery stress is generated (Figure 4.14c). The latter increases up to a maximum value σ_r^{max} occurring in correspondence of A_f^σ which is the temperature at which the SMA element, under stress, becomes fully austenitic, i.e., without thermally induced or stress induced martensitic variants. This latter corresponds indicatively to the so-called martensite desist temperature M_d. Thanks to the TW capability of the SMA, by subsequent cooling, it is possible to induce the forward A→M transition starting from the martensite start temperature under stress M_s^σ of the material associated with a significant relaxation until a zero-stress state at T_s.

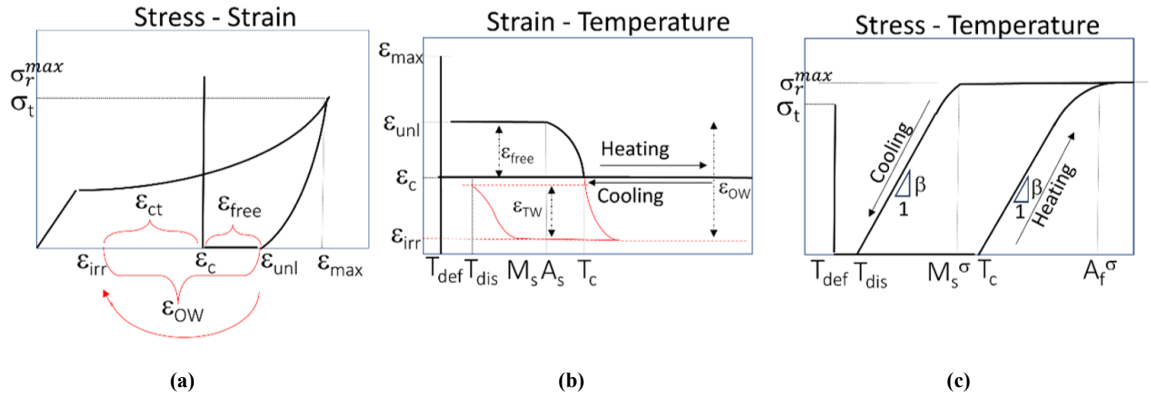

Figure 4.14: Schematic depiction of the uniaxial constrained shape recovery mechanism: **(a)** the stress-strain relationship, **(b)** strain-temperature relationship, and **(c)** stress-temperature relationship.

It is worth pointing out that for polycrystalline SMAs the slope of the measured $\sigma - T$ curve is not constant as the evolution of recovery stress is non-linear. Moreover, the average slope, β, is not a material parameter but depends to some extent on the martensitic pre-strain ϵ_{max}, the contact strain ϵ_{ct} and in general on the thermomechanical history of the alloy [117, 118, 109]. However, β is frequently estimated through linear fits and used as material characteristic

parameters as, in specific conditions, was found close to the Clausius Clapeyron coefficient of the alloy. In a very general case, the total strain of a material exhibiting SME, ϵ_t, can always be subdivided into a transformation component ϵ_{tr}, an elastic component ϵ_{el}, a plastic component ϵ_{pl} and a thermal component ϵ_{th}. During constrained recovery, the total strain ϵ_t is equal to the contact strain ϵ_{ct}, so:

$$\epsilon_t = \epsilon_{ct} = \epsilon_{tr} + \epsilon_{el} + \epsilon_{th} + \epsilon_{pl} \tag{4.37}$$

Under the hypothesis of a mechanical obstacle infinitely rigid and with identical thermal expansion coefficient to the shape memory element the quantity $\epsilon_{cth} = \epsilon_{ct} - \epsilon_{th}$ is independent of both temperature and stress, i.e., ϵ_{cth} is constant during the generation of recovery stresses:

$$\epsilon_{cth} = \epsilon_{ct} - \epsilon_{th} = \epsilon_{tr} + \epsilon_{el} + \epsilon_{pl} = const. \tag{4.38}$$

From Equation 4.38 it follows that, during the constrained shape recovery mechanism, a certain amount of detwinned martensite variants transform to austenite when they are not anymore thermally stable and therefore the quantity ϵ_{tr} decreases while $\epsilon_{el} + \epsilon_{pl}$ increases of the same extent. Consequently, if ϵ_{cth} is sufficiently high, plastic deformation occurs. The yield stress of the material, σ_y, is then an upper limit to σ_r. Recently, experimental evidence demonstrated that reversible twinned austenite formation is coupled with slip mechanisms [109, 117]. Conversely, if ϵ_{cth} is within the elastic deformation range of the SMA sample, a recovery stress equal to $E_A \cdot \epsilon_{cth}$ is generated, where E_A is the Young's modulus of the austenite. This represents a lower bound limit for σ_r.

All the above considerations relate to SMAs whose recovery is constrained by an absolutely rigid substrate with the same coefficient of thermal expansion as the memory material. In reality, the substrate is subjected to elastic or elastic-plastic deformations. During the constrained recovery process, after heating above T_c, the SMA thermo-mechanical path is controlled by the substrate compliance and by the mismatch between the SMA and the substrate thermal expansion coefficients. It is then clear that recovery stress is a path-dependent property, not immediately predictable. Maximum recovery stress, σ_r^{max}, in NiTi-based alloys, ranges from about 300 to 900 MPa depending on the alloy and its microstructure [109, 118, 117, 119, 120, 121, 122]. Generally, σ_r^{max}, is a function of ϵ_{max} and ϵ_{cth} [122]. ϵ_{OW} represents the upper bound value of ϵ_{cth}. In general, the recovery stress for a given ϵ_{cth} at a given temperature (T) is an indication of the stability of the martensite variants at that temperature, so it is directly related to

the stress required to induce the same amount of inelastic strain (ϵ_{cth}) in the same material at that temperature [120]. In fact, several experimental studies confirmed that the $\sigma_r(T, \epsilon_{cth})$ curve obtained by different recovery stress tests can be approximated with a certain error (normally within 20%) by the stress-strain curve of the same material obtained from isothermal tensile tests $\sigma(T, \epsilon)$ [120, 4]. Consequently, given that the typical transformation strains ϵ_{OW} induced by martensite pre-deformation are lower than 7%, a bi-linear stress-strain response is assumed for SMA modeling.

Figure 4.15a schematically shows the hysteretic recovery stress curve of a SMA exhibiting TW-SME obtained by constrained heating/cooling. Figure 4.15b shows the isothermal bi-linear $\sigma - \epsilon$ (or $\sigma_r - \epsilon_{cth}$) curves of a SMA at three different temperatures ($T_1 < T_2 < T_3$). The volume fraction of martensite at the end of the stress plateau, ξ, goes from ξ=1 (fully martensitic state at T_1) to $\xi = 0$ (fully austenitic state at T_3). σ^s_{cr} represents the critical plateau stress to induce inelastic strain in the SMA. The latter may results from reoriented/stress induced martensite phenomena and/or austenite twins/slip formations depending on the temperature. For $\sigma \leq \sigma^s_{cr}$ (elastic region), the SMA is elastically deformed, according to the value of the equivalent Young's modulus, which is defined as a function of the volume fraction of martensite E(ξ). For $\sigma > \sigma^s_{cr}$ (inelastic region), the SMA undergoes inelastic deformations and the stress-strain relation is described by a hardening parameter, H, experimentally evaluated.

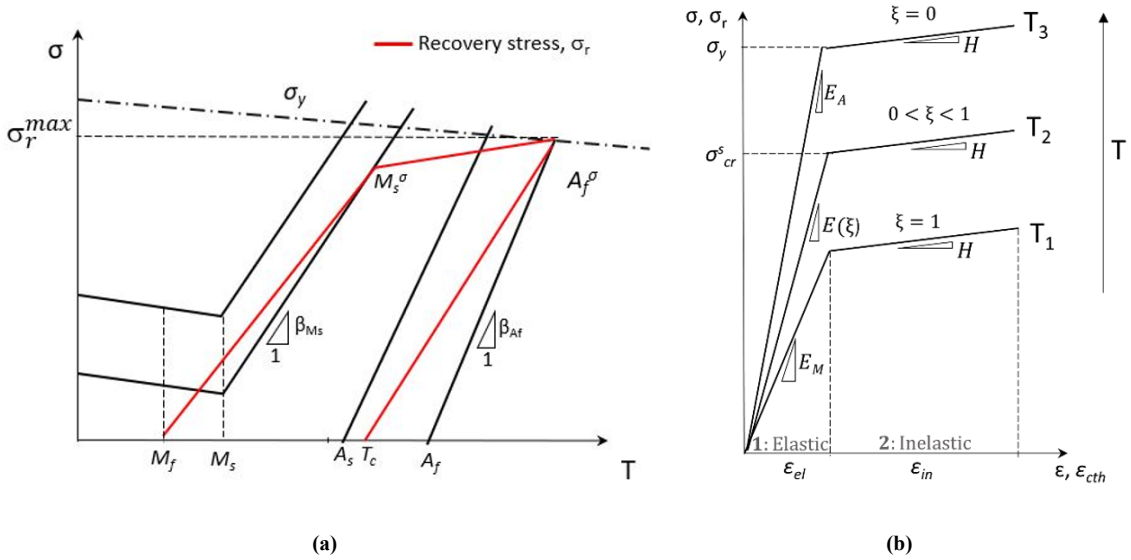

Figure 4.15: Schematic representation of the stress-strain response of a SMA during constrained recovery: **(a)** hysteretic recovery stress curve of a SMA showing TWSME obtained by constrained heating/cooling, **(b)** Stress-strain curve at different temperatures corresponding to three different crystallographic states: fully martensite ($\xi = 1$), 2: martensite + austenite ($0 < \xi < 1$), 3: fully austenite $\xi = 0$.

Figure 4.15a also shows the TTs of the trained SMA (A_s, A_f, M_s, M_f) that are assumed to vary linearly with the applied stress field according to Clausius Clapeyron equation. In constrained recovery applications, the stress field occurring in the SMA is not known a-priori. However, the austenite finish temperature under stress A_f^σ and the martensite start temperature under stress M_s^σ can be expressed as a function of the corresponding recovery stress calculated at the end of the martensite to austenite transformation and at the beginning of the austenite to martensite transition, respectively:

$$A_f^\sigma = A_f + \frac{\sigma(A_f^\sigma)}{\beta_{Af}} \tag{4.39}$$

$$M_s^\sigma = M_s + \frac{\sigma(M_s^\sigma)}{\beta_{Ms}} \tag{4.40}$$

Where A_f and M_s are the austenite finish temperature and martensite start temperature in stress-free conditions and β_{Af} and β_{Ms} the Clausius-Clapeyron coefficients for austenite finish and martensite start temperature, respectively. It is worth noting that when $T \geq A_f^\sigma$, in case of a sufficiently rigid obstacle, austenite twins and plastic deformations occur due to the high stress-temperature state. Consequently, $\sigma(A_f^\sigma)$ corresponds indicatively to the yielding stress of the

material, σ_y (cfr. Figure 4.15a). M_s^σ can be also estimated iteratively knowing $\sigma_e(M_s^\sigma)$ which represents the stress computed after the martensite to austenite transition and the subsequent cooling from A_f^σ to M_s^σ. The latter is assumed to involve only thermoelastic deformations.

TTs, σ_y, β_{Af} and β_{Ms} are experimentally evaluated by isobaric strain-temperature tests and isothermal stress-strain tests. Martensitic and austenitic yield stresses values exhibit a limited variation with temperature (see section 3.2.2), therefore σ_y is modeled as temperature independent.

As experimentally demonstrated [109, 117, 123], the *volume fraction of martensite* measured at the end of the stress plateau as a function of the temperature exhibits a sigmoidal trend between the transformation temperatures during both the inverse (M→A) and direct (A→M) transformations. Therefore, the evolution of the volume fraction of martensite in constrained recovery applications can be analytically described by the following kinetic laws:

$$\xi_{M\to A} = 1 - \frac{k \cdot N_0}{N_0 + (k - N_0)e^{-r_\xi\left(T-\left(|A_s|+\frac{|A_f^\sigma|-|A_s|}{2}\right)\right)} + q} \tag{4.41}$$

$$\xi_{A\to M} = 1 - \frac{k \cdot N_0}{N_0 + (k - N_0)e^{-r_\xi\left(T-\left(|M_s^\sigma|+\frac{|M_f|-|M_s^\sigma|}{2}\right)\right)} + q} \tag{4.42}$$

where k, N_0, r_ξ and q are dimensionless parameters, defining the amplitude (k), the mid-point/symmetry of the S-shape with respect to the x-axis (N_0), the maximum asymptotic intensity (r_ξ), and the slope (q) of the sigmoidal curve, and are calculated by applying the line extension method.

The *recovery strain* ϵ_{tr} is the recoverable deformation due to the OW-SME. In literature [124] the recovery strain is considered to be proportional to the volume fraction of martensite, as reported below:

$$\epsilon_{tr} = \epsilon_{OW}(\xi - \xi_0) \tag{4.43}$$

Where ξ_0 is the volume fraction of martensite at the initial state of the considered transformation step while ϵ_{OW} is the maximum recoverable strain available after the martensitic pre-strain (Figure 4.14). In recovery stress application a certain fraction of ϵ_{OW} is freely recovered, ϵ_{free}, while the rest, ϵ_{ct}, which is impeded by a mechanical obstacle (see Figure 4.14), increases by increasing temperature during M-A transition and results in internal stress generation. For the

sake of simplicity, it is assumed that the SMA material during constrained austenite to martensite transformation ($M_s^\sigma - M_f$) elongates up to the same amount of strain, ϵ_{OW}, thanks to the TW-SME induced during the previous thermomechanical training. Experimental evidence shows that recovery stress of properly trained SMAs drops to zero by cooling down to M_f even if two-way recoverable deformation obtained from stress-free thermal cycles are lower than the one way ($\epsilon_{OW} > \epsilon_{TW}$). This is attributed to the complex deformation mechanisms occurring during M→A constrained heating which causes a certain amount of plastic and/or pseudoplastic deformation which increases the TW-SME of the material. Moreover, the applied stress has a training effect on the SMA itself and it increases the volume fraction of favorably oriented martensite variants, resulting in an enhancement of the TW thermal recovery capabilities.

Previous studies concerning stress free/stress applied thermal cycles on pre-deformed SMA rings and rods demonstrated that the evolution of circumferential strain at the SMA ring inner diameter, $\epsilon_{\theta i}$, as well as the circumferential stress, $\sigma_{\theta i}$, as a function of the temperature can be correctly captured by $\epsilon - T$ and $\sigma - T$ curves recorded from uniaxial thermo-mechanical tests of SMA samples subjected to the same martensitic pre-deformation ($\epsilon_{\theta i,max} = \epsilon_{max}$) [9, 6]. Consequently, it is possible to describe the evolution of the martensite volume fraction in the SMA ring by Equations 4.41 and 4.42 as well as to compute the circumferential recovery strain at the SMA ring inner diameter as $\epsilon_{\theta i,tr} = \epsilon_{tr}$.

The *Equivalent Young's modulus E* is defined by the inverse rule of mixtures (Reuss formula), as follows:

$$E(\xi) = \left(\frac{\xi}{E_M} + \frac{1-\xi}{E_A} \right) \tag{4.44}$$

where E_A and E_M are the Young's modulus of austenite and detwinned martensite, respectively. ϵ_{OW}, E_M, E_A can be identified by uniaxial tests.

As mentioned before, experimental evidences show that the critical plateau stress σ_{cr}^s that define the evolution of stress in a constrained SMA exhibiting OW-SME increases non-linearly with respect to the temperature. This is because recovery stress generation intrinsically involves complex deformation mechanisms at high temperatures and stresses (B2→ B19′→ B2T) beyond the linear Clausius Clapeyron regime [123, 109, 4]. However, for the sake of simplicity, σ_{cr}^s is assumed to increase linearly with respect to the temperatures during both martensite to austenite

($A_s - A_f^\sigma$) and austenite to martensite ($M_s^\sigma - M_f$) transition temperatures according to the following laws:

$$\sigma^s_{cr\,M\to A} = \sigma^s_{cr}(A_s) + \beta_{M\to A}(T - A_s) \tag{4.45}$$

$$\sigma^s_{cr\,A\to M} = \sigma^s_{cr}(M_s^\sigma) + \beta_{A\to M}(T - M_s^\sigma) \tag{4.46}$$

During the constrained heating, $\sigma^s_{cr\,M\to A}$ increases from $\sigma^s_{cr}(A_s)$ until it reaches the yield stress of the material at $T_3 = A_f^\sigma(\sigma^s_{cr} = \sigma_y)$ when twinning and plastic mechanism in the austenite phase occur and the martensite cannot be stress-induced anymore ($\xi = 0$) (Figure 4.15b).

Similar considerations apply for the A→M transition occurring during the cooling stage starting from M_s^σ. The critical stress relaxation is described by $\beta_{A\to M}$. The two material parameters $\beta_{M\to A}$ and $\beta_{A\to M}$ represent the average slope of the critical stress as a function of the temperature within the thermal range of interest, i.e., $A_s < T < A_f^\sigma$ and $M_f < T < M_s^\sigma$, respectively. They can be experimentally evaluated by uniaxial isothermal stress-strain tests or isobaric strain temperature tests (see section 3.2.2).

The tangent modulus H is assumed to be constant during the entire process, as it does not show a significant variation with temperature (see Figure 3.6).

It is worth noting that, the modeling of the complex microstructural deformation mechanisms occurring during recovery stress generation is out of the scope of this work which aims to describe the SMA constrained recovery behavior in a simple phenomenological fashion.

4.5.3 SMA ring constrained recovery modeling

The ring-pipe system can be bi-dimensionally modelled and studied in polar coordinates (see section 4.3), due to the axisymmetric conditions, as depicted in Figure 4.16. In particular, Figure 4.16a shows the initial and final state of the process, where a gap (Δr_0) exists between the pipe and the SMA ring. Figure 4.16b represents all other intermediate steps, from contact to separation, where a radial pressure pi exists at the contact interface.

In this case, the inelastic compatibility equation expressed in terms of stress is obtained by combining Equation 4.6 with Equation 4.7, as shown below:

$$\frac{1}{E(\xi)}\left(\frac{d\sigma_\theta}{dr}+\frac{d\sigma_r}{dr}\right)+\frac{1}{2\cdot r\cdot\sigma_e}\left[3(\sigma_\theta-\sigma_r)+r\left(2\frac{d\sigma_\theta}{dr}-\frac{d\sigma_r}{dr}\right)\right](\sigma_{cr}^s-\sigma_e)$$

$$\left(\frac{1}{E(\xi)}-\frac{1}{H}\right)-\frac{1}{4\cdot\sigma_e^3}\left[2(\sigma_\theta-\sigma_r)\left(\sigma_\theta\left(2\frac{d\sigma_\theta}{dr}-\frac{d\sigma_r}{dr}\right)-\sigma_r\left(\frac{d\sigma_\theta}{dr}-2\frac{d\sigma_r}{dr}\right)\right)\right]$$

$$\left(\frac{\sigma_{cr}^s}{E(\xi)}-\frac{\sigma_{cr}^s}{H}\right) \tag{4.47}$$

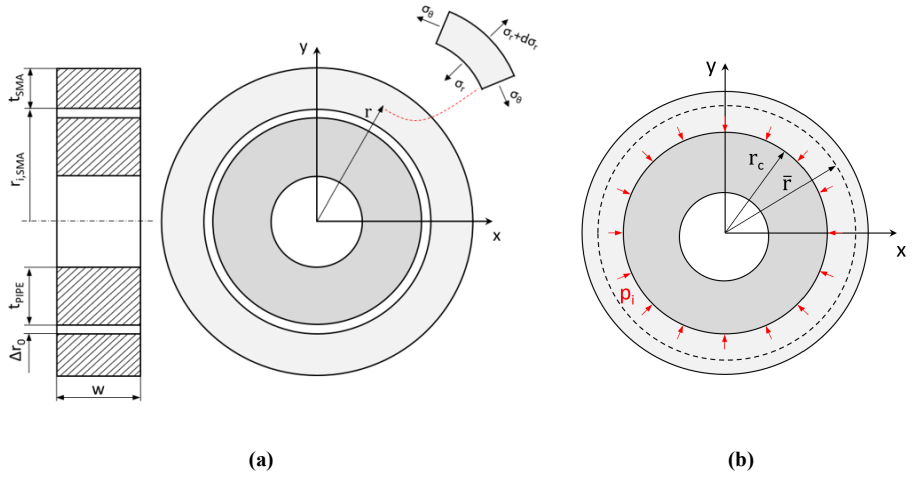

Figure 4.16: Bi-dimensional axisymmetric representation of the pipe-SMA ring system during assembly/disassembly process: **(a)** initial and final state of the process, where a gap Δr_0 exists between the pipe and the SMA ring, and **(b)** all intermediate steps of the process, from contact to separation, where a radial pressure p_i exists at the contact interface.

4.5.4 Load steps and boundary conditions

During phase transformations under constrained-recovery conditions, three different loading cases occur in the SMA ring exhibiting bilinear stress-strain evolution (cfr. paragraph 3.2.2), and can be summarized in the following three steps:

- **Load step #1**: Elastic strain at both $r_{i,SMA}$ and $r_{e,SMA}$;
- **Load step #2**: Inelastic strain at $r_{i,SMA}$ and elastic strain at $r_{e,SMA}$;
- **Load step #3**: Inelastic strain at both $r_{i,SMA}$ and $r_{e,SMA}$.

During a complete phase transition, the SMA ring goes through all load steps, in the order defined by the direction of the transformation: from step #1 to #3 in the case of M→A (heating), from step #3 to #1 in the case of A→M (cooling).

The increase in temperature causes the contraction of the ring against the internal pipes due to OW-SME, resulting in the development of a contact pressure. The prevented circumferential strain at the inner diameter, $\epsilon_{SMA} = \epsilon_{tr}$,increases by increasing temperature from zero up to maximum value (cfr. Equations 4.41. The ring is subjected to an elastic stress state if $\sigma_e(r_{i,SMA}) \leq \sigma^s_{cr}$, where $\sigma_e(r_{i,SMA})$ is the equivalent Von Mises stress at the inner radius. When $\sigma_e(r_{i,SMA}) > \sigma^s_{cr}$, the stress evolution starts to follow the plastic rule and inelastic deformations occur in correspondence of the inner radius of the ring. As long as $\sigma_e(r_{i,SMA}) > \sigma^s_{cr}$ and $\sigma_e(r_{e,SMA}) \leq \sigma^s_{cr}$ two regions coexist in the ring: inelastic at the inner radius and elastic at the outer radius (load step #2). For $\sigma_e(r_{e,SMA}) \geq \sigma^s_{cr}$, the entire ring is in the inelastic region (load step #3), until the maximum one-way strain ϵ_{OW} is fully prevented and the phase transformation is completed. It is worth noting that the pipe to be connected is not modeled as an infinitely rigid body, since it undergoes elastic deformations during the ring contraction. Therefore, the elastic deformation of the pipe is also considered at the load step #1 of the M→A phase transformation as its contribution to the contact pressure is not negligible. At load steps #2 and #3 the computation of the contact pressure is carried out by neglecting the elastic strain in the total prevented strain, as it has been shown experimentally to be at least an order of magnitude lower than the transformation strain of the SMA.

The initial stress-strain state of the A→M transformation ($T = M^\sigma_s$), is assumed to be equal to that corresponding to the end point of the previous M→A transformation ($T = A^\sigma_f$), modified by the thermoelastic contribution occurring between A^σ_f and M^σ_s. The prevented circumferential strain at the inner diameter, decreases by decreasing temperature from its maximum value to zero according to Equation 4.43. Initially, the ring is fully deformed inelastically (step #3). The temperature decrease causes gradual recovery of strain due to TW-SME and a subsequent contact relaxation in the system. For $\sigma_e(r_{i,SMA}) > \sigma^s_{cr}$ and $\sigma_e(r_{e,SMA}) \leq \sigma^s_{cr}$, the ring is in the mixed loading case (step #2), while it undergoes complete elastic deformations when $\sigma_e(r_{i,SMA}) \leq \sigma^s_{cr}$ (step #1).

The critical temperatures that define the three load steps (#1, #2, #3) in both phase transformations are not known a-priori, as they depend on geometry, mechanical properties and loading conditions of the SMA ring and need to be computed during process simulation.

Table 4.5 reports the system of equations and boundary conditions for the three load steps. External boundary conditions are applied in terms of pressure at the inner radius, where $\sigma_r(r_{i,SMA}) = p_i$, and at the outer radius, where $\sigma_r(r_{e,SMA}) = 0$. For the mixed load step (#2), additional conditions are required in correspondence of the transformation radius $\bar{r}$ at the contact interface between ring and pipe, in order to impose the internal stress equilibrium.

Table 4.5: System of equation and boundary conditions defining the load steps that occur during phase Transformations.

Load step #	Condition	System of equations	Boundary conditions
1	$\sigma_e(r_{i,SMA}) \leq \sigma^s_{cr}$	$\begin{cases} E_{el}(Eq.4.1) \\ C_{el}(Eq.4.4) \end{cases}$	$\begin{cases} \sigma^{el}_r(r_{i,SMA}) = -p_i \\ \sigma^{el}_r(r_{e,SMA}) = 0 \end{cases}$
2	$\begin{cases} \sigma_e(r_{i,SMA}) > \sigma^s_{cr} \\ \sigma_e(r_{e,SMA}) \leq \sigma^s_{cr} \end{cases}$	$\begin{cases} E_{el}(Eq.4.1) \\ C_{el}(Eq.4.4) \\ E_{in}(Eq.4.1) \\ C_{in}(Eq.4.47) \end{cases}$	$\begin{cases} \sigma^{in}_r(r_{i,SMA}) = -p_i \\ \sigma^{el}_r(r_{e,SMA}) = 0 \\ \sigma^{el}_r(\bar{r}) = \sigma^{in}_r(\bar{r}) \\ \sigma^{el}_\theta(\bar{r}) = \sigma^{in}_\theta(\bar{r}) \end{cases}$
3	$\sigma_e(r_{i,SMA}) > \sigma^s_{cr}$	$\begin{cases} E_{in}(Eq.4.1) \\ C_{in}(Eq.4.47) \end{cases}$	$\begin{cases} \sigma^{in}_r(r_{i,SMA}) = -p_i \\ \sigma^{in}_r(r_{e,SMA}) = 0 \end{cases}$

4.5.5 Analytical modeling of thermal mounting and dismounting

The model is developed under the assumption of linear elastic behavior of the pipe and small deformations of the SMA ring/pipe assembly. The mounting (M→A) and dismounting (A→M) phases are analyzed below. Several subphases are identified for each phase. Two basic conditions occur depending on the geometric configuration of the system: stress-free and stress-applied. In the case of stress-free conditions, an initial radial gap exists between the pipe and the SMA coupler ($r_{i,SMA} - r_{e,PIPE}$). The final radial gap induced by a certain temperature variation ($T_{fin} - T_{in}$) can be determined according to the total deformations, as written below:

$$\Delta r = r_{i,SMA}(1 + \epsilon_{SMA}) - r_{e,PIPE}(1 + \epsilon_{PIPE}) \tag{4.48}$$

where ϵ_{SMA} and ϵ_{PIPE} are the circumferential strain components at the inner radius of the SMA ring and at the outer radius of the elastic pipe. ϵ_{SMA} includes a thermoelastic and a inelastic strain component: $\epsilon_{SMA} = \epsilon_{th,SMA} + \epsilon_{tr}$, while ϵ_{PIPE} only a thermoelastic component ($\epsilon_{PIPE} = \epsilon_{th,PIPE}$). The transformation component of SMA strain, ϵ_{tr}, is calculated by Equation 4.43 by knowing the maximum recoverable strain ϵ_{OW} obtained from stress-free thermal cycles on SMA

samples/rings.

The general thermoelastic strain ϵ_{th} is defined as:

$$\epsilon_{th} = \alpha(T_{fin} - T_{in}) \tag{4.49}$$

where α denotes the thermal expansion coefficient (CTE) of the material, and T_{in} and T_{fin} are the initial and final temperature of the considered phase, respectively.

In the case of stress-applied conditions the SMA/pipe radial gap is zero, the evolution of the contact pressure p_i can be obtained iteratively, proceeding by small temperature steps when inelastic strains are involved as explained in section 4.5.6. At the generic temperature T the total radial contact pressure p_i is given by the sum of a thermoelastic, p_{th}, and a transformation, p_{tr}, contribution, as shown below:

$$p_i(T) = p_{tr}(T) + p_{th}(T) \tag{4.50}$$

The thermoelastic component of pressure p_{th} is determined according to the geometry and elastic properties of the coupler and pipe, as written below:

$$\Delta r = r_c p_{th} \left[\frac{1}{E(\xi)_{SMA}} \left(\frac{r_{e,SMA}^2 + r_c^2}{r_{e,SMA}^2 - r_c^2} + \nu_{SMA} \right) - \frac{1}{E_{PIPE}} \left(-\frac{r_c^2 + r_{i,PIPE}^2}{r_c^2 - r_{i,PIPE}^2} - \nu_{PIPE} \right) \right] \tag{4.51}$$

Where r_c is the contact radius and Δr is the interference that would result due to the mismatch between the CTEs of the SMA and the pipe material. Δr can be calculated as follows:

$$\Delta r = |r_c(\epsilon_{th,PIPE} - \epsilon_{th,SMA})| \tag{4.52}$$

The computational procedure is described in detail in Section 3.2.2, where a schematic representation of the calculation algorithm is provided by the flowcharts in Figures 4.17, 4.18 and 4.19.

Mounting

In agreement with Figure 4.13, the SMA ring/pipe mounting stage consists of the following steps:

- **Phase 1:** $\boldsymbol{T_o \rightarrow A_s}$: thermoelastic stress-free phase
- **Phase 2:** $\boldsymbol{A_s \rightarrow T_c}$: thermoelastic + inelastic stress-free phase

- **Phase 3: $T_c \rightarrow T_{max}$**: inelastic stress-constrained phase
- **Phase 4: $T_{max} \rightarrow T_o$:** thermoelastic stress-constrained phase

For the sake of simplicity, the starting and ending point of each phase will be denoted by subscripts $N-1$ and N, respectively, where N is the number of the phase under consideration.

Phase 1: $T_o \rightarrow A_s$

In this phase, the temperature is always lower than the austenite start temperature A_s. Therefore, no phase transformation mechanisms occur and both rings are subjected only to linear thermoelastic strain, calculated by applying Equation 4.49 with the following boundary conditions: $T_{in} = T_o$ and $T_{fin} = A_s$. The initial gap between the SMA and the pipe is $\Delta r_0 = r_{i,SMA,0} - r_{e,PIPE,0}$. The thermal deformations establish a new gap between the rings that is determined as follows (Equation 4.48):

$$\Delta r_1 = r_{i,SMA,0}(1 + \epsilon_{th,SMA,1}) - r_{e,PIPE,0}(1 + \epsilon_{th,PIPE,1}) \tag{4.53}$$

Phase 2: $A_s \rightarrow T_c$

At $T = A_s$, the M→A phase transformation starts to take place and the SMA ring deforms based on both thermal (expansion) and recovery (contraction) strains. The combination of the two effects leads to the contraction of the ring since the recovery strain is at least an order of magnitude higher than the thermal strain (Figure 4.13). The pipe continues to expand, as it is only subjected to thermal deformation. The two rings come into contact at $T = T_c$. The thermal deformations of both rings are calculated by applying Equation 4.49 by imposing the proper boundary conditions. The contact condition ($\Delta r_2 = 0$) is given by:

$$\Delta r_1 = |r_{i,SMA,1} \cdot \epsilon_{SMA,2}| + |r_{e,PIPE,1} \cdot \epsilon_{PIPE,2}| \tag{4.54}$$

where $\epsilon_{SMA,2} = \epsilon_{th,SMA,2} + \epsilon_{tr,2}$ and $\epsilon_{PIPE,2} = \epsilon_{th,PIPE,1}$. The system of equations Equations 4.41, 4.43 and 4.54, together with the proper boundary conditions (initial martensite volume fraction $\xi_1 = 1$), allow to calculate the volume fraction of martensite when the contact occurs, $\xi = \xi_2$, and the contact temperature $T = T_c$ and the maximum free recovery circumferential strain at the internal radius of the SMA ring, $\epsilon_{tr,2} = \epsilon_{free}$. At the end of this phase, the two rings are in contact with zero contact pressure at the interface. The contact radius $r_{c,2}$ can be calculated as follows:

$$r_{c,2} = r_{e,PIPE,1}(1 + \epsilon_{PIPE,2}) \tag{4.55}$$

Phase 3: $T_c \rightarrow T_{max}$

After the contact, the temperature increase induces the thermal expansion of the pipe, while the SMA ring would continue to contract due to the recovery properties. A radial contact pressure p_i occurs and can be computed iteratively as explained in section 4.5.6. The prevented deformation can be determined by Equations 4.41 and 4.43; the system of equilibrium, compatibility and boundary conditions equations reported in Table 4.5 is solved in order to obtain the stress and strain state for each calculation step. At $T = A_f^\sigma$, the M→A transformation is completed ($\xi = \xi_3 = 0$) and the SMA is in a fully austenitic structure. The maximum contact pressure $p_i = p_{max}$ is then generated at $T = T_{max}$.

Phase 4: $T_{max} \rightarrow T_o$

From T_{max} to T_o, only thermoelastic deformations (Equation 4.49) are considered, as it is assumed $M_s^\sigma < T_o$ (Section 4.5.2). The decrease in temperature results in a linear variation of the contact pressure due to the SMA/pipe thermal expansion coefficient mismatch ($\alpha_{PIPE} > \alpha_{SMA}$). The thermoelastic contact pressure component $p_{th}(T_{max})$ is obtained from Equations 4.49, 4.51 and 4.52. The total contact pressure at $T = T_o$ (operating condition) is reported below:

$$p_4 = p_o = p_{max} - p_{th,4} \tag{4.56}$$

Dismounting

The dismounting consists of the following steps:

- **Phase 5: $T_o \rightarrow M_s^\sigma$**: thermoelastic stress-constrained phase
- **Phase 6: $M_s^\sigma \rightarrow T_s$**: inelastic stress-constrained phase
- **Phase 7: $T_s \rightarrow M_f$**: thermoelastic + inelastic stress-free phase
- **Phase 8: $M_f \rightarrow T_{min}$**: thermoelastic stress-free phase

Phase 5: $T_o \rightarrow M_s^\sigma$

In this initial phase of disassembly, only thermoelastic deformations occur. Both the ring and pipe contract, and the decrease in temperature results in a linear decrease of the contact pressure according to Equations 4.49, 4.51 and 4.52).

Phase 6: $M_s^\sigma \rightarrow T_s$

At $T = M_s^\sigma$, the A→M transition starts to take place ($\xi > 0$), and this causes the expansion of the SMA ring due to the TW-SME. At the same time, the pipe continues to contract with decreasing temperature. This opposite behavior leads to the separation of the two rings at $T = T_s$. The transformation strain is calculated by applying Equations 4.42 and 4.43, with $\xi_0 = 0$. The contact pressure is obtained by solving the system of equilibrium, compatibility, and boundary conditions according to the proper load step (Table 4.5). The separation condition ($p_6 = 0$) allows the identification of the dismounting temperature (T_s) . The contact/separation radius (r_s) is determined as follows:

$$r_{c,6} = r_s = r_{e,PIPE,o}(1 + \alpha_{PIPE}(T_s - T_o)) \tag{4.57}$$

Phase 7: $T_s \rightarrow M_f$

For $T < T_s$, the two rings are not in contact, the pipe and the SMA ring are unloaded and deform in free recovery conditions. The SMA ring is subjected to both transformation (expansion) and thermal (contraction) strain. The recovery strain in the SMA is determined by Equations 4.42 and 4.43 with the appropriate boundary conditions. The pipe is subjected only to thermoelastic deformations (Equation 4.49), therefore it contracts, allowing the formation of a new gap between the rings Δr_7 (Equation 4.48). At the end of this phase, the A→M transformation is completed.

Phase 8: $M_f \rightarrow T_{min}$

In this phase, both rings contract because of thermal effects, according to Equation 4.49. Since $\alpha_{PIPE} > \alpha_{SMA}$ a radial gap between the rings still exists at the end of the phase, which allows the complete disassembly of the system.

4.5.6 Solution procedure

The analytical model herein proposed is implemented in Wolfram Mathematica ®. The flowcharts in Figures 4.17 and 4.18 show the computational procedure for mounting and dismounting phases, respectively.

The input required to solve the mounting are the initial geometry of the two rings (Figure 4.17). Also, a counter $i = 0$ is set to be used for the step-by-step calculation of the pressure in

the non-linear phases. The step size in terms of temperature variation is defined by the value of ΔT, arbitrarily chosen by the user. The lower ΔT, the higher the accuracy of the solution and the computational time.

The phase 1 ($T_o \rightarrow A_s$) consists in the calculation of the radial gap Δr_1 between the rings at the beginning of the M→A transition ($T = A_s$). In phase 2 ($A_s \rightarrow T_c$), the value of T_c is determined by solving iteratively the system of equations involving both transformation and thermoelastic effects. The iterations terminate when the difference between the contact gap $\Delta r_c = |r_{i,SMA,1}\epsilon_{SMA,2}| + |r_{e,PIPE,1}\epsilon_{PIPE,2}|$ calculated in this phase and the initial gap Δr_1 determined at the end of the previous phase is lower than the tolerance value δr. In phase 3 ($T_c \rightarrow T_{max}$) the contact pressure is determined step-by-step as its evolution is not linear. . More info about this phase are reported at the end of the section (cfr. Figure 4.19). The maximum pressure p_{max} is calculated at the maximum temperature of the process. In phase 4 ($T_{max} \rightarrow T_o$) the operating pressure p_o at the operating temperature T_o is determined simply by decreasing the maximum pressure by the calculated thermoelastic pressure in the considered temperature range.

The stress-strain distribution at the end of the mounting phase represents the input of the dismounting phase (Figure 4.18). In particular, the contact radius and the contact pressure at T_o, which are $r_{c,4} = r_{c,o}$ and p_o, respectively, are given as input for the calculation of the stress-strain evolution upon final cooling. In phase 5 ($T_o \rightarrow M_s^\sigma$), first the martensite start temperature under stress-applied conditions M_s^σ is determined. This calculation requires an iterative procedure, so an initial value of M_s^σ is estimated. The iterations terminate when the difference between the equivalent stress at the inner radius corresponding to a contact pressure $p_i = p_o - p_{th}$ and the equivalent stress calculated by the definition of M_s^σ (Equation 4.40) is lower than the tolerance value $\delta\sigma$. The equivalent stress as a function of p_i is calculated as follows:

$$\sigma_e(r_{i,SMA}) = \sqrt{\sigma_r(r_{i,SMA})^2 + \sigma_\theta(r_{i,SMA})^2 - \sigma_r(r_{i,SMA}) \cdot \sigma_\theta(r_{i,SMA})} \tag{4.58}$$

Once M_s^σ is determined, the linear contact pressure evolution is obtained by considering only the thermoelastic deformations of both the SMA ring and the pipe.

In phase 6 ($M_s^\sigma \rightarrow T_s$), the contact pressure is calculated by a step-by-step procedure, as its evolution is non-linear. At T_s the two rings are in contact with zero pressure, so phase 7 ($T_s \rightarrow M_f$) only involves the calculation of the SMA and pipe deformations due to transformation

and thermoelastic phenomena to obtain the gap between the rings at the end of the A→M transition, $\Delta_{r,7}$. The radial gap at the end of the process $\Delta_{r,8}$ is determined in phase 8 ($M_f \rightarrow T_{min}$) by thermoelastic strain calculation.

The flowchart in Figure 4.19 shows the step-by-step iterative process to solve equilibrium, compatibility and boundary conditions defined in Table 4.5 in the non-linear inelastic phases. The boundary conditions are expressed in terms of radial pressure; all systems of equations are solved numerically. An initial value of temperature, contact pressure and transformation radius (interface radius between elastic and inelastic phase) must be given as input. Such values are: $T = T_c, p_i = 0$ and $\bar{r} = r_{i,SMA}$ for the mounting phase (#3), and $T = M_s^\sigma, p_i = p_i(M_s^\sigma)$ and $\bar{r} = r_{e,SMA}$ for the dismounting phase (#6). Moreover, three counters j, k and h are defined and set to zero at the beginning of each phase. The counter j is used to increment the temperature of a quantity equal to $j\Delta T$. Two other parameters, Δp and Δr, related to k and h, respectively, define the step size used for the iterative calculation of the contact pressure and the critical radius (pressure increment= $k\Delta p$; critical radius increment= $h\Delta r$). Different equations and boundary conditions are used depending on the load step. This latter is determined according to the stress-strain state in the system. First, the impeded deformation $|\epsilon_{tr}| - |\epsilon_{free}|$ and the maximum elastic strain $\epsilon_{el,max}$ are calculated at the internal radius of the SMA ring and at each temperature value. If the prevented strain is lower than $\epsilon_{el,max}$ or the transformation radius $\bar{r}$ is equal to the outer radius of the ring, then load steps #1 and #3 occur, respectively. For the non-mixed steps (#1 and #3) the stress/strain values in the entire ring are within a single region (elastic or inelastic), so the related equilibrium and compatibility equations are combined with the boundary conditions to be solved at all temperature steps. Load step #2 occurs when the impeded strain at the inner radius of the ring is higher than the maximum elastic strain and the transformation radius is lower than the outer radius of the ring. For this step, the calculation of the stress/strain state in the ring involves equilibrium and compatibility equations of two regions, elastic and inelastic. In this case, boundary conditions are defined at inner, outer and transformation radii of the ring. The iterative calculation of the transformation radius continues until the difference between the equivalent stress at that radius and the critical start stress is lower than a tolerance value $\delta\sigma$. The iterative calculation of the contact pressure stops when the difference between the total deformation at that pressure and the transformation strain is lower than the tolerance value $\delta\epsilon$.

All relative tolerance values used for the iterative calculations are set to be less than 0.05%.

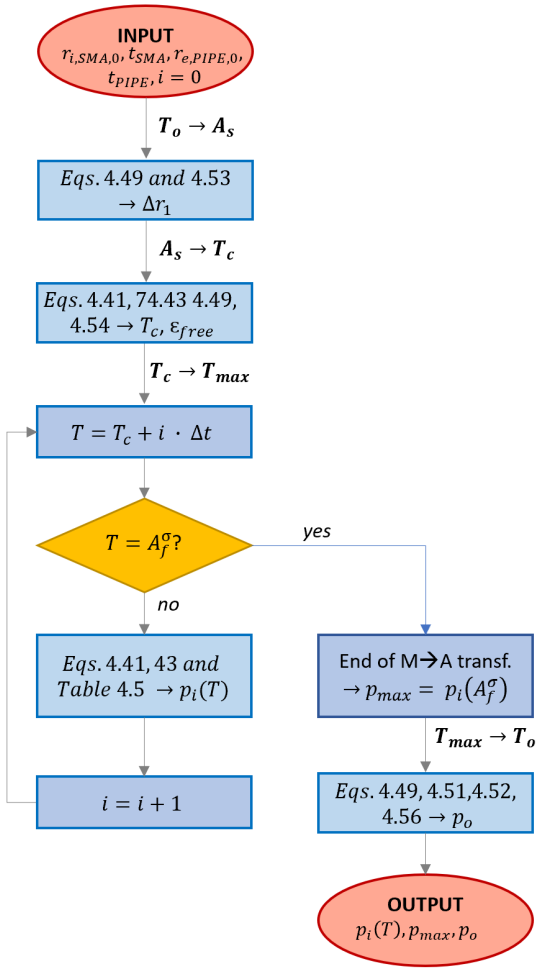

Figure 4.17: Flowchart of the calculation algorithm of the pressure evolution in the mounting phase.

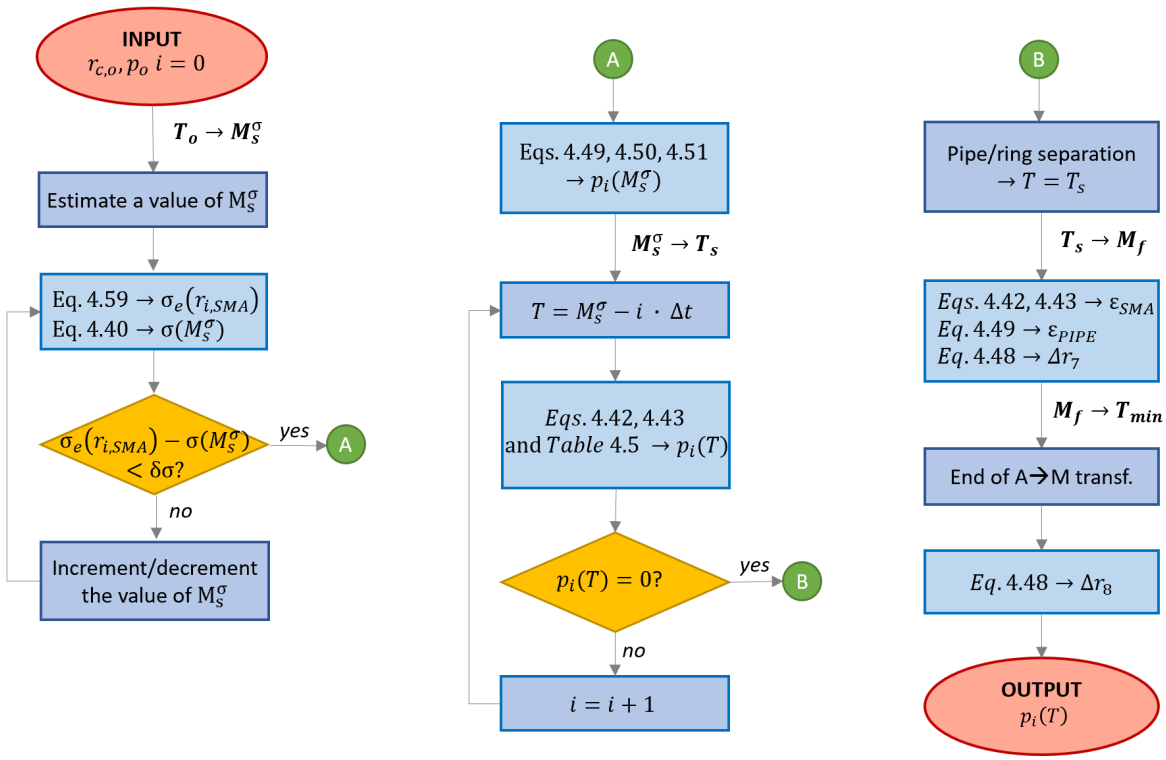

Figure 4.18: Flowchart of the calculation algorithm of the pressure evolution in the dismounting phase.

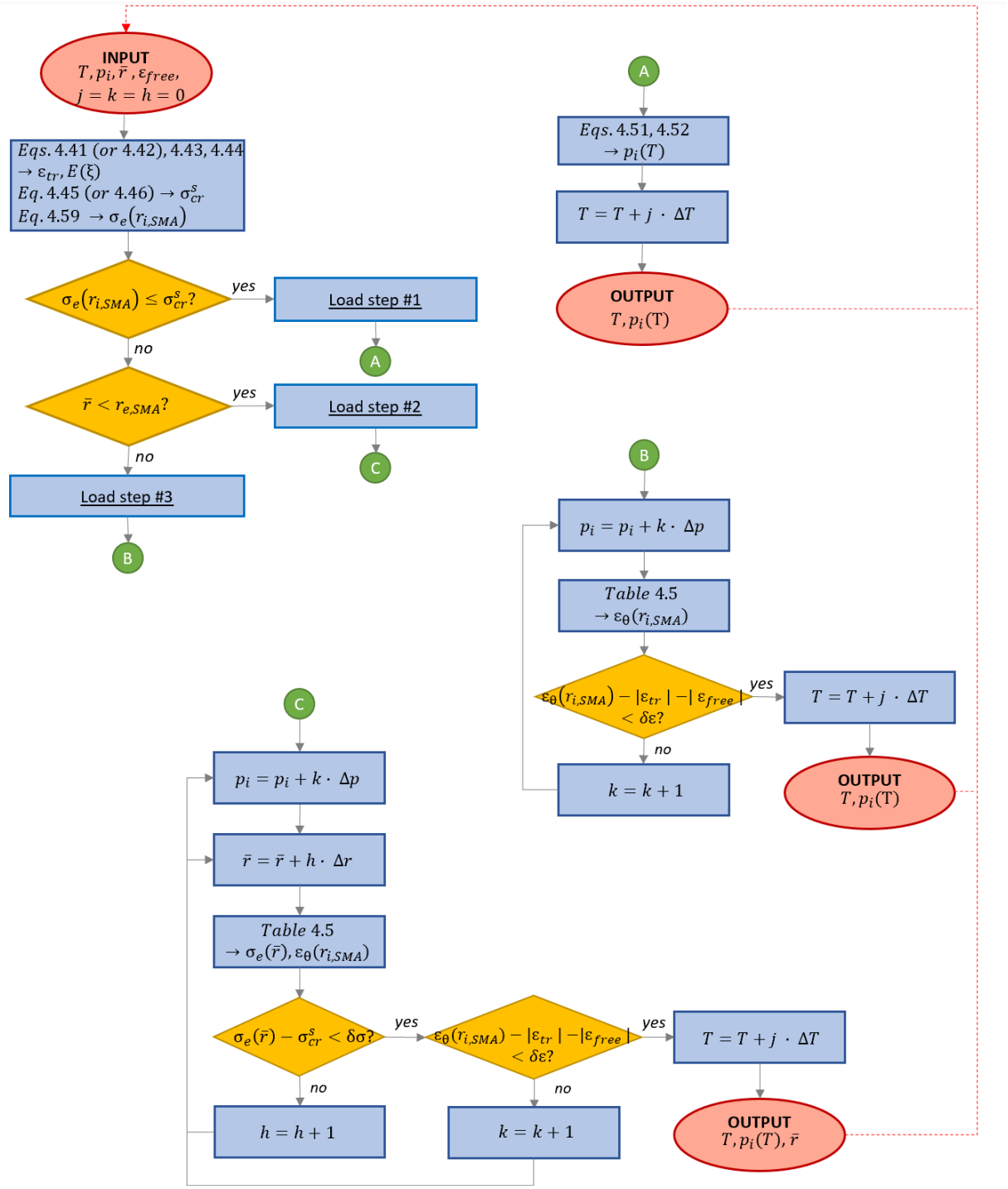

Figure 4.19: Flowchart of the iterative procedure for solving the system of equations in Table 4.5 for the calculation of the transformation pressure p_{tr}.

4.5.7 Model calibration

Uniaxial tests

Experimental tests were performed on Ni50.8Ti49.2 and Ni46.4Ti45.0Nb8.6 dog-bones. In particular, Figure 3.4 shows the thermo-mechanical properties of both NiTi and NiTiNb alloys

obtained from stress-free heating/cooling cycles between TTs. A complete characterization of NiTiNb samples is reported in [6]. Instead, Figure 3.6 illustrates the isothermal true stress-true strain ($\sigma - \epsilon$) response of NiTi alloy at different temperatures, from a completely martensitic to a completely austenitic structure. The figure also shows the yielding stress of the material in both phases as well as the austenite and martensite Young's moduli (E_A, E_M) used for simulations.

Figure 4.20 shows the bilinear stress-strain response implemented in the analytical model. The critical plateau stress, σ^s_{cr}, and the hardening coefficient, H, are computed by applying the OLS (Ordinary Least Squares) method.

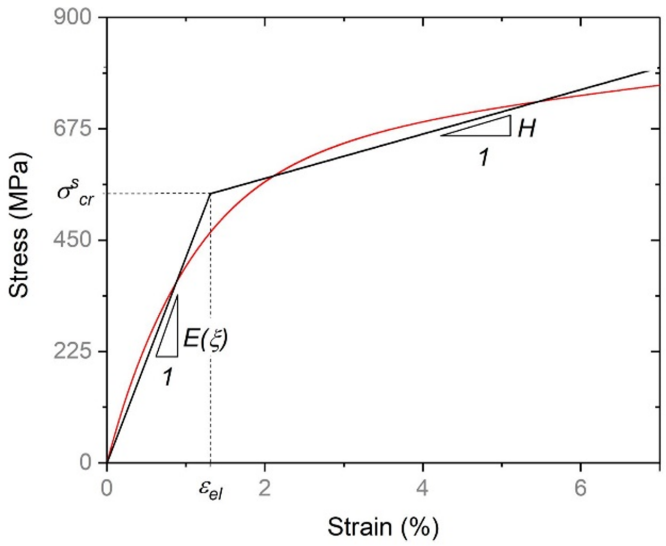

Figure 4.20: (a) Isothermal stress-strain experimental curves of NiTi, and **(b)** bilinear stress-strain curve used for simulations and identification of model parameters

Results from both isothermal and isobaric tests on NiTi samples are reported in Figure 3.5 that shows the stress vs temperature phase diagram of the material. As shown by the figure, σ^s_{cr} increases by increasing temperature from M_s to A^σ_f, but it deviates from Clausius-Clapeyron regime ($\beta_{M\rightarrow A} \neq \beta_{Ms} \approx \beta_{A\rightarrow M}$). Also, σ_y has limited variation with temperatures. A list of the SMA (NiTi and NiTiNb) and steel (316LN and NiCrMo) material parameters used as input for the analytical model is reported in Table 4.6 and 4.7 , respectively. NiTiNb and steel parameters are taken from [7].

Table 4.6: SMA material parameters used for analytical model calibration.

Parameter	NiTi	NiTiNb	Unit
$\mathbf{E_M}$	18.735	15	GPa
$\mathbf{E_A}$	70	64	GPa
$\sigma_\mathbf{y}$	482	600	MPa
$\mathbf{H}$	1000	1000	MPa
$\boldsymbol{\nu}$	0.3	0.3	/
$\boldsymbol{\beta}$	6	5.5	MPa
$\epsilon_{\mathbf{OW}}$	5	5.6	%
$\boldsymbol{\alpha_M}$	$0.7 \cdot 10^{-5}$	$1.1 \cdot 10^{-5}$	$°C^{-1}$
$\boldsymbol{\alpha_A}$	$0.7 \cdot 10^{-5}$	$1.1 \cdot 10^{-5}$	$°C^{-1}$
$\mathbf{M_f}$	-66	-143	$°C$
$\mathbf{M_s}$	-50	-105	$°C$
$\mathbf{A_s}$	41	38	$°C$
$\mathbf{A_f}$	50	75	$°C$
$\boldsymbol{\beta_{M\rightarrow A}}$	1.74	0.21	$MPa \cdot °C^{-1}$
$\boldsymbol{\beta_{A\rightarrow M}}$	3.46	2	$MPa \cdot °C^{-1}$

Table 4.7: Steel material parameters used for analytical model calibration.

Parameter	316LN	NiCrMo	Unit
$\mathbf{E}$	205	210	GPa
$\boldsymbol{\mu}$	0.3	0.3	/
$\boldsymbol{\alpha}$	$1.7 \cdot 10^{-5}$	$1.2 \cdot 10^{-5}$	$°C^{-1}$

4.5.8 Case studies

This section provides the results obtained from the proposed analytical model in comparison with experimental data and FE simulations. In particular, the results obtained from NiTi/316LN and NiTiNb/NiCrMo couplings are here presented and discussed. Different configurations, in terms of geometry and materials, were analyzed by FE simulations and analytical calculation as well as experimental measurements. They are reported in Table 4.8.

Table 4.8: SMA ring and pipe geometry.

Case study #	**SMA material**	**Pipe material**	**Initial SMA ring radius, $r_{i,SMA,0}$ [mm]**	**SMA ring thickness, t_{SMA} [mm]**	**Pipe thickness, t_{PIPE} [mm]**	**Initial radial gap, $\Delta_r 0$ [mm]**
1	NiTi	316LN	22.5	5	10.15	0.75
2	NiTi	316LN	22.5	3	13	0.075
3	NiTi	316LN	22.5	5	13	0.075
4	NiTi	316LN	22.5	8	13	0.075
5	NiTiNb	NiCrMo	22.75	8.2	13	0.075
6	NiTiNb	NiCrMo	22.75	8.2	13	0.425
7	NiTiNb	NiCrMo	22.75	8.2	13	0.8

4.5.9 SMA ring constrained recovery experiments

Constrained recovery tests were performed on SMA/Steel ring assembly systems. The associated pressure-temperature curve was obtained from experimental circumferential and radial strains, ϵ_z and ϵ_θ, respectively, by applying the theory of elasticity for axisymmetric bodies. The experimental procedure is discussed in 3.3.2. The results of configuration #1 reported in 3.3.2. The experimental data for the other configurations are taken from the literature, specifically referring to [106] for configurations #$2, 3, 4$ and to [6] for configurations #$5, 6, 7$.

4.5.10 Finite Element simulations

Finite Element simulations of configurations #$1, 2, 3, 4$ were carried out in a commercial software (ANSYS ®) to reproduce the constrained recovery behavior of the NiTi rings mounted on elastic steel rings. Their thermo-mechanical behavior is described by a recently developed SMA model [9] which was implemented in ANSYS as a User Programmable Feature (UPF). A user-defined material subroutine (USERMAT) was written in Fortran to be linked to the FE software. Such a model for SMA material is able to simulate both OW- and TW-SME effects allowing the modeling of the entire assembly/disassembly processes. The model was calibrated with respect to the experimental data obtained from dog-bone samples, as explained in section 5.3. The input parameters to the USERMAT are reported in Table 5.3 in Chapter 5. The system was modeled in a 3-D space to allow the use of the USERMAT, based on a 3-D formulation [9]. Simulation setting and results are reported in sections 5.6.1 and 5.6.1.

Finite Element simulations of configurations #5, 6, 7 are taken from literature [6].

4.5.11 Results and discussions

NiTi/316LN ring coupling

The contact pressure evolution as a function of the temperature obtained by the analytical computation, numerical simulation and experimental test are reported in Figure 4.21. Results refer to configuration #1 in Table 4.8.

As expected, a marked increase of the contact pressure (experimental curve) is observed when increasing the temperature between $T_c \approx 60°C$ to $A_f^\sigma \approx 130°C$. At A_f^σ, most of the ring volume becomes fully austenitic, i.e. without thermally induced or stress induced martensitic variants. An almost linear trend of the pressure is observed when cooling the ring from the maximum temperature up to the martensite start temperature under stress ($M_s^\sigma \approx 0°C$). This is attributed to the following factors: the mismatch between the thermal expansion coefficients of the two materials, the SMA Young's modulus variation with temperature [125] and the presence of possible residual martensitic variants [126]. A marked drop is induced by further cooling and is related to the thermally induced austenite to martensite transition. The different stages of the process are also visible in both the FE and the analytical models. The graph shows a very good agreement between the three curves, proving the potential and the accuracy of the analytical model. A percentage error between the analytical prediction compared to the numerical or experimental data can be defined as reported below:

$$\%e = \left| \frac{p_{f,AN} - p_{f,EXP,FEM}}{p_{f,EXP,FEM}} \times 100 \right| \tag{4.59}$$

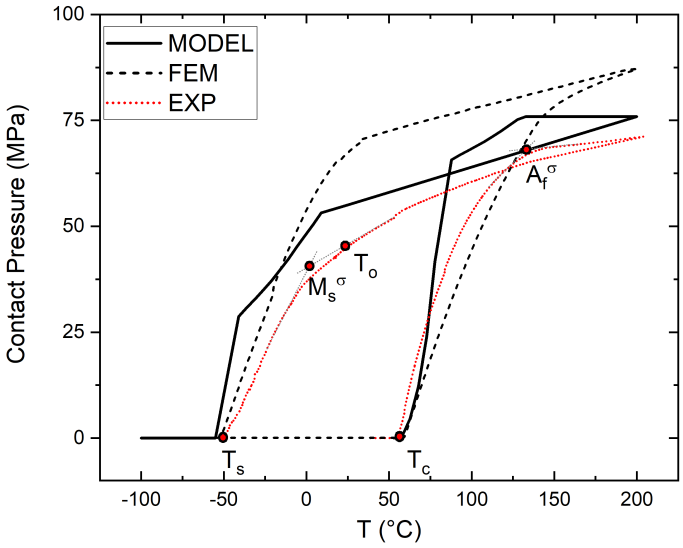

Figure 4.21: Evolution of contact pressure as a function of the temperature during the coupling-uncoupling process of a NiTi-316LN coupler (configuration #1 in Table 4.8).

An absolute error of about 18% was calculated between analytical and numerical models at $T_o = 25\ °C$ while an error lower than 18% is recorded in comparison with the experimental curve. Figure 4.22 shows the analytical prediction and FEM simulation solution of the radial stress distribution as a function of the normalized radius of the SMA ring at $T_o = 25$. As expected, the radial stress at the inner radius of the SMA ring corresponds to the contact pressure and decreases by increasing radius up to the external surface, where the radial stress is zero. The mismatch in trend and values between the two solutions is mainly attributed to the residual stress distribution occurring after the predeformation phase, which is not taken into account in the analytical model.

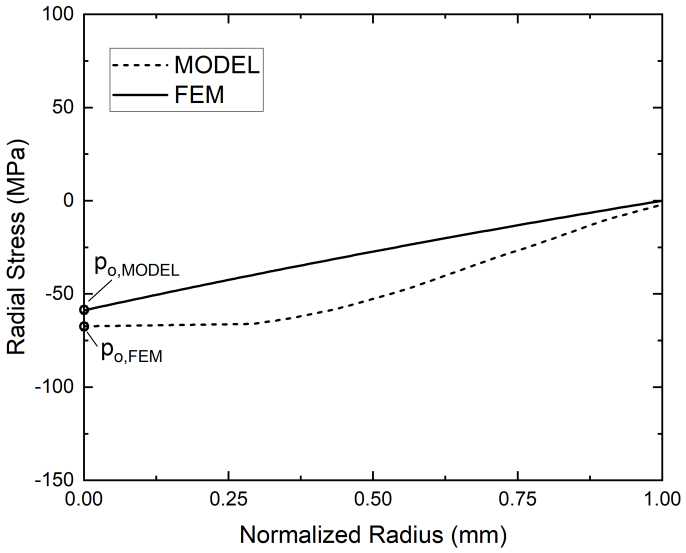

Figure 4.22: Radial stress distribution as a function of the SMA ring normalized radius (configuration #1 in Table 4.8) obtained at $T_o = 25\ °C$ from FEM simulation and analytical model calculation.

NiTiNb/ NiCrMo ring coupling

Figure 4.23 shows contact pressure versus temperature curves obtained from the analytical modeling and experimental tests of a NiTiNb/NiCrMo ring coupling (configuration #5 in Table 4.8). Again, the graph shows a very good match between analytical and experimental data with an absolute error of about 17% at $T_o = 25\ °C$. In this case, the change in slope of the curve during cooling due to the two different regions (thermal and thermal + recovery) is more evident in the experimental curve. The reason for this is that NiTiNb has a higher hysteresis, which allows the two phenomena to be better differentiated.

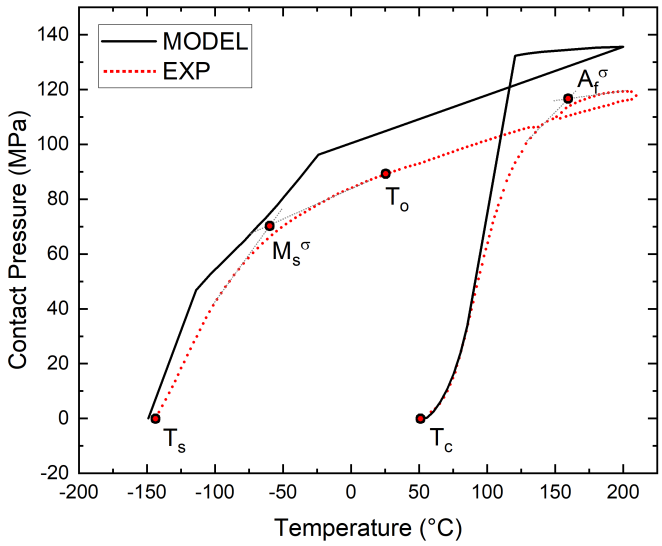

Figure 4.23: Evolution of contact pressure as a function of the temperature during the coupling-uncoupling process of a NiTiNb-NiCrMo coupler (configuration #5 in Table 4.8).

Effect of the thickness of the SMA ring

The variation of the SMA ring's thickness is investigated by testing three different geometries of a NiTi–316LN coupling system (case studies #2, 3, 4 in Table 4.8). The results of analytical calculations, FE simulations and experimental measurements at $T_o = 25\,°C$ are reported in Table 4.9 with respective absolute errors. Results show that the maximum contact pressure increases with increasing SMA ring thickness. A maximum error of 11.5 % (analytical-experimental) is estimated for the maximum value of thickness (configuration #4).

Table 4.9: Contact pressure at the operating temperature ($T_o = 25°C$) obtained by analytical calculation, FE simulation and experimental measurement for NiTi/316LN coupling system at different values of SMA ring thickness.

Case study #	**Analytical contact pressure, $p_{o,AN}$ [MPa]**	**FEM contact pressure, $p_{o,FEM}$ [MPa]**	**Experimental contact pressure, $p_{o,EXP}$ [MPa]**	**Error analytical-FEM, E_{AN-FEM} [%]**	**Error analytical-experimental, E_{AN-EXP} [%]**
2	38.3	65.6	36	41.6	0.64
3	58.2	108.6	53	46.4	1.73
4	81.9	159.6	68	48.7	20.4

Effect of the initial gap

The variation of the initial gap between the SMA ring and the pipe is also evaluated by testing three different geometries of a NiTiNb–NiCrMo coupling system (#$5, 6, 7$ in Table 4.8). The results of analytical calculations, FE simulations and experimental measurements are reported in Table 4.10 with the respective errors. Results show that the maximum contact pressure decreases with increasing initial radial gap. Also, a maximum error of 17% (analytical-experimental) is registered at the maximum value of the gap.

Table 4.10: Contact pressure at the operating temperature ($T_o = 25°C$) obtained by analytical calculation, FE simulation and experimental measurement for NiTiNb/NiCrMo coupling system at different values of initial radial gap.

Case study #	**Analytical contact pressure, $p_{o,AN}$ [MPa]**	**FEM contact pressure, $p_{o,FEM}$ [MPa]**	**Experimental contact pressure, $p_{o,EXP}$ [MPa]**	**Error analytical-FEM, E_{AN-FEM} [%]**	**Error analytical-experimental, E_{AN-EXP} [%]**
5	104	84	89	23.8	17
6	95	82	84	15.9	10
7	85	72	75	18.1	13

4.6 Chapter summary

Two analytical models, based on elastic-plastic theory of axisymmetric geometries, were developed to simulate martensite reorientation/stress-induced transformation mechanisms and constrained-recovery properties of shape memory alloy (SMA) rings. The first model was used to calculate the stress and strain distributions in pre-strained martensitic rings. Different load cases were investigated ranging from a completely elastic condition to plastic deformation of fully reoriented martensite. This model is particularly useful to predict the pressure of expansion and the final size of SMA couplers as a function of the initial ring geometry and the main pre-deformation parameters. Results revealed that the internal pressure needed to induce a certain circumferential pre-deformation (ϵ_{ti}) increases less than linearly by increasing the SMA thickness to internal diameter ratio (t/ID_0). Systematic comparison of the model predictions, in terms of stress and deformation, with finite element analyses based on multilinear hardening material models and with experimental measurements showed a very good agreement. The sec-

ond model was used to calculate the contact pressure evolution during constrained recovery of the SMA ring, during both heating (contraction) and cooling (relaxation) stages. The process involves different load steps, from elastic to completely inelastic deformations. Results revealed that the contact pressure p_i increases by increasing the SMA thickness and reducing the initial gap between the SMA and the internal ring. Systematic comparison of the model predictions, in terms of contact pressure evolution, with finite element analyses based on a user-defined material model and with experimental measurements showed a very good agreement. The proposed models represent a robust design tool for SMA rings with shape recovery capabilities.

Chapter 5

SMA constitutive modeling and FE simulations

5.1 Abstract

The present chapter deals with the numerical modeling of the shape memory alloys. In particular, the first part provides an overview of the SMA constitutive models already available in three of the main commercial FE software, such as ANSYS, COMSOL and ABAQUS. The limitations of these models with respect to the constrained recovery application are presented. In the second part of the chapter, a user-defined material model for SMA simulations, with the additional features of pseudoelasticity and TW-SME, is presented as a solution to improve the accuracy of the FE simulation results of different shapes of couplers for pipe/chamber connection. The results of three-dimensional mechanical simulations of the coupling process performed by ring, oval and C-shaped connectors are presented and discussed. Some of the FEM results are compared with experimental data presented in Chapter 3 to further validate the model and demonstrate the high accuracy of the solution.

5.2 SMA constitutive models in commercial FE codes

Numerical modeling of Shape Memory Alloys (SMAs) plays a crucial role in understanding and predicting the behavior of these materials, which is governed by phase transformation phenomena and non-linear hysteretic constitutive equations. In general, SMAs exhibit Shape Memory Effect (SME) and Superelastic Effect (SE), which allow them to undergo significant recoverable deformations by mechanical or thermal input. Furthermore, the material microstructure depends on the stress-deformation-temperature state, so the number of variables and constants

involved in the process is significantly higher than for traditional materials. This makes it particularly difficult to develop a constitutive model capable of accurately simulating the response of SMA under a wide range of loading and environmental conditions.

Numerical models for SMAs typically involve the coupling of structural mechanics with thermodynamics and phase transformation kinetics, taking into account the unique properties of the material, such as shape memory effect, superelasticity, and temperature-dependent properties. Several constitutive models for SMAs have been developed over the years and are now available in commercial software. In particular, ANSYS, COMSOL, and ABAQUS are considered in the following analysis. All three provide material models to simulate the behavior of shape memory alloys.

The formulation of the constitutive equations in the SMA numerical models is typically based on the definition and calculation of the free energy of the system. In particular, in 1996 *Lagoudas* [127] proposed a model based on the Gibbs free energy G, where the calculation of the stress-strain behavior of the SMA occurs under stress control. The Gibbs energy is a function of the temperature, T, equivalent stress, σ_e, and thermodynamic force, ζ, which governs the phase transformation phenomena ($\zeta\xi \geq 0$) [127]. The material constitutive equations are obtained by the partial derivatives of the Gibbs free energy as a function of the three variables:

- Entropy, $s = \partial_T(-G)$
- Strain, $\epsilon = \partial_\sigma(-G)$
- Transformation strain, $\epsilon_{tr} = \partial_\zeta(-G)$

The *Souza-Auricchio* model is based on the definition of the Helmholtz-free energy Φ and the numerical models are solved under strain control. In this case, the energy formulation involves the following variables, temperature, T; Equivalent strain, and ϵ_{tr}, Transformation strain, ξ [128, 129]. The constitutive equations are obtained by the partial derivatives of the Helmholtz free energy as a function of the three variables:

- Entropy, $s = \partial_T(\Phi)$
- Stress, $\sigma = \partial_\epsilon(\Phi)$

- Thermodynamic force, $\zeta = \partial_{\xi}(\Phi)$

ANSYS has two models: *Superelasticity* and *Shape Memory Effect*. Both models are based on the Souza-Auricchio formulation and use Helmholtz free energy to compute the material constitutive equations. The difference between the two models lies in the phenomena they describe. The *Superelasticity* is used to simulate the stress-induced martensitic transformations. In this case, the elastic moduli of martensite and austenite are assumed to be the same, but different stress-strain slopes during transformations (direct A→M transformation during loading, reverse M→A transformation during unloading) are allowed. A different material behavior under tension or compression loading conditions is allowed, but both tension and compression responses are scaled by stress only. This model simulates only the pseudoelastic effect. The *Shape Memory Effect* model supports different elastic moduli for martensite and austenite structures. The stress-strain slopes are assumed to be the same for both M→A and A→M transformations. The model is not able to simulate very large differences between tension and compression responses (usually not an issue for NiTi alloys). The model can simulate both pseudoelastic and one-way shape memory effects.

COMSOL has two models: *Lagoudas* and *Souza-Auricchio*. In this case, the difference between the two is based on the mathematical formulation and, consequently, the parameters used as input. In both cases, additional internal variables are used to calculate the transformation strain tensor and the martensite volume fraction. Specifically, the *Lagoudas* model uses the Gibbs free energy formulation and involves eight parameters [130]. The *Souza-Auricchio* model, based on the Helmholtz energy definition, uses six input constants and internal variables as input [128, 131]. Both models can be used to model pseudo-elastic and one-way shape memory effects.

ABAQUS has only one model in the library to simulate SMA behavior and, in particular, the pseudoelasticity. Such model is named *Superelasticity* and is based on Helmholtz free energy formulation [132].

5.3 A special user-defined material model

Most of the SMA applications deal with the constrained-recovery process, such as the SMA-based pipe/chamber coupling in the LHC accelerator, which is the subject of the present study. An in-depth investigation of the constrained-recovery application with related transformation phenomena revealed that the material models already available in commercial FE software cannot be used to simulate the entire coupling process within an acceptable error range of the solution. In particular, all the models presented above with reference to ANSYS, COMSOL and ABAQUS simulate the elastic deformations of the SMA and the transformation phenomena related to superelasticity and one-way shape memory effect. However, plasticity and two-way shape memory effect play a fundamental role in the coupling process. First, the SMA device must be trained before it is used as a coupler. The training involves severe pre-deformation of the material in the martensitic state up to plastic deformations, which are the main responsible for the final geometry of the SMA device to be implemented as a coupler. The SMA is then subjected to a heating/cooling cycle to perform both assembly and disassembly of the system by OW- and TW-SME. The last feature is not implemented in the available SMA models, which does not allow, therefore, simulation of the cooling-dismounting phase.

In 2019, a three-dimensional phenomenological model has been developed by Scalet et al. [9] to be used for FE simulations. This new formulation is based on the Helmholtz free energy definition and introduces the two important features of plasticity and TW-SME. In the following sections, a brief summary of the model formulation and its implementation in ANSYS are reported.

The newly developed model allows for the simulation of pseudoelasticity, one-way and two-way SMEs, transformation temperatures' evolution, thermal hysteresis, phase transformations at low stresses, thermal strains and phase-dependent elastic properties. The ability to simulate the plasticity and the TW-SME as a plus, makes this model an important tool for the design of the SMA connectors developed at CERN for the assembly/disassembly of systems for ultra-high vacuum (UHV) applications.

5.3.1 General formulation

The special model [9] is based on the Helmholtz free energy definition and is calibrated to the uniaxial stress-strain response of the material. Stress and strain are 3x3 symmetric tensors, so the model can be applied to three-dimensional simulations. Both isothermal and temperature-dependent processes can be simulated.

The kinematics of the model involves the decomposition of the total strain into four well-defined contributions: thermal, elastic, transformation, and plastic strain, as reported below:

$$\boldsymbol{\epsilon} = \boldsymbol{\epsilon_{th}} + \boldsymbol{\epsilon_{el}} + \mathbf{e_{tr}} + \mathbf{e_{pl}} \tag{5.1}$$

where $\boldsymbol{\epsilon_{el}}$ is the *elastic strain*, and $\boldsymbol{\epsilon_{th}}$ is the *thermal strain* due to temperature variation; it is strictly related to the thermal properties of the material, such as the coefficient of thermal expansion, α. The *transformation strain* (deviatoric component) $\mathbf{e_{tr}}$ is related to martensitic transformations in both stress and temperature induced phenomena. In this case, the deformation is reversible by inducing the opposite phase transformation. For example, in pseudoelasticity, the transformation strain induced in the direct A→M transformation is recovered during the opposite M→A transition. Finally, the *plastic strain* (deviatoric component) $\mathbf{e_{pl}}$ is the permanent deformation of the material.

The Helmholtz free energy is defined as a function of four variables: the total strain, the temperature, the transformation and the plastic strain components, $\Phi = \Phi(\boldsymbol{\epsilon}, T, \mathbf{e_{tr}}, \mathbf{e_{pl}})$, as follows:

$$\begin{aligned}\Phi = &\frac{1}{2}K\Theta^2 + G||\mathbf{e} - \mathbf{e_{tr}} - \mathbf{e_{pl}}||^2 - 3\alpha K\Theta(T - T_0) + \tau_M||\mathbf{e_{tr}}|| + \\ &+ \frac{1}{2}h_{tr}{\mathbf{e_{tr}}}^2 + \frac{1}{2}h_p{\mathbf{e_{pl}}}^2 - B\mathbf{e_{tr}} : \mathbf{e_{pl}} + I_{\epsilon_L}(\mathbf{e_{tr}})\end{aligned} \tag{5.2}$$

where Θ and $\boldsymbol{e}$ are the volumetric and deviatoric strain, respectively; K and $G = G(e_{tr})$ are the bulk and shear modulus, respectively; $\tau_M = \beta < T - T^* >$, where $\beta > 0$ defines the dependence of the critical stress on temperature, T^* is the reference temperature, and $< . >$ takes the positive part of the function; h_{tr} and h_p are the linear transformation and plastic hardening, respectively; $B > 0$ is a coupling parameters between transformation and plastic strains; finally, $I_{\epsilon_L}(\boldsymbol{e_{tr}})$ is an indicator function that satisfies the following constraint:

$$I_{\epsilon_L}(\mathbf{e^{tr}}) = \begin{cases} 0, & \text{if } ||\mathbf{e_{tr}}|| \leq \epsilon_L \\ +\infty, & \text{if } otherwise \end{cases} \tag{5.3}$$

The constitutive stress-strain equations are determined by differentiating the Helmholtz energy with respect to the total strain ϵ to obtain the hydrostatic (P) and deviatoric (S) stress components, as follows:

$$P = \frac{\partial \Phi}{\partial \Theta} = K\Theta - 3\alpha K(T - T_0) \tag{5.4}$$

$$\mathbf{S} = \frac{\partial \Phi}{\partial \mathbf{e}} = 2G(\mathbf{e} - \mathbf{e_{tr}} - \mathbf{e_{pl}}) \tag{5.5}$$

The thermodynamic forces **X** and **Y** are calculated by differentiating the Helmholtz energy by $\mathbf{e_{tr}}$ and $\mathbf{e_{pl}}$, respectively. The thermodynamic forces allow the definition of the transformation and plastic strain rate, by:

$$\dot{\mathbf{e}}_{\mathbf{tr}} = \dot{\xi}\frac{\mathbf{X}}{||\mathbf{X}||} \tag{5.6}$$

$$\dot{\mathbf{e}}_{\mathbf{pl}} = \dot{\mu}\frac{Y}{||\mathbf{Y}||} \tag{5.7}$$

where $\dot{\xi}$ and $\dot{\mu}$ are positive consistency parameters.

5.3.2 Model parameters

The SMA model requires some constant and variable parameters as input. They include mechanical, thermal, and functional properties of the SMA. Figure 5.1 shows a schematic representation of the stress-strain response of the material used to calibrate the model. Some of the parameters are also shown in the figure.

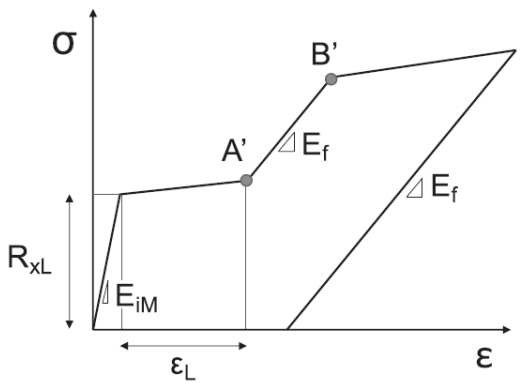

Figure 5.1: Schematic representation of stress-strain response of the SMA and model parameters in case of a stress-induced transformation in the fully martensitic state at $T < T^* - \Delta R/\beta$, from [9].

A complete list of the material model parameters are given in Table 5.1.

Table 5.1: Input material properties.

Input material properties	
1.	$\mathbf{E_A}$, austenite Young's modulus
2.	$\mathbf{E_{i,M}}$, martensite initial Young's modulus
3.	$\mathbf{E_f}$, martensite finish Young's modulus
4.	ν, Poisson's coefficient
5.	$\mathbf{h_{tr}}$, transformation hardening
6.	$\mathbf{h_p}$, plastic hardening
7.	ϵ_L, maximum transformation strain
8.	α, thermal expansion coefficient
9.	$\mathbf{T_0}$, initial temperature
10.	$\mathbf{T}^*$, transformation temperature
11.	β, temperature coefficient
12.	$\mathbf{R_{XH}}$, critical transformation stress (high)
13.	$\mathbf{R_{XL}}$, critical transformation stress (low)
14.	$\mathbf{R_Y}$, plastic stress
15.	$\mathbf{T}$, current temperature
16.	$\mathbf{B}$, transformation-plastic coupling parameter

The elastic domain, $\mathbf{R_{XH}}$ and $\mathbf{R_{XL}}$, and the initial Young's modulus of martensite, $\mathbf{E_{i,M}}$, are defined according to the initial conditions and the process to be simulated. Figure 5.2 shows the definition of both parameters as a function of temperature.

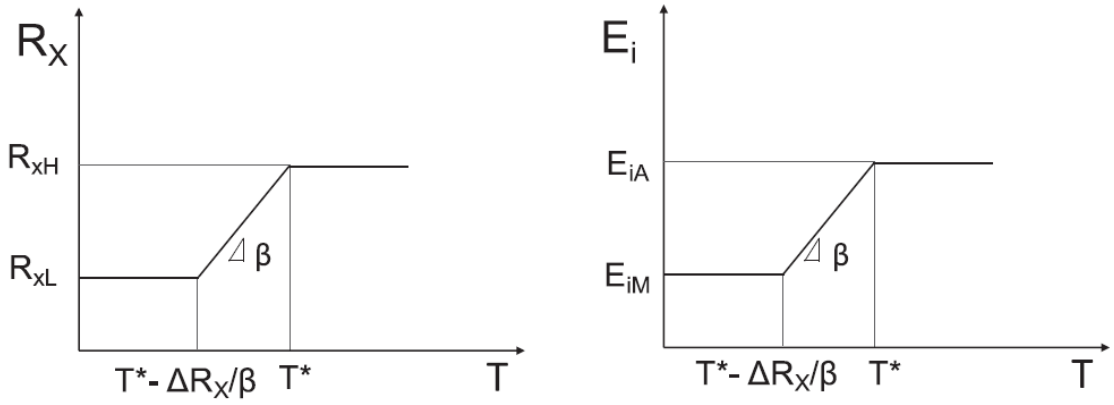

Figure 5.2: Temperature dependence fort the elastic domain radius $\mathbf{R_X}$ and the initial Young's modulus of martensite $\mathbf{E_i}$, from [9].

The model formulation includes the definition of state variables, which are internal variables

for the constitutive equations. They are the transformation and plastic strain components along the three Cartesian directions (1=x, 2=y, 3=z), the norm of the two tensors and the coefficients involved in the numerical computation. All state variables are listed in Table 5.2.

Table 5.2: Input state variables.

	Input state variables
1.	$\boldsymbol{\epsilon_{tr,11}}$, transformation strain xx component
2.	$\boldsymbol{\epsilon_{tr,22}}$, transformation strain yy component
3.	$\boldsymbol{\epsilon_{tr,33}}$, transformation strain zz component
4.	$\boldsymbol{\epsilon_{tr,12}}$, transformation strain xy component
5.	$\boldsymbol{\epsilon_{tr,23}}$, transformation strain yz component
6.	$\boldsymbol{\epsilon_{tr,13}}$, transformation strain xz component
7.	$\boldsymbol{\lambda_{tr}} > 0$, evolution coefficient for transformation deformations
8.	$\boldsymbol{\epsilon_{p,11}}$, plastic strain xx component
9.	$\boldsymbol{\epsilon_{p,22}}$, plastic strain yy component
10.	$\boldsymbol{\epsilon_{p,33}}$, plastic strain zz component
11.	$\boldsymbol{\epsilon_{p,12}}$, plastic strain xy component
12.	$\boldsymbol{\epsilon_{p,23}}$, plastic strain yz component
13.	$\boldsymbol{\epsilon_{p,13}}$, plastic strain xz component
14.	$\boldsymbol{\lambda_{p}} > 0$, evolution coefficient for plastic deformations
15.	$\boldsymbol{\gamma}$, saturation coefficient
16.	$\|\|\boldsymbol{\epsilon_{tr}}\|\|$, norm of the transformation strain tensor
17.	$\|\|\boldsymbol{\epsilon_{p}}\|\|$, norm of the plastic strain tensor

5.3.3 Implementation in ANSYS

The material model was implemented in the ANSYS V.222 Finite Element Analysis (FEA) software as a User Programmable Feature (UPF). The material model was written in Fortran77 code, compiled against the Intel Fortran compiler V.2022.2 and linked into a custom ANSYS executable via Microsoft Visual Studio 2019 Professional.

5.4 Benchmark simulations

The results of benchmark simulations are presented in this section. The purpose is to evaluate the performance of the subroutine and to demonstrate the correct operation of the code, especially in the additional features of plasticity and two-way shape memory effect. In particu-

lar, the thermomechanical training and thermal activation cycle (heating and cooling) processes are simulated with respect to the real preparation and operation phases that an SMA coupler is subjected to. The same FE model is used to make a comparison between the results of SMA USERMAT, implemented by an external code, and the built-in Shape Memory Effect (SME) model, already available in the ANSYS material library, as explained in paragraph 5.2.

5.4.1 Model setup and parameter values

The FE simulations are performed in ANSYS on a single element (SOLID186) NiTi cube ($1mm$ x $1mm$ x $1mm$). The cube is constrained by a frictionless support (normal displacement prevented) applied to one face with one of the four vertices fixed. A uniform body temperature is applied to the cube during training (T=const) and thermal cycling simulations.

The input parameters used in the FEA are given in Table 5.3.

Table 5.3: NiTi mechanical and functional properties used in the FE simulations.

Parameter	**Value**	**Unit**
Austenite Young's modulus, E_A	70'000	MPa
Martensite (twinned) Young's modulus, $E_{i,M}$	30'000	MPa
Martensite (detwinned) Young's modulus, E_f	18'735	MPa
Transformation hardening, h_{tr}	1000	MPa
Plastic hardening, h_p	735	MPa
Transformation strain, ϵ_{tr}	0.05	mm/mm
Elastic domain radius (at high T), R_{XH}	326.6	MPa
Elastic domain radius (at low T), R_{XL}	90	MPa
Inelastic domain radius, R_Y	482	MPa
Transformation-plastic coupling parameter, B	1200	MPa
Thermal expansion coefficient, α	7e-6	1/°C
Temperature coefficient, β	6	MPa/°C

5.4.2 Martensitic pre-deformation

The *thermomechanical training* FEM simulates the experimental conditions. In particular, a temperature of $T = -80°C$ is applied to the cube to have a fully martensitic structure. The pre-deformation is given by applying a normal displacement of $v_{max} = 0.16mm$ to one of the free faces of the cube. In the second step, the elastic unloading to zero stress is simulated. Loading and boundary conditions are shown in Figure 5.3.

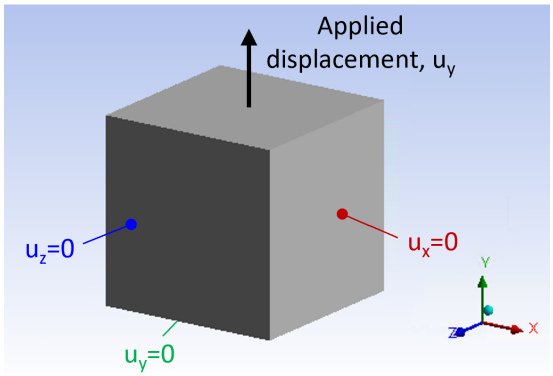

Figure 5.3: SMA single element cube: finite element discretization boundary conditions.

Figure 5.4 shows the countour plot of the displacement in the y-direction at loading (Figure 5.4a) and at unloading (Figure 5.4b). The displacement evolves consistently with the boundary and loading conditions, reaching its maximum value of $0.16mm$ during loading. After unloading, the maximum displacement is still $\approx$ 80% of that applied. This is due to inelastic deformations (transformation and plastic) developed in the cube and not recovered after simple mechanical unloading.

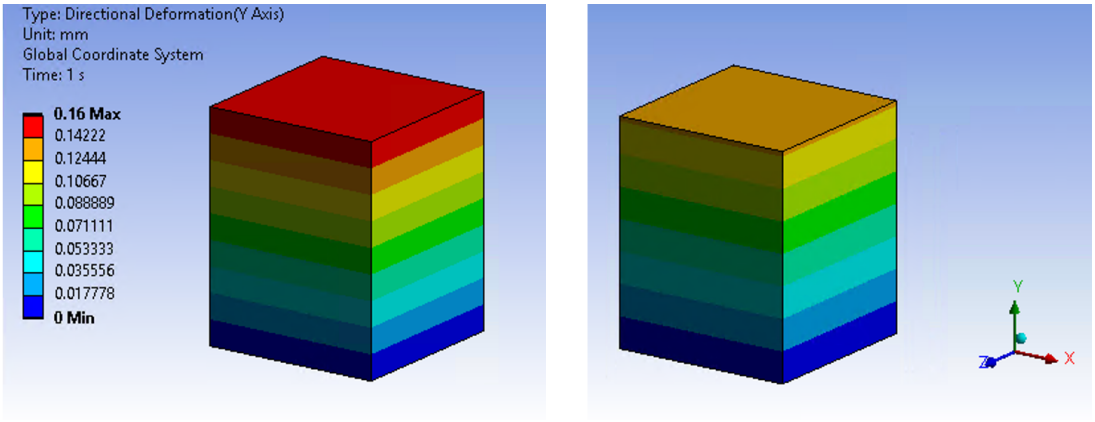

(a) (b)

Figure 5.4: FE numerical simulation results of mechanical pre-deformation of a unitary cube obtained by USERMAT: **(a)** Contour plot of the displacement in y-direction (in mm) at loading, $v_{max} = 0.16mm$, and **(b)** Contour plot of the displacement in y-direction (in mm) at unloading.

The stress-strain curve obtained by USERMAT FE simulations is compared with the built-in SME model and the experimental data (see section 3.2.1) in the graph in Figure 5.5. The simulated stress-strain curve by USERMAT is in good agreement with experimental data. In particular, it exhibits four distinct regions: twinned martensite elasticity, transformation plateau, detwinned martensite elasticity, plasticity. The ability to simulate plastic deformations is of paramount importance, since they have a great influence on the final geometry of the SMA coupler, which is responsible for the connection of pipes/chambers with predefined dimensions, and on the residual stresses and strains, which causes TW-SME. This is highlighted especially in the comparison with the SME model curve, which exhibits only three regions: twinned martensite elasticity, transformation phase, and detwinned martensite elasticity. However, at high values of pre-strain, $\epsilon_{max} > 8\%$, the effect of plasticity on the stress-strain state of the material is significant, and the built-in SME model is unable to represent the real case, as the solution diverges dramatically from the experimental data. As a result, the final deformation of the SMA is greatly underestimated by the SME model.

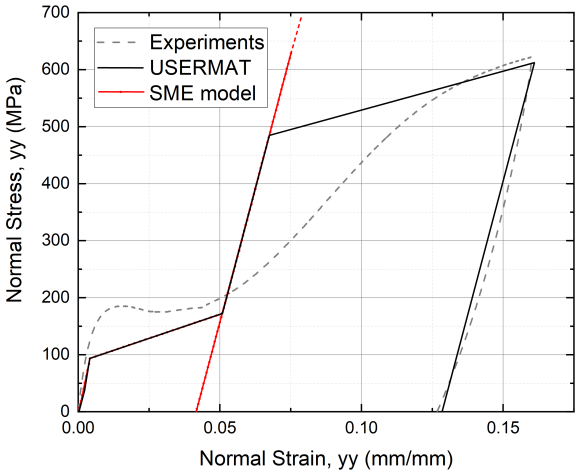

Figure 5.5: Stress-strain response of the NiTi alloy to the pre-deformation process by USERMAT, SME model and experimental tests.

The USERMAT calculates the total strain tensor as the sum of four components: thermal, elastic, transformation and plastic. During the training process, the thermal strain is zero because the temperature is kept constant, so the total strain is the sum of the elastic, transformation and plastic strains. Figures 5.6 and 5.7 show the evolution of the norm of the transformation and plastic strain tensors and of the equivalent total strain, respectively, during the training process. The evolution of the transformation and plastic strain tensors shown in Figure 5.6 describes well the transformation phenomena that take place during mechanical training. At the very beginning of the process, both transformation and plastic deformations are zero because only elastic deformations occur until the value of the elastic limit is exceeded, as shown by the zoom reported on the graph. Then the transition from twinned to detwinned martensite takes place, as shown by the stress-strain curve in Figure 5.5, and the associated transformation strain develops and saturates once the phase transition is complete. The elastic deformation of the detwinned martensite then occurs until the yield stress is exceeded. At this point, plastic deformation develops until the end of the loading phase. During unloading, as expected, the transformation and plastic strain are not recovered. Only the elastic deformations are reversible, as shown by the total deformation evolution graph in Figure 5.7.

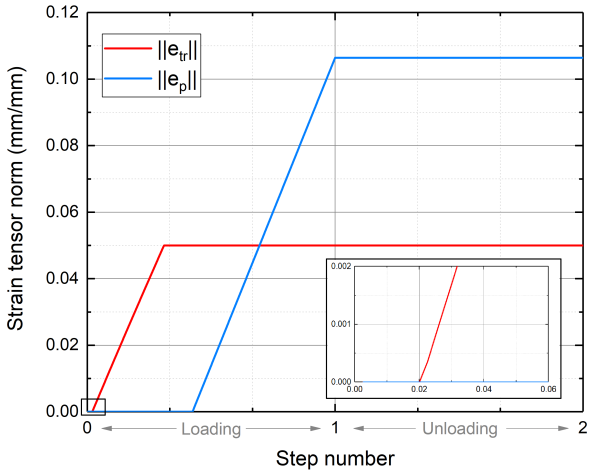

Figure 5.6: Evolution of the norm of transformation and plastic deformation tensors during the pre-deformation process (USERMAT results).

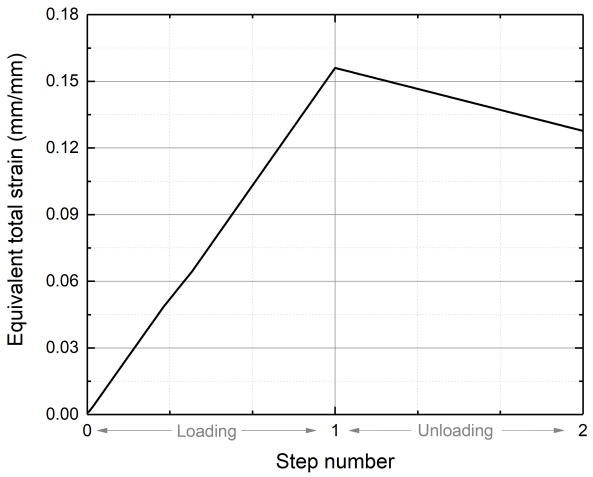

Figure 5.7: Evolution of the equivalent total deformation during the pre-deformation process (USERMAT results).

The effect of the pre-strain on OW- and TW-SME is shown graphically in Figure 5.8 with reference to the NiTi properties listed in Table 5.3. Both ϵ_{OW} and ϵ_{TW} saturate to the same value at $\epsilon_{pre-strain} > 20\%$. This is a mathematical result due to the the term that allows to couple transformation and plastic strains in the Helmholtz free energy definition (Eq. 5.2).

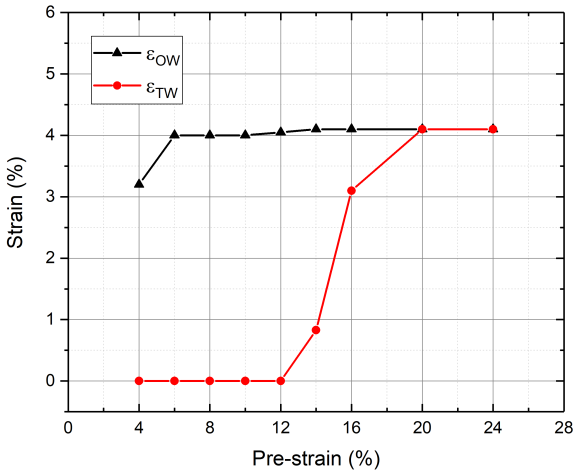

Figure 5.8: Evolution of the maximum OW and TW recoverable strains as a function of the applied pre-strain (USERMAT results).

5.4.3 Thermal activation

The *thermal activation* is simulated by applying a heating/cooling cycle to the cube to simulate the stress-free recovery. Figure 5.9 shows the evolution of the equivalent strain as a function of temperature for both USERMAT and SME models. In particular, Figure 5.9a reports the numerical results obtained by USERMAT. The curve clearly shows the effect of both the OW and the TW shape recovery. As expected, $\epsilon_{OW} > \epsilon_{TW}$. Figure 5.9b shows the results obtained by the SME model. In this case, only the one-way shape memory effect is simulated.

The evolution of the norm of the transformation and plastic strain tensors during the process is shown in Figure 5.10. The two reversible phase transformations occur: detwinned martensite to austenite upon heating and austenite to detwinned martensite upon cooling.

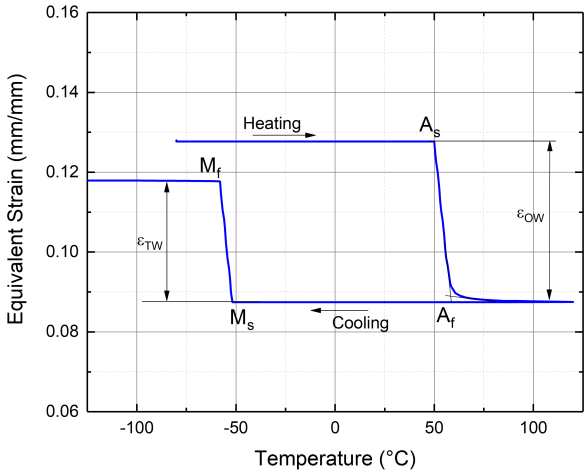

(a)

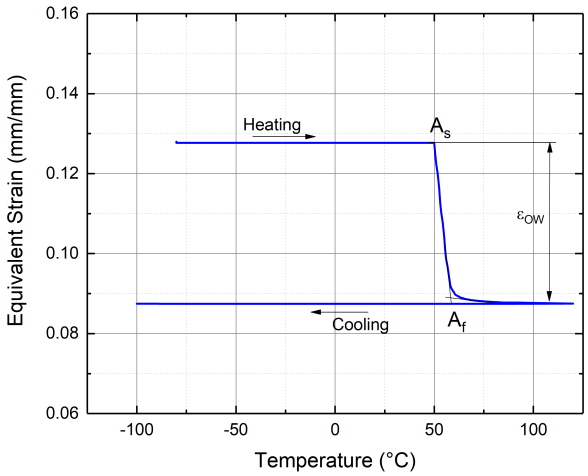

(b)

Figure 5.9: Strain-temperature response of the NiTi alloy during the thermal activation cycle: **(a)** USERMAT FEM simulation results, and **(b)** Shape Memory Effect model FEM simulation results.

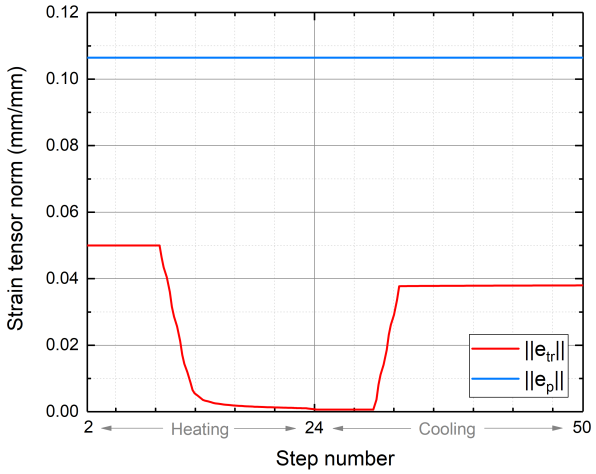

Figure 5.10: Evolution of the norm of transformation and plastic deformation tensors during the thermal activation process (USERMAT results).

5.5 General simulation settings by USERMAT

Benchmark FE simulations demonstrated the strong influence of plasticity and TW-SME on the solution accuracy of coupling process simulations. Consequently, USERMAT is used for all FEAs of NiTi couplers performed in ANSYS and presented in the following sections. For the sake of brevity, the use of USERMAT will not be specified from now on.

The mechanical and functional properties of the NiTi alloy used in the simulations are given in Table 5.3 and are obtained by calibrating the experimental uniaxial stress-strain curve.

Three-dimensional simulations are performed to enable the application of USERMAT. Planar symmetry and axisymmetry are exploited whenever possible to simplify the model, reduce the number of elements and nodes, and thus the computational time.

Static structural analyses are performed since the SMA properties are time-independent and the loading is applied in quasi-static conditions. Geometrical nonlinearities are considered in the numerical calculation. The number of steps and substeps is chosen according to the complexity of the simulation.

5.6 Ring connectors

This section presents the results of three-dimensional FEM simulations by USERMAT with respect to the coupling process performed by SMA ring connectors. Both the pre-expansion and the thermal activation cycle are simulated and the results are compared with experimental data. Different systems are analyzed to study the effect of geometric parameters on the tightness of the joint. Finally, bi-material connections are simulated with reference to the real case of the steel-titanium coupling discussed in section 2.6.1.

5.6.1 Homogeneous connections

The pipe-coupler system is modeled by exploiting both circumferential and planar symmetries to minimize the number of elements and nodes to be solved during the simulations. Figure 5.11 shows the FE model discretization and boundary conditions in a bi-dimensional plane. Only a 2° angle section of the system is modeled. The two rings are not aligned at the beginning of the simulation because the SMA ring needs to be trained first in order to have a gap between the ring and the pipe for mounting. The mesh consists in total of less than 13'000 quadratic elements (type SOLID187) of different sizes since a refinement is made in correspondence of the contact surfaces to increase the accuracy of the solution. Axial and planar symmetries are imposed as boundary conditions. The dimensions of the two rings, both considered before training, and the material properties refer to the experimentally tested system (see paragraph 3.3.2). They are given below:

- NiTi ring coupler: $ID = 39.6mm$, $t = 5mm$, $w = 5mm$, Table 5.3;
- 316LN internal pipe: $OD = 43.5mm$, $t = 10.15mm$, $w = 5mm$, $E = 205GPa$, $\nu = 0.3$, $\alpha = 1.7 \times 10^{-5} °C^{-1}$.

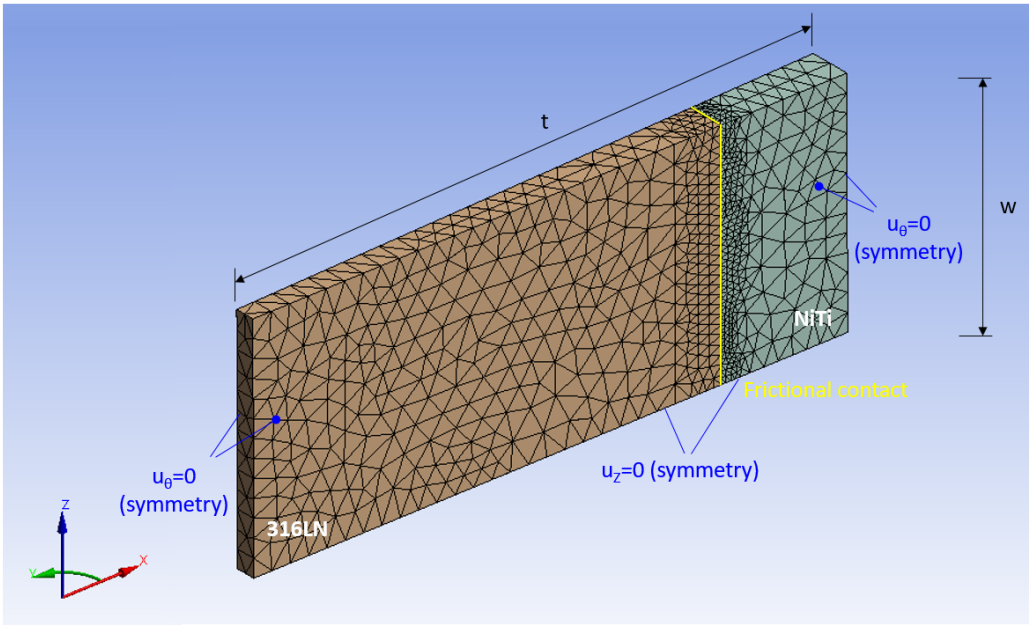

Figure 5.11: Ring SMA coupler/steel pipe couplings: finite element discretization and boundary conditions

Mechanical training

The pre-expansion of the NiTi ring is simulated under displacement control. A radial displacement of $u_r = 3.5mm$ is applied to the inner surface of the ring, corresponding to a maximum circumferential strain at the inner diameter $\epsilon_{max} = 16\%$. At unloading, the residual radial deformation on the inner surface is uniform along the thickness and amounts to $u_r = 2.7mm$, corresponding to an inner diameter at unloading equal to $ID = 45mm$. Consequently, the radial gap between the NiTi ring and the inner tube after training is $\Delta r = 0.75mm$. This is the initial configuration for the mounting process.

Thermal coupling of steel pipes

Assembly and disassembly of the system are simulated by applying a heating/cooling cycle starting from the martensitic conditions, at $T = -80°C$. The maximum and minimum temperatures of the cycle are $T_{max} = 200°C$ and $T_{min} = -150°C$.

Frictional contact conditions are applied to model the SMA-pipe interface using the Augmented Lagrange method, which ensures minimum penetration and zero gap between the two contact surfaces. The friction is set to 0.3, which is a typical coefficient for the NiTi-steel contact.

The results in terms of contact pressure-temperature evolution are shown in Figure 5.12 in

comparison with the experimental curve. The figure shows a very good agreement between the numerical and experimental data, proving the correct functioning and the potential of the SMA USERMAT. The thermal hysteresis is well described by the numerical model, as well as the contact and release temperatures, which are $T_c \approx 60°C$ and $T_s \approx -50°C$, respectively. However, during the cooling phase, the FE solution shows a significant change in the slope of the curve corresponding to the martensite start temperature (${M^\sigma}_s \approx 30°C$), which allows to distinguish the pure thermal deformation, at $T > M_s^\sigma$, from the thermal and recovery deformations, at $M_s^\sigma < T < M_f$. The mismatch between experiments and simulations is due to three main reasons. First, the geometry modeled for the FEA represents an ideal case, where the shapes of the two rings are perfectly circular and concentric over the process as a consequence of the absolute uniformity of stress and strain distributions. In the real case, for example, the misalignment of the inner and outer rings may cause a non-uniform initial gap between them and, consequently, a non-uniform contact pressure developed along the radius. In addition, the mechanical and functional properties assumed for the NiTi are obtained from the uniaxial experimental of dog-bone samples. However, the manufacturing process and thermomechanical history influence the final properties of the SMA, and the NiTi ring properties may not match perfectly those of the dog bones. Finally, during the constrained recovery of the SMA coupler, high temperatures and stresses develop in the system and mixed SIM and TIM transformations may occur. However, these phenomena are not yet well-known and are still under investigation [123, 109, 117], so they are not taken into account in the numerical model, which only considers the shape memory effect due to the martensite to austenite transformation. At the end of the assembly, the NiTi ring microstructure is considered to be fully austenitic. The conclusion is that despite the imperfect overlap of the FE and experimental pressure-temperature curves, the FE model is a very powerful tool that can be used in the design phase to predict the behavior of an SMA coupler within an acceptable range of error. In particular, the difference in contact pressure between FEM and experimental data is $26MPa$ at $T_{max} = 200°C$, which corresponds to a relative error of $E_{FEM-EXP} = 40\%$, and about $29MPa$ at $T_o = 25°C$ under operating conditions, which corresponds to a relative error of $E_{FEM-EXP} = 69\%$.

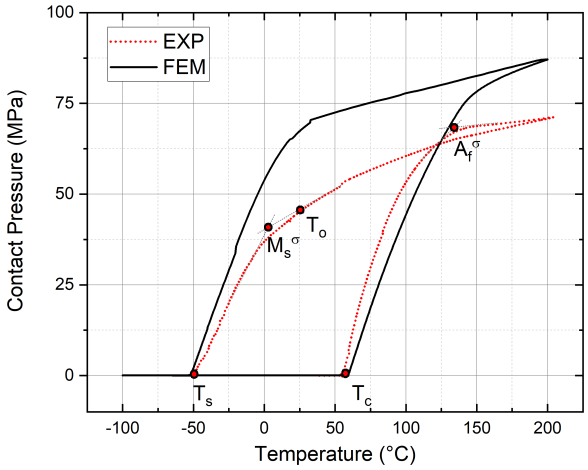

Figure 5.12: Evolution of the contact pressure exerted by a NiTi ring on a 316LN ring as a function of temperature: FE simulation results versus experimental curve.

Figure 5.13 shows the plot of the radial stress on the contact surface of the steel ring and its evolution along the thickness. The figure shows that the contact pressure is uniform for almost the 90% of the contact thickness. Edge effects occur out of this region where localized higher stresses develop. The plot of the equivalent stress in both NiTi and 316LN rings is shown in Figure 5.14 with respect to the following steps of the process: a) after training (mounting), b) at the maximum temperature (maximum pressure), c) at the room temperature (operating conditions), and d) at the minimum temperature (dismounting) of the process. The figure shows that there is an initial gap between the rings after the training that allows the mounting of the system. At the maximum temperature and under operating conditions the two rings are in perfect contact, ensuring a stable and tight connection of the system. At the end of cooling, there is a gap between the two rings, which allows easy and complete disassembly.

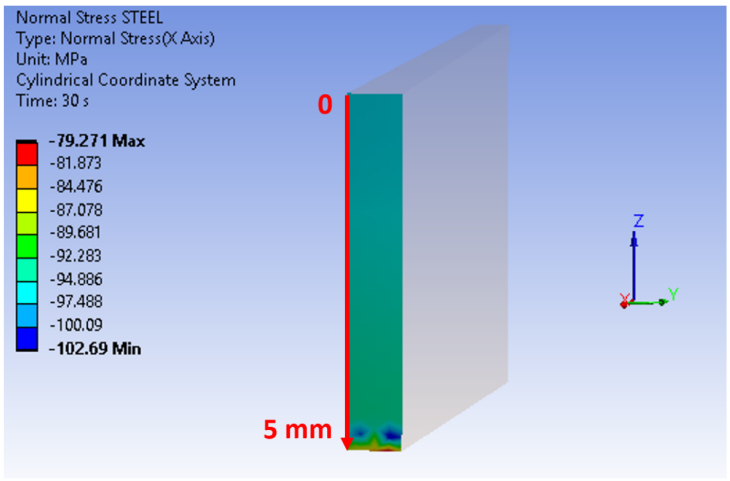

(a)

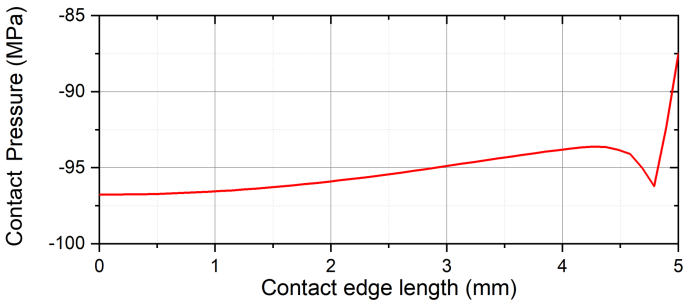

(b)

Figure 5.13: Radial contact stress on the steel ring (outer diameter) at $T_{max} = 200°C$: **(a)** Plot of the radial contact stress distribution on the surface, and **(b)** Evolution of the radial contact stress along the contact edge.

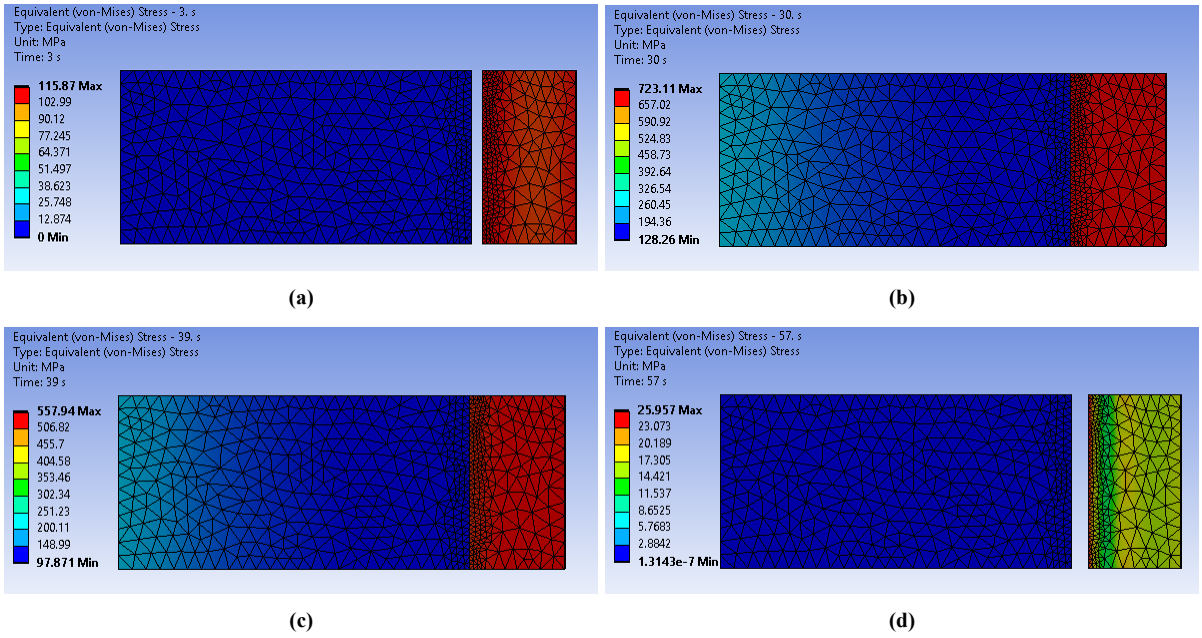

Figure 5.14: Plot of the equivalent stress in the system: **(a)** after training (mounting), **(b)** at the maximum temperature (maximum pressure), **(c)** at the room temperature (operating conditions), and **(d)** at the minimum temperature (dismounting) of the process.

The transformation and plastic strains are evaluated by the state variables defined in the subroutine. In particular, Figure 5.15 shows the plot of the norm of the two strain tensors in the NiTi ring at the maximum and minimum temperature of the process, when the M→A and A→M transformations are completed, respectively.

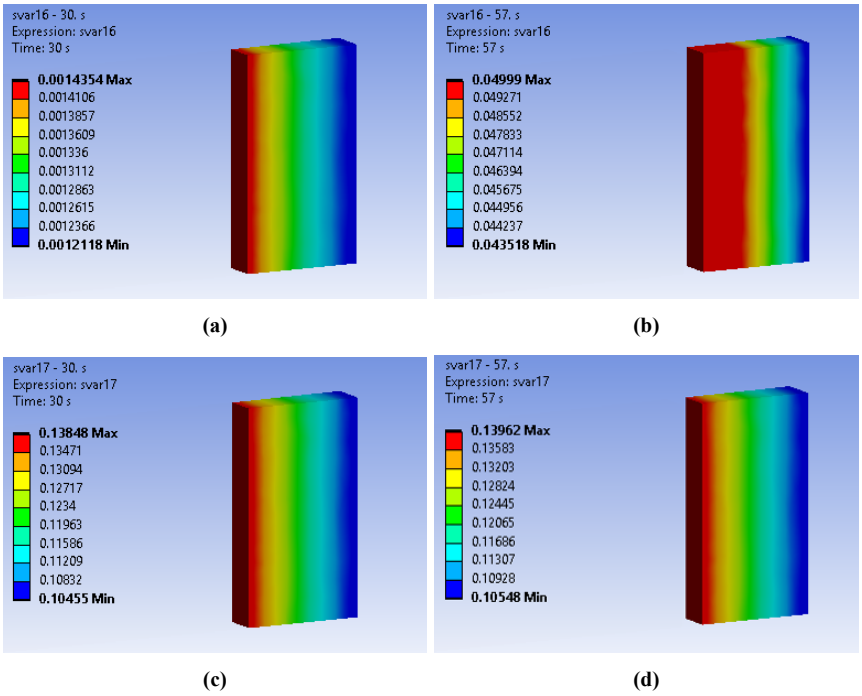

Figure 5.15: Plot of the norm of the transformation and plastic strain tensors in the NiTi ring at the maximum and the minimum temperatures of the process: **(a)** Norm of the transformation strain tensor at $T_{max} = 200°C$, **(b)** Norm of the transformation strain tensor at $T_{min} = -80°C$, **(c)** Norm of the plastic strain tensor at $T_{max} = 200°C$, and **(b)** Norm of the plastic strain tensor at $T_{min} = -80°C$.

Effect of the thickness and initial gap on the final contact pressure

In the SMA coupler-pipe system, some geometric parameters can play a very important role in the coupling process, influencing the pressure that develops at the contact interface and ensures the tightness of the system, such as the initial gap between SMA coupler and pipe, and the thickness of the SMA coupler. In order to quantify these effects, a parametric study is proposed here.

The effect of the initial gap on the coupling is studied by simulating various configurations of the system. The same NiTi coupler ($ID_{NiTi} = 39.6mm$, $t_{NiTi} = 5mm$) and steel ring ($t_{316LN} = 10.15mm$) are used in all cases, but different radial gaps are imposed between the rings at the beginning of the process, which are: $\Delta r = 0.36, 0.46, 0.56, 0.66$ and $0.76mm$. The results are shown in the two diagrams reported in Figure 5.16: a) contact pressure evolution as a function of the temperature, and (b) contact pressure at the maximum and operating temperatures of the process,p_{max} and p_o, respectively, as a function of the initial gap. The simulated curves show that, as expected, the larger the initial radial gap, the lower the contact pressure developed because the higher the amount of recovery strain needed to cover the gap. This is a consequence

of the higher contact temperature, namely the temperature at which the two rings come into contact.

The effect of the thickness is investigated by simulating five other cases: $t = 2, 3, 5, 8, 11mm$ with an almost constant initial gap of $\Delta r = 0.35mm$. The results are shown in Figure 5.17. In this case, there is a linear evolution of the maximum and operating pressure as a function of the thickness. As expected, the higher the coupler thickness, the higher the pressure that can be developed during the coupling process.

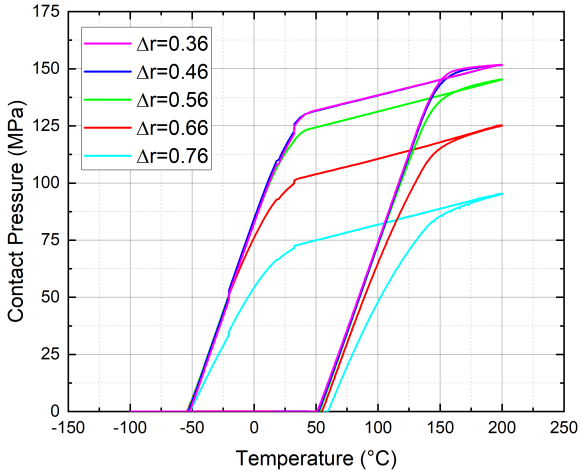

(a)

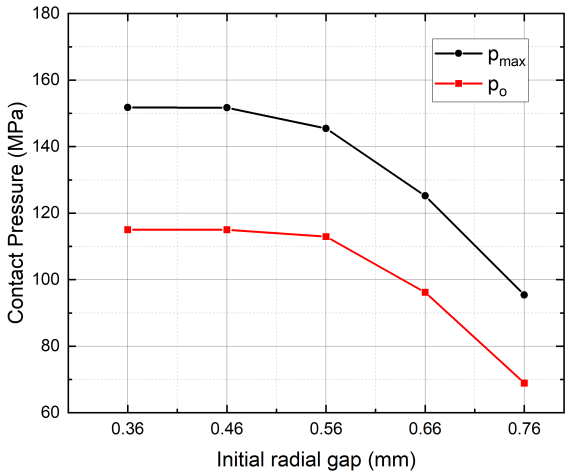

(b)

Figure 5.16: Effect of the initial radial gap between the NiTi and 316LN rings on the contact pressure: **(a)** Contact pressure as a function of temperature at different values of the initial gap, and **(b)** Contact pressure as a function of the initial radial gap at the maximum temperature, $p_{max} = p(T = 200°C)$, and at the operating temperature, $p_o = p(25°C)$.

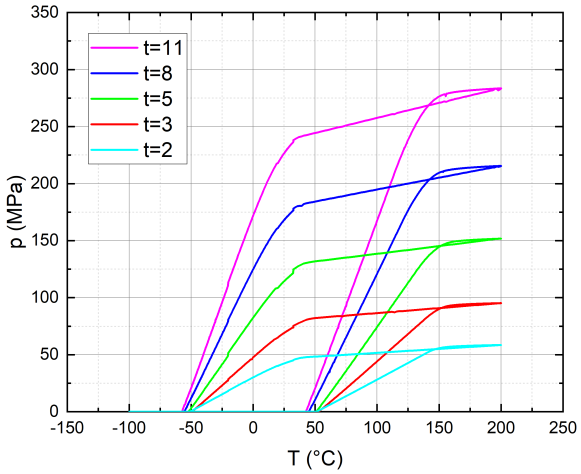

(a)

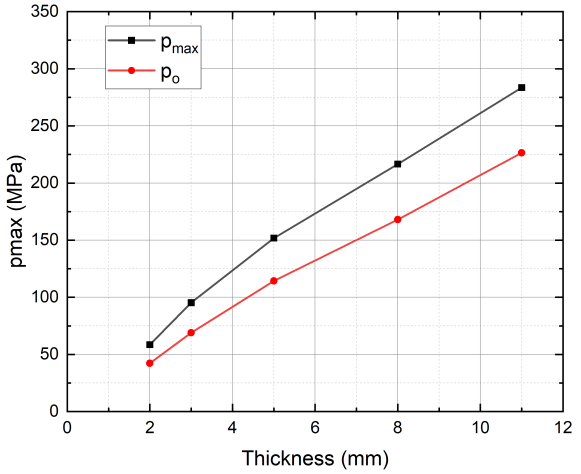

(b)

Figure 5.17: Effect of the NiTi ring thickness on the contact pressure at the NiTi coupler-316LN ring interface: **(a)** Contact pressure evolution as a function of temperature for different values of NiTi ring thickness, and **(b)** Contact pressure as a function of the SMA ring thickness at the maximum temperature, $p_{max} = p(T = 200°C)$, and at the operating temperature, $p_o = p(25°C)$.

5.6.2 Bi-material connections

The connection of different materials inside the LHC is particularly challenging because traditional techniques, both permanent and dismountable, must meet the stringent requirements imposed by vacuum operating conditions. Reliable connections, therefore, require very precise and complex operations. SMA couplers provide a viable alternative as their use in vacuum for bi-material connections is relatively simple and does not require the use of particularly sophisticated

machines or techniques, such as complex brazing procedures for UHV. This section presents some results of the coupling process of two different materials. In particular, the FE simulation replicates the real case of steel-titanium coupling by NiTi rings implemented in a dump entrance window of the LHC (see paragraph 2.6.1). The geometry and properties of the SMA, steel and titanium rings used in the simulation are given below:

- NiTi ring: $ID = 38.5mm$, $t = 5mm$, $w = 39.4mm$, Table 5.3.
- Elastic 316LN internal pipe: $OD = 43.55mm$, $t = 7.5mm$, $w = 19.7mm$, $E = 205GPa$, $\nu = 0.3$, $\alpha = 1.7 \times 10^{-5} °C^{-1}$.
- Elastic titanium internal pipe: $OD = 43.55mm$, $t = 7.5mm$, $w = 19.7mm$, $E = 120GPa$, $\nu = 0.3$, $\alpha = 9.4 \times 10^{-6} °C^{-1}$, .

A 2° section of the system is modeled by exploiting the axial symmetry. Axial symmetry is imposed as a boundary condition. The modeled system is shown in Figure 5.18.

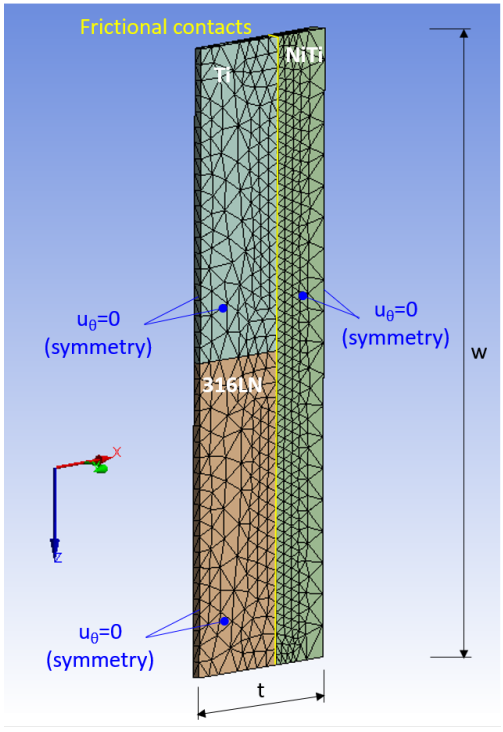

Figure 5.18: Ring SMA coupler/titanium and steel pipes coupling: finite element discretization and boundary condition.

Mechanical training

The pre-expansion of the NiTi ring is simulated by a radial displacement of $u_r = 3.4mm$ applied to the inner surface of the ring, corresponding to a $\epsilon_{max} = 16\%$. At unloading, the residual radial deformation on the inner surface is uniform along the thickness and amounts to $u_r = 2.6mm$, corresponding to an inner diameter at unloading of $ID = 43.7$. Consequently, the radial gap between the NiTi ring and the inner tube after training is $\Delta r = 0.075mm$. This represents the initial configuration of the system for the assembly process.

Thermal coupling of steel-titanium pipes

Mounting and dismounting of the system are simulated by a heating/cooling cycle, starting from martensitic conditions, at $T = -80°C$. The maximum and the minimum temperatures of the cycle are $T_{max} = 200°C$ and $T_{min} = -100°C$.

Frictional contacts are imposed between the NiTi and the steel and titanium rings, and between the steel and the titanium, by using the Augmented Lagrange formulation and the following friction coefficients: NiTi-316LN = 0.3, NiTi-Ti = 0.36, 316LN-Ti =0.3.

The graph in Figure 5.19 shows the evolution of the average contact pressure developed on the NiTi ring contact face as a function of temperature. Figure 5.20 shows the plot of the radial stress on the SMA ring contact face at the maximum temperature of the thermal cycle and its evolution along the thickness. The diagram shows that the pressure is approximately constant along the thickness, with a discontinuity step of $\Delta p = 35MPa$ corresponding to the contact interface between the steel and the titanium rings. The pressure jump is due to the change of material properties in contact with the NiTi coupler. The radial stress distribution in the system at the operating temperature ($T = 25°C$) is displayed in Figure 5.21.

The radial displacement (in mm) of the two pipes at the maximum contact pressure ($T = 200°C$) is reported in Figure 5.22. The titanium ring deforms more than the steel, as expected, due to the lower (almost half) elastic stiffness.

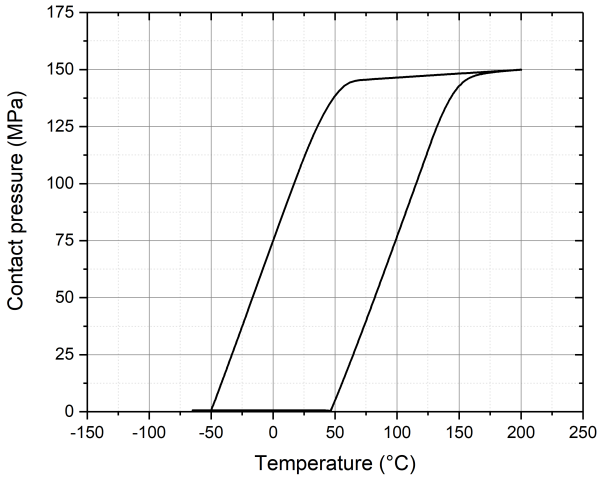

Figure 5.19: Average contact pressure developed on the contact surface of the NiTi ring as a function of the temperature during the steel-titanium coupling process.

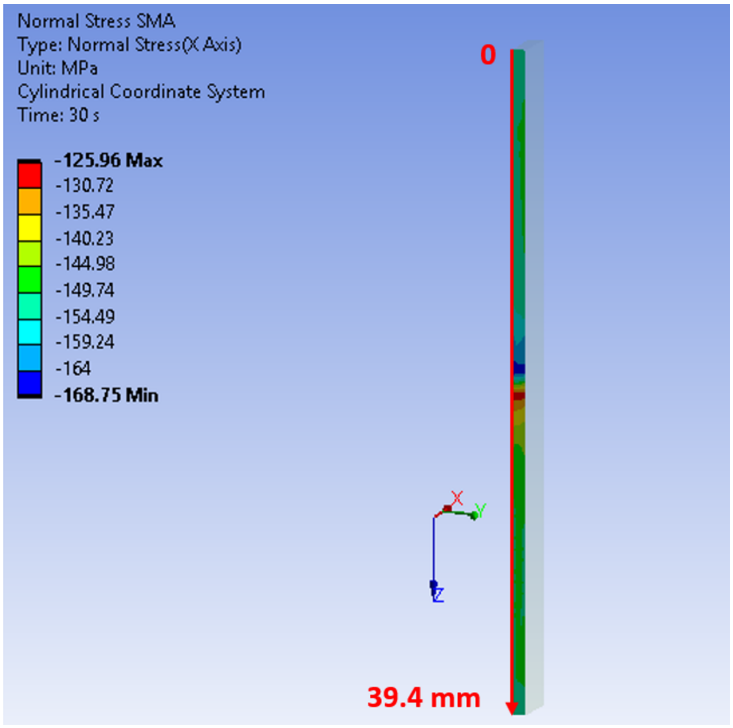

(a)

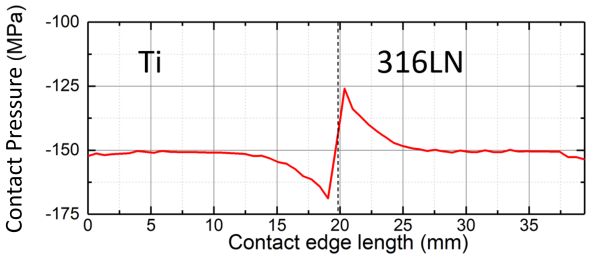

(b)

Figure 5.20: Radial contact stress on the NiTi ring (inner diameter) at $T_{max} = 200°C$: **(a)** Plot of the radial contact stress distribution on the surface, and **(b)** Evolution of the radial contact stress along the contact edge.

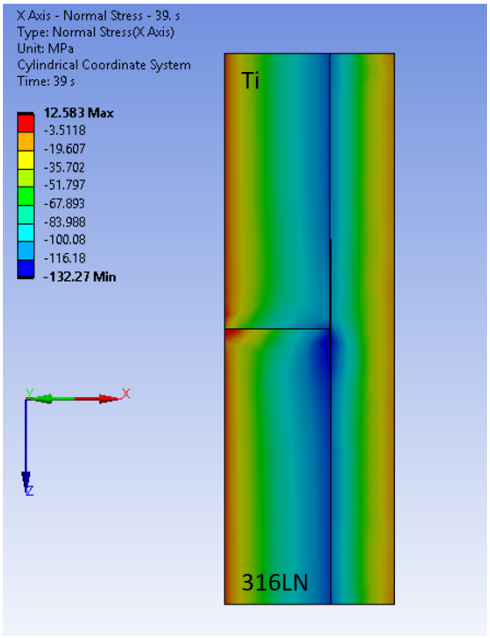

Figure 5.21: Radial stress distribution in the bi-material connection system at $T_{room} = 25°C$.

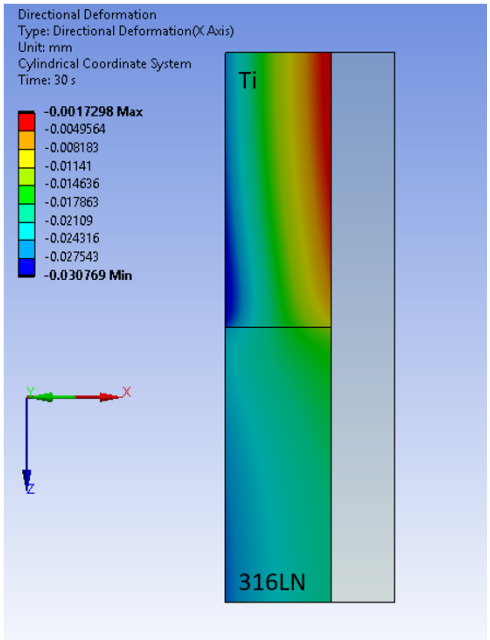

Figure 5.22: Radial displacement (in mm) of the steel and titanium rings at $T = 200°C$.

5.7 Oval connectors

The oval SMA-based connectors are developed from a circular geometry. It would be very difficult to train an oval by applying a uniform local radial strain, as discussed in section 3.4. For this reason, an initial ring ($ID = 122mm$, $w = 20mm$ and $t = 9mm$) is first expanded

to perform the training of the material and then it undergoes the ovalization process. The oval case study presented here describes the real case of the NiTi oval coupler designed to connect oxygen-free copper oval chambers ($2a = 89mm$, $2b = 62mm$, $w = 20mm$ and $t = 30mm$) in the context of the FCC-ee project. The system simulated here consists of three elements: the SMA coupler (initially ring-shaped), the oval chamber, and a rigid bar that performs the ring compression in the ovalization process. The initial geometry and material properties of the SMA connector and oval chamber are given below:

- NiTi connector: $ID = 122mm$, $t = 9mm$, $w = 20mm$, Table 5.3.
- Elastic oxygen-free copper oval chamber: $2a = 89mm$, $2b = 62mm$, $t = 30mm$, $w = 20mm$, $E = 115GPa$, $\nu = 0.3$, $\alpha = 1.7 \times 10^{-5}°C^{-1}$.

A 90° half-sector of the system is modeled by exploiting the planar symmetry by means of roller constraints. Figure 5.23 shows the geometry and the constrained conditions imposed on the system.

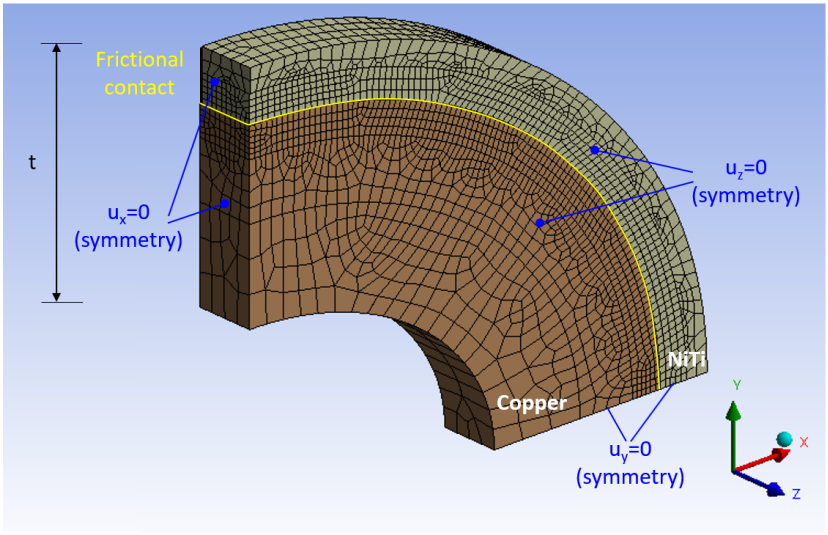

Figure 5.23: Oval-shaped SMA connector/copper chamber couplings: finite element discretization and boundary conditions

5.7.1 Mechanical training

A radial displacement of $u_r = 11.15mm$ is imposed on the inner surface of the coupler to simulate the mechanical training of the material. The corresponding maximum pre-strain is of $\epsilon_{max} = 16\%$. The temperature of the process is $T = -65°C$, so fully martensitic conditions.

The radial deformation on the inner surface of the ring after unloading is plotted in Figure 5.24. The internal diameter of the ring after thermal training is $ID_{NiTi} = 137mm$.

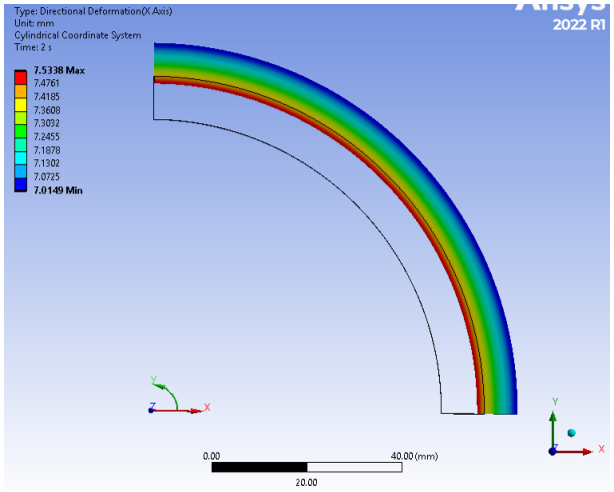

Figure 5.24: Residual radial deformation of the NiTi ring at the end of the pre-expansion process.

5.7.2 Ovalization process

After training, the ring is compressed to obtain the oval shape, at $T = -65°C$ (fully martensite). The bar moves vertically against the coupler by a displacement of $w = 16mm$ and is then lifted to simulate the elastic unloading. Figure 5.25 shows the distribution of the equivalent Von Mises stress in the NiTi coupler at the maximum lowering of the crossbar and after complete unloading.

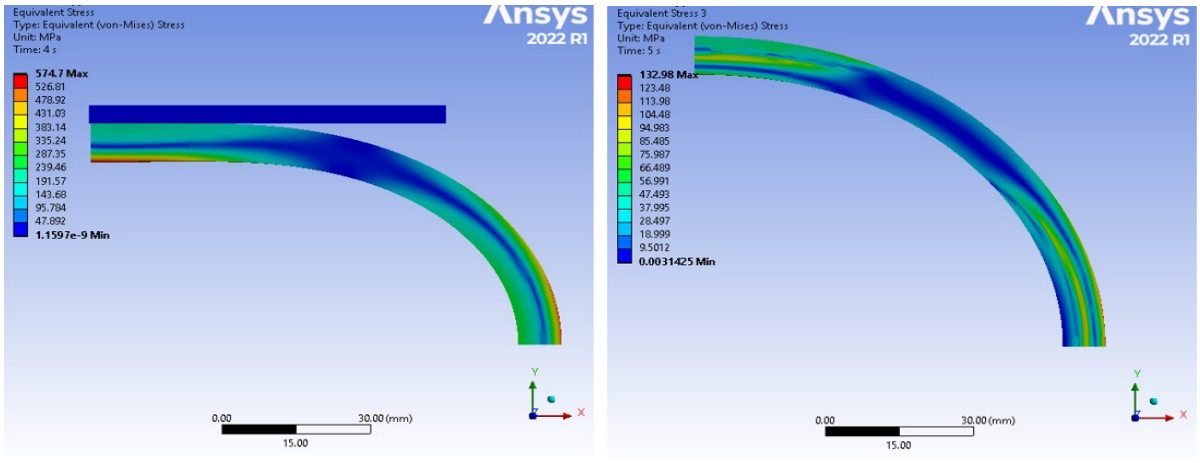

(a) **(b)**

Figure 5.25: Equivalent Stress distribution in the NiTi coupler during ovalization: **(a)** Maximum loading displacement, $w_{max} = 16mm$, and **(b)** Complete unloading.

After unloading, the oval shape is determined by evaluating the directional deformations on the inner surface of the connector and along the x- and y-axes. The maximum and minimum axis dimensions of the oval-shaped coupler are $2a = 148.4mm$ and $2b = 122mm$. The thickness t and width w remain approximately unchanged. Figure 5.26 shows the x-directional and the equivalent displacement of the NiTi coupler at the end of the ovalization process. In particular, Figure 5.26a shows the x-directional deformation (in mm), and the oval shape of the coupler is compared with the undeformed shape (ring before training). Figure 5.26b shows the total deformation (in mm) of the chamber-connector system. The latter represents the initial configuration of the system at the start of the thermal activation cycle.

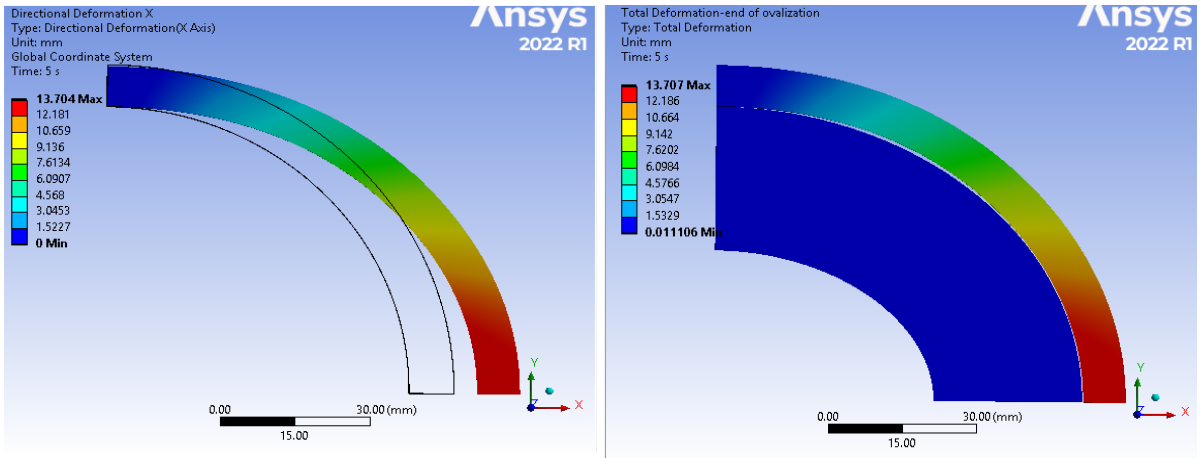

(a) **(b)**

Figure 5.26: Directional and total deformations of the NiTi connector after the ovalization process: **(a)** x-directional strain distribution (in mm) on the new shape of the coupler compared with the undeformed shape (ring before training), and **(b)** Total deformation (in mm) of the chamber-connector system.

5.7.3 Thermal coupling of oval copper chambers

The thermal coupling consists of a heating/cooling cycle starting from the martensitic conditions, at $T = -65$. The maximum and minimum temperatures of the cycle are $T_{max} = 200°C$ and $T_{min} = -100°C$. During heating, the NiTi connector contracts due to the thermoelastic martensitic transformation, allowing for the development of a tightening pressure at the contact interface with the internal oval chamber. Figure 5.27 shows the evolution of contact pressure as a function of temperature, calculated at $T_{max} = 200°C$ and at three different points (A, B and C) placed along the median plane of the ovals and spaced 45° apart. The graph shows that the pressure is not uniformly distributed over the surface. In addition, the contact and separation

temperatures are not the same for the three points. This result is due to the non-uniform gap between the ovals at the beginning of the process, which results from the non-regular shape of the connector. In fact, the latter is obtained by compression of an already pre-deformed ring, as explained in the previous section. In addition, the recovery properties developed in the connector are not isotropic, so the oval does not contract uniformly upon heating. At $T_{min} = -100°C$, when the A→M transformation is complete, there is a gap between the oval chamber and the connector (Figure 5.27) that allows complete disassembly.

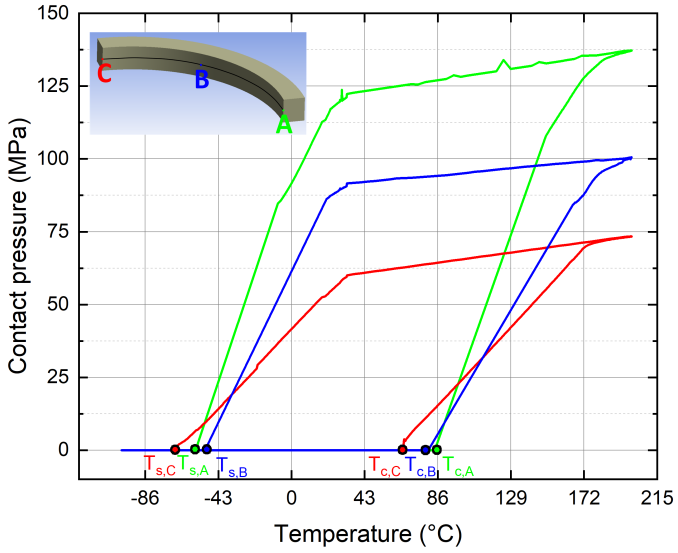

Figure 5.27: Evolution of the average contact pressure exerted by a NiTi oval connector on an oxygen-free copper oval chamber as a function of temperature calculated at three different points of the contact surface spaced 45 °C a part along the midplane of the ovals: A, B and C.

5.8 C-shaped connectors

C-shaped connectors have been studied as a viable alternative to the heavy collars for connecting QF flanges. For the FE simulations, the pre-deformation and thermal activation process of a single connector is simulated. Only a half of the fastener is modeled by exploiting the planar symmetry (length=$15.9mm$). A steel element representing the inner flange is modeled. The system is shown in Figure 5.28. The internal element represents the steel flange, which properties are given below:

- 316LN bar: $E = 205GPa$, $\nu = 0.3$, $\alpha = 1.7 \times 10^{-5}°C^{-1}$

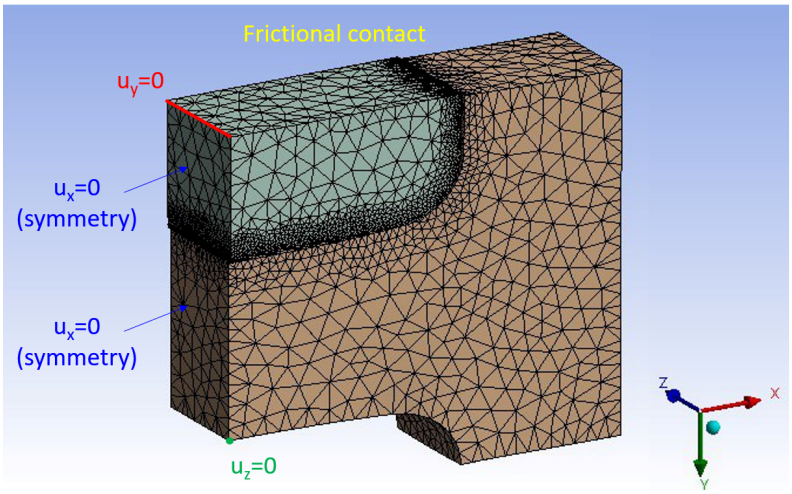

Figure 5.28: C-Shaped SMA fastener/steel bar couplings: finite element discretization and boundary conditions.

5.8.1 Mechanical training

The pre-strain is performed by applying a uniform displacement of $u_x = 2mm$ to the fastener under fully martensitic conditions, at $T = -65°$. Figure 5.29 shows the plot of the norm of the transformation and plastic strain tensors. Results reveal a significant plasticization of the connector, as the pre-strain induces mainly tensile deformations in the component. The maximum plastic strain is in correspondence with the fillet radius and amounts to 23%. The maximum allowable transformation strain of $||e_{tr}||$ = 5% is reached in most of the volume of the connector.

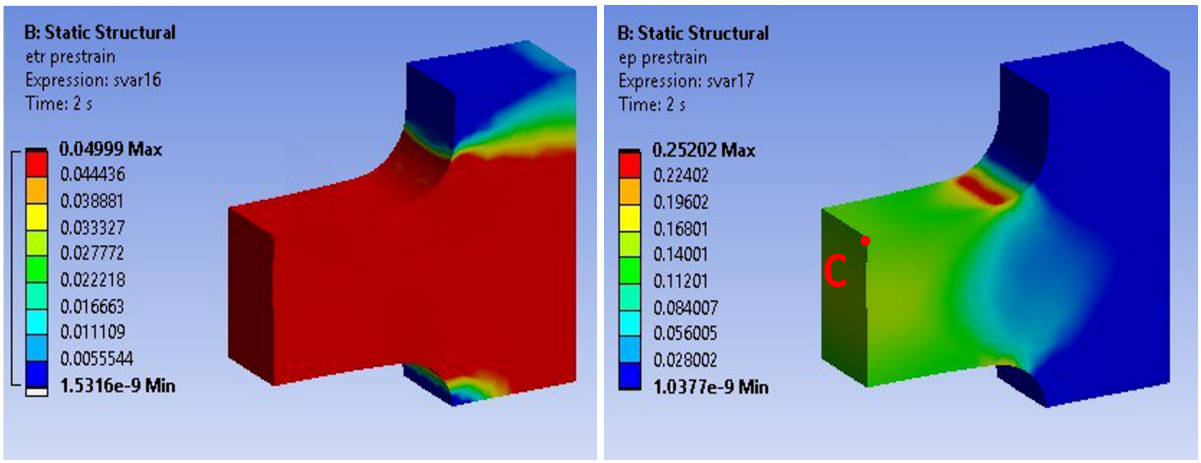

(a) **(b)**

Figure 5.29: Plot of the norm of the transformation and plastic strain tensors in the C-shaped connector at the end of the pre-strain: **(a)** Norm of the transformation strain tensor, and **(b)** Norm of the plastic strain tensor.

5.8.2 Thermal coupling of QF steel flanges

A thermal heating/cooling cycle is applied, starting from martensitic conditions, at $T = -65°C$. The maximum and minimum temperatures of the cycle are $T_{max} = 200°C$ and $T_{min} = -200°C$. Figure 5.30a shows the experimental axial recovery force, F_{rec}, (obtained from strain gauge tests) as a function of temperature, while Figure 5.30b reports the corresponding numerical data from FE simulations. F_{rec} sharply increases from the beginning of the SMA/steel contact (occurring approximately at the austenite start temperature A_s) up to the austenite finish temperature (under stress), A_f^σ. A similar trend was obtained from constrained uniaxial SMA samples [9]. The simulations were found to be relatively accurate in comparison to experiments with errors lower than 16%. It is worth noting that NiTi clamps material show an error on the TTs of about +/- 7 °C owing to metallurgy and manufacturing processes. This directly affects the value of the maximum recovery force generated when installed (+/- 15 % variation within the same material batch). The good agreement between experimental (Figure 5.30a) and numerical results (Figure 5.30b) confirms the capability of the model in capturing the evolution of the recovery forces generated by such SMA devices by temperature variations. Figure 5.30b shows also the evolution of plastic strains (point C in Figure 5.29b) as a function of temperature during the constrained recovery test. It is worth highlighting that they accumulate during both the isothermal pre-deformation phase and the subsequent constrained thermal cycle. In the latter stage, stress-induced martensitic variants transform to austenite involving slip deformations [9, 117, 133].

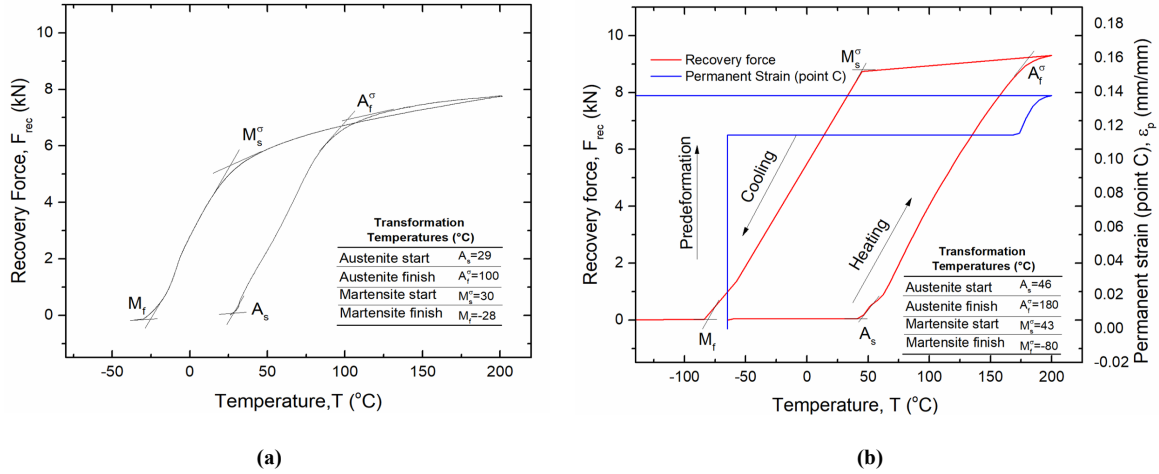

Figure 5.30: Experimental and numerical results for a constrained thermal recovery of a C-shaped fastener: **(a)** Experimental recovery force as a function of temperature from strain gauge measurements, and **(b)** Numerical recovery force and permanent strain (point C in Figure 5.29b) as a function of temperature from FE simulations.

5.9 Chapter summary

This chapter discusses numerical FE modeling and simulation of SMAs. The first part provides an overview of SMA material models available in commercial FE software such as ANSYS, COMSOL, and ABAQUS. An in-depth study of the phenomena occurring during the constrained recovery application revealed that these models cannot accurately describe the assembly/disassembly process performed by a SMA connector. In particular, martensite plasticity and TW-SME are not considered in the formulations. These two features are of fundamental importance, since plastic deformations of martensite occur during the mechanical training and the TW-SME is responsible for the austenite to martensite transformation during cooling and, therefore, for the system dismounting.

A recently developed three-dimensional phenomenological model of SMA is implemented in ANSYS by a user-defined material FORTRAN subroutine, the USERMAT. The model was developed by Scalet et al. in 2019 [9] to introduce the two important features of plasticity and TW-SME. A brief summary of the model formulation is presented and its implementation as a User Programmable Feature (UPF) in ANSYS is discussed.

FE simulation results by USERMAT are presented and discussed, with respect to a simple cube (benchmark simulations) and ring, oval and C-shaped connectors with OW and TW recovery capabilities. Both the training and thermal activation cycle (mounting and dismounting

process) against different internal material elements are simulated. FE results demonstrate both the accuracy of the model in comparison with experimental curves from Chapter 3 and the ability of different shaped NiTi couplers to perform tight pipe/chamber coupling.

Conclusions

The project presented in the thesis concerns the development and validation of experimental methods and theoretical models to characterize the behavior of SMA pipe couplers for ultra-high vacuum systems of particle accelerators.

Chapter 1 and Chapter 2 describe the context of the project. Particle accelerators operate under vacuum conditions, namely at very low pressures on the order of $p = 10^{-6}$–$10^{-12}\ mbar$. Different levels of vacuum are required depending on the accelerator equipment and its purpose. The Large Hadron Collider (LHC) at CERN is a $27\ km$ diameter ring in which protons or heavy ions circulate to finally collide at the four detector points placed along the machine. It consists of two main vacuum systems, the insulation vacuum ($p \propto 10^{-6}\ mbar$) and the beam vacuum ($p \propto 10^{-10}\ mbar$). The large number of components involved in the construction of the LHC implies the use of many seals and joints. The latter play a very important role in the functioning of the accelerator because they are the main responsible for the leak-tightness of the systems. Traditional joining techniques include mainly welding or brazing as permanent seals, and vacuum flanges (such as CF, KF or ISO-K) as detachable joints. All connection systems to be used in the LHC must meet special requirements. They must be compact, radiation resistant, and easy to be assembled and maintained to reduce the presence of the human operators in the radioactive areas of the accelerator. In this regard, traditional techniques present some limitations. Permanent connections, such as welding and brazing, are often complex to be done and can be very expensive. On the other hand, vacuum flanges for removable connections are not compact systems, as they require the use of bolts or heavy collars to be fixed. Also, the presence of operators *in-loco* is required in this case.

Shape Memory Alloy (SMA) couplers are designed to overcome these limitations. They are low-cost, compact, can be used to make bi-material connections (replacing brazing, which is complex and expensive), and can be remotely controlled by temperature variation. All the advantages offered by the SMA couplers come from the special properties of these alloy. Specif-

ically, they are able to recover large deformations if subjected to stress or temperature change. These properties are known as the Pseudoelastic Effect (PE) and Shape Memory Effect (SME) and are due to phenomena occurring at the microstructural scale, namely thermoelastic martensitic transformations in the solid state between two crystallographic structures: austenite (body-centered cubic) and martensite (monoclinic/orthobic/tetragonal). Phase transformations can be induced either by stress and by temperature and are reversible processes. This means that the original shape can almost be recovered upon a complete loading/unloading cycle. SMA couplers exploit the thermo-mechanically induced TW-SME, so they contract upon heating and relax upon cooling, being able to realize the mounting and dismounting of a system, respectively. The recovery properties of the alloy are also measured by thermocycling tests and can be conferred to the material and tuned by proper experimental training. Finally, most of the functional properties, such as the maximum recoverable strains, Transformation Stresses (TSs), and the mechanical properties, such as elastic moduli, yield strength, plastic hardening parameter are determined by tensile loading/unloading tests. NiTi-based alloys were selected for the design and development of SMA joints for vacuum applications because their properties are suitable for the operating conditions of interest.

Chapter 3 presents the methods and results of an extensive experimental campaign on NiTi and NiTiNb specimens. First, the NiTi material has been characterized by uniaxial isobaric and isothermal tests. The repeatability of the material response has been verified by tensile loading/unloading tests. Thermal cycles at different stresses, from 100 to $400\ MPa$, were applied to study the one-way and the two-way shape memory effect, OW-SME and TW-SME, respectively, under constrained recovery conditions. The evolution of the material properties as a function of the temperature has been investigated by tensile tests at different temperatures, from 150 to $-60\ °C$, spanning austenite, martensite and mixed intermediate microstructuaral phases. The second part of the experimental campaign concerned the investigation of the behavior of ring, oval and C-shaped connectors. In this case, the primary purpose of the tests was the definition of the methods used to perform the material pre-deformation, fundamental to confer and tune the shape memory properties to the material. In addition, the constrained-recovery of NiTi rings was studied by using a 316LN ring as an internal constraint. Experimental evidence demonstrates the ability of even thin NiTi rings ($3\ mm$ thick) of developing high contact forces to achieve tight connections. All the experimental data were used to develop and calibrate theoretical models describing the behavior of SMA connectors.

Chapter 4 presents two analytical models developed for simulating the pre-deformation and the thermal activation (mounting and dismounting) process of a SMA ring. Both models are based on elastic-plastic theory of axisymmetric geometries, and have been developed to simulate 1) martensite reorientation or stress-induced transformation mechanisms, and 2) temperature induced phase transformations under stress-applied conditions in SMA rings. The first model was used to calculate the stress and strain distributions in pre-strained martensitic rings. Different load cases were investigated ranging from a completely elastic condition to plastic deformation of fully reoriented martensite. Systematic comparison of the model predictions, in terms of stress and deformation, with finite element analyses based on multilinear hardening material models and with experimental measurements showed a very good agreement. This model is particularly useful to predict the pressure of expansion and the final size of SMA couplers as a function of the initial ring geometry and the main pre-deformation parameters. The second model was used to calculate the contact pressure evolution with temperature during the entire assembly/disassembly process. Mechanical properties variation with stress-temperature conditions have been analytically defined thanks to previous experiments. The comparison between analytical solutions, in terms of pressure-temperature evolution, with finite element analysis by a three-dimensional phenomenological model based on the formulation of the Helmholtz free energy of the system, and experimental measurements show a good agreement. The two models related to the pre-deformation and the constrained recovery application phases represent a robust design tool for SMA rings with shape recovery capabilities.

Chapter 5 deals with the Finite Element (FE) simulations of the coupling process performed by different shaped SMA couplers. A user-defined material routine (USERMAT) was implemented in ANSYS. An initial comparison with the already available material model in ANSYS (the Shape Memory Effect) demonstrates the superior accuracy of the USERMAT in simulating both the martensitic pre-deformation and the thermal activation process due to two additional features: the modeling of the plasticity and the TW-SME. The USERMAT was used to simulate the coupling process of different NiTi couplers. The FE studies allowed to investigate the effect of geometrical parameters (initial gap between the rings and the thickness of the NiTi couplers) on the SMA ring/pipe contact pressure, to simulate the bi-material connection, to model and study the effect of the predeformation process of an oval connector on the final coupling as well as to analyze the stress-strain developed in the C-shaped fastener during the coupling process. When possible, FE analysis results are compared with the experimental data, proving the

high accuracy and reliability of the USERMAT model, which represents an important and very flexible tool in the design stage of a SMA connector.

List of Figures

List of Tables

Bibliography

[1] O Gröbner. The LHC Vacuum System. 1998.

[2] O Brüning, H Burkhardt, and S Myers. The large hadron collider. *Progress in Particle and Nuclear Physics*, 67(3):705–734, 2012.

[3] Linda Stoel, Michael Barnes, Wolfgang Bartmann, Florian Burkart, Brennan Goddard, Werner Herr, Thomas Kramer, Attilio Milanese, Giovanni Rumolo, and Elena Shaposhnikova. High Energy Booster Options for a Future Circular Collider at CERN. page MOPOY007, 2016.

[4] TW Duerig, KN Melton, and DWCM Stöckel. *Engineering aspects of shape memory alloys*. Butterworth-heinemann, 2013.

[5] K Otsuka and X Ren. Physical metallurgy of ti–ni-based shape memory alloys. *Progress in materials science*, 50(5):511–678, 2005.

[6] F Niccoli, C Garion, C Maletta, E Sgambitterra, F Furgiuele, and P Chiggiato. Beam-pipe coupling in particle accelerators by shape memory alloy rings. *Materials & Design*, 114:603–611, 2017.

[7] Fabrizio Niccoli, Cedric Garion, Carmine Maletta, and Paolo Chiggiato. Shape-memory alloy rings as tight couplers between ultrahigh-vacuum pipes: Design and experimental assessment. *Journal of Vacuum Science & Technology A: Vacuum, Surfaces, and Films*, 35(3):031601, 2017.

[8] F Niccoli, C Garion, C Maletta, C Cangialosi, A Infantino, S Danzeca, and P Chiggiato. Particle radiation effects on shape memory alloy couplers for ultra-high vacuum sealing: A preliminary study. *Smart Materials and Structures*, 28(8):085023, 2019.

[9] Giulia Scalet, Fabrizio Niccoli, Cedric Garion, Paolo Chiggiato, Carmine Maletta, and Ferdinando Auricchio. A three-dimensional phenomenological model for shape memory alloys including two-way shape memory effect and plasticity. *Mechanics of Materials*, 136:103085, 2019.

[10] A. Roth. *Vacuum Technology*. Elsevier Science, 2012.

[11] S Turner. Cas cern accelerator school vacuum technology. proceedings, 1999.

[12] L Evans and P Bryant. Lhc machine. *Journal of instrumentation*, 3(08):S08001, 2008.

[13] JM Jimenez. Lhc: The world's largest vacuum systems being operated at cern. *Vacuum*, 84(1):2–7, 2009.

[14] CERN. *CAS - CERN Accelerator School : Vacuum in Accelerators: Platja d'Aro, Spain 16 - 24 May 2006. CAS - CERN Accelerator School and ALBA Synchrotron Light Facility : Course on Vacuum in Accelerators*, Geneva, 2007. CERN.

[15] M Abedi Masir, M Aghaie, and Gh Alahyarizadeh. Simulation of separative gaseous molecular flow through porous membrane with dsmc method. *Progress in Nuclear Energy*, 118:103150, 2020.

[16] C Benjamin Nakhosteen and Karl Jousten. *Handbook of vacuum technology*. 2016.

[17] Marek Grabski. Vacuum technology for particle accelerators. Budapest, Hungary, October 2016.

[18] Paolo Chiggiato. Vacuum technology for ion sources. *arXiv preprint arXiv:1404.0960*, 2014.

[19] CERN. *CAS Vacuum for Particle Accelerators*, Glumslov, Sweden, 2017. CERN.

[20] Paolo Chiggiato. Outgassing properties of vacuum materials for particle accelerators. *arXiv preprint arXiv:2006.07124*, 2020.

[21] F Niccoli. *Shape Memory Alloy connectors for Ultra High Vacuum applications: a breakthrough for accelerators technologies*. PhD thesis, Universitá della Calabria, Italy, 2018.

[22] JM Jiménez and P Chiggiato. Vacuum science and technology at cern. *Europhysics News*, 51(4):24–26, 2020.

[23] Cristoforo Benvenuti, Paolo Chiggiato, P Costa Pinto, A Escudeiro Santana, T Hedley, A Mongelluzzo, V Ruzinov, and I Wevers. Vacuum properties of tizrv non-evaporable getter films. *Vacuum*, 60(1-2):57–65, 2001.

[24] O Gröbner. Overview of the lhc vacuum system. *Vacuum*, 60(1-2):25–34, 2001.

[25] Serge Dailler. Cross section of LHC dipole.. Dipole LHC: coupe transversale. AC Collection. Legacy of AC. Pictures from 1992 to 2002., 1999.

[26] K Otsuka and CM Wayman. Shape memory materials cambridge univ. *Press, New York*, 1998.

[27] V Birman. Review of mechanics of shape memory alloy structures. *Applied Mechanics Reviews*, 1997.

[28] Y Bellouard. Shape memory alloys for microsystems: A review from a material research perspective. *Materials Science and Engineering: A*, 481:582–589, 2008.

[29] A Ölander. An electrochemical investigation of solid cadmium-gold alloys. *Journal of the American Chemical Society*, 54(10):3819–3833, 1932.

[30] AB Greninger and VG Mooradian. Strain transformation in metastable beta copper-zinc and beta copper-ti alloys. *Aime Trans*, 128:337–369, 1938.

[31] GV Kurdyumov and LG Khandros. On the thermoelastic equilibrium on martensitic transformations. In *Dokl. Akad. Nauk SSSR*, volume 66, pages 211–214, 1949.

[32] A Bystrom and KE Almin. X-ray investigation of gold-cadmium alloys rich in gold. *Acta chem. scand.*, 1:76–89, 1947.

[33] Lo C Chang and TA Read. Plastic deformation and diffusionless phase changes in metals—the gold-cadmium beta phase. *Jom*, 3(1):47–52, 1951.

[34] WJ Buehler and RC Wiley. Nickel-base alloys, United States Patent N 3 174 851, 1965.

[35] CM Jackson, HJ Wagner, and Wasilewsli RJ. *55-Nitinol–the alloy with a memory: its physical metallurgy, properties, and applications; a report*. Technology Utilization Office, National Aeronautics and Space Administration, 1972.

[36] K Otsuka and K Shimizu. Memory effect and thermoelastic martensite transformation in cu-al-ni alloy. *Scripta metallurgica*, 4(6):469–472, 1970.

[37] K Otsuka. Origin of memory effect in cu-al-ni alloy. *Japanese Journal of Applied Physics*, 10(5):571, 1971.

[38] R Dasgupta. A look into cu-based shape memory alloys: Present scenario and future prospects. *Journal of Materials Research*, 29(16):1681–1698, 2014.

[39] J Perkins. The microstructure of rapidly solidified β-phase cu-zn-al alloys. *Metallurgical Transactions A*, 14:2229–2234, 1983.

[40] JD Stice and CM Wayman. Observations of aging effects in a cu-sn shape memory alloy. *Metallurgical Transactions A*, 13:1687–1692, 1982.

[41] V Asanović, K Delijić, and N Jauković. A study of transformations of β-phase in cu–zn–al shape memory alloys. *Scripta Materialia*, 58(7):599–601, 2008.

[42] GB Brook. Gold alloys with shape-memory. *Gold Bulletin*, 6(1):8–11, 1973.

[43] GB Brook and RF Iles. Gold-copper-zinc alloys with shape memory. *Gold Bulletin*, 8(1):16–21, 1975.

[44] N Nakanishi, Y Murakami, and S Kachi. Pseudoelasticity and elastic anisotropy in the β phase thermoelastic alloys. *Scripta metallurgica*, 5(5):433–439, 1971.

[45] A Cladera, B Weber, C Leinenbach, C Czaderski, M Shahverdi, and M Motavalli. Iron-based shape memory alloys for civil engineering structures: An overview. *Construction and building materials*, 63:281–293, 2014.

[46] YH Wen, HB Peng, Dierk Raabe, Ivan Gutiérrez-Urrutia, Jie Chen, and YY Du. Large recovery strain in fe-mn-si-based shape memory steels obtained by engineering annealing twin boundaries. *Nature communications*, 5(1):4964, 2014.

[47] AV Druker, A Perotti, I Esquivel, and J Malarría. Design of devices and manufacturing of fe-mn-si shape memory alloy couplings. *Procedia Materials Science*, 8:878–885, 2015.

[48] H Ju, C Lin, Y Tian, Z Liu, H Jiang, and D Sun. Mechanical properties study of fe-mn-si shape memory alloys welding seam formed by laser welding with filler powder. *Materials*, 11(8):1454, 2018.

[49] H Sehitoglu, C Efstathiou, HJ Maier, and Y Chumlyakov. Hysteresis and deformation mechanisms of transforming fenicoti. *Mechanics of materials*, 38(5-6):538–550, 2006.

[50] R Sidharth, Y Wu, F Brenne, W Abuzaid, and H Sehitoglu. Relationship between functional fatigue and structural fatigue of iron-based shape memory alloy femnnial. *Shape Memory and Superelasticity*, 6:256–272, 2020.

[51] XM Zeng, Z Du, C A Schuh, N Tamura, and CL Gan. Microstructure, crystallization and shape memory behavior of titania and yttria co-doped zirconia. *Journal of the European Ceramic Society*, 36(5):1277–1283, 2016.

[52] Z Du, XM Zeng, Q Liu, A Lai, S Amini, A Miserez, C A Schuh, and CL Gan. Size effects and shape memory properties in zro2 ceramic micro-and nano-pillars. *Scripta Materialia*, 101:40–43, 2015.

[53] Alan Lai, Zehui Du, Chee Lip Gan, and Christopher A Schuh. Shape memory and superelastic ceramics at small scales. *Science*, 341(6153):1505–1508, 2013.

[54] PM Kelly and LR Francis Rose. The martensitic transformation in ceramics—its role in transformation toughening. *Progress in materials science*, 47(5):463–557, 2002.

[55] SH Kirby and LA Stern. Experimental dynamic metamorphism of mineral single crystals. *Journal of structural geology*, 15(9-10):1223–1240, 1993.

[56] WM Kriven. Possible alternative transformation toughеners to zirconia: crystallographic aspects. *Journal of the American Ceramic Society*, 71(12):1021–1030, 1988.

[57] M Rühle and AG Evans. High toughness ceramics and ceramic composites. *Progress in Materials Science*, 33(2):85–167, 1989.

[58] AH Heuer, M Ruhle, and DB Marshall. On the thermoelastic martensitic transformation in tetragonal zirconia. *Journal of the American Ceramic Society*, 73(4):1084–1093, 1990.

[59] G Subhash and S Nemat-Nasser. Dynamic stress-induced transformation and texture formation in uniaxial compression of zirconia ceramics. *Journal of the American Ceramic Society*, 76(1):153–165, 1993.

[60] Patricio E Reyes-Morel, JS Cherng, and IW Chen. Transformation plasticity of ceo2-stabilized tetragonal zirconia polycrystals: Ii, pseudoelasticity and shape memory effect. *Journal of the American Ceramic Society*, 71(8):648–657, 1988.

[61] E Camposilvan and M Anglada. Size and plasticity effects in zirconia micropillars compression. *Acta Materialia*, 103:882–892, 2016.

[62] Andreas Lendlein and Steffen Kelch. Shape-memory polymers. *Angewandte Chemie International Edition*, 41(12):2034–2057, 2002.

[63] Changdeng Liu, Haihu Qin, and PT Mather. Review of progress in shape-memory polymers. *Journal of materials chemistry*, 17(16):1543–1558, 2007.

[64] M Behl and A Lendlein. Shape-memory polymers. *Materials today*, 10(4):20–28, 2007.

[65] RS Langer, A Lendlein, A Schmidt, and H Grablowitz. Shape memory polymers, United States Patent N 6 160 084, 2000.

[66] A Concilio, V Antonucci, F Auricchio, L Lecce, and E Sacco. *Shape Memory Alloy Engineering (Second Edition)*. Butterworth-Heinemann, Boston, second edition edition, 2021.

[67] E Patoor, DC Lagoudas, PB Entchev, and X Brinson, LC nd Gao. Shape memory alloys, part i: General properties and modeling of single crystals. *Mechanics of materials*, 38(5-6):391–429, 2006.

[68] K Bhattacharya et al. *Microstructure of martensite: why it forms and how it gives rise to the shape-memory effect*, volume 2. Oxford University Press, 2003.

[69] B Fultz. *Diffusionless transformations*, page 355–382. Cambridge University Press, 2014.

[70] WX Zhang, YZ Chen, YB Cong, YH Liu, and F Liu. On the austenite stability of cryogenic ni steels: microstructural effects: a review. *Journal of Materials Science*, 56(22):12539–12558, 2021.

[71] K Otsuka. Crystallography of martensitic transformations and lattice invariant shears. In *Materials Science Forum*, volume 56, pages 393–404. Trans Tech Publ, 1990.

[72] JS Bowles and CM Wayman. The bain strain, lattice correspondences, and deformations related to martensitic transformations. *Metallurgical Transactions*, 3:1113–1121, 1972.

[73] PM Kelly. Crystallography of martensite transformations in steels. In *Phase transformations in steels*, pages 3–33. Elsevier, 2012.

[74] HY Luo and EW Abel. A comparison of methods for the training of niti two-way shape memory alloy. *Smart materials and structures*, 16(6):2543, 2007.

[75] A Falvo, F Furgiuele, and C Maletta. Two-way shape memory effect of a ti rich niti alloy: experimental measurements and numerical simulations. *Smart materials and structures*, 16(3):771, 2007.

[76] K Otsuka and X Ren. Recent developments in the research of shape memory alloys. *Intermetallics*, 7(5):511–528, 1999.

[77] Y Xiao, P Zeng, and L Lei. Experimental observations on mechanical response of three-phase niti shape memory alloy under uniaxial tension. *Materials Research Express*, 3(10):105701, 2016.

[78] P Abrahamsson and R Bjämemo. The need for product design tools in shape memory technology. In *Ecomaterials*, pages 1171–1174. Elsevier, 1994.

[79] DJ Wever, AG Veldhuizen, MM Sanders, JM Schakenraad, and JR Van Horn. Cytotoxic, allergic and genotoxic activity of a nickel-titanium alloy. *Biomaterials*, 18(16):1115–1120, 1997.

[80] Jorma Ryhänen. Biocompatibility evaluation of nickel-titanium shape memory metal alloy. 1999.

[81] TW Duerig. Applications of shape memory. In *Materials science forum*, volume 56, pages 679–691. Trans Tech Publ, 1990.

[82] Dieter Stöckel. The shape memory effect-phenomenon, alloys and applications. *Proceedings: Shape Memory Alloys for Power Systems EPRI*, 1:1–13, 1995.

[83] Jaronie Mohd Jani, Martin Leary, Aleksandar Subic, and Mark A Gibson. A review of shape memory alloy research, applications and opportunities. *Materials & Design (1980-2015)*, 56:1078–1113, 2014.

[84] D Chute and D Hodgson. Eyeglass frames and sma—the challenge and the product. *Engineering and Aspects of Shape Memory Alloys*, pages 420–425, 1990.

[85] JD Harrison, DE Hodgson, and J Perkins. Shape memory effects in alloys. *New York*, page 517, 1975.

[86] Robert W Benson, RF Flot, and CL Sandberg. The use of shape memory effect alloys as an engineering material. *Society for the Advancement of Material and Process Engineering,*, pages 403–414, 1983.

[87] GB Brook. Applications of titanium-nickel shape memory alloys. *Materials & Design*, 4(4):835–840, 1983.

[88] JR Yaeger. A practical shape-memory electromechanical actuator. *Mechanical engineering (New York, NY 1919)*, 106(7):51–55, 1984.

[89] Aniket Kolekar, Akshay Natak, Kiran Navratne, and Amol Mali. Recent advancement in shape memory alloy. *International Research Journal of Engineering and Technology (IRJET)*, 4(4):2120–2125, 2017.

[90] Osman E Ozbulut, Stefan Hurlebaus, and Reginald DesRoches. Seismic response control using shape memory alloys: a review. *Journal of Intelligent Material Systems and Structures*, 22(14):1531–1549, 2011.

[91] Massimiliano Ferraioli, Domenico Nuzzo, Salvatore Ameduri, et al. Shape memory alloys for earthquake building protection. In *Sensors and Smart Structures Technologies for Civil, Mechanical, and Aerospace Systems 2019*, volume 10970, pages 487–504. SPIE, 2019.

[92] Papia Sultana and Maged A Youssef. Seismic performance of modular steel frames equipped with shape memory alloy braces. *Bulletin of Earthquake Engineering*, 16:5503–5527, 2018.

[93] RC Sachdeva and Shuichi Miyazaki. Superelastic ni-ti alloys in orthodontics. *Engineering aspects of shape memory alloys*, 452, 1990.

[94] Fujio Miura, Masakuni Mogi, Yoshiaki Ohura, and Hitoshi Hamanaka. The super-elastic property of the japanese niti alloy wire for use in orthodontics. *American Journal of Orthodontics and Dentofacial Orthopedics*, 90(1):1–10, 1986.

[95] Charles T Dotter, RW Buschmann, Montgomery K McKinney, and J Rösch. Transluminal expandable nitinol coil stent grafting: preliminary report. *Radiology*, 147(1):259–260, 1983.

[96] NB Morgan. Medical shape memory alloy applications—the market and its products. *Materials Science and Engineering: A*, 378(1-2):16–23, 2004.

[97] L Petrini and F Migliavacca. Biomedical applications of shape memory alloys. *Journal of Metallurgy*, 2011, 2011.

[98] G Costanza and ME Tata. Shape memory alloys for aerospace, recent developments, and new applications: A short review. *Materials*, 13(8):1856, 2020.

[99] JN Kudva. Overview of the darpa smart wing project. *Journal of intelligent material systems and structures*, 15(4):261–267, 2004.

[100] James P Dunne, Mark A Hopkins, Erwin W Baumann, Dale M Pitt, and Edward V White. Overview of the sampson smart inlet. In *Smart Structures and Materials 1999: Industrial and Commercial Applications of Smart Structures Technologies*, volume 3674, pages 380–390. SPIE, 1999.

[101] DJ Hartl, DC Lagoudas, FT Calkins, and JH Mabe. Use of a ni60ti shape memory alloy for active jet engine chevron application: I. thermomechanical characterization. *Smart Materials and Structures*, 19(1):015020, 2009.

[102] DJ Hartl, JT Mooney, DC Lagoudas, FT Calkins, and JH Mabe. Use of a ni60ti shape memory alloy for active jet engine chevron application: Ii. experimentally validated numerical analysis. *Smart Materials and Structures*, 19(1):015021, 2009.

[103] M Pratik and P Esawara. Shape memory alloys market. *Allied Market Research*, 2021.

[104] Fabrizio Niccoli, Carmine Maletta, Cedric Garion, and Paolo Chiggiato. Heavy industry and high-energy physics. In *Shape Memory Alloy Engineering*, pages 809–853. Elsevier, 2021.

[105] Fabrizio Niccoli, Valentina Giovinco, Cedric Garion, Carmine Maletta, and Paolo Chiggiato. A simplified analytical model to simulate martensite reorientation and plasticity in shape memory alloy ring couplers. *Journal of Intelligent Material Systems and Structures*, 33(12):1497–1512, 2022.

[106] F Niccoli, V Giovinco, C Garion, C Maletta, and P Chiggiato. Niti shape memory alloy pipe couplers for ultra-high vacuum systems: development and implementation. *Smart Materials and Structures*, 31(6):065014, 2022.

[107] Lucio Rossi and Oliver Bruning. *High Luminosity Large Hadron Collider, The: The New Machine For Illuminating The Mysteries Of Universe*, volume 24. World Scientific, 2015.

[108] F Niccoli, G Scalet, V Giovinco, C Garion, C Maletta, P Chiggiato, and F Auricchio. Novel c-shaped shape memory alloy connectors for vacuum flanges: Modeling and tests. *Shape Memory and Superelasticity*, pages 1–12, 2023.

[109] P Šittner, L Heller, P Sedlák, Y Chen, O Tyc, O Molnárová, L Kadeřávek, and H Seiner. B2□ b19′□ b2 t martensitic transformation as a mechanism of plastic deformation of niti. *Shape Memory and Superelasticity*, 5:383–396, 2019.

[110] Bingfei Liu and Chunzhi Du. Effects of external pressure on phase transformation of shape memory alloy cylinder. *International Journal of Mechanical Sciences*, 88:8–16, 2014.

[111] Reza Mirzaeifar, Mahmoud Shakeri, Reginald DesRoches, and Arash Yavari. A semi-analytic analysis of shape memory alloy thick-walled cylinders under internal pressure. *Archive of Applied Mechanics*, 81:1093–1116, 2011.

[112] Bingfei Liu, Guansuo Dui, Lijun Xue, and Benming Xie. On macroscopic behaviors of shape memory alloy thick-walled cylinder under combined internal pressure and radial temperature gradient. *Computer Modeling in Engineering & Sciences*, 94(3):239–260, 2013.

[113] Boris Piotrowski, Tarak Ben Zineb, E Patoor, and A Eberhardt. A finite element-based numerical tool for ni47ti44nb9 sma structures design: Application to tightening rings. *Journal of Intelligent Material Systems and Structures*, 23(2):141–153, 2012.

[114] Majid Tabesh, James Boyd, Kadri Can Atli, Ibrahim Karaman, and Dimitris Lagoudas. Design, fabrication, and testing of a multiple-actuation shape memory alloy pipe coupler. *Journal of Intelligent Material Systems and Structures*, 29(6):1165–1182, 2018.

[115] Tomaz Videnic, Franc Kosel, Viktor Sajn, and Miha Brojan. Biaxial constrained recovery in shape memory alloy rings. *Journal of intelligent material systems and structures*, 19(8):861–874, 2008.

[116] Enrico Radi. Evolution of multiple martensite variants in a sma thick-walled cylinder loaded by internal pressure. *International Journal of Solids and Structures*, 155:15–35, 2018.

[117] P Šittner, P Sedlák, H Seiner, P Sedmák, J Pilch, R Delville, L Heller, and L Kadeřávek. On the coupling between martensitic transformation and plasticity in niti: Experiments and continuum based modelling. *Progress in Materials Science*, 98:249–298, 2018.

[118] Rudy Stalmans, Jan Van Humbeeck, and Lucas Delaey. Thermodynamic modelling of shape memory behaviour: Some examples. *Le Journal de Physique IV*, 5(C8):C8–203, 1995.

[119] Curtis Maitland Jackson, Herbert Julius Wagner, and Roman Jerzy Wasilewski. 55-nitinol-the alloy with a memory: it's physical metallurgy, properties, and application. Technical report, Jena Univ., 1972.

[120] Jeff Perkins. *Shape memory effects in alloys*. Springer Science & Business Media, 2012.

[121] CM Friend. The effect of applied stress on the reversible strain in cuznal shape memory alloys. *Scripta metallurgica*, 20(7):995–1000, 1986.

[122] William B Cross, Anthony H Kariotis, and Frederick J Stimler. Nitinol characterization study. Technical report, NASA, 1969.

[123] L Heller, P Šittner, P Sedlák, H Seiner, O Tyc, L Kadeřávek, P Sedmák, and M Vronka. Beyond the strain recoverability of martensitic transformation in niti. *International Journal of Plasticity*, 116:232–264, 2019.

[124] J Lubliner and Ferdinando Auricchio. Generalized plasticity and shape-memory alloys. *International Journal of Solids and Structures*, 33(7):991–1003, 1996.

[125] CERN. *CAS - CERN Accelerator School : Vacuum Technology: Snekersten, Denmark 28 May - 3 Jun 1999. CAS - CERN Accelerator School : Vacuum Technology*, Geneva, 1999. CERN. Be aware that this URL points to the most recent conference. If this record doesn't concern the most recent one, this URL does.

[126] M LIN and C ROGERS. Analysis of stress distribution in shape memory alloy composite beam. In *32nd Structures, Structural Dynamics, and Materials Conference*, page 1164, 1991.

[127] James G Boyd and Dimitris C Lagoudas. A thermodynamical constitutive model for shape memory materials. part i. the monolithic shape memory alloy. *International journal of plasticity*, 12(6):805–842, 1996.

[128] Angela C Souza, Edgar N Mamiya, and Nestor Zouain. Three-dimensional model for solids undergoing stress-induced phase transformations. *European Journal of Mechanics-A/Solids*, 17(5):789–806, 1998.

[129] F Auricchio, A Reali, and U Stefanelli. A three-dimensional model describing stress-induced solid phase transformation with permanent inelasticity. *International Journal of plasticity*, 23(2):207–226, 2007.

[130] Dimitris C Lagoudas. *Shape memory alloys: modeling and engineering applications*. Springer, 2008.

[131] Ferdinando Auricchio and Lorenza Petrini. A three-dimensional model describing stress-temperature induced solid phase transformations: solution algorithm and boundary value problems. *International journal for numerical methods in engineering*, 61(6):807–836, 2004.

[132] Ferdinando Auricchio and Robert L Taylor. Shape-memory alloys: modelling and numerical simulations of the finite-strain superelastic behavior. *Computer methods in applied mechanics and engineering*, 143(1-2):175–194, 1997.

[133] Huseyin Sehitoglu, Y Wu, S Alkan, and Elif Ertekin. Plastic deformation of b2-niti–is it slip or twinning? *Philosophical Magazine Letters*, 97(6):217–228, 2017.